Stable Purely Organic Radical Thin Films and Interfaces for Applications

Dissertation
der Mathematisch-Naturwissenschaftlichen Fakultät
der Eberhard Karls Universität Tübingen
zur Erlangung des Grades eines
Doktors der Naturwissenschaften
(Dr. rer. nat.)

vorgelegt von
Ewa Malgorzata Nowik-Boltyk
aus Pszczyna/Polen

Tübingen
2024

Gedruckt mit Genehmigung der Mathematisch-Naturwissenschaftlichen Fakultät der Eberhard Karls Universität Tübingen.

Tag der mündlichen Qualifikation:	28.11.2024
Dekan:	Prof. Dr. Thilo Stehle
1. Berichterstatter/-in:	apl. Prof. Dr. Maria Benedetta Casu
2. Berichterstatter/-in:	Prof. Dr. Reinhold Fink

Dedicated to my husband Dr. Patryk Nowik-Boltyk
and my son Luke Nowik-Boltyk

"Sorrow is knowledge: they
who know the most must
mourn the deepest o'er
the fatal truth,
the Tree of Knowledge is not that of Life."

–Lord Byron, Manfred[1]

"Be thou the rainbow in the storms of life.
The evening beam that smiles the clouds away,
and tints tomorrow with prophetic ray."

–Lord Byron, The Bride of Abydos: A Turkish Tale[1]

"Why do we have to listen to our hearts?" the boy asked. "Because, wherever your heart is, that is where you will find your treasure."

–Paulo Coelho, The Alchemist[2]

"And now here is my secret, a very simple secret; it is only with the heart that one can see rightly, what is essential is invisible to the eye."

–Antoine de Saint Exupéry, The Little Prince[3]

"All men have stars, but they are not the same things for different people. For some, who are travelers, the stars are guides. For others they are no more than little lights in the sky. For others, who are scholars, they are problems... But all these stars are silent. You-You alone will have the stars as no one else has them...

–Antoine de Saint Exupéry, The Little Prince[3]

Abstract

English Version

The spotlight of this work is on purely organic radicals, which built an exciting playground for spintronic applications due to their structural diversity, functionality, and intrinsic magnetic moment. The selected radicals were evaporated and deposited on various substrates by organic molecular beam deposition and characterized by joined methods such as X-ray photoelectron spectroscopy, near-edge X-ray fine structure and scanning electron microscopy.

The first part of the thesis is dedicated to the dicyano tetrazolinyl radical that shows a strong tendency toward island formation when evaporated and deposited on different substrates under the presented preparation conditions. The radical forms assemblies with a nanoneedle morphology on SiO_2/Si(111) surface and "monoliths" on gold. The study of radical assemblies on the hybrid substrate, consisting of SiO_2/Si(111) and polycrystalline gold, allowed to investigate the influence of radical-substrate interaction and substrate nature on the assembly morphology. Improved understanding of the growth process on the hybrid interface can aid in the development of a strategy to achieving nanostructures with specific morphology as an integral component of nanodevices.

The second part of the work is dedicated to the Blatter radical derivatives. The stability of Blatter-pyr and diBlatter films is probed under air exposure. The superior air stability of Blatter-pyr with one radical site in comparison to diBlatter that poses two radical center can be explained by water-resistance of Blatter-pyr molecules in films. The following part captures the electronic and magnetic properties of the Blatter-pyr/Co hybrid interface. Hybridization and charge transfer at the interface result in loss of the radical functionality of film molecules and the suppression of the magnetic moment of Co atoms bonded to the organic molecules. The results demonstrate that interface interaction defines the hybrid interface's local chemical and magnetic properties and can be viewed as a powerful approach for manipulating and controlling spin transport in future molecular-based spintronic devices.

Deutsche Version

Der Schwerpunkt dieser Arbeit liegt auf rein organischen Radikalen, die aufgrund ihrer strukturellen Vielfalt, ihrer Funktionalität und ihres intrinsischen magnetischen Moments eine spannende Spielwiese für Anwendungen in der Spintronik darstellen. Die ausgewählten Radikale wurden aufgedampft und durch organische Molekularstrahlabscheidung auf unterschiedliche Substraten abgeschieden, anschießend wurden die Proben mit Hilfe von kombinierten Methoden wie die Röntgenphotoelektronenspektroskopie, Röntgen-Nahkanten-Absorptions-Spektroskopie und Rasterelektronenmikroskopie charakterisiert.

Der erste Teil der Arbeit ist dem Dicyano-Tetrazolinyl-Radikal gewidmet, das eine starke Tendenz zur Inselbildung aufweist, wenn es aufgedampft und auf verschiedenen Substraten abgeschieden wird. Das Radikal bildet Cluster mit einer Nanonadel-Morphologie auf der SiO_2/Si(111)-Oberfläche und Nanostäbchen auf Gold. Die Untersuchung der Radikale auf einem hybriden Substrat, bestehend aus SiO_2/Si(111) und polykristallinem Gold, ermöglichte die Untersuchung des Einflusses der Wechselwirkung zwischen Radikal und Substrat und der Art des Substrats auf die Morphologie der Radikale. Ein besseres Verständnis des Wachstumsprozesses an der hybriden Grenzfläche kann, bei der Entwicklung einer Strategie zur Herstellung eindimensionaler Nanostrukturen mit spezifischer Morphologie als integraler Bestandteil von Nanobauteilen, helfen.

Der zweite Teil der Arbeit ist dem Radikalderivat Blatter gewidmet. Die Stabilität von Blatter-pyr- und diBlatter-Filmen wird unter Luftexposition untersucht. Die überlegene Luftstabilität von Blatter-pyr mit einem Radikalzentrum im Vergleich zu diBlatter, das zwei Radikalzentren aufweist, lässt sich durch die Wasserbeständigkeit der Blatter-pyr-Moleküle in den Filmen erklären. Im folgenden Teil werden die elektronischen und magnetischen Eigenschaften der Blatter-pyr/Co-Hybrid-Grenzfläche beschrieben. Hybridisierung und Ladungstransfer an der Grenzfläche führen zum Verlust der radikalen Funktionalität der Filmmoleküle und zur Unterdrückung des magnetischen Moments der an die organischen Moleküle gebundenen Co-Atome. Die Ergebnisse zeigen, dass die Interaktion an der Grenzfläche die lokalen chemischen und magnetischen Eigenschaften der hybriden Grenzfläche bestimmt und als ein leistungsfähiger Ansatz zur Manipulation und Kontrolle des Spintransports in zukünftigen molekularen spintronischen Bauelementen angesehen werden kann.

Contents

1. Introduction

Purely organic radicals, a particular class of organic compounds with open shell structure, are promising candidates for spintronic materials and quantum technologies. The intrinsic magnetic moment and unique physical and chemical properties of radical molecules are linked to the spin of the unpaired electron or electrons[4,5]. The light element composition of radicals manifests in a reduced weak spin-orbit coupling and weak hyper-fine interaction, representing two main pathways for the spin relaxation process. Consequently, spins of organic radicals retain their orientations for a long time and distance defined by coherence time and length[6–8]. Furthermore, sustainable chemical synthesis enables the design of radical molecules with diverse structures and properties that can be fine-tuned by integrating specific functional groups[7]. These advantages of organic molecules and magnetism united in one package advocates for preferential exploitation of organic radicals in the future spintronic devices compared to their inorganic magnetic counterparts.

Organic radical molecules can serve as quantum bits[5], switchable spin-filters[7], and potential spin current source[9]. Moreover, organic radicals are successfully integrated into the single-molecular junctions (SMJ) by contacting radical molecules with the gold electrodes. In these systems, unpaired spins of radicals give rise to phenomena including Kondo resonance, magnetoresistance (MR), and enhanced conductance[4,8,10].

Purely organic radicals capture attention as potential candidates for hybrid organic/ferromagnetic metal interfaces in potential organic-based spintronic devices. Spinterfaces are realized in organic spin valves (OSV) or organic magnetic tunnel junctions (OMTJs)[11] by placing a thin organic layer between two ferromagnetic metallics electrodes. A strong organic-metal interaction at the interface leads to hybridization between organic molecule orbitals and electronic d states of the ferromagnet. The newly formed hybrid interface states (HIS) and charge transfer give rise to novel spin-dependent and magnetic properties. These interfacial effects determine spin polarisation, spin injection, and transport at the interface and play a significant role in control over device performance[12,13]. Interfacial hybridization and charge transfer shape the electronic structure and magnetic properties of organic and metallic components of the interface[12]. For instance, the adsorption of an organic layer can enhance the magnetic anisotropy and a reduction in the magnetic moment of Co atoms bonded directly to the organic molecules[14,15].

Despite the immense progress in the field of radical-based spintronics and molecular electronics, the limited number of organic radicals possessing sufficient stability for real applications impend future development. To address this particular issue, the first part of this work is dedicated to characterizing a recently synthesized dicyano tetrazolinyl radical as a potential quantum bit due to the long spin coherence time and thermal stability[16].

For a potential integration in devices, the dicyano-substituted radical was evaporated and deposited using organic molecular beam deposition (OMBD) on technologically relevant SiO_2/Si(111) and polycrystalline gold substrates under ultra-high vacuum (UHV) conditions. The first part of the study focuses on the investigation of the electronic structure and bonding mechanism at the organic-substrate interfaces by applying X-ray photoelectron spectroscopy (XPS). The integrity of the radical in the assemblies is investigated by a combination of the electron paramagnetic resonance (EPR) measurements and a fit procedure of the N 1s core-level spectra. Scanning electron microscopy (SEM) is used to determine the assembly morphology. The promising results and intricacies of investigation for both radical interfaces lay the groundwork for the second part of the research, which examines a hybrid system comprising a silicon wafer and a polycrystalline gold surface with the deposited assemblies of dicyano tetrazolinyl radical. The study's main objective is to investigate how the substrate's nature and the radical-substrate interaction at the interface influence the radical assemblies' morphology and structure. Understanding the growth process of dicyano-substituted radical on the hybrid interface is crucial for fabricating nanostructures of the investigated radical with a specific morphology for nanodevices.

The second part of the work focuses on the Blatter-radical derivatives. This class of radicals exhibits extraordinary thermal and chemical stability at ambient conditions coupled to the unique electronic and magnetic properties[17]. These characteristics opened the pathway for successful employment of Blatter-type radicals in various applications such as organic batteries[18], molecular electronics[19], controlled polymerization[20] and photodetectors[21]. Thin films of Blatter radicals can be utilized as an active material in future devices and might close the gap between the research-based and industrial applications. In this context, the study puts special attention on the degradation mechanism of Blatter radical derivatives when exposed to air. Furthermore, drawing inspiration from current advancements in organic-based spintronics with nonmagnetic molecules, this work aims to design and characterize a model radical/Co system. The hybrid interface was prepared by depositing Blatter-pyr radical on a polycrystalline Co surface as a potential active material for spintronics. A combination of soft X-ray-based techniques is used to investigate the electronic structure of radical molecules and Co atoms at the interface and the extent of their interaction. The work focuses on finding evidence for a possible interfacial charge transfer and hybridization and comprehending how the deposited radical layer alters the electronic and magnetic properties of the Co surface. The magnetic moment of cobalt atoms in contact with the organic layer is estimated by using the XPS Co 3*s* core-level spectra analysis and supported by DFT calculations.

The work is organized as follows:

Chapter 1 introduces the general concept of purely organic radicals as spin sources for spintronic and quantum computing applications and defines the main goals of this work.
Chapter 2 presents the organic materials and theoretical foundations of the experimental techniques used in this work.
Chapter 3 provides an overview of the experimental set-up and essential information on the data analysis that was performed.
Chapter 4 discusses the characterisation of the radical assemblies deposited on SiO_2/Si(111) and gold surface. The second part aims to understand the underlying degradation mechanism of Blatter-radical derivatives films upon air exposure. Furthermore, this chapter comprehensively probes the interfacial properties of the hybrid interface between the Blatter-pyr radical and metallic Co.
Chapter 5 highlights the most important results on the presented radical systems.
Chapter 6 summarizes the abbreviations, units, and symbols used throughout the text.
Chapter 7 offers a list of publications that build the foundation of this work and describes the contributions of all authors in detail
The appendices contain all publications, including their supporting information, that build the foundation for this work. Additionally, unpublished material is also included.

2. Theoretical Background

This chapter will briefly introduce the organic radicals investigated in this work, their chemical structure, and their properties. The second part of this chapter will discuss in greater detail the experimental set-up and the soft X-ray techniques used to characterize the radical-based thin films.

2.1. Materials

2.1.1. Blatter Radical Derivatives

The Blatter radical is characterized by extraordinary chemical stability in ultra high vacuum and air due to the extensive delocalization of the unpaired electron or electrons over the ring system[17,22,23]. The high degradation temperature onset enables the controllable growth of radical thin films with intact molecules. Therefore the chemical and thermal stability make Blatter radical derivatives suitable candidates for this work.

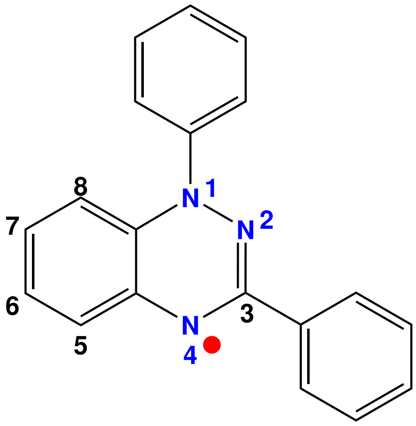

Figure 2.1.: Molecular structure of Blatter radical.

The synthesis of 1,3-diphenyl-1,4-dihydro-1,2,4-benzotriazin-4-ylradical, called Blatter radical (figure 2.1), was first published by H. Blatter in 1968[24]. The central core of the radical molecule has a 1,2,4-triazin ring with three aromatic sites that provide opportunities for chemical modification[17,18].

2.1.1.1. Blatter-pyr Radical

Blatter-pyr (figure 2.2) is a Blatter radical substituted with a pyrene-group in the C_7 position (figure 2.1). Introducing the pyrene group to the Blatter radical increases the molecular weight and decreases the overall vapor pressure, resulting in good film-forming properties and thermal stability of the Blatter-pyr films[22,25]. Additionally, the substituent at the C_7 position protects the radical site against oxidation[23,26]. The spin density is distributed mainly over the triazine core and into the pyrene-substituent[5,22]. The important properties of Blatter-pyr are summarized in table 2.1.

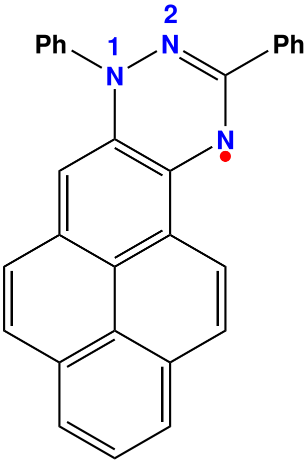

Figure 2.2.: Molecular structure of the Blatter-pyr.

Chemical Formula	$C_{29}H_{18}N_3^{\bullet}$
Formula Weight	408.46 ($\mathrm{g\,mol^{-1}}$)
Density	1.397 ($\mathrm{g\,cm^{-3}}$)
Spin	$\frac{1}{2}$

Table 2.1.: Properties of Blatter-pyr.

2.1.1.2. diBlatter Radical

The diBlatter molecule with a triplet ground-state (S=1) is based on two linked Blatter radical moieties (Appendix C, *ACS Appl. Mater. Interface* **2023**, *15*, 30935-30943). The molecular structure of the diradical (figure 2.3) can be described as a Blatter radical bearing a second Blatter molecule as a substituent at the position C_3 and tert-Butyl group at position C_7[27]. diBlatter shows an onset of decomposition in thermogravimetric analysis (TGA) above 260 °C allowing to obtain thermally stable films. The unpaired electrons are distributed on the fused Blatter radical units. Relevant properties of diBlatter for this work are listed in table 2.2[27].

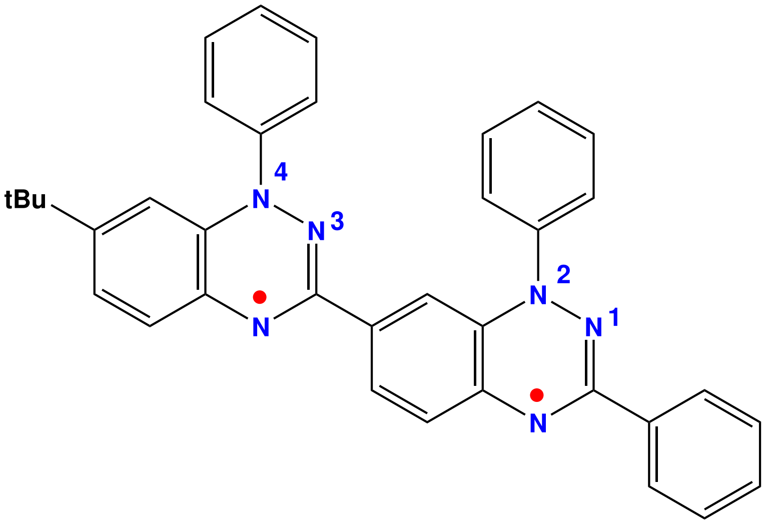

Figure 2.3.: Molecular structure of diBlatter.

Chemical Formula	$C_{36}H_{30}N_6{}^{2\bullet}$
Formula Weight	546.66 ($\mathrm{g\,mol^{-1}}$)
Density	1.356 ($\mathrm{g\,cm^{-3}}$)
Spin	1

Table 2.2.: Properties of diBlatter.

2.1.2. Dicyano Tetrazolinyl Radical

The tetrazolinyl main building block of the radical (figure 2.4), contains a heterocyclic five membered ring with one carbon atom and four nitrogen atoms[16]. The phenyl substituents at the N_2 and N_3 nitrogen atoms are fused to the biphenyle group with two dicyano groups located at the para position. The unpaired electron delocalises across the tetrazolinyl core and the fused benzene rings. The radical is characterized by high thermal stability with an onset of thermal decomposition at 269 °C (Appendix A, *J. Am. Chem. Soc.* **2023**, *145*, 13335-13346).

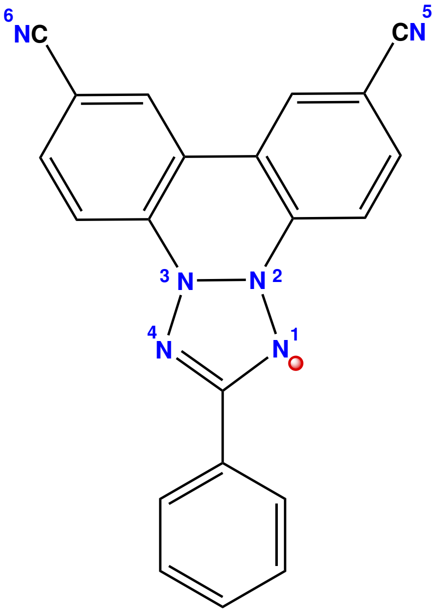

Figure 2.4.: Molecular structure of dicyano tetrazolinyl radical.

A significant spin density at the para-position of the radical is crucial for synthesizing polyradicals with a high spin ground state (S=1). Radicals with paramagnetic properties at room temperature can be created by linking monoradicals together[28]. The X-ray crystallography analysis revealed that the tetrazolinyl and biphenylen-fused units are planar. The radical crystallizes in the monoclinic space group $P2_{1/n}$, and the unit cell comprises one benzene molecule. The radical molecules are arranged into a one-dimensional chain along the crystallographic a-axis, with the closest intermolecular "$N_1 \cdots C_5$" contact between the neighbouring molecules at 3.346 Å. The positive spin density associated with these atoms may be a reason for the antiferromagnetic interaction of radical molecules within the crystal. Furthermore, the close proximity of N_1 and C_5 atoms of two different molecules may also affect the photoemission line of tetrazolinyl moiety (Appendix A, *J. Am. Chem. Soc.* **2023**, *145*, 13335-13346 and paragraph 4.1.2 in this work). Relevant properties of dicyano tetrazolinyl radical are listed in table 2.3.

Chemical Formula	$C_{27}H_{17}N_6^{\bullet}$
Formula Weight	425.46 $(\mathrm{g\,mol^{-1}})$
Density	1.356 $(\mathrm{g\,cm^{-3}})$
Spin	$\frac{1}{2}$

Table 2.3.: Properties of dicyano tetrazolinyl radical.

2.2. Methods

2.2.1. Organic Molecular Beam Deposition

Organic molecular beam deposition has proven successful in the controlled preparation of radical films in a clean UHV environment[25]. The organic material is placed in a crucible of a Knudsen cell and heated until the evaporation temperature is reached. Molecules in vapor escape through a small orifice at the cell's end. The dimension of an orifice with a diameter smaller than the mean free path of organic molecules ensures that a beam of non-interacting molecules is formed and directed onto the substrate surface[29]. The evaporation temperature is adjusted above the sublimation temperature and below the decomposition temperature of the organic material. Controlling and monitoring the evaporation rates during the evaporation process allow reproducible preparation of the organic thin films with defined thickness in the range from mono to multilayers.

2.2.1.1. Growth of Organic Thin Films

Film growth is a complex process in which thermodynamic arguments and kinetic principles must be considered[30]. Thin film formation on a substrate surface could be divided into three characteristic growth modes (showed in figure 2.5): the Volmer-Weber with island, the Frank-Van der Merwe with layer, and the Stranski-Krastanov with layer grow followed by island formation. The classification can be understood in terms of the interaction strength between molecule-molecule and substrate-molecule[30–32]]. Pure island growth occurs when the molecule-molecule bonding strength dominates. Small clusters form on the substrate surface and grow into three dimensional (3D) islands. By contrast, in layer-by-layer mode, the interaction between the substrate and molecules exceeds the molecule-molecule interaction. A stable nucleus grows in two dimensions (2D), forming uniform planar sheets. The growth of the second layer begins when the first layer is completed[30]. The combination of island and layer growth modes characterizes the Stranski-Krastanov growth. After the surface is covered by one or more uniform layers at the initial stage, molecules nucleate into clusters that grow into three dimensional islands[30].

The growth mode of an organic film can be determined using thickness-dependent XPS measurements[30]. For this purpose, the signal intensity attenuation of the substrate is plotted against film coverage. In the case of layer growth, there is a fast exponential signal progression with increasing film thickness. In contrast, island growth shows a slight decrease in substrate intensity. The Stranski-Krastanov growth mode exhibits a characteristic bend in the curve, attributed to the transition from layer-by-layer mode to island growth.

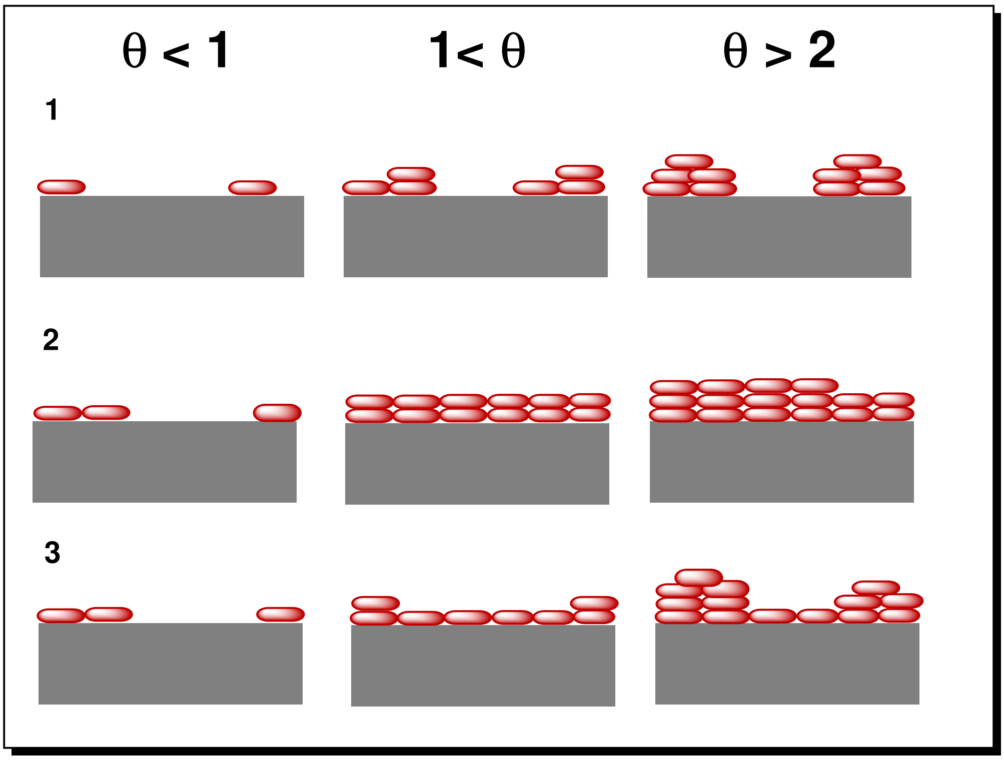

Figure 2.5.: Film growth modes as a function of the coverage Θ in monolayers (ML).

The film deposition parameters, like the deposition rate, substrate temperature, and substrate surface properties, including roughness, directly impact organic material nucleation and film formation[33–35].

A deposition by OMBD occurs under non-equilibrium conditions in supersaturation[36,37]. Supersaturation can be controlled by parameters such as the substrate temperature, evaporation rate, molecular weight, the heat of sublimation, and the entropy of sublimation[30,38]. In the case of radical films, evaporation rates are low to avoid the degradation of the sensitive radical materials. Further, the molecule's properties affect the film deposition. The film preparation of molecules with two or more radical centers is more challenging due to their reactivity, which limits the temperature window for evaporation. Under this consideration, molecules form islands preferentially rather than grow in 2D layers[35].

2.2.2. X-Ray Photoelectron Spectroscopy

X-ray photoelectron spectroscopy is a well-established method for surface characterization that allows the determination of element composition, chemical bonding, and stoichiometry of the material in the sample[39]. A matter exposed to the X-ray radiation of sufficient energy emits electrons (photoelectrons) from the surface (figure 2.6). The process is known as the photoelectric effect[40–42]. The incoming photons interact and yield their entire energy to the electrons in the atomic shells. Excited electrons emerge from the material into the vacuum when the incident light energy exceeds their ionization energy. The number of photoelectrons increases with higher light intensity. However, if the energy of the photons is lower than the threshold value, no photoemission occurs[39,42]. The emitted photoelectrons enter an analyzer with the kinetic energy that depends linearly on the incident photon energy hv according to Einstein's relation[42]:

$$E_{kin} = hv - E_B \tag{2.1}$$

where E_B correlates to the binding energy of the electron in the atom of molecules. In free atoms and molecules, the binding energy E_B of electron in a specific core-level is referenced to the vacuum level E_{vac}. In solid materials, electrons require additional energy to surpass a potential barrier at the surface and exit into the vacuum. The barrier's strength is related to the work function ϕ, which is the difference in energy between the vacuum level and the Fermi level E_F. The electron binding energy in solids is referred to the Fermi level and can be calculated by equation 2.2 :

$$E_B^F = hv - E_{kin} - \phi \tag{2.2}$$

A typical XPS spectrum (figure 2.7) displays the intensity of photoemission signals as a function of the binding energy or kinetic energy[43]. The binding energies of photoelectrons are characteristic quantities for each element and its orbitals. The presence of the element's photoemission lines in the spectrum reflect the chemical composition of the sample.

In addition to photoemission lines, the XPS spectrum exhibits the Auger peaks, satellites, and plasmon features. Their presence originates from the relaxation processes accompanying a core-hole formation. The Auger peaks correspond to the excitation of electrons from the

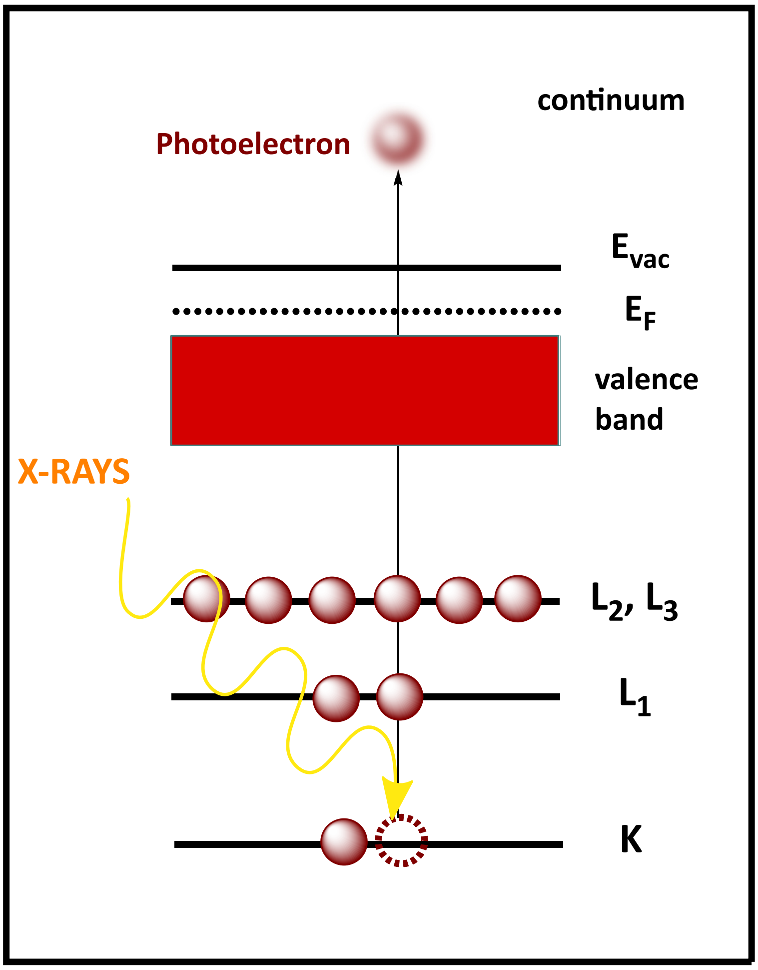

Figure 2.6.: Scheme of the photoemission of core-electrons.

outer shells to a continuum. The energy is provided by the de-excitation of the core hole, where an electron from the upper level fills the vacancy[44].

The excitation of valence electrons simultaneously with the ionization of the core leads to the shake-up satellites, with higher binding energies than the main peaks (Appendix A, *J. Am. Chem. Soc.* **2023**, *145*, 13335-13346 and Appendix C, *ACS Appl. Mater. Interface* **2023**, *15*, 30935-30943). The satellite features are characteristic for the XPS spectra of aromatic conjugated molecules, and their analysis provides information on the intramolecular charge redistribution after photoionization. In metals, an outgoing photoelectron interacts with the plasmon vibrations, and the spectrum displays a series of low-intensity peaks on the higher energy side of the main line[44]. Furthermore, the position of the photoemission lines in spectra depends on the chemical environment of the emitting atom, and the signal intensity corresponds to the element concentration in the system. Accordingly, XPS can be used for

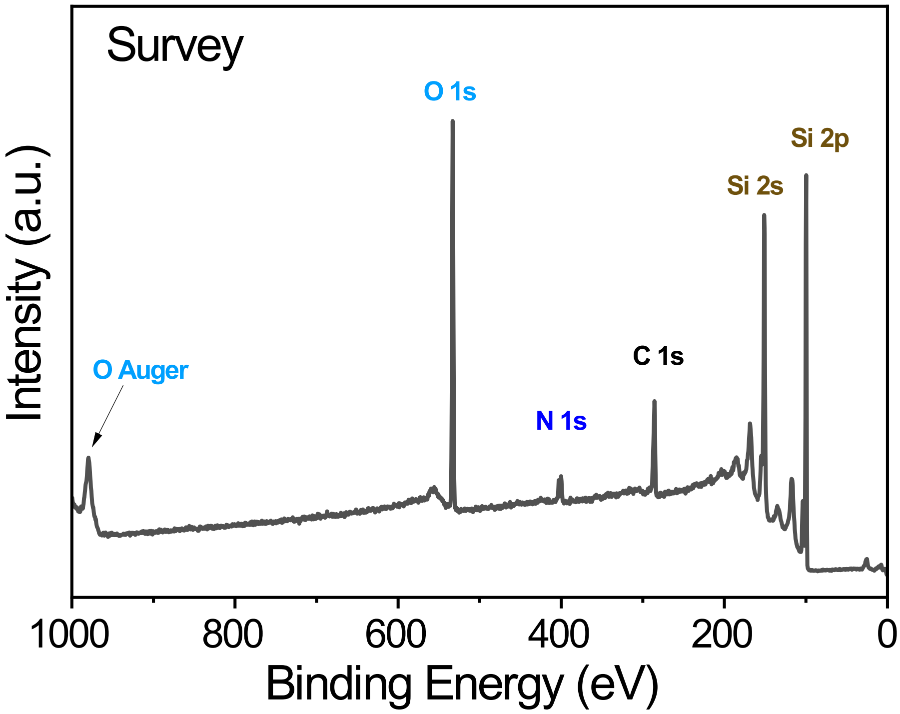

Figure 2.7.: Survey spectrum of dicyano tetrazolinyl radical assembly on the SiO_2/Si(111) surface recorded with the X-ray incident energy of 1486,6 eV (Al Kα).

analytical purposes[45].

One of the essential advantages of X-ray photoelectron spectroscopy is its ability to provide surface-sensitive information. The inelastic mean free path λ_{IMPF} (IMPF) determines the sensitivity of XPS and refers to the distance that a photoelectron with a certain kinetic energy can travel between two inelastic collision events, assuming elastic scattering is not taken into account[40]. λ_{IMPF} is considered a limiting parameter for XPS because only photoelectrons that reach the detector without energy loss contribute to the photoemission lines in the spectra. By contrast, any inelastically scattered electrons with enough kinetic energy to escape the surface will appear as a background signal. The inelastic electron-electron and electron-phonon collisions lead to the energy loss of photoelectrons. Most of the solids display a similar relationship between IMPF and kinetic energy within the range of 10-2000 eV, which is represented by the “universal curve” show in figure 2.8. The IMPF values reach a minimum at energies 50-200 eV and steadily increase for higher kinetic energies[40].

The λ_{IMPF} can be determined according to equation 2.3 developed by Seah and Dench[46]:

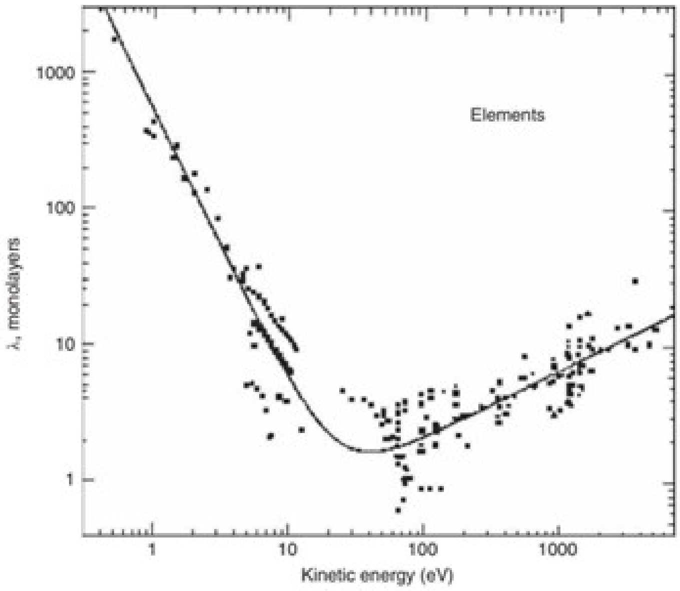

Figure 2.8.: Inelastic mean free path as a function of kinetic energy[44].

$$\lambda_{IMPF} = A \cdot E_{kin}^{-2} + B \cdot E_{kin}^{0.5} \tag{2.3}$$

Parameters A and B describe the material properties affecting the IMPF. In the case of organic materials, the values for A and B are 49 and 0.11, respectively[46]. Tunable radiation sources enable variation of the kinetic energy of photoelectrons and the surface sensitivity. The photoelectron's probability for reaching the surface decreases exponentially with increasing depth d. The escape depth Δ of photoelectrons defines an average distance normal to the surface, from which photoelectrons are emitted with no energy loss[40]. Δ and IMPF are connected by the relation:

$$\triangle = \lambda_{IMPF} \cdot cos\Theta \tag{2.4}$$

with Θ as the electron emission angle to the surface normal. For normal emission ($\Theta = 0°$) follows:

$$\triangle = \lambda_{IMPF} \tag{2.5}$$

The Lambert-Beer law describes the intensity reduction of the photoelectrons without any energy loss during transmission through a sample with a thickness d:

$$I_t = I_0 exp^-(\frac{d}{\lambda_{IMPF} \cdot cos\Theta}) \tag{2.6}$$

where I_0 represents the incident intensity and I_t the transmitted intensity. Equation 2.6 allows to define the information depth d = $3\lambda_{IMPF}$. It is the maximum distance perpendicular to the surface from which 95 % of all detected photoelectrons originate[44].

2.2.3. Near Edge X-Ray Absorption Fine Structure Spectroscopy

Near edge X-ray absorption fine structure (NEXAFS) spectroscopy works by exciting core levels through the absorption of X-ray radiation (figure 2.9)[43,47].

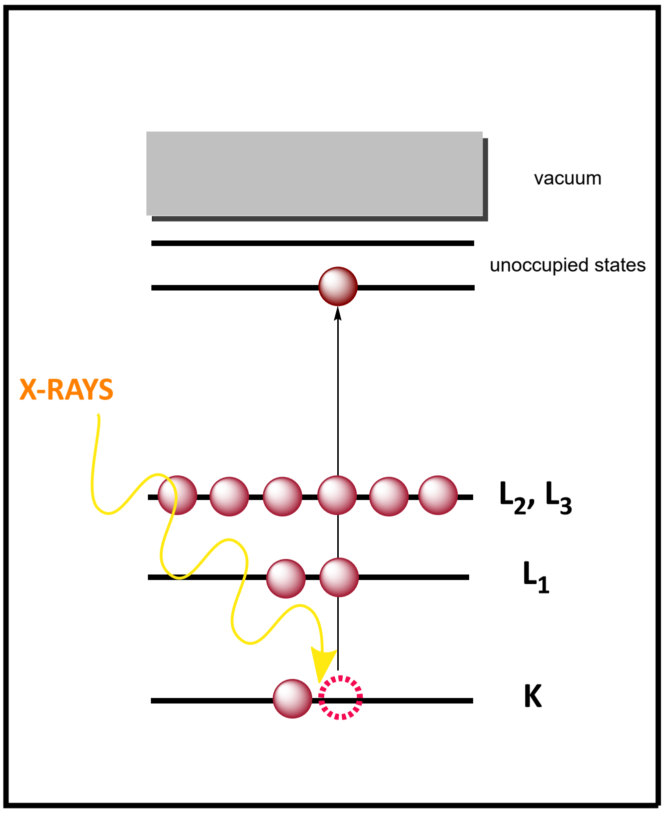

Figure 2.9.: Scheme of the X-ray absorption process.

When the incident radiation reaches the binding energy of the core level, electrons are excited to the unoccupied states below the vacuum level. A sharp jump, known as the absorption edge, is observed in the spectrum. Elements possess unique energies for their core-levels, and respectively distinct absorption energies. This method is sensitive to elements and is valuable for investigating the oxidation state, electronic structure, and coordination chemistry of atoms[48].

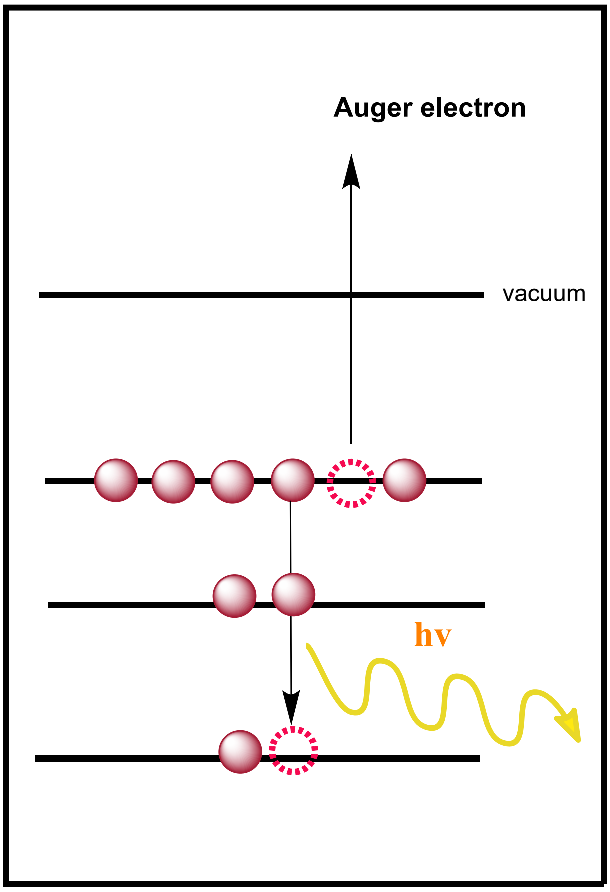

Figure 2.10.: De-excitation process of the core-hole by emission of an Auger electron and photon.

The absorption coefficient μ characterizes the absorption of X-ray radiation passing through an absorbing sample with thickness d and depends strongly on the excitation energy[48]. μ is derived from the attenuation of the incident beam intensity due to the absorption event, using the modified Lambert-Beer law (equation 2.6).

$$I_d = I_0 exp(-\mu d) \tag{2.7}$$

NEXAFS measures the intensities I_0 and I_d. The resulting spectrum represents the fine structure of the X-ray absorption coefficient in dependence on the incident photon energy[49]. The transmission mode is restricted to sufficiently thin samples, which allow transmission of the X-ray beam through the entire specimen. Both surface and bulk signals contribute to the overall absorption coefficient.

Absorption measurements of adsorbate molecules on the substrate surface and samples with arbitrary thickness rely on detecting core-hole decay products[43,50]. Absorption of X-ray and excitation of a photoelectron leaves a core-hole behind (as depicted in figure 2.10). The deexcitation of the core-hole follows two main pathways. An electron from the upper energy state drops and fills the hole. The free energy can be released as an X-ray photon (fluorescence). The second decay channel involves energy transfer to an electron in the outer shell and emission of the Auger electron into the continuum.

The Auger electron yield (AEY) and fluorescence yield (FI) corresponds to the number of core-holes. Both are proportional to the absorption coefficient[43,48,50]. The total electron yield mode (TEY) measures the drain current from the sample with a pico-amperometer. It reaches probing depths of 3-10 nm[43]. The most sensitive surface detection mode is AEY, which measures only Auger electrons that come from the first few layers[48]. In order to perform NEXAFS and energy-dependent XPS measurements, a tunable X-ray source is necessary. Synchrotron radiation provides a photon source with high brilliance, a wide range of accessible photon energies, and a pulsed time structure[51,52].

3. Experimental

This section will focus on the experimental set-up and the preparation of the substrate and the radical films. The second part will provide a brief description of the measurements that were performed and will introduce the data analysis.

3.1. The UHV System at Home Laboratory

A series of XPS experiments were performed in a 4-chamber UHV system, which enables cleaning of the substrate surface, radical thin film deposition, and characterization without breaking the vacuum. The UHV system is designed around the analytical unit (base pressure: 2×10^{-9} mbar) with the attached preparation chamber (base pressure: 5×10^{-9} mbar) and a deposition chamber for organic evaporation (base pressure: 3×10^{-8}).

A substrate is introduced to the system through a load lock and transferred further to the preparation chamber, designed for surface cleaning. A Specs IQE 10 ion source is incorporated in this chamber for surface cleaning by sputtering, which operates with argon gas. The sample holder enables the annealing of the samples with a heated metal filament. The chamber designed for preparing organic films is equipped with a Knudsen evaporator. The integrated components of the effusion cell, K-type thermocouple, and DC controller enable precise control over the evaporation temperature of organic materials. A quartz microbalance positioned above the aperture of a Knudsen cell measures evaporation rates during film deposition.

The substrate surfaces and radical thin films were investigated by using XPS in the analytical module. It is equipped with a monochromatic Al-$K\alpha$ source (SPECS Focus 500) and a SPECS Phoibos 150 MCD hemispherical electron analyser. XPS survey spectra were recorded at 50 eV pass energy and high-resolution core-level spectra at 20 eV pass energy. All measured binding energies were calibrated by taking the substrate signals as a reference (Si $2p$ at 99.8 eV, Au $4f_{7/2}$ at 84.0 eV, Co $2p$ at 778.3 eV and In $3d_{5/2}$ at 444.3 eV[53,54]).

3.2. Preparation of the Substrate Surfaces

Cobalt foil (MaTeck, 99.9 % purity), polycrystalline Co films with a thickness in a range from 7 to 13 nm deposited on Al_2O_3/(0001), SiO_2/Si(111) wafers, and polycrystalline Au foil (GoodFellow, 99.9 % purity) were used as the substrates for the radical thin film deposition.

For measurements of the radical powder samples, the powder was embedded in indium foil (Chempur, 99.9 % purity) by pressing into the surface. Organic polycrystalline compounds are subjected to the charging effects occurring during the XPS measurements due to the low conductivity. This is characterized by the energy shifts and line-broadening in the spectrum[37]. Embedding the radical material in indium metal with good conductivity minimizes the sample charging.

The cleaning routine of the cobalt surface consists of repeated sputtering and heating cycles. The substrate was cleaned by sputtering with 2 keV argon ions and following 25 min annealing at 280-320 °C. The cleanness of the substrate was controlled by recording a XPS survey spectrum. The cleaning procedure of the cobalt substrate was repeated until no trace of contaminants was detectable in the survey spectrum.

The Co films deposited on Al_2O_3/(0001) substrate were prepared by the research group led by Alek Dediu (CNR-ISMN). The samples were fixed on the sample holder using carbon tape. Due to the insulating properties of aluminum oxide, a silver paste was used to establish a conductive contact between the sample holder and the cobalt layer. The silver contacts prevented sample charging during XPS measurements but, at the same time, did not allow the annealing step after sputtering of the surface with Ar ions (800 eV).

SiO_2/Si(111) wafers underwent an ultrasonic cleaning in acetone and methanol for one hour each, followed by annealing at 500 K for several hours. The effectiveness of the cleaning procedure was verified by XPS.

The cleaning procedure of the gold substrate was divided into two separate protocols. The first protocol included three alternating cycles of sputtering with Ar ions at 800 eV for 30 minutes, followed by annealing at 200 °C for 10 minutes. In experiments where the dicyano tetrazolinyl radical was deposited on a hybrid substrate consisting of SiO_2/Si(111) and Au surfaces, the substrates were cleaned by one cycle of sputtering at 500 eV for 30 min and annealing at 200 °C for 10 min.

3.3. Preparation of the Radical Films

Molecule	**Substrate**	**Evaporation Pressure (mbar)**	**Evaporation Rate (nm/min)**
Blatter-pyr	Co foil Co/Al_2O_3/(0001)	10^{-7}	0.1 – 0.5
diBlatter	SiO_2/Si(111) wafers	10^{-8}	0.2
Dicyano tetrazolinyl radical	SiO_2/Si(111) wafers Au foil Hybrid: Au-SiO_2/Si(111)	10^{-7}	0.1 – 0.3

Table 3.1.: Evaporation parameters for the Blatter-pyr, diBlatter and dicyano tetrazolinyl radical.

The film preparation of the Blatter-pyr, diBlatter, and growth of the dicyano tetrazolinyl radical assemblies follows the same procedure in the deposition chamber. The radical molecules were evaporated and deposited on the clean substrate surface using a Knudsen cell. During film deposition, the substrates were kept at room temperature. All evaporation parameters for the three radicals are listed in table 3.1. The evaporation rates were determined before and after the evaporation process with a quartz crystal microbalance. The freshly prepared films and assemblies were directly transferred to the analysis chamber and characterized by XPS. For experiments investigating the air film stability, the radical films were exposed to air in dark and again investigated by XPS, tracking the changes visible in the spectra after air exposure.

3.4. Experiments at the BESSY II Synchrotron Facility

A series of NEXAFS measurements were conducted at the CoESCA end-station installed at UE-52 PGM beamline and at the LowDosePES end-station located at the PM-4 soft-X-ray dipole beamline of BESSY II in Berlin. The CoESCA and LowDosePES end-stations share a similar design. They both feature a radial distribution chamber that connects the analysis chamber with a load lock, sample storage, and preparation chambers. The preparation chamber is equipped with a 4-axis sample manipulator with resistive heating capabilities, a sputter gun, and ports for evaporator cells. The analysis chamber is equipped with an angle-resolved time-of-flight (ArTOF) spectrometer. The main characteristics of ArTOF, such as high transmission, fast acquisition time, and reduced dose rate, make it a suitable tool for studying radiation-sensitive samples[55,56]. The CoESCA station, in contrast to the LowDosePES station, features two ArTOF spectrometers positioned at a 54.6° angle with respect to the photon beam. This setup enables measurements to be taken in coincidence mode or separately[57]. The Coesca, with a soft X-ray plane grating monochromator, is characterized by photon energies ranging from 120 eV to 1600 eV and a photon flux of 10^{12} ph/s/100 mA. The resolving power can reach more than $E/\Delta E$=10 000 at 400 eV[57]]. By comparison, the LowDose provides photon energies in the range of 7 to 2000 eV and $E/\Delta E$=60 000 at 400 eV[58].

The preparation of the substrates, and film deposition of Blatter-pyr, diBlatter and dicyano tetrazolinyl radical followed the procedures described in sections 3.2 and 3.3. The same Knudsen cell was used for the radical film growth as at the home lab to achieve reproducible film preparation conditions.

The XPS survey spectra and the C 1s, N 1s, Si 2p, and O 1s core-level spectra were measured with a linearly polarized photon beam with the energy at 850, 700, and 560 eV. For the valence band spectra and Co 2p high-resolution spectra, the excitation energies at 150 and 990 eV were used, respectively.

The NEXAFS spectra were recorded in total energy yield. For the normalization of the spectra, the clean substrate signal and the ring current were used, and all spectra were scaled to achieve an equal edge jump. The NEXAFS measurements were carried out in the normal incidence at 90° and grazing incidence at an angle of 20-30°.

3.5. Data Analysis

3.5.1. Film Thickness

The Beer's law (equation 2.6 in paragraph 2.2.2) can be applied to estimate the attenuation of the substrate signal intensity I_1 as a function of film thickness d (nm)[44]. Thickness is defined by equation 3.1[59]:

$$d = -\lambda_{IMPF} \cos\theta \ln\left(\frac{I_1}{I_0}\right) \tag{3.1}$$

where, I_0 represents the intensity of substrate spectroscopic line without organic overlayer and λ_{IMPF} its inelastic mean free path length. The XPS spectra were recorded in normal emission, where the emission angle of the photoelectrons θ with respect to the surface normal equals 0° ($\cos 0° = 1$). The nominal film thickness was determined by extracting the integrated substrate signal intensities from survey spectra of both clean and radical layer-coated substrates. The survey spectra were subjected to the baseline correction before integration. The λ_{IMPF} value for Co $2p$ was calculated from equation 2.3 using factors for inorganic compounds $A = 641$ and $B = 0.096$[46]. The IMPF for Si $2p$ and Au $4f_{7/2}$ were derived by the interpolation of the calculated IMPF values given in Ref.[60]. The λ_{IMPF} values used in this work are listed in table 3.2.

Core-level	**Si 2p**	**Co 2p**	**Au 4f$_{7/2}$**
λ_{IMPF} (nm)	3.17	2.32	1.74

Table 3.2.: Estimated IMPF values using the photon energy of 1486.6 eV for all substrates.

3.5.2. Quantitative Analysis

XPS enables to estimate the concentration of elements present in the samples. The integrated area of the element's photoemission lines, including their satellites, corresponds to the element concentration n_i and can be calculated by equation 3.2[44]:

$$n_i = \frac{A_i}{S_i} \tag{3.2}$$

A_i represents a measured peak area of an element corrected by its S_i standardized sensitivity factor[61]. The empirically obtained sensitivity factors include an energy correction for the transmission function of the analyzer, the elemental cross-section and the λ_{IMPF} of the photoelectrons[62]. For quantitative analysis of the radical films, the carbon and nitrogen concentration were estimated, with the signal areas extracted from the overview spectra with the following sensitivity factors: C $1s = 0.25$, N $1s = 0.42$[61]. Element percentage of nitrogen and carbon in the films were calculated according to equation 3.3[44]:

$$\%n_i = 100(\frac{n_i}{\sum n_i}) \tag{3.3}$$

The total sum includes the concentrations of carbon and nitrogen, which are the elements visible in XPS that build the radical molecule. For stoichiometric radical films, where molecules retain their radical character upon film deposition, the obtained intensity ratio C/N agrees with the theoretical values determined by the chemical structure of the radical molecule.

3.5.3. Fit Analysis

The fit analysis is a mathematical tool used to approximate the experimental XPS curves and identify the binding energies of the single contributions to the main lines in the spectra (see paragraph 2.2.2). The peak assignment reveals information on the chemical bonds and screening processes in the system under investigation[63]. The XPS lines are fitted with the Voigt profile, a convolution of the Lorentzian and Gaussian functions. The stoichiometry, electronegativity, bond strength, and experimental resolution set the fit procedure's limitations[64,65]. The Lorentzian profile describes the intrinsic life-time broadening and vibronic broadening. The Lorentzian width is given by the Heisenberg uncertainty principle (equation 3.4) with the finite life-time of the core-hole τ[44,66]:

$$\Gamma = \frac{h}{\tau} \tag{3.4}$$

The h represents the Plank constant (eV/second). The values for τ (second) are accessible from the high resolution absorption spectra and are published. In performing the fit analysis of the C 1s and N 1s core-level spectra, the constant Lorentzian widths, 0.08 eV for C 1s and 0.1 eV for N 1s were used as fit parameters[67,68].

The Gaussian profile takes into account all the factors contributing to the inhomogeneous line broadening from experiments, including the analyzer's resolution and the dispersion of the monochromatic X-ray beam. Additionally, the impact of film morphology and molecular orientation in the layer on the line width is also considered[69]. For stoichiometric films, the ratios of the estimated relative signal intensities agree with the molecule structure. The fit procedure gives information on the film stoichiometry and provides direct evidence for the successful film deposition[25].

4. Results and Discussions

The first two sections will highlight the key findings from the investigation of the assemblies of the dicyano tetrazolinyl radical deposited on SiO_2/Si(111) wafer, polycrystalline Au foil and hybrid substrate. Further, the study will cover the degradation mechanism of Blatter-pyr and diBlatter radical films and the stability of dicyano tretrazolinyl radical assemblies upon exposure to air. Finally, a comprehensive analysis of the interface between Blatter-pyr and ferromagnetic cobalt will be provided.

4.1. Dicyano Tetrazolinyl Radical on SiO_2/Si(111)

The following section introduces a new radical system based on dicyano tetrazolinyl radical grown on SiO_2/Si(111) wafer and it is presented in figure 4.1.

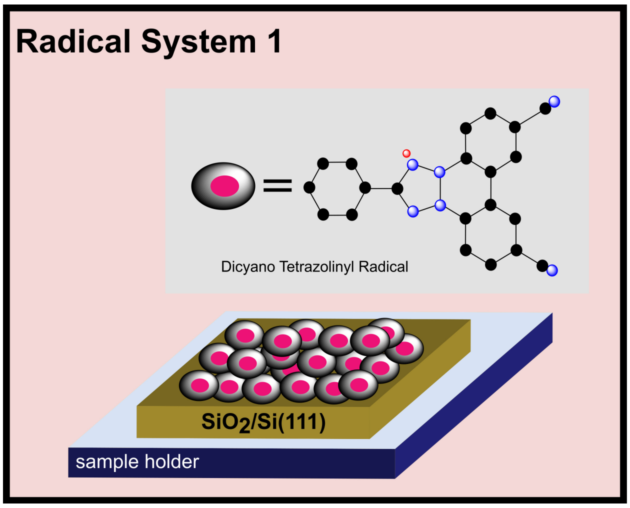

Figure 4.1.: The first system of the dicyano tetrazolinyl radical: radical assembly deposited on SiO_2/Si(111) substrate.

4.1.1. Motivation

As mentioned in the introduction, organic radicals are considered as promising materials for molecular spintronics[9,10], organic magnets[9,28], quantum computing, and quantum information processing[5,70]. Successful realization of organic radicals as spin source materials in spintronics and quantum computing technologies depends on the availability of the suitable radical candidates. The limited number of radicals with a sufficient stability at ambient condition represents a major challenge for further progress in this field. Consequently current development concentrates on finding new suitable radical-candidates. In this context, this study concentrates on the $2,2'$-biphenylene-fused tetrazolinyl radical with two cyano substituents. The dicyano tetrazolinyl radical, with properties like high thermal and chemical stability in combination with a long electron spin coherence time ($T_m \approx 7$ µs at 40–80 K), meets the expectations as a promising candidate for spin-based devices (Appendix A, *J. Am. Chem. Soc.* **2023**, *145*, 13335-13346).

Dicyano tetrazolinyl radical was evaporated on the SiO_2/Si(111) substrate by OMBD (section 3.3). Radical molecules form assemblies on the surface during the deposition process. An XPS analysis was performed to determine the concentration of elements, chemical composition, and stoichiometry of radical molecules in assemblies. The assembly's growth, morphology, and stability upon air exposure were also examined. This part of the work refers to the results published in *J. Am. Chem. Soc.* **2023**, *145*, 13335-13346 (Appendix A).

4.1.2. Quantitative Analysis

This paragraph will highlight the most significant results obtained from the XPS analysis of dicyano tetrazolinyl radical assemblies. Element concentrations were calculated from a survey spectrum (as outlined in paragraph 3.5.2) to verify the stoichiometry of radical assemblies. The experimental ratio C/N is consistent with the chemical composition of the molecule.

The fit analysis of the N 1*s* and C 1*s* core-level spectra (figure 4.2) provide additional quantitative evidence for the radical deposition without degradation. The contributions of the single components and their satellites to the N 1*s* and the C 1*s* photoemission lines agree with the molecule stoichiometry. These findings are further supported by the analysis of the powder spectra (figure 4.2). The fit results demonstrate that the radical molecules of the assemblies maintain their radical property, as confirmed by EPR measurements (Appendix A, *J. Am. Chem. Soc.* **2023**, *145*, 13335-13346).

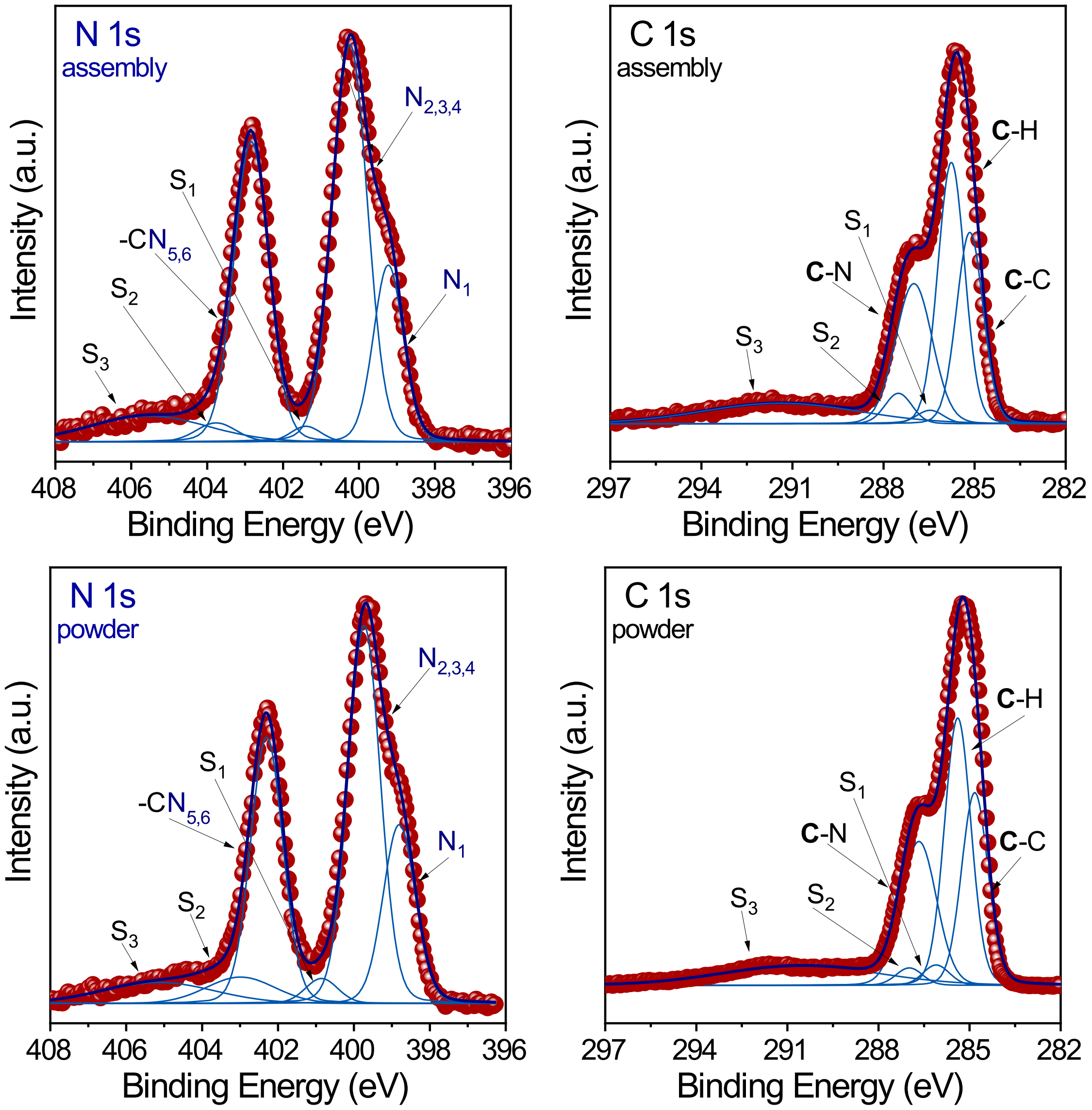

Figure 4.2.: (top panel) N 1*s* and C 1*s* core-level spectra with their fit components of a dicyano tetrazolinyl radical assembly on SiO_2/Si(111) compared (bottom panel) to the powder spectra.

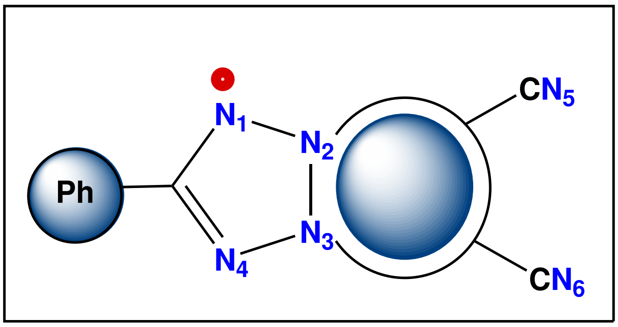

Figure 4.3.: Schema of the dicyano tetrazolinyl radical molecule.

The radical molecule contains four nitrogen atoms in the tetrazolinyl unit and two nitrogen atoms in the cyano substituents (CN) (figure 4.3). The first main line at 400.4 eV includes a combined contribution of photoelectrons assigned to the aminic nitrogen atoms N_2 and N_3 and the imine-like N_4 atom of the tetrazolinyl species. The nitrogen atoms in the tetrazolinyl ring have a very similar chemical environment, causing their photoemission lines to overlap and to emerge as a single line in the spectrum. The one asymmetric line is also detected in the N 1*s* spectra of molecules with a tetrazole functionalization[71,72].

As opposed to tetrazoles, the radical nitrogen component N_1 appears in the N 1*s* spectrum as a distinct shoulder at 399.4 eV. The possible explanation takes into consideration the crystal structure of the dicyano tetrazolinyl radical described in paragraph 2.1.2. As mentioned, the closest distance between the two neighbouring molecules involves the N_1 and C_5 atoms. This short intramolecular "$N_1 \cdots C_5$" contact with only 3.346 Å may enhance the core-hole screening and lowers the binding energy of photoelectrons of N_1 atoms. The close inspection of the N 1*s* core-level spectra of the radical powder (figure 4.2) also reveals the presence of the characteristic shoulder at lower binding energies associated with the radical nitrogen atom. This suggests that the molecules in both assemblies and powder are arranged similarly.

The C 1*s* core-level spectrum exhibits two main features at 286.0 eV and 287.2 eV. The first signal at lower binding energy corresponds to the photoelectrons emitted by the carbon atoms involved in the C−C and C−H bonds. The second photoemission line at 287.0 eV is assigned to the carbon atoms with electronegative nitrogen atoms as bonding partners.

4.1.3. Growth

The growth mode and morphology of radical assemblies were studied by XPS and scanning electron microscopy. The observed exponential profile of the attenuation curve of the substrate Si 2*p* intensity with increased assembly thickness indicates Volmer-Weber (VW) growth mode, where only islands are formed. The still strong substrate signal at higher coverage speaks against a Stranski–Krastanov (layer(s) + islands) growth process (paragraph 2.2.1.1). The XPS findings yield excellent agreement with the scanning electron microscopy measurements of the radical assembly. SEM images (figure 4.4) reveal needle-like morphology on the surface with diameters ranging from 10 to 100 nm.

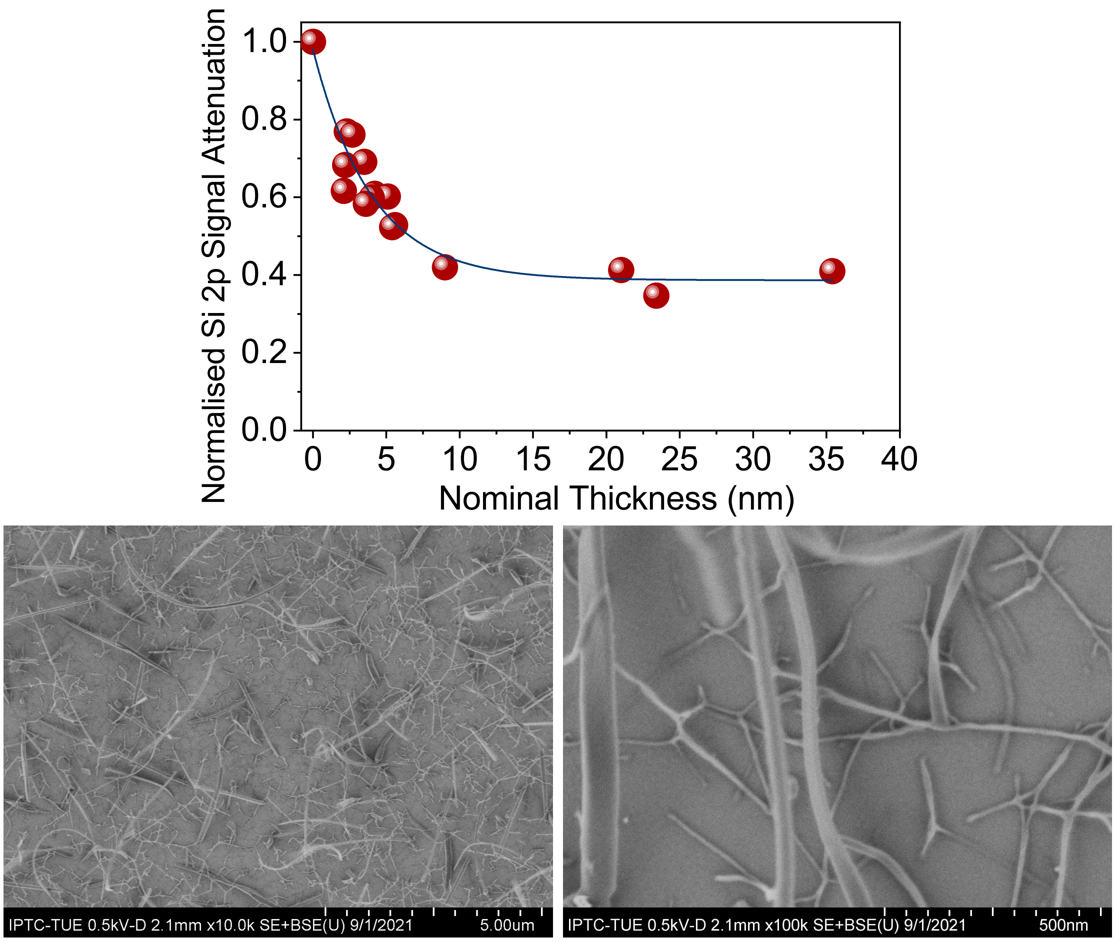

Figure 4.4.: Attenuation of the Si 2*p* substrate signal in dependence of the dicyano tetrazolinyl radical coverage (top) and SEM images of the radical nanoneedles (bottom).

4.2. Nanostructure of Dicyano Tetrazolinyl Radical Assemblies

This section introduces a second system of dicyano tetrazolinyl radical based on the assemblies deposited on polycrystalline gold surface and followed by investigation of assemblies grown on the hybrid substrate, consisting of gold and SiO_2/Si(111) surfaces. The results of the fit procedure of the XPS core-level spectra can be found in Appendix B.

4.2.1. Dicyano Tetrazolinyl Radical on Polycrystalline Gold

Nanomaterials with special morphologies such as nanorods, nanobelts, nanowires, and nanoneedles exhibit unique optical and electrical properties. Due to those characteristics, the are regarded as the base structure for designing new electronic and spintronic devices[73]. Section 4.1 demonstrated that dicyano tetrazolinyl radicals grown on a SiO_2/Si(111) substrate forms islands with a characteristic nanoneedle shape. The nanoneedle morphology, in connection to air stability, radical character, and hence magnetic properties, laid a solid foundation for potential future applications in nanoscale electronics and optoelectronics[73].

In analogy to the dicyano tetrazolinyl radical/SiO_2/Si(111) system (section 4.1, Appendix A, *J. Am. Chem. Soc.* **2023**, *145*, 13335-13346), the radical assemblies deposited on polycrystalline gold foil (figure 4.5) were investigated by thickness-dependent XPS measurements and SEM techniques. A special emphasis was put on the growth process and the interaction between the radical assemblies and the gold surface. The results of the fit procedure of the core-level spectra are included in Appendix B.

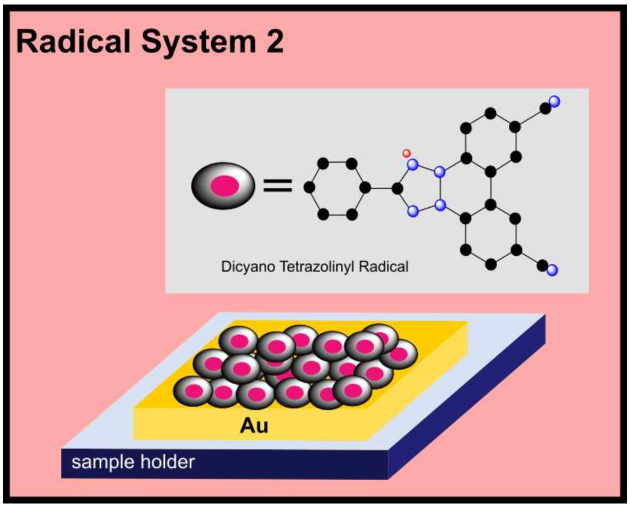

Figure 4.5.: The second system of the dicyano tetrazolinyl radical: radical assembly deposited on polycrystalline gold.

Thickness-dependent XPS spectra assist in understanding the radical molecule-metal interaction at the interface and allow to distinguish between physisorption and chemisorption, the two main mechanisms responsible for bonding adsorbate onto the substrate surface. Chemisorption is characterised by a strong chemical interaction that results in bond formation between the organic molecules and substrate atoms due to hybridization. The redistribution of electron density upon interaction modifies the electronic structure of molecules and, consequently, the XPS line-shape and intensity, respectively[74,75]. The counterpart, physisorption, relies on weak van der Wals forces, which do not perturb the core-level states significantly, and the observed shifts of energy position of XPS lines in core-level spectra of physisorbed organic

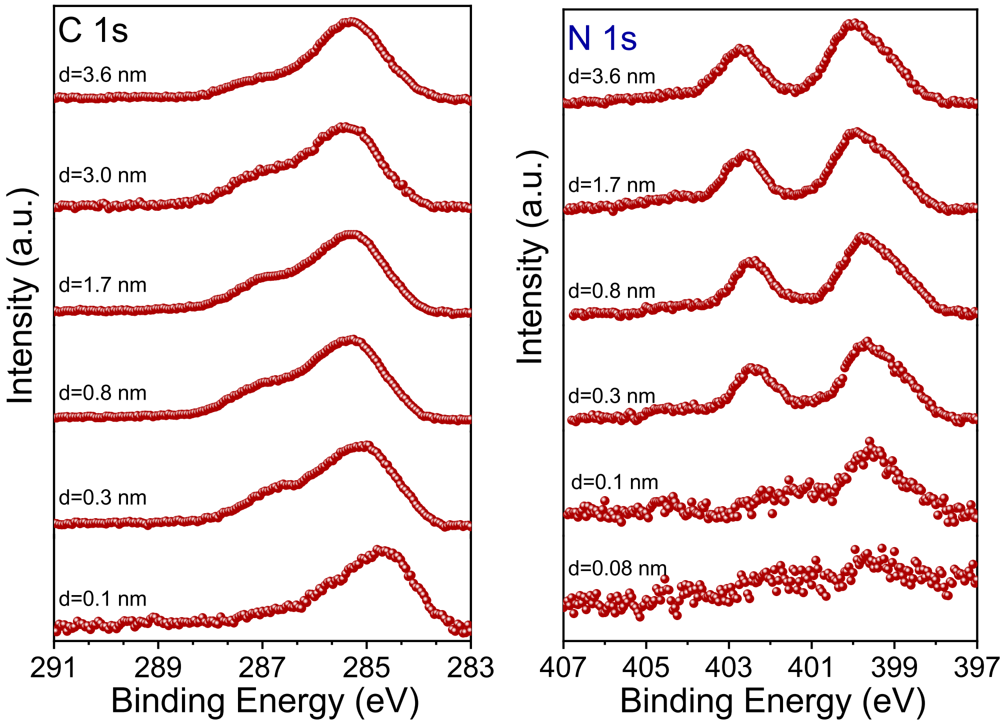

Figure 4.6.: Development of the C 1*s* and N 1*s* photoemission lines with an increased assembly thickness.

molecules can be explained by image charge potential or charge transfer process[75].

The direct comparison between the N 1*s* core-level spectra for thinner and thicker assemblies presented in figure 4.6 evidences two significant changes: the energy shift of the spectroscopic lines towards lower binding energies and substantial modification of the line shape and intensities for radical molecules in direct contact with the gold surface. This behaviour of the XPS signals stands in contrast to those of the radical/SiO_2/Si(111) system, where the XPS lines, apart from small energy shifts, are invariant to changes in thickness.

Performing a fit analysis of the N 1*s* and C 1*s* core-level spectra (figure 4.7, Appendix B) of the assemblies with different thickness provides a detailed description of the interaction-induced changes in spectra of radical molecules in contact to gold surface. The N 1*s* and C 1*s* photoemission lines of the thicker assemblies (figure 4.7, top panel) show all the characteristic features that are observed in the spectra of radical assemblies deposited on SiO_2/Si(111) substrate (figure 4.2, section 4.1, Appendix A, *J. Am. Chem. Soc.* **2023**, *145*, 13335-13346). The intensity ratios of the single contributions to the main lines, including their satellites, satisfy the radical molecule stoichiometry. The different nature of the gold substrate in

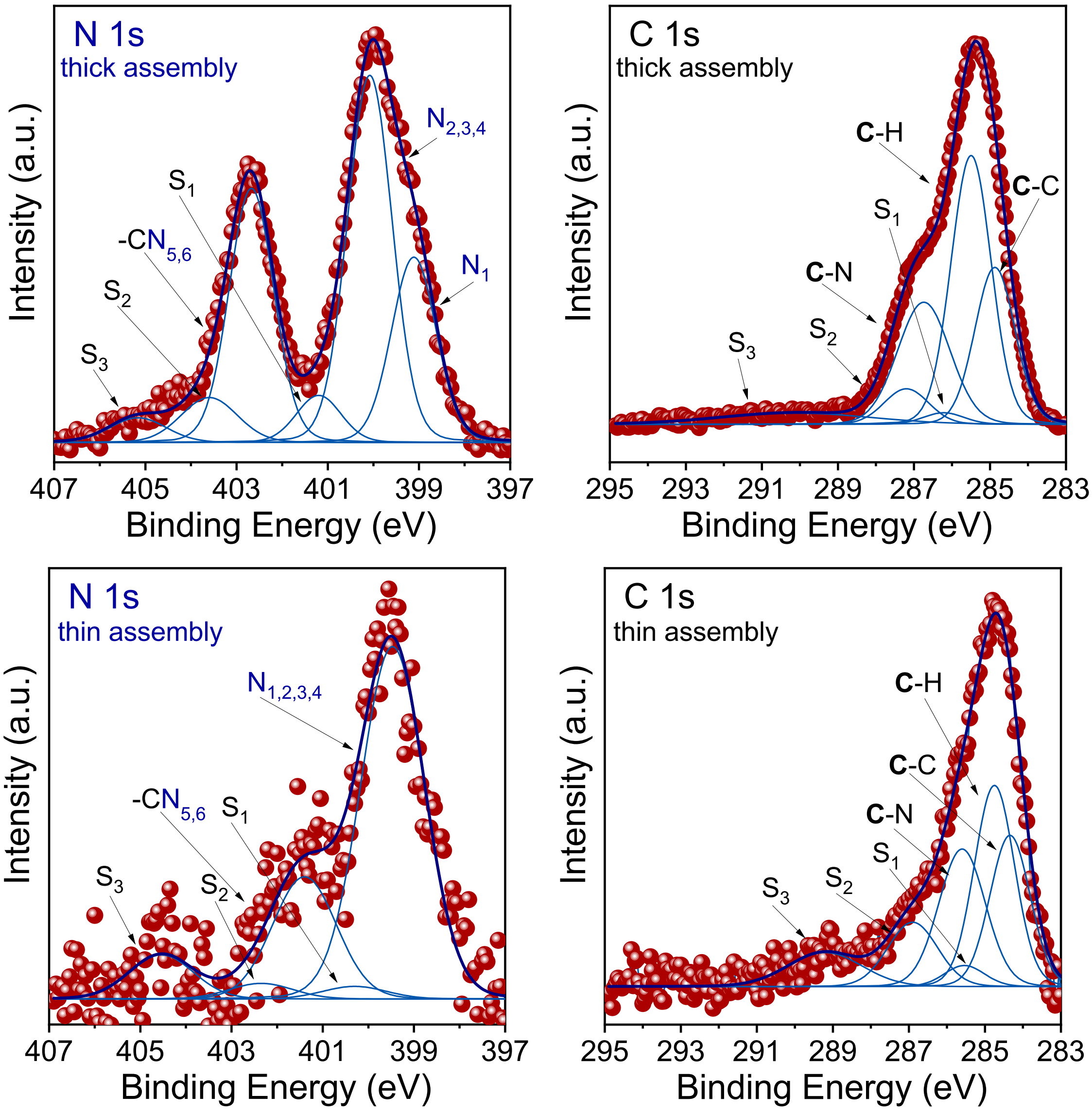

Figure 4.7.: Dicyano tetrazolinyl radical deposited on gold. (top panel) N 1*s* and C 1*s* core-level spectra (including their fits) of a thicker assembly (nominally 2.9 nm) compared to (bottom panel) the spectra of a thin assembly (nominally 0.1 nm).

comparison to SiO_2/Si(111) affects slightly the energy positions of the C 1*s* and N 1*s* lines of the thicker assemblies in systems. Furthermore, the lines are narrower, with smaller Gaussian widths (Appendix B), and they hint at different arrangements of the radical molecules on the gold surface[63].

By reducing the assembly thickness to 0.3 nm, the two dominant features in the N 1*s* core-level spectrum of thicker assemblies, attributed to the photoelectrons of the tetrazolinyl unit

($N_{2,3,4}$ component at 399.1 eV and N_1 component at 400.1 eV) and the cyano group at 402.7 shift to lower energy site (∼ 0.3 eV). The shake-up satellite energy positions and intensities are affected differently. The shake-up satellites S_1 and S_3 experience different shifts (0.1 eV and 0.5 eV) in the opposite direction to S_2, which moves 0.5 eV to higher binding energy. In addition, the intensity of the S_1 and S_2 features increases, and that of the S_3 satellite decreases.

Reaching the interfacial region (0.1 nm thickness, figure 4.6, lower panel in figure 4.7), where molecules are in direct contact with the gold surface, the N 1*s* core-level spectrum displays distinct changes in the line shape and intensities. The feature corresponding to the photoelectrons coming from the radical nitrogen and observed in the N 1*s* spectra of thicker assemblies at 399.1 eV merges together with the contribution of the photoelectrons from the three nitrogen atoms of the tetrazolinyl group. The component at 399.4 eV represents all four nitrogen atoms of the tetrazolinyl unit, and its relative signal intensity of 66.9 %, including satellite S_1, agrees with the theoretical value. The spectroscopic line belonging to the nitrogen atoms of the cyano groups is most affected by the interaction with the substrate and assigned to a broad peak signal at 401.4 eV. The two satellites, one intense at 404.5 eV and the second with lower intensity at 402.4 eV, are ascribed to the CN contribution to fulfil the stoichiometric requirements of the radical molecule.

The C 1*s* line follows the trend of the thickness-related changes observed in the N 1*s* core-level spectra. At the interface, the main features associated with the photoelectrons of the aromatic ring system (C−C and C−H components) are shifted about 0.7 eV to the lower binding energy. The contribution of the carbon atoms bonded to the nitrogen atoms shows a shift in position at 1.1 eV and a closer distance to the C−H component. Additionally, a strong interaction between radical molecules and gold visibly affects the satellite features, increasing their relative intensities[76,77]. The differences in the satellite intensities at the interface and for thicker assemblies are attributed to the different charge redistribution upon photoexitation.

The N 1*s* and C 1*s* lines of the assembly at the interface manifest a relevant modification of the line shape and intensity, implying the chemisorption of the radical molecules on the gold surface. The contribution of the tetrazolinyl-core and the CN component are significantly affected in the N 1*s* and C 1*s* core-level spectra, indicating that the whole molecule engages in the interaction with the gold substrate and the molecules lose their radical functionality. Furthermore, chemisorption impacts visibly the intensities of the satellite features in core-level spectra as reported for the CN substituted pentacene derivative deposited on Au(111) single crystals[76]. The alterations regarding the CN contribution in the C 1*s* and N 1*s* spectra suggest a chemical coupling between the cyano groups and gold atoms. In the literature examples are published for organic molecules attached to the gold surface through bond forming between their cyano functionality and gold atoms. In fact, the high affinity of the CN group towards gold favours a chemical bond to the metal surface[78–80].

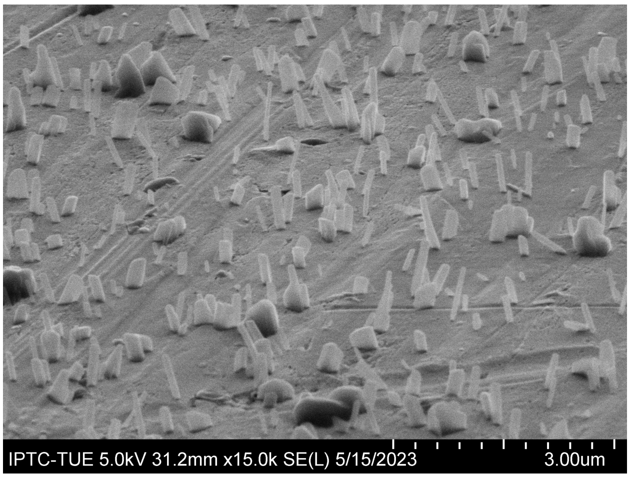

Figure 4.8.: SEM image of the dicyano tetrazolinyl radical assembly on gold.

The SEM investigation (figure 4.8) of the radical assemblies on gold reveals a island growth mode with the unmistakeable morphology, that is called in this work “monolith”. Monolith morphology is characterised by compact vertical islands with a random distribution.

The monolith morphology of dicyano tetrazolinyl radical deposited on gold differs indisputably from the nanoneedles of assemblies on SiO_2/Si(111) wafers. The following paragraph 4.2.2 is dedicated to examine the dissimilarities in electronic structure and island morphology of the radical assemblies in two systems.

4.2.2. Dicyano Tetrazolinyl Radical on Hybrid Substrates

This part of work discusses the dicyano tetrazolinyl radical assemblies that are evaporated and deposited on a hybrid substrate consisting of polycrystalline gold and SiO_2/Si(111) surfaces (as depicted in figure 4.9). Implementation of a hybrid substrate ensures identical conditions for preparation and deposition, such as deposition rate and substrate temperature on two surfaces. The substrate itself is the only factor to consider that influences the growth process (see paragraph 2.2.1.1). The following experiment gives an opportunity to examine the interplay between the radical-substrate interaction at the interface and the assembly preferential morphology. The motivation for this study arises from the fact that the adsorbate-substrate interaction plays a prominent role in defining and controlling the film growth, molecular orientation, and film morphology at the hybrid interfaces[77]. An enhanced understanding of the growth process of the target radical on different surfaces may enable the precise fabrication of nanostructures with a specific morphology.

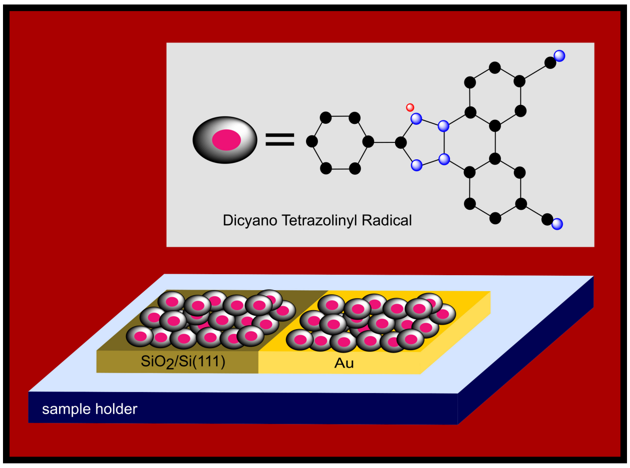

Figure 4.9.: Radical assemblies deposited on Au-$SiO_2/Si(111)$ substrate.

XPS and SEM measurements were conducted on the radical assembly grown on the gold and $SiO_2/Si(111)$ surfaces of a hybrid system . The main focus is laid on the comparison of the XPS core-level spectra of radical assembly in both system based on the results of the fit analysis and their islands morphology visible in the corresponding SEM images. The fit results and fit parameters are included in Appendix B.

Figure 4.10 shows the N 1*s* core-level spectra of a thicker radical assembly deposited on the hybrid polycrystalline Au-$SiO_2/Si(111)$ surface. The intensities of the single contributions of the experimental N 1*s* lines, obtained through the fit analysis, agree with the radical molecule stoichiometry and confirm intact radical molecules on both surfaces. The main features in the N 1*s* core-level spectrum of the assembly deposited on gold are shifted at around 0.2-0.3 eV towards lower binding energies, compared to the photoemission lines of the assembly on $SiO_2/Si(111)$. The N 1*s* line on gold shows a slight line broadening, and the characteristic shoulder at lower binding energy correlated to the Nrad contribution is less pronounced in contrast to the N 1s spectrum on $SiO_2/Si(111)$. The most striking dissimilarities between the two N 1*s* core-level spectra are the higher signal intensities of the first shake-up satellite S_1

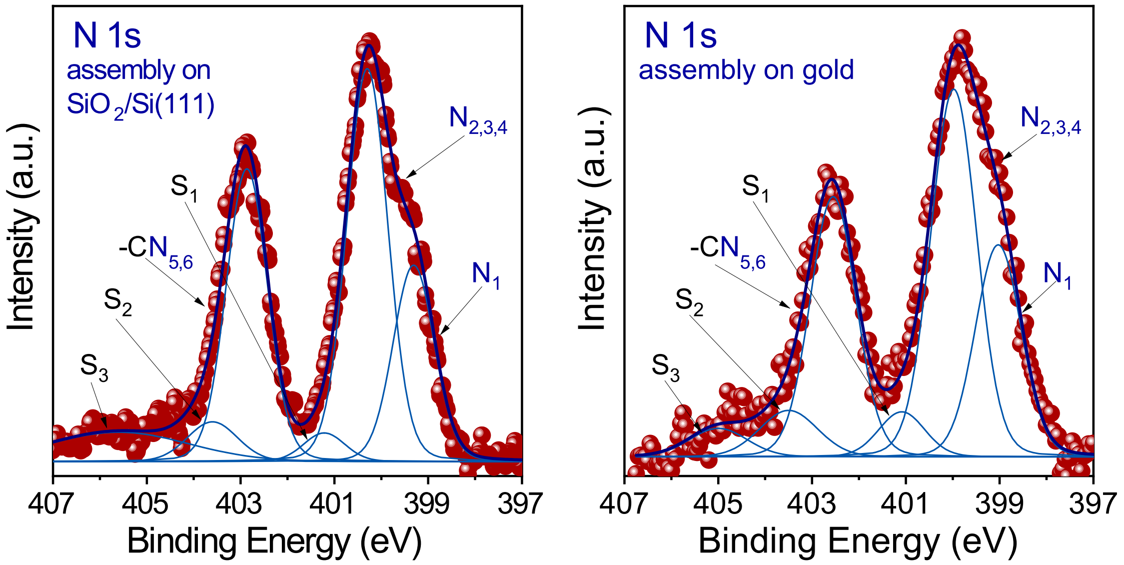

Figure 4.10.: N 1s spectroscopic lines with the fit components of the radical assemblies deposited (left) on SiO_2/Si(111) and (right) on polycrystalline gold.

(4.6 %) at 401.1 eV and the second satellite features S_2 (5.9 %) at 403.5 eV on gold. For the assembly deposited on SiO_2/Si(111), the corresponding satellite signal S_1 shows 2.7 % lower intensity. The S_3 satellite feature (8.0 %) is the most intense satellite. The dissimilarities in the core-level spectra of the radical assemblies deposited on two surfaces reflect their different morphology in agreement with SEM measurements.

The SEM images in figure 4.11 illustrate the radical assemblies with two different morphology grown on the hybrid substrate. On SiO_2/Si(111) surfaces the nanostructure show a nanoneedle morphology and on polycrystalline gold, the characteristic monoliths. These findings correlate with the results of the investigation on the single radical systems (figure 4.4, paragraph 4.1.3) and (figure 4.8, paragraph 4.2.1).

Comparison of the core-level spectra of the radical assemblies on the hybrid substrate establishes a clear link between the satellite intensities and the assembly's morphology. Importantly, the strength of molecule-substrate interaction differs for radical assemblies in the two systems and plays an active role in determining the assembly morphology. Dicyano tetrazolinyl radical molecules are chemisorbed on polycrystalline gold and physisorned on SiO_2/Si(111). It can be assumed that a strong interaction of the radical with gold affects the molecule arrangement in the assembly deposited on the gold surface. Presumably, the assembly molecules have a different molecular orientation than molecules deposited on the SiO_2/Si(111), where

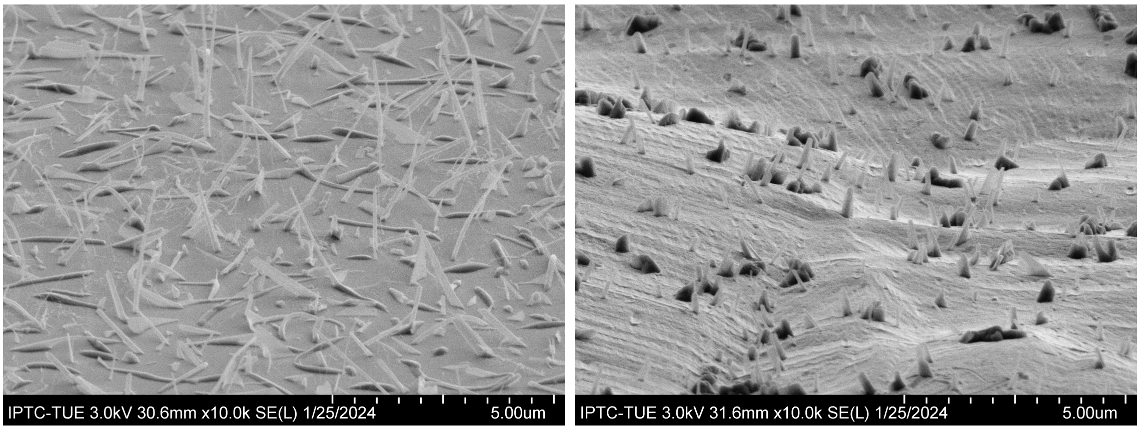

Figure 4.11.: SEM images of dicyano tetrazolinyl assemblies grown on the hybrid substrate: on SiO_2/Si(111) (left) and on polycrystalline gold (right).

interaction with substrate is weak. Future NEXAFS measurements can verify this aspect. The successful deposition of radical assemblies on the hybrid substrate under controlled environment proves, that the nature of the substrate, degree of the molecule-substrate interaction and bonding mechanism (chemisorption or physisorption) determine the assembly morphology.

4.3. Radical Thin Films Stability Under Air Exposure

The present chapter will thoroughly explore the chemical stability of Blatter radical films and their degradation mechanism in air. Furthermore, it will examine the impacts of air exposure on the electronic structure and radical functionality of the recently synthesized and characterized dicyano tetrazolinyl radical assemblies.

4.3.1. Blatter-pyr and diBlatter Radical

Organic radicals, when exposed to air, tend to undergo recombination, hydrogen abstraction, or oxidation to fulfil their valency requirements[81]. However, in recent years, progress has been made in engineering radical molecules with remarkable chemical stability[82]. Radical states can be protected by delocalizing an unpaired electron in the aromatic systems or introducing steric demanding groups[5,22,25,82].

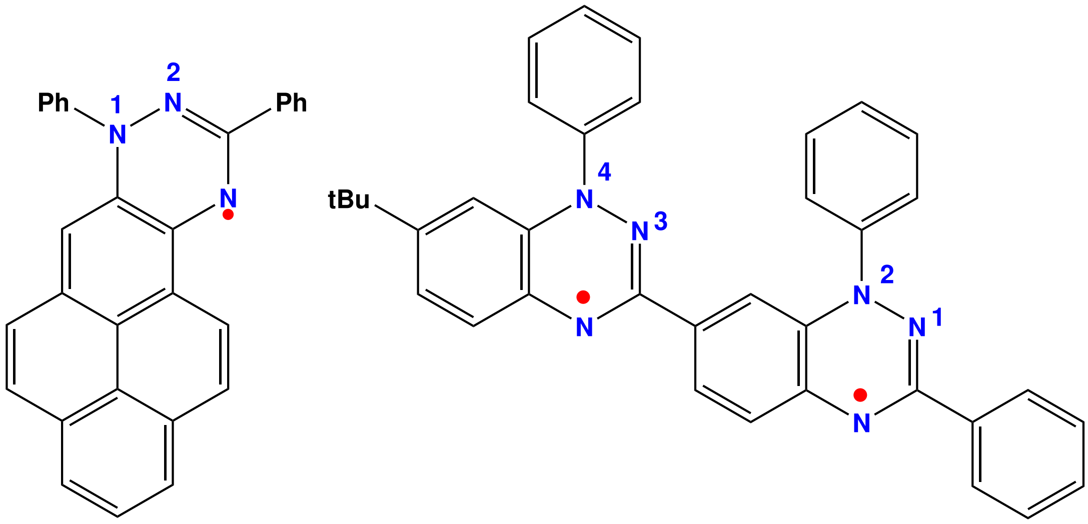

Figure 4.12.: Molecular structures of Blater-pyr and diBlatter.

Specifically, Blatter radical derivatives are a class of radicals with strong chemical stability due to the extend delocalisation of an unpaired electron or electrons across the triazinyl ring (see paragraph 2.1.1). Although the lifespan of Blatter radical films in the air is longer when compared to other open and closed shell organic molecules (as cited in references[5,83,84], see also paragraph 2.1.1), it still remains limited[22,27]. This work aims to deepen the understanding of these long-term degradation mechanisms in Blatter radical thin films and how they affect the film molecule's radical character and magnetic properties. The knowledge of the degradation mechanism will be valuable for the engineering of radicals with improving stability for applications in devices. For this purpose, two Blatter radical derivatives, Blatter-pyr and diBlatter (figure 4.12), were selected. The thin films of both radicals were prepared and characterized by XPS before and after exposure to air. The results of those examinations are included in Appendix C and published in *ACS Appl. Mater. Interface* **2023**, *15*, 30935-30943.

In the initial phase of the investigation, the stoichiometry of the freshly evaporated Blatter-pyr and diBlatter films is determined by a fit analysis of the N 1s and C 1s core-level spectra. The fit results are used as a reference to capture potential variations in the N 1s and C 1s lines after exposure to air. Here, the N 1s line can be regarded as a sensitive indicator for modification in the local chemical surroundings of nitrogen atoms, the spin carrying units of the molecule. In the case of degradation of the film molecules, changes in the line shape and intensity are expected[22]. Consequently, the main focus of this study lies in the detailed analysis of the N 1s lines of radical films.

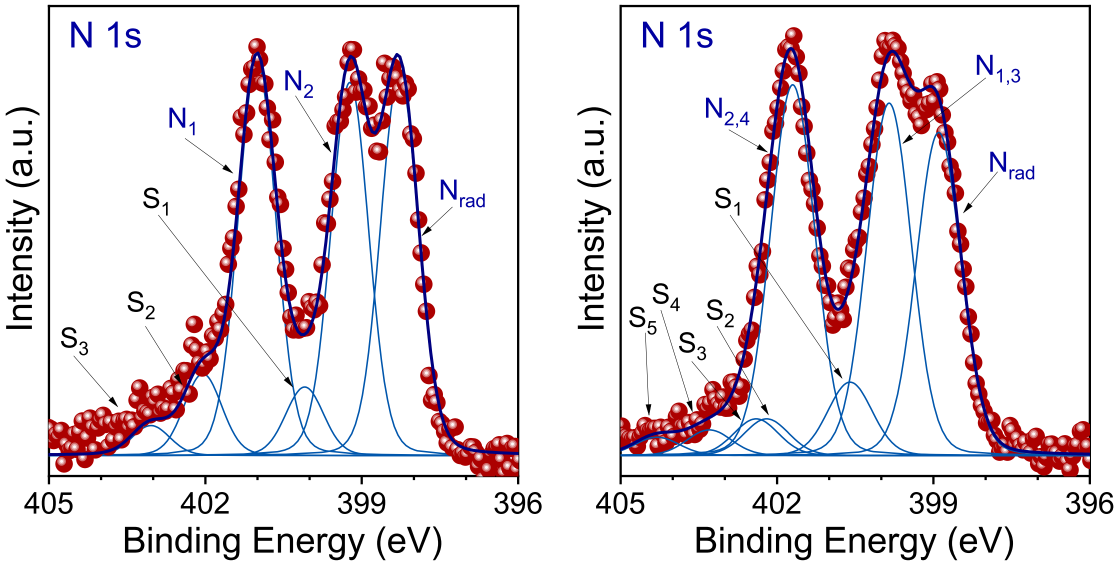

Figure 4.13.: N 1*s* core-level spectra of fresh Blatter-pyr (left, nominal thickness: 6 nm) and diBlatter (right, nominal thickness: 1 nm) films with their fit components.

As shown in figure 4.13, three main features dominate the N 1*s* core-level spectrum of Blatter-pyr films, assigned to the three chemically distinct nitrogen atoms of the triazine ring. The component with the lowest binding energy of 398.3 eV corresponds to the photoelectrons of radical nitrogen Nrad because of the delocalized nature of the unpaired electron[22]. The obtained signal intensity ratios of the main lines 1:1:1 match the molecule structure. The expected Blatter-pyr stoichiometry and the presence of the Nrad feature prove that the radical molecules retain their radical character upon film deposition (Appendix C, *ACS Appl. Mater. Interface* **2023**, *15*, 30935-30943).

diBlatter contains two fused Blatter radicals. In both molecules, the atoms experience very similar chemical environments. As a consequence, the features in the N 1*s* (figure 4.13) and C 1*s* core-level spectra (Appendix C, *ACS Appl. Mater. Interface* **2023**, *15*, 30935-30943) of Blatter-pyr resemble those of diBlatter. The N 1*s* line shows three characteristic contributions of nitrogen atoms of the triazin-ring (1:1:1) and confirms intact radical molecules in the film.

In the second step of the study, the lifetime of Blatter-pyr and diBlatter films was examined by exposing freshly evaporated films to air and characterizing them with XPS. The core-level spectra of the air-exposed films were compared to the fresh films' spectra.

After being exposed to air for 45 h, the N 1*s* core-level spectrum of the Blatter-pyr film

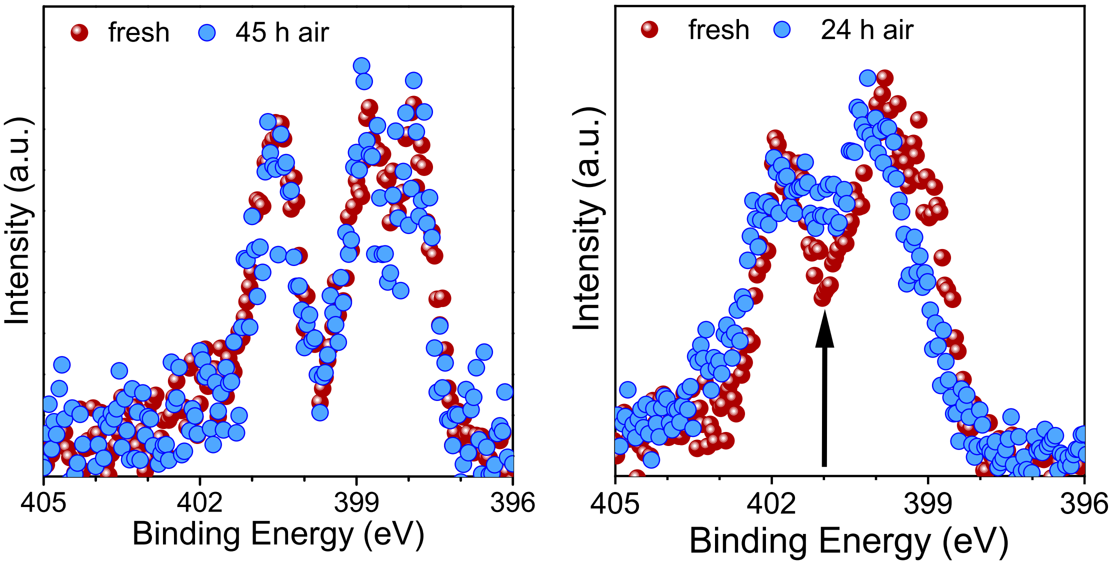

Figure 4.14.: Comparison of N 1*s* core-level spectra of a freshly evaporated film and after air exposure for Blatter-pyr (left, 45 h in air) and diBlatter (right, 24 h in air).

seen in figure 4.14 showed no significant changes, indicating no molecule degradation. By contrast, the N 1*s* main line of diBlatter film is altered only after 24 h in air. The N 1*s* core-level spectrum shows changes in line shape and intensity. The characteristic dip between the second and third main line decreases and is accompanied by a gain in intensity at around 401 eV. The alteration of the N 1*s* line of diBlatter indicates that film molecules undergo degradation to some extent when exposed to air. Furthermore, the difference in lifetime of Blatter-pyr and diBlatter is evident and supported by the fit analysis (Appendix C, *ACS Appl. Mater. Interface* **2023**, *15*, 30935-30943).

The fit analysis of the core-level spectra of Blytter-pyr (figure 4.15) confirms a robust film stability in air. The intensity of the photoemission line Nrad associated with the photoelectrons emitted by a radical decreases less than 2 % in comparison to the fresh film. In general, film stoichiometry do not change significantly upon air exposure and the film molecules preserve their radical character. This findings correlate to the electron paramagnetic resonance spectroscopy measurements that demonstrated the Blatter-pyr stability in air for 3 month[22].

The opposite situation is observed for diBlatter film exposed to air for 72 h. The N 1*s* core-level spectrum (figure 4.15) displays indications of the degradation of molecules, leading to changes in the chemical surrounding of the nitrogen atoms. The contributions Nrad and $N_{2,4}$ to the N 1*s* main line decrease in intensity, and a new feature appears at 400 eV.

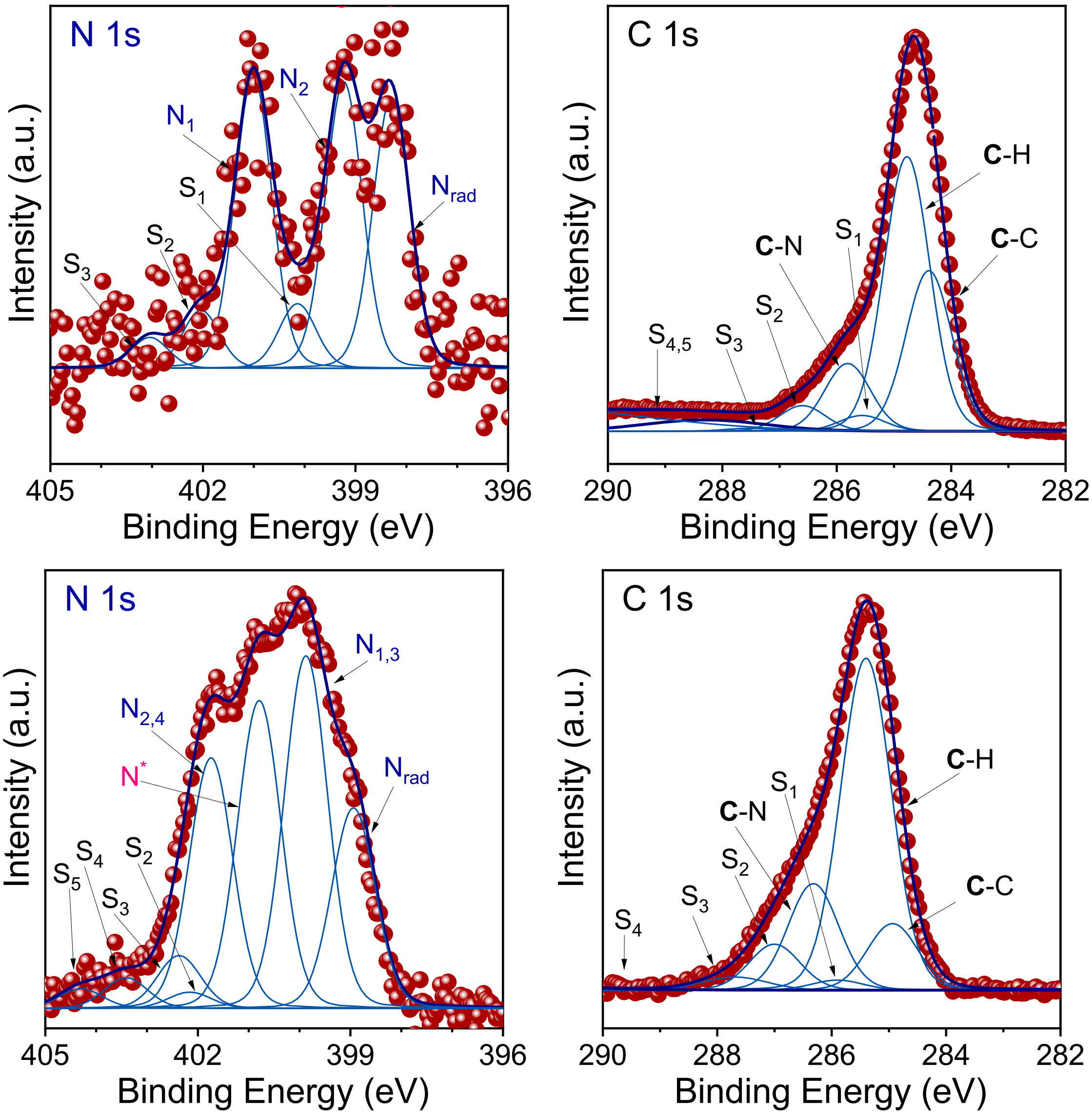

Figure 4.15.: N 1*s* and C 1*s* core-level spectra with the fit components of Blatter-pyr fim after 45 h in air (top) and diBlatter-fim after 72 h in air (bottom).

The loss in intensity of Nrad contribution indicates that the radical moiety of the molecule participates in the degradation process. According to the results of the fit procedure of the N 1*s* line, 38 % of film molecules lost their radical character after air exposure for 72 h. The C 1*s* line (figure 4.15) shows only small changes in intensity concerning the C−N component assigned to the carbon atoms bonded to the nitrogen atoms. The C 1*s* core-level spectrum reveals no evidence for oxidation of carbon atoms under air exposure. In the case of oxidation, the presence of C=O features at higher binding energy side would be expected. The minor noticeable changes in the intensity of C−N component resonates with the alteration of a chemical surrounding of the nitrogen atoms.

The identity of the new N^* feature in the N 1*s* core-level spectrum of diBlatter film (figure 4.15) can clarify how film molecules degrade when exposed to air. The ab initio calculations done by Arrigo Calzolari (CNR-NANO Istituto Nanoscienze), provide information on the potential degradation pathways for Blatter-pyr and diBlatter radicals (Appendix C, *ACS Appl. Mater. Interface* **2023**, *15*, 30935-30943).

Among the impurities present in the air, the adsorption of H and NH_2 plays a major role in the degradation of Blatter-pyr and diBlatter. A bond formation H−N between the contaminants and the nitrogen atoms (Nrad or N_2 in case of Blatter-pyr, Appendix C, *ACS Appl. Mater. Interface* **2023**, *15*, 30935-30943) of radical molecules causes a loss of the magnetic moment in both radicals. The ab initio calculation states that the interaction with H and NH_2 affects the binding energies of three main contributions in the N 1*s* core-level spectrum. Most notably, the gain in intensity in the range 400-401 eV correlates with the adsorption of NH_2 and H at the Nrad atom of the Blatter-pyr and diBlatter molecule (Appendix C, *ACS Appl. Mater. Interface* **2023**, *15*, 30935-30943).

Blatter-pyr and diBlatter form hydrogen bonds O−H···N with molecular water. The interaction with water does not alter the radical character of the Blater-pyr molecules that maintain their magnetic moment. A contrasting behaviour is observed for diBlatter films. Interaction with water results in quenching of the magnetic moment of the radical molecules. Regarding film stability, the adsorption of molecular water may be responsible for the difference in the lifetime upon air exposure between the Blatter-pyr and diBlatter films. diblatter with two radical units is water-sensitive, and the films degrade in contact with the molecular water present in the air. Blatter-pyr with one radical site poses a high water resistance, and films stay longer intact upon air exposure. This good stability of Blatter-pyr might establish the transition from academic-related applications to commercial devices based on organic radicals (Appendix C, *ACS Appl. Mater. Interface* **2023**, *15*, 30935-30943).

4.3.2. Dicyano Tetrazolinyl Radical

Accordingly, the air stability of the dicyano tetrazolinyl radical assemblies at ambient conditions was probed, too, using XPS (Appendix A, *J. Am. Chem. Soc.* **2023**, *145*, 13335-13346). XPS spectra were recorded directly after the deposition of assembles and again after air exposure for 64 h. As mentioned above, the N 1*s* line is a sensitive indicator for changes in the local bonding of the nitrogen atoms of the tetrazolinyl-ring. If the radical character of the molecules is affected, the N 1*s* core-level spectra shows evident changes in the line-shape and intensity accompanied by the appearance of new features[5,25,65].

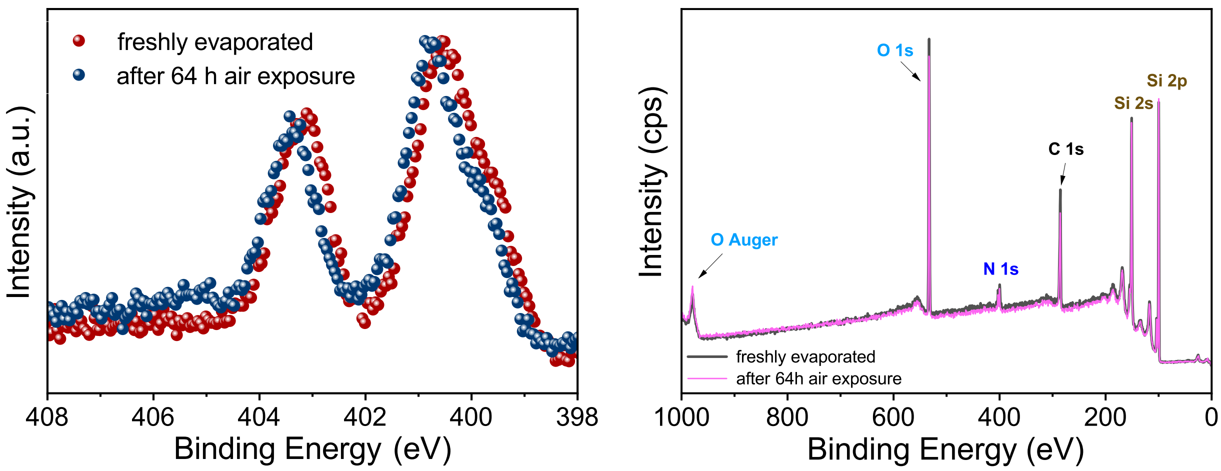

Figure 4.16.: N 1*s* core-level spectra of an assembly directly after deposition and after 64 h air exposure (left) and their corresponding survey spectra (right).

The evolution of the N 1*s* line (figure 4.16) reveals no evidence for radical molecule degradation after the assembles were exposed to air for 64 h. However, the signals experience an energy shift towards higher binding energies and the intensity of the satellite peak increases. This observation point to possible desorption of assembly molecules from the substrate. This conclusion is further supported by the decrease in the intensity of the C 1*s* and N 1*s* lines in the survey spectrum recorded after 64 h in air. At the same time, the substrate signals experience an increase in their intensity, indicating that the substrate surface is more exposed over time. The EPR measurements confirmed a long half-life of the radical nanoneedles of 50 days in the air (Appendix A, *J. Am. Chem. Soc.* **2023**, *145*, 13335-13346).

4.4. Blatter-pyr/Cobalt Interface

Organic radicals hold great potential for building hybrid interfaces in spintronic devices. Radicals with low lying single occupied molecular orbitals open the possibility for spin-dependent electron transport and modulation of molecular spin by electromagnetic fields[81]. This work takes a step further in the development and deposit purely organic Blater-pyr radical on a polycrystalline Co substrate.

This section addresses the electronic structure and chemical properties of the Blatter-pyr/polycrystalline cobalt interface. A combination of XPS and NEXAFS measurements was employed to determine the strength and nature of the interaction between the radical molecules and the metallic cobalt. The impact of the radical-substrate interaction was independently analysed on the molecular and metallic side, and the results of the study can be found in Appendix D and *Angew. Chem. Int. Ed.* **2024**, e202403495.

The first part will dive deep into the characterization of the film molecules XPS core-level spectra as a function of the film thickness. For comparison purposes, figure 4.17 presents the N 1*s* and C 1*s* spectra, along with the results of the fitting procedure, for the highest and lowest film coverage. The N 1*s* and C 1*s* regions of the 6.0 nm radical film exhibit typical features of the intact Blatter-pyr molecules, characterized in detail in paragraph 4.3.1, Appendix C, *ACS Appl. Mater. Interface* **2023**, *15*, 30935-30943.

Going down to the lowest coverage, the C 1*s* and N 1*s* lines (figure 4.17) are perturbed by close proximity to the cobalt surface. The N 1*s* core-level spectrum of a 0.4 nm film is characterized by a broad asymmetric signal at 397.3 eV and a second feature at 399.2 eV. The obtained intensity ratios of the single contributions to the main line differ with respect to the intensity ratios of the thicker films providing direct evidence for a change in the chemical environment of the nitrogen atoms upon the interaction with the cobalt surface. At lower coverage, the C 1*s* core-level spectrum shows changes in the line-shape and energy position of its components but to a lesser extent than observed in the N 1*s* core-level spectrum. The three main components do not experience an equal energy shift. The binding energy of the C−N contribution that is most affected shifts towards the lower energy side, while the C−C and C−H components experience shifts in opposite directions. As the thickness of the film increases from 0.4 to 6.0 nm, the energy separation between the C−N and C−H contribution rises from 0.7 eV to 1.1 eV (as shown in figure 4.17). Notably, the C−N feature becomes more prominent in the thick film.

To better understand the bonding situation at the interface, the N 1*s* core-level spectra of films with different thickness were fitted with the same number of components as the thickest film. Figure 4.18 (lower panel) shows a development of the individual contributions as a function of film coverage. Upon closer inspection, it becomes evident that there is a noticeable shift towards higher binding energies as the film thickness increases. Moreover, a gain in the

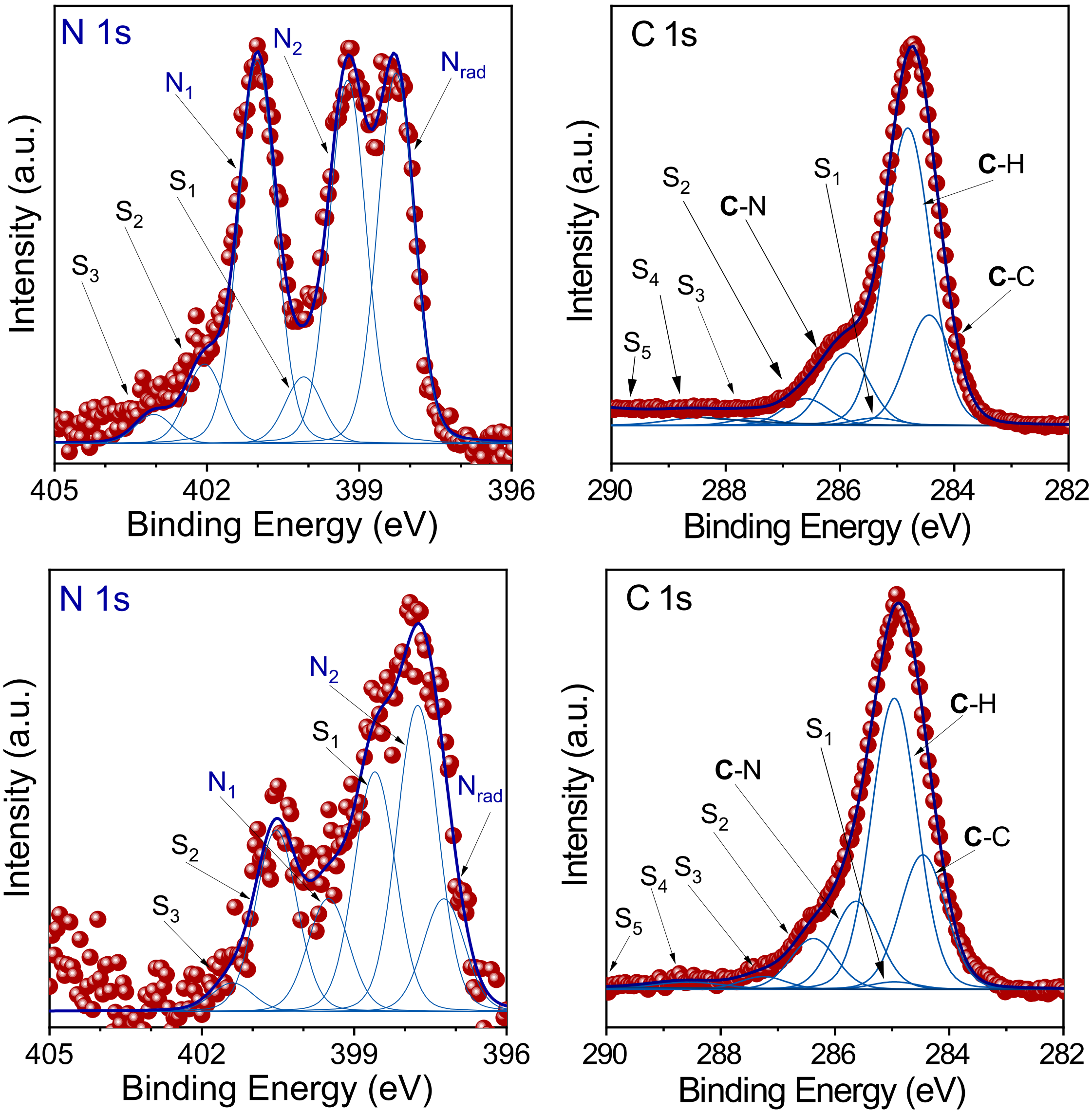

Figure 4.17.: N 1*s* and C 1*s* core-level spectra for a thick (6.0 nm) Blatter-pyr film (top) compared to a thin (1.1 nm) Blatter-pyr film (bottom) with their fit components deposited on polycrystalline cobalt.

intensity of the contributions Nrad and N_1 contradicts the trend of the intensity decrease observed for the satellite features S_1 and S_2. Component N_2 decreases until film thickness reaches 1.6 nm, followed by a slight increase for thicker films. For film coverages exceeding 1.6 nm, the N 1*s* line exhibits the typical behaviour of thicker films that correspond to the changes observed in C 1*s* core-level spectra (Appendix D, *Angew. Chem. Int. Ed.* **2024**, e202403495). The low intensity of the component Nrad associated with the photoelectron emitted from the nitrogen radical atom correlates with film molecules that lost their radical functionality.

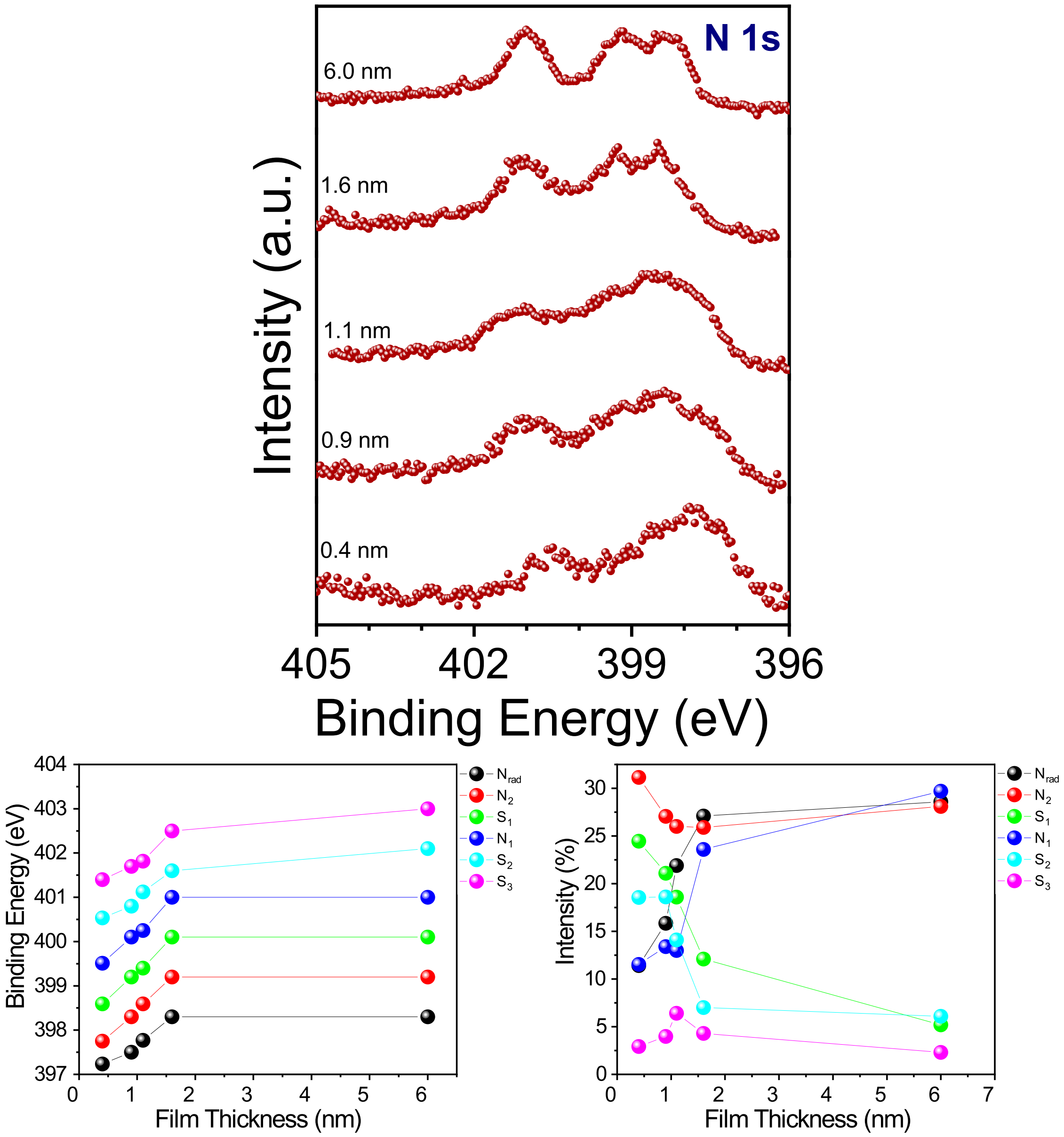

Figure 4.18.: Upper panel: Thickness-dependent N1s core-level spectra of Blatter-pyr thin films on polycrystalline cobalt. Lower panel: Evolution of the energy position [left) and the relative intensities (right) of the single components in the N 1s core-level spectra with increasing film thickness.

The substantial dissimilarities in the N 1*s* and to lower extend in the C 1*s* core-level spectra for interfacial and multilayers (figure 4.17 and figure 4.18) imply a strong modification in the electronic structure of radical molecules induced by a strong substrate-molecule interaction at the interface. Upon adsorption, a chemical bond is formed between the radical molecules and the cobalt atoms that results in the loss of the radical character of the molecules in the film. NEXAFS measurements provide additional confirmation for this strong interaction and allow access information about the unoccupied states, type of chemical bonding, and possible charge transfer process at the organic/metal interface and molecular orientation on the surface[85,86].

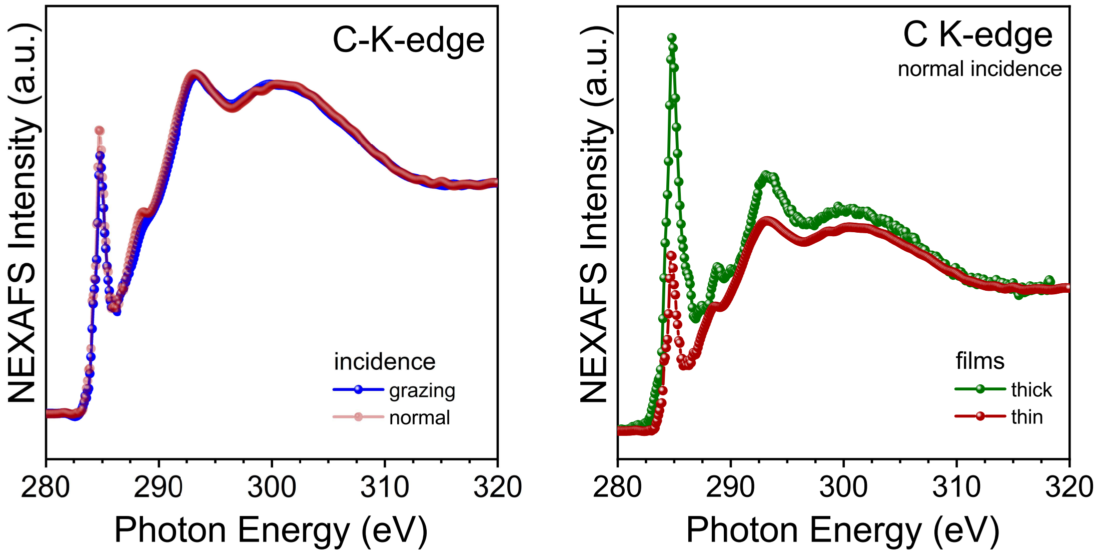

Figure 4.19.: C K-edge NEXAFS spectrum for a nominally thin Blatter-pyr film on the polycrystalline cobalt surface recorded in normal and grazing incidence (left) and C K-edge NEXAFS spectra for the interfacial and thick radical film measured in normal incidence (right).

Features in the C K-edge spectra (figure 4.19 (right)) show clearly visible thickness-dependent modifications. For instance, the pre-edge contribution assigned to the transition from the C 1s core-level to the single unoccupied molecular orbital (SUMO) and the π^* resonances located at 287.3 eV, and 288.7 eV[87,88] are suppressed in the spectrum for radical molecules close to the interface. This phenomenon indicates a charge transfer from the Co metal to the Blatter-pyr, resulting in the filling of SUMO and other previously unoccupied states of the radical molecules.

The combination of XPS and NEXAFS delivers a whole picture of the occupied and unoccupied states of radical molecules at interface. The spectral profile of radical molecules changes close to the surface, indicating a strong interaction at the interface[5,75]. Radical molecules form a chemisorbed layer on the cobalt surface[89,90] and the charge transfer takes place from the ferromagnetic substrate to the organic radical layer.

At this point of the investigation, the attention will shift to the cobalt surface. Again, NEXAFS and XPS measurements were applied, this time to explore in depth the influence of chemisorbed radical molecules on the electronic structure of the metallic Co surface. Both techniques are sensitive to Co atoms' valence state, allowing differentiation between Co species in different oxidation states[91].

The NEXAFS spectra recorded at the Co $L_{2,3}$-edges (figure 4.20) for clean surface and interfacial layer display no significant dissimilarities apart from a slight increase in signal intensities after deposition. Two intense features at 776.2 and 791.2 eV ascribe to the transition between the Co $2p$ and $3d$ states. The peak positions and the line-shapes correlate with the metallic cobalt, and the features, which would be associated with the oxidized Co species[92] are not present in both spectra. Further XPS inspection of the Co $2p$ region before and after radical deposition supports this conclusion. The two dominant signals at 793.3 eV and 778.3 eV belong to the spin-orbit splitting components Co $2p_{1/2}$ and Co $2p_{3/2}$ of the metallic Co (0) state and broad photoemission line at around 770 eV corresponds to the Co LMM Auger peak[93,94]. There is no eviden for the oxidized Co species.

Thus, the combined results of XPS and NEXAFS measurements for a clean Co surface and surface interfaced with radical molecules provide no indications for oxidation of the Co surface. The origin of the slight enhancement of the Co $L_{2,3}$-edge signal intensities, observed for the Co surface with the radical layer, points towards lower occupancy of the Co $3d$ states[92,95] as result of chemisorption. This finding agrees with a charge-transfer process directed from the Co atoms to the radical molecules at the interface and correlates with the interpretation of NEXAFS C−K edge spectra (figure 4.19) and XPS spectra of the Blatter-pyr molecule (figure 4.17) in the films.

Ab-initio density functional theory calculations were performed by Andrea Droghetti (Trinity College, University of Dublin) on the Blatter-pyr/Co(0001) system (Appendix D, *Angew. Chem. Int. Ed.* **2024**, e202403495) to understand the chemical interaction at the radical/cobalt interface. The study confirms a strong hybridization between the molecular orbitals of the radical and the Co $3d$ states. The interfacial bonds alter the magnetic moment of the Cobalt surface atoms, reducing it from 1.7 μ_B, the value calculated for the clean surface, to

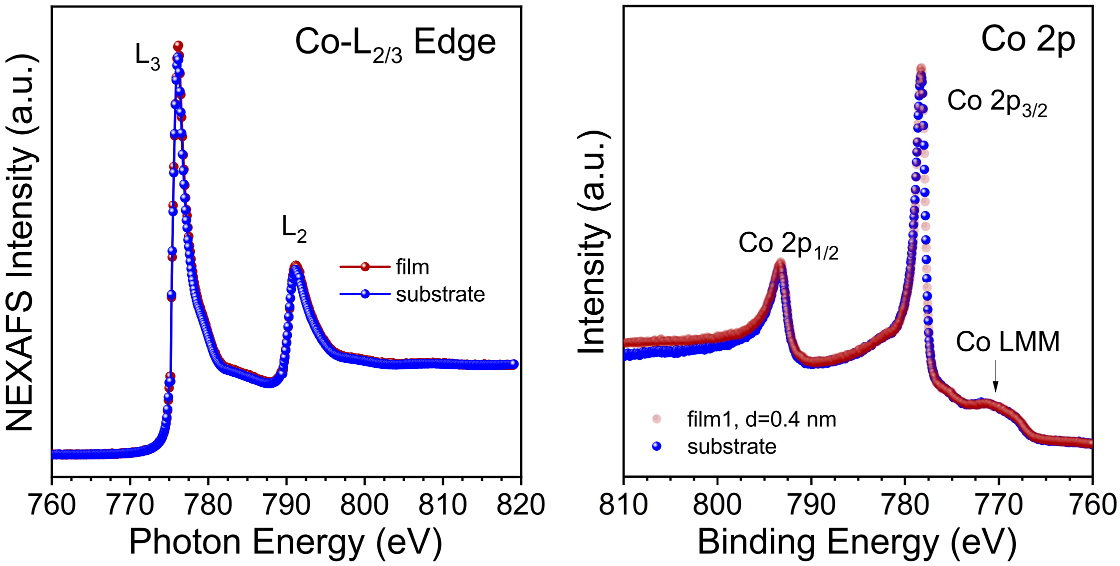

Figure 4.20.: NEXAFS Co $L_{2,3}$-edge spectra (left) and XPS Co $2p$-spectra (right) before (blue) and after (red) Blater-pyr thin film deposition.

0.25 μ_B (Appendix D, *Angew. Chem. Int. Ed.* **2024**, e202403495). Chemisorbed molecules on the metallic Co do not preserve their radical character, as previously estimated based on the XPS data.

The reduction of the Co magnetic moment at the interface was proved experimentally by performing a fit analysis of the Co $3s$ core-level spectra. The Co $3s$ spectrum is characterised by a multiplet splitting related to the interaction between unfilled d-states and ionized $3s$ state[96,97]. As consequence, the intensity ratio of the doublet components $\frac{I_2}{I_1}$ correlates to the total spin S of the unpaired $3d$ electrons, which can be calculated with the equation 4.2[97]:

$$\frac{I_2}{I_1} = \frac{S}{S+1} \tag{4.1}$$

The magnetic moment of Co atoms μ_s can be estimated by using the relation[97]:

$$\mu_s = 2\mu_B\sqrt{(S+1)S} \tag{4.2}$$

where μ_B is the Bohr magneton.

Figure 4.21 shows the Co 3*s* core-level spectra before and after deposition of Blatter-pyr film. The two contributions to the main line were estimated by using a Doniach-Sunjic line shape[96].

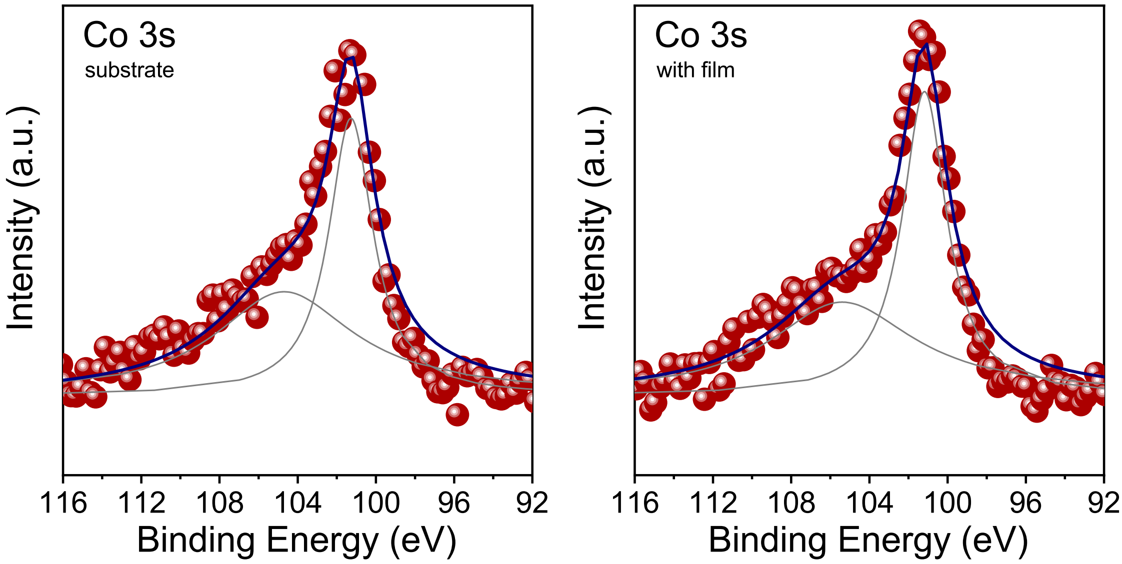

Figure 4.21.: Co 3s core-level spectra with the fit components of the clean Co surface and after deposition of Blatter-pyr thin films.

The magnetic moment of the Co atom of the clean surface with 1.88 μ_B is close to the value of 1.72 μ_B reported in literature[98,99] and decreases to 1.53 μ_B upon radical film deposition. The interface-induced reduction of the Co magnetic moment reflects the trend determined by the DFT calculations (Appendix D, *Angew. Chem. Int. Ed.* **2024**, e202403495).

Notably, the change in the magnetic properties of the Co surface due to the hybridization with the Blatter-pyr follows a similar pattern to the C_{60}/Co interface. In general, the deposition of a C_{60} layer suppresses the magnetization of the ferromagnet around 15-30 %[100,101]. For instance, theoretical calculations on the C_{60}/Co system estimated that C_{60} layer reduces the Co magnetic moment to 1.25 μ_B[14,102]. The decrease of the magnetization of 0.27 μ_B was measured for the C_{60}/Co interface. This was realized by the deposition of a 20 nm thick C_{60} layer on the 5 nm thin Co film[100]. This value is comparable to the value of 0.35 μ_B estimated for the Blatter-pyr/Co interface.

Based on these findings it is evident that the chemical bonding of radical molecules with the Co surface, alters the electronic structure of the ferromagnet and results in a decrease of its magnetic moment. It demonstrates that radical-substrate interactions define the local chemical and magnetic properties of the hybrid interface. This can be viewed as a powerful approach to manipulate and control the spin transport in future molecular-based spintronic devices. These findings offer insight into the magnetic properties of the cobalt surface, relying only on investigating the XPS Co core-level spectra. XPS technique proved to be an alternative tool to asses the magnetization of the ferromagnetic surfaces compared to well-established methods such as magneto-optical Kerr-effect (MOKE) or X-ray magnetic circular dichroism (XMCD), which depends in comparison to XPS , on the external magnetic fields[102,103].

5. Conclusions and Outlook

The presented work studies the electronic properties, air stability, chemical interaction, and phenomena occurring at the purely organic radical interface with various substrates. The main results and conclusions derived from the characterization of the selected radical systems by the X-ray techniques, SEM, and DFT calculation are summarized below:

- We demonstrated the first evaporation and deposition of a novel dicyano tetrazolinyl radical on SiO_2/Si(111) surface. The molecules of the radical assemblies maintain their radical functionality upon deposition and exposure to air for at least 64 h and longer confirmed by XPS and EPR measurements.

- The investigation uncovers a strong tendency of dicyano tetrazolinyl radical to form islands upon deposition, whose morphology depends heavily on the substrate and molecule-substrate interaction. The assemblies form nanoneedles on the SiO_2/Si(111) surface, and radical molecules are weakly physisorbed. Conversely, radical assemblies grown on polycrystalline gold reveal an inland formation with a distinct "monolith structure". Moreover, the radical manifests a chemisorptive bonding character on the gold surface.

- We introduced a fabrication of the assemblies of dicyano tetrazolinyl radical with two distinct morphologies in one-step deposition on the hybrid substrate.

- Blatter radical derivatives exhibit an extraordinary chemical stability upon air exposure. Blatter-pyr, with one radical side show high water resistance and retain radical functionality at least for 45 h and longer, when exposed to air. diBlatter, with two radical-side is water sensitive and show evidences for degradation in air after 24 h exposure.

- The interfacial hybridization and charge transfer at Blatter-pyr/Co interface reduce the magnetic moment of the ferromagnet, and chemisorbed Blatter-pyr molecules do not sustain their radical character. XPS technique has proved to be an useful tool to probe the magnetic properties of the ferromagnetic surfaces without use of magnetic fields.

- From the point of view of the applications in spintronics, the radical state of the Blatter-pyr in thin films on Co can be enhanced by attaching molecules to a metal surface using a terminal linker group and reduce the strength of radical-metal interaction[8].

Our findings on the magnetic properties of the hybrid Blatter-pyr/Co interface show a strong correlation to the popular spintronic C_{60}/Co system. This allows us to predict a potential modulation of the magnetic anisotropy of Co by adsorbed Blatter-pyr films, which can be subject to future measurements. Most importantly, chemical coupling and hybridization between the radical and the ferromagnet surface can be viewed as a powerful approach to control and tune local magnetic and spin-transport properties of the hybrid radical/Co interfaces for spintronics applications. On the other hand, the assemblies of dicyano tetrazolinyl radical with nanoneedles and monolith morphology hold great promise for integrating and patterning in nanodevices. In-situ deposition opens a versatile platform for tailoring nanostructure shape and size by changing deposition parameters or preferential growth direction by selecting substrates with a specific geometry[65].

6. Symbols and Abbreviations

%	percent
A_i	peak area
AEY	Auger electrons yield
Al	element symbol of aluminium
ArTOF	angular-resolved time of flight (electron analyser)
a.u.	arbitrary units
Au	element symbol of gold
C	element symbol of carbon
$^\circ C$	degrees Celsius
CCD	charge-coupled device
CN	cyano group
Co	element symbol of cobalt
cos	cosine
d	nominal film thickness
Δ	escape depth
D (e.g. 2D)	dimensional
E_B	binding energy
E_{vac}	vacuum level
E_F	Fermi level
eV	electron Volt
FI	fluorescence yield
g	gramme
h (constant)	Planck constant
h (unit)	hour
H	element symbol of hydrogen
GW	Gaussian width
HIS	hybrid interface states

HZB	Helmholtz-Zentrum Berlin
K	Kelvin
ln	natural logarithm
λ	wavelength
λ_{IMPF}	inelastic mean free path
$\%n_i$	element percentage
n_i	element concentration
μ	absorption coefficient
μ_B	Bohr magneton
μ_S	spin magnetic moment
m	metre
mbar	millibar
μs	microsecond
Mg	element symbol of magnesium
MOKE	magneto-optical Kerr-effect
MR	magnetoresistance
ν	frequency
N	element symbol of nitrogen
NEXAFS	near-edge x-ray absorption fine structure spectroscopy
O	element symbol of oxygen
OMBD	organic molecular beam deposition
OMTJs	organic magnetic tunnel junctions
OSV	organic spin valves
ϕ	work function
PES	photoelectron spectroscopy
PTM	Perchlorotriphenylmethyl
rad	radian
s	second
S	total spin angular momentum
SEM	scanning electron microscopy
SMJ	single-molecular junctions
Si	element symbol of silicon
S_i	standardized sensitivity factor
sin	sine
SUMO	singly-unoccupied molecular orbital

Θ	a specified angle
TEY	total electron yield mode
TGA	thermogravimetric analysis
UHV	ultra-high vacuum
wL	Lorentzian width
XMCD	X-ray magnetic circular dichroism
XPS	X-ray photoelectron spectroscopy

7. List of Publications

Published Publications

I

E. M. Nowik-Boltyk, T. Junghoefer, M. Glaser, E. Giangrisostomi, R. Ovsyannikov, S. Zhang, C. Shu, A. Rajca, A. Calzolari, M. B. Casu, "Long-Term Degradation Mechanisms in Application-Implemented Radical Thin Films", *ACS Applied Materials & Interfaces* **2023**, *15*, 30935–30943, DOI `10.1021/acsami.3c02057`, `https://doi.org/10.1021/acsami.3c02057`.

II

Z. Yang, M. Pink, E. M. Nowik-Boltyk, S. Lu, T. Junghoefer, S. Rajca, S. Stoll, M. B. Casu, A. Rajca, "Thermally Ultrarobust S = 1/2 Tetrazolinyl Radicals: Synthesis, Electronic Structure, Magnetism, and Nanoneedle Assemblies on Silicon Surface", *Journal of the American Chemical Society* **2023**, *145*, 13335–13346, DOI `10.1021/jacs.3c03402`, `https://doi.org/10.1021/jacs.3c03402`.

III

E. M. Nowik-Boltyk, T. Junghoefer, E. Giangrisostomi, R. Ovsyannikov, C. Shu, A. Rajca, A. Droghetti, M. B. Casu, "Radical-Induced Changes in Transition Metal Interfacial Magnetic Properties: A Blatter Derivative on Polycrystalline Cobalt", *Angewandte Chemie International Edition* **2024**, *63*, e202403495, DOI `https://doi.org/10.1002/anie.202403495`.

Publications Not Directly Related to This Work

IV

T. Junghoefer, E. M. Nowik-Boltyk, J. A. de Sousa, E. Giangrisostomi, R. Ovsyannikov, T. Chassé, J. Veciana, M. Mas-Torrent, C. Rovira, N. Crivillers, M. B. Casu, “Stability of radical-functionalized gold surfaces by self-assembly and on-surface chemistry”, *Chemical Science* **2020**, *11*, 9162–9172, DOI `10.1039/D0SC03399E`, `http://dx.doi.org/10.1039/D0SC03399E`.

V

J. A. de Sousa, F. Bejarano, D. Gutiérrez, Y. Leroux, E.-M. Nowik Boltyk, T. Junghoefer, E. Giangrisostomi, R. Ovsyannikov, M. B. Casu, J. Veciana, M. Mas-Torrent, B. Fabre, C. Rovira, N. Crivillers, “Exploiting the Versatile Alkyne-based Chemistry for Expanding the Applications of a Stable Triphenylmethyl Organic Radical on Surfaces”, *Chemical Science* **2019**, *11*, 516–524, DOI `10.1039/c9sc04499j`.

Contributions

Contributions by Co-Authors

Tobias Junghöfer and I (University of Tübingen) performed the measurements on dicyano tetrazolinyl radical (publication II).

Andrzej Rajca, Shuyang Zhang and Chan Shu (University of Nebraska) synthetized and provided Blatter-pyr and diBlatter radical (publication I, III).

Andrzej Rajca, Zhimin Yang, Suchada Rajca (University of Nebraska), and Shutian Lu (University of Washington) are responsible for design and synthesis and characterisation of dicyano tetrazolinyl radical (publication II).

Maren Pink (Indiana University) provided the crystal structure of dicyano tetrazolinyl radical. Mathias Glaser, Tobias Junghöfer and Maria Benedetta Casu (University of Tübingen) participated in the measurements of the Blatter-pyr and diBlatter radical films (publication I).

Tobias Junghöfer, Maria Benedetta Casu and I (University of Tübingen) participated in the measurements of the Blatter-pyr on Co at Bessy II (publication III).

Tobias Junghöfer and I (University of Tübingen) performed a fit analysis of the Blatter-pyr and diBlatter films (publication I).

Tobias Junghöfer, Arkaprava Das and I (University of Tübingen) performed measurements of dicyano tetrazolinyl radical on gold and hybrid substrate.

Erika Giangrisostomi and Ruslan Ovsyannikov (Helmholtz-Zentrum Berlin (BessyII)) provided as beamtime scientists the technical and scientific support for the measurements taken at Bessy II (publication I, II).

Andrea Droghetti (Trinity College, University of Dublin) performed the DFT calculations of the Blatter-pyr radical on Co (publication I).

Arrigo Calzolari (CNR-NANO) executed the DFT calculations of the Blatter-pyr and diBlatter radical (publication I).

Elke Nadler (University of Tübingen) took the SEM images of the dicyano tetrazolinyl radical (publication II, Chapter 4.2).

Maria Benedetta Casu (University of Tübingen) conceived and supervised the BMBF-funded project, that build the foundation for this work. She oversaw the X-ray based measurements performed at the home lab and at the Bessy II in Berlin. She wrote the text for publication and provided the interpretation of the experimental results contributed by me.

Own Contributions

My contributions are summarized as follows:

I carried out the deposition and XPS experiments on the dicyano tetrazolinyl radical on SiO_2/Si(111), polycrystalline gold and hybrid substrates at the home lab. I contributed to the film deposition, XPS and NEXAFS measurements of the Blatter-pyr films on the cobalt surface at the synchrotron facility Bessy II in Berlin.

I performed the XPS analysis of the experimental data (energy calibration, normalization, estimation of the element concentration, film stoichiometry and film growth) and the fit procedure of the core-level spectra, taken at the home laboratory, for the radical systems (unless stated otherwise in publications) presented in the publications and Appendix B.

As co-author, I contributed to the discussions and comments on all publications.

Bibliography

[1] L. Bayron, *The Complete Works of Lord Byron*, e-arthnow, **2019**.

[2] P. Coelho, *The Alchemist*, trans. by A. R. Clarke, HarperOne, **2015**.

[3] A. d. S. Exupéry, *The Little Prince*, trans. by D. De Angelis, Stargatebook, **2018**.

[4] L. Li, C. R. Prindle, W. Shi, C. Nuckolls, L. Venkataraman, "Radical Single-Molecule Junctions", *Journal of the American Chemical Society* **2023**, *145*, 18182–18204, DOI `10.1021/jacs.3c04487`.

[5] F. Ciccullo, A. Calzolari, K. Bader, P. Neugebauer, N. M. Gallagher, A. Rajca, J. van Slageren, M. B. Casu, "Interfacing a Potential Purely Organic Molecular Quantum Bit with a Real-Life Surface", *ACS Appl. Mater. Interfaces* **2019**, *11*, 1571–1578, DOI `10.1021/acsami.8b16061`.

[6] H. Yeo, S. Debnath, B. P. Krishnan, B. W. Boudouris, "Radical polymers in optoelectronic and spintronic applications", *RSC Applied Polymers* **2024**, *2*, 7–25, DOI `10.1039/D3LP00213F`.

[7] A. Bajaj, P. Kaur, A. Sud, M. Berritta, M. E. Ali, "Anomalous Effect of Quantum Interference in Organic Spin Filters", *The Journal of Physical Chemistry C* **2020**, *124*, 24361–24371, DOI `10.1021/acs.jpcc.0c08199`.

[8] G. Mitra, J. Z. Low, S. Wei, K. R. Francisco, M. Deffner, C. Herrmann, L. M. Campos, E. Scheer, "Interplay between Magnetoresistance and Kondo Resonance in Radical Single-Molecule Junctions", *Nano Lett* **2022**, *22*, 5773–5779, DOI `10.1021/acs.nanolett.2c01199`.

[9] C. Nicolaides, F. Bazzi, E. Vouros, D. F. Flesariu, N. Chrysochos, P. A. Koutentis, C. P. Constantinides, T. Trypiniotis, "Metal-Free Organic Radical Spin Source", *Nano Letters* **2023**, *23*, 4579–4586, DOI `10.1021/acs.nanolett.3c01044`.

[10] J. Z. Low, G. Kladnik, L. L. Patera, S. Sokolov, G. Lovat, E. Kumarasamy, J. Repp, L. M. Campos, D. Cvetko, A. Morgante, L. Venkataraman, "The Environment-Dependent Behavior of the Blatter Radical at the Metal–Molecule Interface", *Nano Letters* **2019**, *19*, 2543–2548, DOI `10.1021/acs.nanolett.9b00275`.

[11] N. Jha, A. Pariyar, T. S. Parvini, C. Denker, P. K. Vardhanapu, G. Vijaykumar, A. Ahrens, T. Meyer, M. Seibt, N. Atodiresei, J. S. Moodera, S. K. Mandal, M. Münzenberg, "Interface-Assisted Room-Temperature Magnetoresistance in Cu-Phenalenyl-Based Magnetic Tunnel Junctions", *ACS Applied Electronic Materials* **2023**, *5*, 1471–1477, DOI `10.1021/acsaelm.2c01428`.

[12] F. Djeghloul, F. Ibrahim, M. Cantoni, M. Bowen, L. Joly, S. Boukari, P. Ohresser, F. Bertran, P. Le Fèvre, P. Thakur, F. Scheurer, T. Miyamachi, R. Mattana, P. Seneor, A. Jaafar, C. Rinaldi, S. Javaid, J. Arabski, J. P. Kappler, W. Wulfhekel, N. B. Brookes, R. Bertacco, A. Taleb-Ibrahimi, M. Alouani, E. Beaurepaire, W. Weber, "Direct observation of a highly spin-polarized organic spinterface at room temperature", *Scientific Reports* **2013**, *3*, 1272, DOI `10.1038/srep01272`.

[13] X. Gu, L. Guo, Y. Qin, T. Yang, K. Meng, S. Hu, X. Sun, "Challenges and Prospects of Molecular Spintronics", *Precision Chemistry* **2024**, *2*, 1–13, DOI `10.1021/prechem.3c00071`.

[14] K. Bairagi, A. Bellec, V. Repain, C. Chacon, Y. Girard, Y. Garreau, J. Lagoute, S. Rousset, R. Breitwieser, Y.-C. Hu, Y. C. Chao, W. W. Pai, D. Li, A. Smogunov, C. Barreteau, "Tuning the Magnetic Anisotropy at a Molecule-Metal Interface", *Physical Review Letters* **2015**, *114*, 247203, DOI `10.1103/PhysRevLett.114.247203`.

[15] Y.-J. Hsu, Y.-L. Lai, C.-H. Chen, Y.-C. Lin, H.-Y. Chien, J.-H. Wang, T.-N. Lam, Y.-L. Chan, D. H. Wei, H.-J. Lin, C.-T. Chen, "Enhanced Magnetic Anisotropy via Quasi-Molecular Magnet at Organic-Ferromagnetic Contact", *The Journal of Physical Chemistry Letters* **2013**, *4*, 310–316, DOI `10.1021/jz301757x`.

[16] Z. Yang, M. Pink, E. M. Nowik-Boltyk, S. Lu, T. Junghoefer, S. Rajca, S. Stoll, M. B. Casu, A. Rajca, "Thermally Ultrarobust S = 1/2 Tetrazolinyl Radicals: Synthesis, Electronic Structure, Magnetism, and Nanoneedle Assemblies on Silicon Surface", *J Am Chem Soc* **2023**, *145*, 13335–13346, DOI `10.1021/jacs.3c03402`.

[17] Y. Ji, L. Long, Y. Zheng, "Recent advances of stable Blatter radicals: synthesis, properties and applications", *Mater. Chem. Front.* **2020**, *4*, 3433–3443, DOI `10.1039/D0QM00122H`.

[18] A. Saal, L. Elbinger, K. Schreyer, X. Fataj, C. Friebe, U. S. Schubert, "Structural Improvement of the Blatter Radical for High-Current Organic Batteries", *ACS Appl. Energy Mater.* **2022**, *5*, 15019–15028, DOI `10.1021/acsaem.2c02559`.

[19] Y. Zhang, Y. Zheng, H. Zhou, M.-S. Miao, F. Wudl, T.-Q. Nguyen, "Temperature Tunable Self-Doping in Stable Diradicaloid Thin-Film Devices", *Adv. Mater.* **2015**, *27*, 7412–7419, DOI `10.1002/adma.201502404`.

[20] J. Areephong, K. M. Mattson, N. J. Treat, S. O. Poelma, J. W. Kramer, H. A. Sprafke, A. A. Latimer, J. Read de Alaniz, C. J. Hawker, "Triazine-mediated controlled radical polymerization: new unimolecular initiators", *Polymer Chemistry* **2016**, *7*, 370–374, DOI `10.1039/C5PY01563D`.

[21] Y. Zheng, M.-s. Miao, G. Dantelle, N. D. Eisenmenger, G. Wu, I. Yavuz, M. L. Chabinyc, K. N. Houk, F. Wudl, "A solid-state effect responsible for an organic quintet state at room temperature and ambient pressure", *Advanced materials (Deerfield Beach Fla.)* **2015**, *27*, 1718–1723, DOI `10.1002/adma.201405093`.

[22] F. Ciccullo, N. M. Gallagher, O. Geladari, T. Chasse, A. Rajca, M. B. Casu, "A Derivative of the Blatter Radical as a Potential Metal-Free Magnet for Stable Thin Films and Interfaces", *ACS Appl. Mater. Interfaces* **2016**, *8*, 1805–1812, DOI `10.1021/acsami.5b09693`.

[23] C. P. Constantinides, P. A. Koutentis, H. Krassos, J. M. Rawson, A. J. Tasiopoulos, "Characterization and Magnetic Properties of a "Super Stable" Radical 1,3-Diphenyl-7-trifluoromethyl-1,4-dihydro-1,2,4-benzotriazin-4-yl", *J. Org. Chem.* **2011**, *76*, 2798–2806, DOI `10.1021/jo200210s`.

[24] H. M. Blatter, H. Lukaszewski, "A new stable free radical", *Tetrahedron Lett.* **1968**, *9*, 2701–2705, DOI `http://dx.doi.org/10.1016/S0040-4039(00)89678-1`.

[25] M. B. Casu, "Nanoscale Studies of Organic Radicals: Surface, Interface, and Spinterface", *Acc. Chem. Res.* **2018**, *51*, 753–760, DOI `10.1021/acs.accounts.7b00612`.

[26] E. M. Nowik-Boltyk, T. Junghoefer, M. Glaser, E. Giangrisostomi, R. Ovsyannikov, S. Zhang, C. Shu, A. Rajca, A. Calzolari, M. B. Casu, "Long-Term Degradation Mechanisms in Application-Implemented Radical Thin Films", *ACS Applied Materials & Interfaces* **2023**, *15*, 30935–30943, DOI `10.1021/acsami.3c02057`.

[27] S. Zhang, M. Pink, T. Junghoefer, W. Zhao, S.-N. Hsu, S. Rajca, A. Calzolari, B. W. Boudouris, M. B. Casu, A. Rajca, “High-Spin (S = 1) Blatter-Based Diradical with Robust Stability and Electrical Conductivity”, *J. Am. Chem. Soc.* **2022**, *144*, 6059–6070, DOI `10.1021/jacs.2c01141`.

[28] N. M. Gallagher, A. Olankitwanit, A. Rajca, “High-Spin Organic Molecules”, *The Journal of Organic Chemistry* **2015**, *80*, 1291–1298, DOI `10.1021/jo502505r`.

[29] S. R. Forrest, “Ultrathin Organic Films Grown by Organic Molecular Beam Deposition and Related Techniques”, *Chemical Reviews* **1997**, *97*, 1793–1896, DOI `10.1021/cr941014o`.

[30] M. Ohring in **2002**, pp. 357–415, DOI `10.1016/B978-012524975-1/50010-0`.

[31] K. Oura, M. Katayama, A. V. Zotov, V. G. Lifshits, A. A. Saranin, *Growth of Thin Films*, Springer Berlin Heidelberg, **2003**, pp. 357–387, DOI `10.1007/978-3-662-05179-5_14`.

[32] E. Bauer, “Phänomenologische Theorie der Kristallabscheidung an Oberflächen. II”, *Zeitschrift für Kristallographie - Crystalline Materials* **1958**, *110*, 395–431, DOI `doi:10.1524/zkri.1958.110.16.395`.

[33] A. A. Virkar, S. Mannsfeld, Z. Bao, N. Stingelin, “Organic Semiconductor Growth and Morphology Considerations for Organic Thin-Film Transistors”, *Advanced Materials* **2010**, *22*, 3857–3875, DOI `https://doi.org/10.1002/adma.200903193`.

[34] G. Witte, C. Wöll, “Growth of Aromatic Molecules on Solid Substrates for Applications in Organic Electronics”, *Journal of Materials Research* **2004**, *19*, 1889–1916, DOI `10.1557/JMR.2004.0251`.

[35] A. Calzolari, A. Rajca, M. B. Casu, “From radical to triradical thin film processes: the Blatter radical derivatives”, *J. Mater. Chem. C* **2021**, *9*, 10787–10793, DOI `10.1039/D1TC01541A`.

[36] J. A. Venables, *Introduction to Surface and Thin Film Processes*, Cambridge University Press, Cambridge, **2000**, DOI `DOI:10.1017/CBO9780511755651`.

[37] J. Barth, G. Costantini, K. Kern, “Engineering atomic and molecular nanostructures at surfaces”, *Nature* **2005**, *437*, 671–9, DOI `10.1038/nature04166`.

[38] S. Verlaak, S. Steudel, P. Heremans, D. Janssen, M. S. Deleuze, “Nucleation of organic semiconductors on inert substrates”, *Physical Review B* **2003**, *68*, PRB, 195409, DOI `10.1103/PhysRevB.68.195409`.

[39] K. Siegbahn, “Electron Spectroscopy for Chemical Analysis (E.S.C.A.)”, *Philosophical Transactions of the Royal Society of London. Series A Mathematical and Physical Sciences* **1970**, *268*, 33–57.

[40] S. Hüfner in *Photoelectron Spectroscopy: Principles and Applications*, (Ed.: S. Hüfner), Springer Berlin Heidelberg, **2003**, pp. 1–60, DOI `10.1007/978-3-662-09280-4_1`.

[41] *Handbook of X-ray Photoelectron Spectroscopy*, **1992**.

[42] A. Einstein, “Über einen die Erzeugung und Verwandlung des Lichtes betreffenden heuristischen Gesichtspunkt”, *Annalen der Physik* **1905**, *322*, 132–148, DOI `https://doi.org/10.1002/andp.19053220607`.

[43] A. Bianconi, “Surface X-ray absorption spectroscopy: Surface EXAFS and surface XANES”, *Applications of Surface Science* **1980**, *6*, 392–418, DOI `https://doi.org/10.1016/0378-5963(80)90024-0`.

[44] J. C. Vickerman, I. S. Gilmore, *Surface Analysis – The Principal Techniques*, John Wiley & Sons, Ltd, Chichester, UK, **2009**, DOI `10.1002/9780470721582`.

[45] K. Siegbahn, K. V.-s. Uppsala, *ESCA; Atomic, Molecular and Solid State Structure Studied by Means of Electron Spectroscopy*, Almqvist & Wiksells, **1967**.

[46] M. P. Seah, W. A. Dench, “Quantitative Electron Spectroscopy of Surfaces: A Standard Data Base for Electron Inelastic Mean Free Paths in Solids”, *Surface and Interface Analysis* **1979**, *1*, 2–11, DOI `10.1002/sia.740010103`.

[47] R. d. L. Kronig, “Zur Theorie der Feinstruktur in den Röntgenabsorptionsspektren”, *Zeitschrift für Physik* **1931**, *70*, 317–323, DOI `10.1007/BF01339581`.

[48] J. Stöhr, *NEXAFS Spectroscopy*, **1992**.

[49] J. Rehr, R. Albers, “Theoretical Approaches to X-Ray Absorption Fine Structure”, *Rev. Mod. Phys.* **2000**, *72*, 621–654, DOI `10.1103/RevModPhys.72.621`.

[50] *Core Level Spectroscopy of Solids (1st ed.)* CRC Press, **2008**, DOI `10.1201/9781420008425`.

[51] G. Margaritondo, *Introduction to Synchrotron Radiation*, Oxford University Press, **1988**.

[52] P. Willmott, *An Introduction to Synchrotron Radiation*, **2019**, DOI `10.1002/9781119280453`.

[53] B. V. Crist, *Commercially Pure Binary Oxides and a few Common Carbonates and Hydroxides*, XPS International, LLC, **2005**.

[54] D. Vaughan, "X-Ray Data Booklet. Center for X-Ray Optics. [Tables]", **1985**, DOI `10.2172/6359890`.

[55] R. Ovsyannikov, P. Karlsson, M. Lundqvist, C. Lupulescu, W. Eberhardt, A. Föhlisch, S. Svensson, N. Martensson, "Principles and operation of a new type of electron spectrometer – ArTOF", *Journal of Electron Spectroscopy and Related Phenomena* **2013**, *191*, DOI `10.1016/j.elspec.2013.08.005`.

[56] A. Vollmer, R. Ovsyannikov, M. Gorgoi, S. Krause, M. Oehzelt, A. Lindblad, N. Mårtensson, S. Svensson, P. Karlsson, M. Lundvuist, T. Schmeiler, J. Pflaum, N. Koch, "Two dimensional band structure mapping of organic single crystals using the new generation electron energy analyzer ARTOF", *Journal of Electron Spectroscopy and Related Phenomena* **2012**, *185*, 55–60, DOI `https://doi.org/10.1016/j.elspec.2012.01.003`.

[57] T. Leitner, A. Born, I. Bidermane, R. Ovsyannikov, F. Johansson, Y. Sassa, A. Föhlisch, A. Lindblad, F. Schumann, S. Svensson, N. Mårtensson, "The CoESCA station at BESSY: Auger electron–photoelectron coincidences from surfaces demonstrated for Ag MNN", *Journal of Electron Spectroscopy and Related Phenomena* **2021**, *250*, 147075, DOI `https://doi.org/10.1016/j.elspec.2021.147075`.

[58] E. Giangrisostomi, R. Ovsyannikov, F. Sorgenfrei, T. Zhang, A. Lindblad, Y. Sassa, U. B. Cappel, T. Leitner, R. Mitzner, S. Svensson, N. Mårtensson, A. Föhlisch, "Low Dose Photoelectron Spectroscopy at BESSY II: Electronic structure of matter in its native state", *Journal of Electron Spectroscopy and Related Phenomena* **2018**, *224*, 68–78, DOI `https://doi.org/10.1016/j.elspec.2017.05.011`.

[59] S. Suga, A. Sekiyama in *Photoelectron Spectroscopy: Bulk and Surface Electronic Structures*, (Eds.: S. Suga, A. Sekiyama), Springer Berlin Heidelberg, Berlin, Heidelberg, **2014**, pp. 91–98, DOI `10.1007/978-3-642-37530-9_4`.

[60] H. Shinotsuka, S. Tanuma, C. J. Powell, D. R. Penn, "Calculations of electron inelastic mean free paths. X. Data for 41 elemental solids over the 50 eV to 200 keV range with the relativistic full Penn algorithm", *Surface and Interface Analysis* **2015**, *47*, 1132–1132, DOI `https://doi.org/10.1002/sia.5861`.

[61] C. Wagner, "Sensitivity factors for XPS analysis of surface atoms", *Journal of Electron Spectroscopy and Related Phenomena* **1983**, *32*, 99–102, DOI `https://doi.org/10.1016/0368-2048(83)85087-7`.

[62] K. Siegbahn, “Atomic, Molecular and Solid State Structure Studied by Means of Electron Spectroscopy”, *ESCA* **1967**.

[63] T. Junghoefer, E. M. Nowik-Boltyk, J. A. de Sousa, E. Giangrisostomi, R. Ovsyannikov, T. Chassé, J. Veciana, M. Mas-Torrent, C. Rovira, N. Crivillers, M. B. Casu, “Stability of radical-functionalized gold surfaces by self-assembly and on-surface chemistry”, *Chemical Science* **2020**, *11*, 9162–9172, DOI `10.1039/D0SC03399E`.

[64] S.-A. Savu, S. Abb, S. Schundelmeier, J. D. Saathoff, J. M. Stevenson, C. Tönshoff, H. F. Bettinger, P. Clancy, M. B. Casu, T. Chassé, “Pentacene-based nanorods on Au(111) single crystals: Charge transfer, diffusion, and step-edge barriers”, *Nano Research* **2013**, *6*, 449–459, DOI `10.1007/s12274-013-0322-x`.

[65] S.-A. Savu, I. Biswas, L. Sorace, M. Mannini, D. Rovai, A. Caneschi, T. Chassé, M. B. Casu, “Nanoscale Assembly of Paramagnetic Organic Radicals on Au(111) Single Crystals”, *Chem.-Eur. J.* **2013**, *19*, 3445–3450, DOI `10.1002/chem.201203247`.

[66] W. Heisenberg, “Über den anschaulichen Inhalt der quantentheoretischen Kinematik und Mechanik”, *Zeitschrift für Physik* **1927**, *43*, 172–198.

[67] A. Schoell, Y. Zou, D. Huebner, S. G. Urquhart, T. Schmidt, R. Fink, E. Umbach, “A comparison of fine structures in high-resolution x-ray-absorption spectra of various condensed organic molecules”, *The Journal of Chemical Physics* **2005**, *123*, DOI `10.1063/1.1978872`.

[68] A. Schöll, Y. Zou, M. Jung, T. Schmidt, R. Fink, E. Umbach, “Line shapes and satellites in high-resolution x-ray photoelectron spectra of large -conjugated organic molecules”, *The Journal of Chemical Physics* **2004**, *121*, 10260–10267, DOI `10.1063/1.1807812`.

[69] M. B. Casu, B.-E. Schuster, I. Biswas, C. Raisch, H. Marchetto, T. Schmidt, T. Chassé, “Locally Resolved Core-hole Screening, Molecular Orientation, and Morphology in Thin Films of Diindenoperylene Deposited on Au(111) Single Crystals”, *Advanced Materials* **2010**, *22*, 3740–3744, DOI `https://doi.org/10.1002/adma.201001265`.

[70] A. S. Poryvaev, E. Gjuzi, D. M. Polyukhov, F. Hoffmann, M. Fröba, M. V. Fedin, “Blatter-Radical-Grafted Mesoporous Silica as Prospective Nanoplatform for Spin Manipulation at Ambient Conditions”, *Angewandte Chemie International Edition* **2021**, *60*, 8683–8688, DOI `https://doi.org/10.1002/anie.202015058`.

[71] P. Knecht, N. Suryadevara, B. Zhang, J. Reichert, M. Ruben, J. V. Barth, S. Klyatskaya, A. C. Papageorgiou, “The self-assembly and metal adatom coordination of a linear bis-tetrazole ligand on Ag(111)”, *Chemical Communications* **2018**, *54*, 10072–10075, DOI `10.1039/C8CC04323J`.

[72] X. Du, S.-Y. Wang, M. Wei, J.-R. Zhang, G. Ge, W. Hua, “A theoretical library of N1s core binding energies of polynitrogen molecules and ions in the gas phase”, *Physical Chemistry Chemical Physics* **2022**, *24*, 8196–8207, DOI `10.1039/D2CP00069E`.

[73] M. U. Farooq, Z. Duan, M. I. Farooq, K. Fatima, M. A. Khan, L. Zhang, Y. Liu, M. Yousaf, B. Zou, “Spin-induced magnetic anisotropy in novel Co-doped GaN nanoneedles and their related photoluminescence”, *New Journal of Chemistry* **2018**, *42*, 8338–8341, DOI `10.1039/C8NJ00645H`.

[74] I. Bergenti, A. Dediu, “Spinterface: A new platform for spintronics”, *Nano Materials Science* **2019**, *1*, DOI `10.1016/j.nanoms.2019.05.002`.

[75] S. A. Savu, G. Biddau, L. Pardini, R. Bula, H. F. Bettinger, C. Draxl, T. Chassé, M. B. Casu, “Fingerprint of Fractional Charge Transfer at the Metal/Organic Interface”, *The Journal of Physical Chemistry C* **2015**, *119*, 12538–12544, DOI `10.1021/acs.jpcc.5b03768`.

[76] C. Dobler, C. Tönshoff, H. F. Bettinger, T. Chassé, M. B. Casu, “Cyano-Functional Group as an Anchoring Tool for Organic Small Molecules on Gold”, *The Journal of Physical Chemistry C* **2017**, *121*, 13660–13665, DOI `10.1021/acs.jpcc.7b02077`.

[77] A. Schöll, Y. Zou, T. Schmidt, R. Fink, E. Umbach, “High-Resolution Photoemission Study of Different NTCDA Monolayers on Ag(111): Bonding and Screening Influences on the Line Shapes”, *The Journal of Physical Chemistry B* **2004**, *108*, 14741–14748, DOI `10.1021/jp049005z`.

[78] K. S. Lokesh, K. De Wael, A. Adriaens, “Self-Assembled Supramolecular Array of Polymeric Phthalocyanine on Gold for the Determination of Hydrogen Peroxide”, *Langmuir* **2010**, *26*, 17665–17673, DOI `10.1021/la102740s`.

[79] R. Holze, “Competition of anchoring groups in adsorption on gold electrodes—a comparative spectroelectrochemical study of 4-mercaptobenzonitrile and aromatic nitriles”, *Journal of Solid State Electrochemistry* **2013**, *17*, 1869–1879, DOI `10.1007/s10008-013-2076-5`.

[80] F. Ciccullo, S.-A. Savu, A. Gerbi, M. Bauer, R. Ovsyannikov, A. Cassinese, T. Chassé, M. B. Casu, “Chemisorption, Morphology, and Structure of a n-Type Perylene Diimide Derivative at the Interface with Gold: Influence on Devices from Thin Films to Single Molecules”, *Chemistry – A European Journal* **2015**, *21*, 3766–3771, DOI `https://doi.org/10.1002/chem.201404901`.

[81] H. Yeo, S. Debnath, B. P. Krishnan, B. W. Boudouris, “Radical polymers in optoelectronic and spintronic applications”, *RSC Applied Polymers* **2024**, *2*, 7–25, DOI `10.1039/D3LP00213F`.

[82] A. Rajca, “Organic Diradicals and Polyradicals: From Spin Coupling to Magnetism?”, *Chemical Reviews* **1994**, *94*, 871–893, DOI `10.1021/cr00028a002`.

[83] T. Junghoefer, N. M. Gallagher, K. Kolanji, E. Giangrisostomi, R. Ovsyannikov, T. Chassé, M. Baumgarten, A. Rajca, A. Calzolari, M. B. Casu, “Challenges in controlled thermal deposition of organic diradicals”, *Chem. Mat.* **2021**, *33*, 2019–2028, DOI `http://dx.doi.org/10.1021/acs.chemmater.0c03880`.

[84] L. Tesi, E. Lucaccini, I. Cimatti, M. Perfetti, M. Mannini, M. Atzori, E. Morra, M. Chiesa, A. Caneschi, L. Sorace, R. Sessoli, “Quantum coherence in a processable vanadyl complex: new tools for the search of molecular spin qubits”, *Chem. Sci.* **2016**, *7*, 2074–2083, DOI `10.1039/C5SC04295J`.

[85] R. Kakavandi, P. Ravat, S. A. Savu, Y. B. Borozdina, M. Baumgarten, M. B. Casu, “Electronic Structure and Stability of Fluorophore–Nitroxide Radicals from Ultrahigh Vacuum to Air Exposure”, *ACS Appl. Mater. Interfaces* **2015**, *7*, 1685–1692, DOI `10.1021/am508854u`.

[86] R. Kakavandi, S.-A. Savu, A. Caneschi, M. B. Casu, “Paramagnetic Character in Thin Films of Metal-Free Organic Magnets Deposited on TiO2(110) Single Crystals”, *The Journal of Physical Chemistry C* **2013**, *117*, 26675–26679, DOI `10.1021/jp410038m`.

[87] E. M. Nowik-Boltyk, T. Junghoefer, M. Glaser, E. Giangrisostomi, R. Ovsyannikov, S. Zhang, C. Shu, A. Rajca, A. Calzolari, M. B. Casu, “Long-Term Degradation Mechanisms in Application-Implemented Radical Thin Films”, *ACS Applied Materials & Interfaces* **2023**, *15*, 30935–30943, DOI `10.1021/acsami.3c02057`.

[88] T. Junghoefer, A. Calzolari, I. Baev, M. Glaser, F. Ciccullo, E. Giangrisostomi, R. Ovsyannikov, F. Kielgast, M. Nissen, J. Schwarz, N. M. Gallagher, A. Rajca, M. Martins, M. B. Casu, “Magnetic behavior in metal-free radical thin films”, *Chem* **2022**, *8*, 801–814, DOI `10.1016/j.chempr.2021.11.021`.

[89] S. Shi, Z. Sun, X. Liu, A. Bedoya-Pinto, P. Graziosi, H. Yu, W. Li, G. Liu, L. Hueso, V. A. Dediu, M. Fahlman, “11,11,12,12-Tetracyanonaphtho-2,6-quinodimethane in Contact with Ferromagnetic Electrodes for Organic Spintronics”, *Advanced Electronic Materials* **2018**, *4*, 1800077, DOI `https://doi.org/10.1002/aelm.201800077`.

[90] S. Shi, Z. Sun, A. Bedoya-Pinto, P. Graziosi, X. Li, X. Liu, L. Hueso, V. A. Dediu, Y. Luo, M. Fahlman, “Hybrid Interface States and Spin Polarization at Ferromagnetic Metal–Organic Heterojunctions: Interface Engineering for Efficient Spin Injection in Organic Spintronics”, *Advanced Functional Materials* **2014**, *24*, 4812–4821, DOI `https://doi.org/10.1002/adfm.201400125`.

[91] V. Uvarov, J. Krutel, K. Mašek, J. Mysliveček, V. Johánek, “Thermal stability of cobalt oxide thin films and its enhancement by cerium oxide”, *Applied Surface Science* **2022**, *593*, 153430, DOI `https://doi.org/10.1016/j.apsusc.2022.153430`.

[92] L. Chen, F. Hu, H. Duan, Q. Liu, H. Tan, W. Yan, T. Yao, Y. Jiang, Z. Sun, S. Wei, “Intrinsic ferromagnetic coupling in Co3O4 quantum dots activatedby graphene hybridization”, *Applied Physics Letters* **2016**, *108*, DOI `10.1063/1.4954715`.

[93] M. C. Biesinger, B. P. Payne, A. P. Grosvenor, L. W. Lau, A. R. Gerson, R. S. Smart, “Resolving surface chemical states in XPS analysis of first row transition metals, oxides and hydroxides: Cr, Mn, Fe, Co and Ni”, *Applied Surface Science* **2011**, *257*, 2717–2730, DOI `https://doi.org/10.1016/j.apsusc.2010.10.051`.

[94] D. Cabrera-German, G. Gomez-Sosa, A. Herrera-Gomez, “Accurate peak fitting and subsequent quantitative composition analysis of the spectrum of Co 2p obtained with Al K radiation: I: cobalt spinel”, *Surface and Interface Analysis* **2016**, *48*, 252–256, DOI `https://doi.org/10.1002/sia.5933`.

[95] B. Senkovskiy, D. Usachov, A. V. Fedorov, O. Vilkov, A. Shelyakov, V. Adamchuk, “Electronic structure of Ti–Ni alloys: An XPS and NEXAFS study”, *Journal of Alloys and Compounds* **2012**, *537*, 190–196, DOI `10.1016/j.jallcom.2012.05.059`.

[96] J. F. van Acker, Z. M. Stadnik, J. C. Fuggle, H. J. W. M. Hoekstra, K. H. J. Buschow, G. Stroink, “Magnetic moments and x-ray photoelectron spectroscopy splittings in Fe 3s core levels of materials containing Fe”, *Physical Review B* **1988**, *37*, 6827–6834, DOI `10.1103/PhysRevB.37.6827`.

[97] I. N. Shabanova, N. S. Terebova, “Application of the XPS for Studying the Magnetic Moment of 3d Metals in Carbon–Metal Nanostructures”, *Surface and Interface Analysis* **2010**, *42*, 846–849, DOI `https://doi.org/10.1002/sia.3214`.

[98] M. L. B. Isabelle, A. Châtelain, W. A. de Heer, "Magnetism from the Atom to the Bulk in Iron, Cobalt, and Nickel Clusters", *Science* **1994**, *265*, 1682–1684.

[99] D. G. Van Campen, L. E. Klebanoff, "Spin-resolved and high-energy-resolution XPS studies of the 3s and 2s levels of metallic cobalt", *Physical Review B* **1994**, *49*, 2040–2046, DOI `10.1103/PhysRevB.49.2040`.

[100] T. Moorsom, M. Wheeler, T. Mohd Khan, F. Al Ma'Mari, C. Kinane, S. Langridge, D. Ciudad, A. Bedoya-Pinto, L. Hueso, G. Teobaldi, V. K. Lazarov, D. Gilks, G. Burnell, B. J. Hickey, O. Cespedes, "Spin-polarized electron transfer in ferromagnet/C_{60} interfaces", *Physical Review B* **2014**, *90*, PRB, 125311, DOI `10.1103/PhysRevB.90.125311`.

[101] D. Li, C. Barreteau, S. L. Kawahara, J. Lagoute, C. Chacon, Y. Girard, S. Rousset, V. Repain, A. Smogunov, "Symmetry-selected spin-split hybrid states in C_{60}/ferromagnetic interfaces", *Physical Review B* **2016**, *93*, PRB, 085425, DOI `10.1103/PhysRevB.93.085425`.

[102] A. Halder, S. Bhandary, D. D. O'Regan, S. Sanvito, A. Droghetti, "Theoretical perspective on the modification of the magnetocrystalline anisotropy at molecule-cobalt interfaces", *Physical Review Materials* **2023**, *7*, PRMATERIALS, 064409, DOI `10.1103/PhysRevMaterials.7.064409`.

[103] M. Benini, G. Allodi, A. Surpi, A. Riminucci, K.-W. Lin, S. Sanna, V. A. Dediu, I. Bergenti, "In-Depth NMR Investigation of the Magnetic Hardening in Co Thin Films Induced by the Interface with Molecular Layers", *Advanced Materials Interfaces* **2022**, *9*, 2201394, DOI `https://doi.org/10.1002/admi.202201394`.

Appendices

A. Thermally Ultrarobust S = 1/2 Tetrazolinyl Radicals: Synthesis, Electronic Structure, Magnetism, and Nanoneedle Assemblies on Silicon Surface

Reprinted with permission from
Z. Yang, M. Pink, E. M. Nowik-Boltyk, S. Lu, T. Junghoefer, S. Rajca, S. Stoll, M. B. Casu, A. Rajca, “Thermally Ultrarobust S = 1/2 Tetrazolinyl Radicals: Synthesis, Electronic Structure, Magnetism, and Nanoneedle Assemblies on Silicon Surface”, *Journal of the American Chemical Society* **2023**, *145*, 13335–13346, DOI `10.1021/jacs.3c03402`, `https://doi.org/10.1021/jacs.3c03402`.

J|A|C|S
JOURNAL OF THE AMERICAN CHEMICAL SOCIETY

pubs.acs.org/JACS Article

Thermally Ultrarobust S = 1/2 Tetrazolinyl Radicals: Synthesis, Electronic Structure, Magnetism, and Nanoneedle Assemblies on Silicon Surface

Zhimin Yang, Maren Pink, Ewa Malgorzata Nowik-Boltyk, Shutian Lu, Tobias Junghoefer, Suchada Rajca, Stefan Stoll,* Maria Benedetta Casu,* and Andrzej Rajca*

Cite This: J. Am. Chem. Soc. 2023, 145, 13335−13346 Read Online

ACCESS | Metrics & More | Article Recommendations | Supporting Information

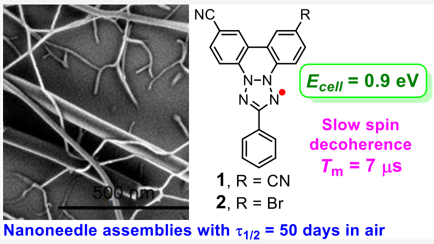

ABSTRACT: Open-shell organic molecules, including S = 1/2 radicals, may provide enhanced properties for several emerging technologies; however, relatively few synthesized to date possess robust thermal stability and processability. We report the synthesis of S = 1/2 biphenylene-fused tetrazolinyl radicals **1** and **2**. Both radicals possess near-perfect planar structures based on their X-ray structures and density-functional theory (DFT) computations. Radical **1** possesses outstanding thermal stability as indicated by the onset of decomposition at 269 °C, based on thermogravimetric analysis (TGA) data. Both radicals possess very low oxidation potentials <0 V (vs. SCE) and their electrochemical energy gaps, $E_{\text{cell}} \approx 0.9$ eV, are rather low. Magnetic properties of polycrystalline **1** are characterized by superconducting quantum interference device (SQUID) magnetometry revealing a one-dimensional S = 1/2 antiferromagnetic Heisenberg chain with exchange coupling constant $J'/k \approx -22.0$ K. Radical **1** in toluene glass possesses a long electron spin coherence time, $T_{\text{m}} \approx 7$ μs in the 40−80 K temperature range, a property advantageous for potential applications as a molecular spin qubit. Radical **1** is evaporated under ultrahigh vacuum (UHV) forming assemblies of intact radicals on a silicon substrate, as confirmed by high-resolution X-ray photoelectron spectroscopy (XPS). Scanning electron microscope (SEM) images indicate that the radical molecules form nanoneedles on the substrate. The nanoneedles are stable for at least 64 hours under air as monitored by using X-ray photoelectron spectroscopy. Electron paramagnetic resonance (EPR) studies of the thicker assemblies, prepared by UHV evaporation, indicate radical decay according to first-order kinetics with a long half-life of 50 ± 4 days at ambient conditions.

INTRODUCTION

Recent advances in the design and synthesis of thermally robust high-spin di- and triradicals based on the Blatter radical[1−6] have expedited the preparation of organic radical thin films via controlled evaporation under ultrahigh vacuum (UHV).[1,4−6] Notable developments include thin films of an S = 1/2 Blatter radical derivative exhibiting magnetic ordering[7] and a high-spin (S = 1) Blatter-based diradical with robust stability and electrical conductivity.[6] In addition, robustness and synthetic availability of S = 1/2 Blatter radicals[8] enabled their recent applications as paramagnetic liquid crystals,[9,10] batteries,[11] and potential molecular spin qubits.[12] Likely, other novel properties will emerge from the remarkable Blatter radical; however, we are in search of new S = 1/2 building blocks for future development.

2,2′-Biphenylene-fused tetrazolinyl (BFTZ) monoradicals, or so-called phototetrazolinyl radicals,[13] have attracted our attention because of their exceptional stability and, most importantly, the potential to achieve relatively large spin densities at the *para*-positions (and *ortho*-positions) with respect to the nitrogens of the tetrazolinyl moiety (Figure 1). Large spin densities at the *para*/*ortho* positions are the essential prerequisite in the design of high-spin polyradicals with large energy gaps between the high-spin ground state and low-spin excited state.[14−17]

Spin densities at the *para*/*ortho*-positions may be derived from experimental ^{1}H hyperfine couplings via the McConnell linear relationship,[18] that is, a larger hyperfine coupling corresponds to a greater spin density. For example, in the BFTZ radical (R = Ph, X = Y = H), the hyperfine coupling at the *para*-position is $|A(^1\text{H})| = 5.2$ MHz.[19] In other nitrogen-centered stable radicals, analogous values of *para* $|A(^1\text{H})|$ are 5.0 MHz (***p***) and 1.6 MHz (***p′***) in the Blatter radical,[20,21] 1.8 MHz in the oxo-verdazyl radical,[22] 3.1 MHz in the verdazyl radical,[23] and only 2.7 MHz in simple tetrazolinyl radicals.[24]

Received: April 1, 2023
Published: June 7, 2023

ACS Publications

https://doi.org/10.1021/jacs.3c03402
J. Am. Chem. Soc. 2023, 145, 13335−13346

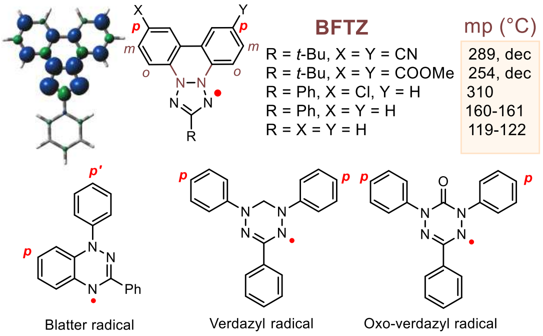

Figure 1. Top: 2,2′-Biphenylene-fused tetrazolinyl (BFTZ) radicals and spin density map at the UB3LYP/6-31G(d)+ZPVE level. Bottom: Blatter and verdazyl radicals. *Para*-positions are indicated with a red symbol ***p*** or ***p***′.

BFTZ radicals possess exceptional thermal stability. While the parent radical (R = X = Y = H) melts at about 120 °C,[25] its derivatives (R = *t*-Bu, X = Y = CN or CO_2Me) melt with decomposition at temperatures >250 °C, according to the literature.[24] Remarkably, a BFTZ derivative (R = Ph, X = Cl, Y = CN) was reported to melt at temperatures as high as ~300 °C.[20,21] Some of these radicals could be prepared not only in good yields but also with nearly quantitative spin concentrations. Also, they were found to be monomeric in the solid state and in solution.[13,19,24−26] In more recent studies, the mechanism of photochemical formation and ultrafast excited-state dynamics of tetrazolinyl radicals and 2,2′-biphenylene-fused tetrazolium cations (Figure 1: R = Ph, X = Y = H) were elucidated.[27,28]

Here, we report the synthesis and comprehensive characterization of $S = 1/2$ 2,2′-biphenylene-fused tetrazolinyl radicals **1** and **2** (Figure 2). Radicals **1** and **2** are designed to take advantage of the exceptional stability of the BFTZ backbone, with the long-term goal of thermally and magnetically robust high-spin radicals. In particular, Br-substituted **2** would likely enable cross-coupling chemistry.

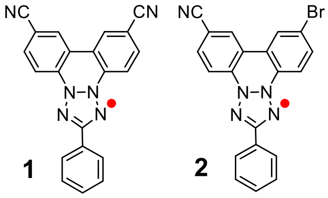

Figure 2. Radicals **1** and **2**.

Both radicals were prepared as crystalline solids with near-perfect spin concentrations and characterized by X-ray crystallography, electron paramagnetic resonance (EPR) spectroscopy (including electron spin relaxation properties for **1**), superconducting quantum interference device (SQUID) magnetometry, voltammetry, UV−vis−NIR absorption spectroscopy, and thermogravimetric analysis (TGA). Radical **1** was evaporated under UHV, forming, under the present preparation conditions, nanoneedles, as shown by scanning electron microscopy (SEM). The nanoneedles' UHV- and air-stability were further investigated by using X-ray photoelectron spectroscopy (XPS) and EPR spectroscopy.

The nanoneedle morphology is very interesting for nanoelectronics applications because of device miniaturization and the favorable ratio between surface and bulk that is beneficial for various devices such as sensors and transistors.[29−32] Several examples of small diamagnetic molecules, p- and n-type semiconductors, have been shown to grow following this morphology.[32−37] However, to our knowledge, among adequately characterized thin films of radicals, only the tris(2,4,6-trichlorophenyl)methyl radical shows a mixed morphology, with the coexistent presence of islands and fibers when grown on graphene.[38] Conversely, radical **1** shows a distinct nanoneedle self-assembled morphology under the present preparation conditions.

■ RESULTS AND DISCUSSION

Synthesis. Formazans **4** are synthesized using a phase transfer catalysis approach,[39−41] in which suspensions of diazonium salts, prepared in situ from 4-cyano- or 4-bromo-aniline, are added to hydrazone **3** in a mixture of dichloromethane (DCM) and water in the presence of tetraalkylammonium salt (Scheme 1). Oxidation of formazans **4** with *N*-bromo-succinimide (NBS) provides the tetrazolium salts **5**.[24,41] Photochemical ring closure of **5** gives fused tetrazolium (phototetrazolium) salts **6**.[24,25] Finally, reduction of salts **6**, using $SnCl_2$ under basic conditions in water/benzene under inert atmosphere,[26] yields radicals **1** and **2**. Spin concentrations for all prepared samples of radicals are summarized in the Supporting Information (SI).

Scheme 1. Synthesis of Radicals 1 and 2

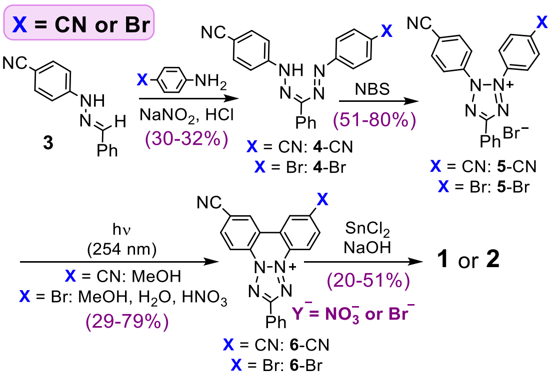

X-ray Crystallography. The structures of radicals **1** and **2** are confirmed by X-ray crystallography (Figure 3). In both radicals, the tetrazolinyl-and-biphenyl-fused moieties are planar. As illustrated by the small values of the dihedral angles, the phenyl substituent connected to C1 is approximately co-planar with the planes defined by the phenyl group (C14−C19) and the tetrazolinyl/biphenyl (C1−C13, C20, C21, N1-N6, Br1) tilted relative to each other by 10.18(9) and 1.2(2)° in **1** and **2**, respectively.

Both **1** and **2** crystallize in the monoclinic space group $P2_1/n$. However, one molecule of benzene per formula unit is co-crystallized with **1**. The crystals of **2** that are obtained from either pentane/toluene (0.17-mm-long needle) or pentane/ethyl acetate (0.87-mm-long needle) possess identical

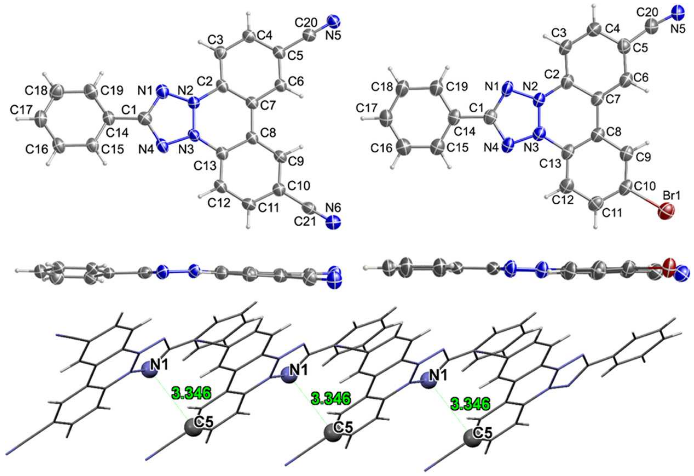

Figure 3. Molecular structure and crystal packing of **1** at 100 K and of **2** at 153 K. For **1**, a molecule of co-crystallized benzene is omitted. Top and Middle: Ortep plots (top and side views) with carbon, nitrogen, and bromine atoms depicted with thermal ellipsoids set at the 50% probability level (top and side views). For **1**, a molecule of co-crystallized benzene is omitted and for **2**, Br/CN disorder is not shown. Bottom: tetramer of molecules of **1** forming a one-dimensional (1-D) chain along the crystallographic *a*-axis with short intermolecular contacts, N1···C5 = 3.346 Å. Further details are reported in Tables S1−S3 and Figures S1−S6, SI.

structures at 153 and 296 K, respectively; in both structures, the Br and CN groups are disordered over two positions.

In the crystal of **1** at 100 K, the molecules are π-stacked, forming one-dimensional (1-D) chains along the crystallographic *a*-axis, with an average plane-to-plane distance of 3.28(9) Å, with planes defined by the C/N atoms of the entire molecule (Figure 3). Because intermolecular close contacts, such as N1···C5 = 3.346 Å,[42] primarily involve atoms with positive spin densities, significant intermolecular antiferromagnetic interactions are anticipated in crystalline radical **1**. Also, co-crystallized molecules of benzene magnetically isolate the 1-D chains (predominantly along the *c*-axis).

In the crystal of **2** at 153 K, the molecules are also π-stacked, forming alternating 1-D chains along the crystallographic *a*-axis, with plane-to-plane distances of 3.24(4) and 3.35(4) Å, when Br/CN disorder is not considered (planes defined by the Br/C/N atoms of the entire molecule). In the crystal of **2** at 296 K, 1-D chains with an average plane-to-plane distance of 3.40(4) Å are found, when Br/CN disorder is taken into account. For the nearest-neighbor molecules, intermolecular contacts, such as N1···C5 = 3.407 Å, are found. Thus, we anticipate that intermolecular antiferromagnetic interactions in **2** will be relatively weak and, most likely not 1-D, because of the spatial proximity of 1-D chains in the crystal.

Density-Functional Theory (DFT) Computations. DFT (UB3LYP-D3BJ/6-31G(d,p)/PCM-UFF+ZPVE) optimized geometries for **1** and **2** in benzene (or DCM) indicate perfectly planar structures with C_{2v} and C_s symmetry, respectively.[43] In these computations, the UB3LYP functional is augmented with Grimme's empirical dispersion correction (D3 version)[44] and with the Becke−Johnson damping function.[45]

Based on the relatively small value of the lowest vibrational frequency of 16 cm^{-1} (A_2-symmetric mode) in **1**, primarily involving twisting of the phenyl group at C1 (Figure 3), we suspect that small distortions from planarity observed in the solid state structures of especially **1** are due to crystal packing effects. (For comparison in **2**, the lowest vibrational frequency of 22 cm^{-1} is computed.) Both radicals follow the typical Aufbau rule, with electrons in their singly occupied molecular orbital (SOMOs) at higher energy, compared to electrons in the corresponding highest occupied molecular orbitals (HOMOs), in contrast to the SOMO/HOMO inversions found in selected nitrogen-centered radicals.[46−52]

EPR Spectroscopy. The purity of samples for radicals **1** and **2** is determined by EPR spectroscopic spin counting (SI). In addition, treatment of **1** with HCl in methanol/water at room temperature gives cleanly the 1-electron-oxidized product, i.e., diamagnetic tetrazolium cation **6**-CN.

Neugebauer and Russell carried out ^{15}N labeling in symmetrically substituted BFTZ (X = Y) derivatives (Figure 1)[53] and established that the values of $A(^{14}N) \approx 11$ MHz associated with N1 and N4 (Table 1) were almost independent of substitution; the values of $A(^{14}N) \approx 22{-}16$ MHz associated with N2 and N3 (Table 1) were following the relationship, $CH_3 > H > CO_2CH_3 > CN$.[19,24,53] Also, in the un-substituted derivatives (X = Y = H), values of $A(^1H)$ at the *ortho* and *para* positions (Figure 1) were identical.[19]

Due to significant spin densities at the four nitrogens of the tetrazolinyl moiety and at the *ortho*-carbons (and protons), CW EPR spectra of radicals **1** and **2** in benzene at room temperature show resolvable isotropic ^{14}N and ^1H hyperfine couplings, $A(^{14}N)$ and $A(^1H)$ (Figure 4 and Table 1).[54]

The inclusion of unresolved ^{79}Br- and ^{81}Br-hyperfine couplings at natural isotopic abundance,[54] which serves as an effective additional line broadening contribution, provides an improved spectral fit for **2** (Figure S21, SI). The resultant value of $A(^{79}Br) = 0.78$ MHz indicates a non-negligible amount of spin density on bromine, which is in qualitative agreement with the DFT-computed $A(^{79}Br) = 1.7$ MHz (Table S4, SI).

We evaluate electron spin relaxation properties of **1** in frozen dilute toluene solution as a function of temperature. Longitudinal relaxation properties are measured using inversion recovery and fitted with an exponential recovery $V(T) = a - b\exp(-T/T_1)$, yielding the longitudinal relaxation time T_1 (Figure S22, SI). As shown in Figure 5A, the relaxation

Table 1. Summary of DFT-Computed (UB3LYP-D3BJ/6-31G(d,p)/PCM-UFF+ZPVE in Benzene) and Experimental Hyperfine Coupling Constants (A in MHz)

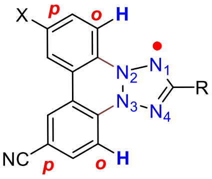

	1R = Ph X = CN		2R = Ph X = Br		R = *t*-Bu X = CN
	DFT	EPR	DFT	EPR	EPR[a]
N$_1$	11.9	10.5	11.6	10.4	10.7
N$_2$	10.9	15.8	13.8	20.1	15.7
N$_3$	10.9	15.8	10.0	14.8	15.7
N$_4$	11.9	10.5	11.9	10.4	10.7
H(*o*)	−7.2	5.8	−7.1	5.6	5.0
			−7.9	6.0	
N (CN)	1.6		1.8		

[a] Ref 24.

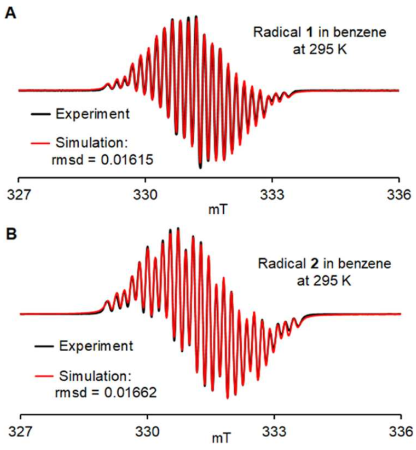

Figure 4. EPR spectra of radicals 0.29 mM **1** and ~0.2 mM **2** in benzene. (A) 9.2918 GHz, modulation amplitude = 0.02 mT; simulation:[54] g = 2.0042, $A(^{14}N)$ = 15.79 MHz (n = 2), $A(^{14}N)$ = 10.51 MHz (n = 2), $A(^{1}H)$ = 5.74 MHz (n = 2), linewidths peak-to-peak (lwpp), Gaussian = 0.00043 mT and Lorentzian = 0.1179 mT; (B) 9.2956 GHz, modulation amplitude = 0.04 mT; simulation:[54] g = 2.0046, $A(^{14}N)$ = 20.10 MHz (n = 1), $A(^{14}N)$ = 10.40 MHz (n = 2), $A(^{14}N)$ = 14.79 MHz (n = 1), $A(^{1}H)$ = 6.02 MHz (n = 1), $A(^{1}H)$ = 5.64 MHz (n = 1), lwpp, Gaussian = 0.00146 mT and Lorentzian = 0.1225 mT; g-values are uncorrected. Further details are in the SI: Table S4 and Figures S19−S21.

rate, $1/T_1$, shows a steep monotonic increase with temperature, progressing from 0.033(5) ms^{-1} at 19 K to 2.3(5) ms^{-1} at 160 K.

To quantify the transverse relaxation, Hahn echo decays are measured and fitted with a stretched exponential decay $V(2\tau) = V(0)\ \exp(-(2\tau/T_m)^{\xi})$, yielding the electron spin phase memory (or coherence) time T_m and the stretch exponent ξ. The Hahn echo decays show substantial modulations due to ^{14}N (see Figure S23, SI), which are neglected in the stretched exponential model. As shown in Figure 5B, $1/T_m$ shows a nonmonotonic temperature dependence, in which it initially decreases to a minimum of about 0.14(1) μs^{-1} around 60 K (corresponding to $T_m \approx 7\ \mu s$), before it increases until about 120 K. Values of $1/T_m$ above 120 K are unreliable and associated with large uncertainties, since in this range the echo decay is on the same time scale as the period of the strong ^{14}N nuclear echo modulation. We tentatively attribute the increased transverse relaxation rate at very low temperatures to the dynamics of the methyl groups of the solvent molecules (toluene-h_8). Protons on these methyl groups are responsible for enhancing decoherence. Such effects have been observed in a variety of other methyl-containing systems.[55−58] The decrease of the stretch exponent at low temperatures corroborates this interpretation.

One of the key prerequisites for the use of paramagnetic molecules as spin qubits for potential quantum sensing applications is a long coherence time T_m.[59,60] For **1** in toluene-h_8, the value of $T_m \approx 7\ \mu s$ in the 40−80 K temperature range is comparable to T_m = 7.2 μs for a Blatter radical derivative measured in toluene-d_8 at 25 K.[61] The value of $T_m \approx 7\ \mu s$ is significantly longer than T_m = 3−4 and 4−5 μs in the 40−80 K range for typical *gem*-dimethyl and optimized spirocyclic pyrroline nitroxide radicals, respectively,[58] or T_m = 4−6 μs and T_m < 4 μs in the 40−80 K range for Blatter radicals immobilized on silica and optimized vanadium complexes in protiated solvents/matrices, respectively.[12,59,60]

SQUID Magnetometry. Polycrystalline **1** and **2** are studied by SQUID magnetometry (Figures S24−S27, SI). We focus on the study of radical **1** (Figure 6) because **1** exhibits much stronger exchange interactions, compared to **2**, as indicated by the values of mean-field parameters ($|\theta|$) differing by a factor of 3 (Figure S26, SI). The value of χT_{max} = 0.351 emu K mol^{-1} in the high-temperature plateau (280−320 K) is in excellent agreement with a spin concentration of 94%, as determined by EPR spin counting. At lower temperatures, the χT vs. T plot shows a profound downward turn, with crystal defects (magnetically isolated S = 1/2 radicals), significantly contributing to the values of χT (and χ) at 1.8 K. The χ vs T plot has a characteristic broad maximum at $T_{max} \approx$ 14 K, suggesting a low-dimensional magnetic behavior. Three sets of χ vs. T data may be well fit to one-dimensional (1-D) S = 1/2 antiferromagnetic Heisenberg chain,[62−64] to provide the coupling constant, $J'/k = -21.85 \pm 0.70$ K (mean ± SE, n = 3). The common relationship for such 1-D chains, $T_{max}/|J'/k|$ = 0.641, is well satisfied for radical **1**.[62] Notably, another limiting model for such intermolecular antiferromagnetic coupling, such as pairs of S = 1/2 radicals (dimers),[15] gives much inferior fits for the χ vs. T data (Figure S25, SI).[4,65,66]

Electrochemistry. Cyclic, differential pulse, and square-wave voltammograms (SWV) for radical **1** present approximately reversible processes with the oxidation and reduction peaks at $E^{+/0} \approx -0.14$ V and $E^{-/0} \approx -1.07$ V vs. SCE.[67] Because radical **2** is derived from **1** by replacing one of the strongly electron-withdrawing cyano groups with bromine, it is easier to oxidize at $E^{+/0} \approx -0.28$ V to the diamagnetic cation and slightly more difficult to reduce at $E^{-/0} \approx -1.14$ V (Figure 7).

The highly negative oxidation potentials (e.g., $E^{+/0} \approx -0.3$ V for **2**) may impede its Pd-catalyzed cross-coupling reactions, as already observed for Blatter radicals with $E^{+/0} \approx +0.1 - (+0.3)$ V,[68,69] requiring a highly reactive Pd-catalyst,[5] compared to oxo-verdazyl radicals with $E^{+/0} \approx +0.8$ V.[70,71]

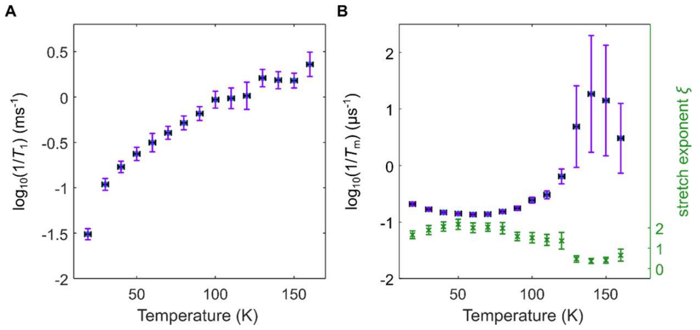

Figure 5. Relaxation properties of **1** at X-band (9.70 GHz, 346 mT). (A) Temperature dependence of $1/T_1$ (blue circles) with experimental errors of temperature (black) and 95% confidence intervals of $1/T_1$ (purple). (B) Temperature dependence of $1/T_m$ (blue circles, left axis) and the stretch exponent ξ (green crosses, right axis), including 95% confidence intervals. Values are listed in Table S5, SI.

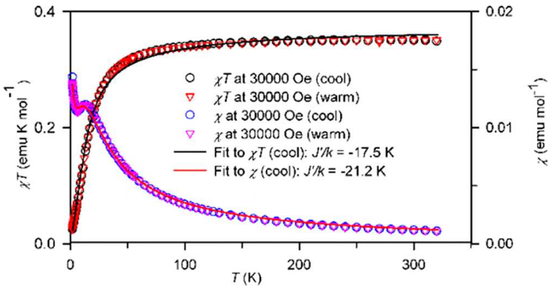

Figure 6. SQUID magnetometry of polycrystalline radical **1**: experimental data plotted as χT vs. T and χT vs. T and the selected numerical fits to one-dimensional $S = 1/2$ antiferromagnetic Heisenberg chain (eq S1A,B, SI). Fitting parameters, such as J'/k and weight factors, and relevant statistical parameters are summarized in Table S6, and illustrated in Figures S24–S27, SI.

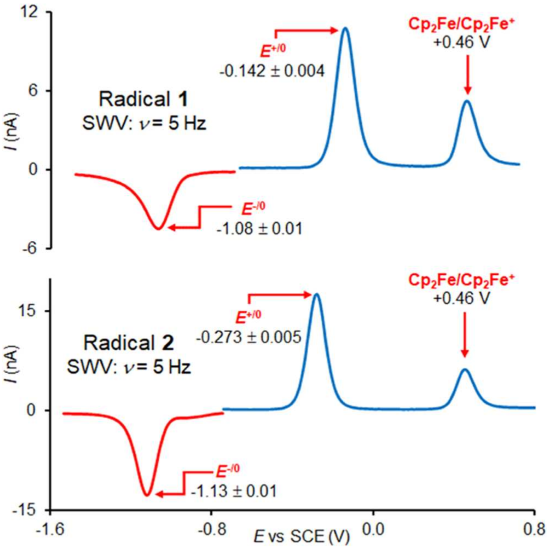

Figure 7. Square-wave voltammetry (SWV) of radicals **1** and **2** in 0.1 M tetrabutylammonium hexafluorophosphate in dichloromethane at room temperature. Redox potentials are given as mean ± stddev with n = 4–9 (**1**) and 6–9 (**2**). For further details, including cyclic and differential pulse voltammetries; see the SI, Figures S15–S18.

For radicals **1** and **2**, electrochemical band gaps, $E_{\text{cell}} = E^{+/0} - E^{-/0}$, are rather low with $E_{\text{cell}} = 0.935 \pm 0.015$ and 0.866 ± 0.003 eV, respectively. Because E_{cell} may be related to the gas phase IP − EA and to disproportionation energies for the $2\text{R}^\bullet \rightarrow \text{R}^+ + \text{R}^-$ reaction, the low values of E_{cell} are one of the favorable factors in the design of neutral radical conductors.[6,72−75]

UV–Vis–NIR Spectroscopy. UV–vis–NIR spectra of **1** and **2** in dichloromethane (DCM) show the longest-wavelength bands at $\lambda_{\max}$ = 717–729 nm with broad absorption envelopes (Figure 8). The spectrum for **1** can be reasonably well reproduced by time-dependent density-functional theory (TD-DFT) computations (after shifting the computed band positions by −0.6 eV, Figure S7, SI).[43] Plots of molar absorbance (extinction coefficient), ε, vs. wavenumber, $\tilde{\nu}$, for radical **1** in DCM and in benzene demonstrate that the longest-wavelength band at $\lambda_{\max} \approx 730$ nm (the lowest-wavenumber band at $\tilde{\nu}_{\max} \approx 13{,}700$ cm^{-1}) is symmetrical, and it shows negligible solvent dependence (Figure 8, inset).

For radical **1** in DCM or benzene, the optical band gap, $E_g = 1.12 \pm 0.002$ eV, is slightly higher, compared to $E_g = 1.09$ eV for radical **2** in DCM (Figures S9–S12, SI), which parallels the trend in the values of E_{cell}; though for **1** in DCM, the longest-wavelength band, $\lambda_{\max}$ = 726–729 nm, possesses a bathochromic shift, compared to corresponding $\lambda_{\max}$ = 717 nm for **2** in DCM. For comparison, BFTZ (R = *t*-Bu, X = Y = CN) radical in dioxane was reported to possess $\lambda_{\max}$ = 695 nm.[24]

Diamagnetic cations (salts) **6**-CN and **6**-Br, precursors to **1** and **2**, possess much higher E_g = 2.50 and 2.00 eV, respectively (Figures S13 and S14).

Stability of Radicals by TGA. Thermogravimetric analysis (TGA) data indicate that the onset of thermal decomposition of **1**, corresponding to a 1% mass loss, is at 269 °C. At 301 °C, the decomposition rate reaches a sharp maximum (with a shoulder at ∼290 °C). In contrast, for **2**, the primary decomposition has the onset and maximum rate temperatures that are by 50–80 °C lower, and the secondary decomposition possesses a maximum rate at 338 °C (Figure 9).

We note that radical **1** in benzene at room temperature is quite persistent with about 3% (vs. TEMPONE) and 5% decrease of double-integrated intensity of its EPR spectrum in one and two weeks, respectively; this corresponds to a half-life of the order of 5–6 months. As mentioned before, radical **1** in the presence of a strong acid, such as concentrated HCl in

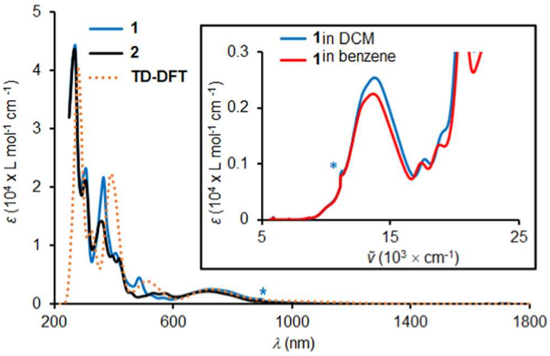

Figure 8. Main plot: UV−vis−NIR (294 K) absorption spectra for 0.31 and 0.30 mM radicals **1** and **2** in DCM, as well as TD-DFT-computed spectrum for **1** in DCM solvent model. For **1**, bands at λ_{max} = 270, 306, 365, 406, 485, and 729 nm have the following extinction coefficients (L mol^{-1} cm^{-1}): $\varepsilon_{270} = 4.4 \times 10^4$, $\varepsilon_{306} = 2.3 \times 10^4$, $\varepsilon_{365} = 2.2 \times 10^4$, $\varepsilon_{406} = 8.7 \times 10^3$, $\varepsilon_{485} = 4.5 \times 10^3$, and $\varepsilon_{729} = 2.5 \times 10^3$. The values of ε are not corrected for spin concentration of the radicals. Inset plot: Expanded spectra for **1** in DCM and benzene, plotted vs wavenumbers ($\tilde{\nu}$) and showing the longest-wavelength band at $\lambda_{max} \approx$ 730 nm. The feature at $\lambda \approx 900$ nm, marked with a blue asterisk, is an instrumental artifact (change of grating). Further details may be found in the SI: Figures S7−S14.

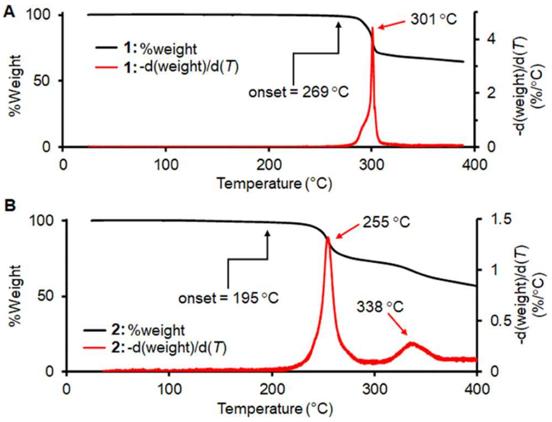

Figure 9. Thermogravimetric analysis (TGA) of radicals **1** (A) and **2** (B) under N_2; heating rate = 5 °C min^{-1}. Further details may be found in the SI: Figures S28−S31.

methanol/water, at room temperature undergoes a nearly quantitative conversion to the precursor tetrazolium salt **6**-CN (see SI, Section 1e).

Controlled Deposition of Radical 1 on SiO_2/Si(111) Wafers. Using a well-established method,[76,77] we evaporated radical **1** on native SiO_2 on Si(111) wafers. We used organic molecular beam deposition (OMBD) which allows precise control of the evaporation parameters.[78] The radical assemblies were investigated, without breaking the vacuum, by using XPS. This experimental technique, based on the photoelectric effect, can be used to determine quantitatively the concentration of the elements adsorbed onto a surface.[79,80] The intensity and binding energies of the spectroscopic lines are sensitive to the chemical environment of the elements forming the radicals.[79] Thus, we were able to: (1) compare the core-level spectra of the assemblies with those of the powder (i.e., with the signal from radical **1** that did not undergo evaporation, Figure 10); (2) calculate the stoichiometry of the obtained assemblies, comparing them to the molecular stoichiometry (Table S7, SI); and (3) fit the main spectroscopic line adopting a fit procedure that we developed for radicals[81] that allows assessing the integrity of the molecules and, therefore, their radical character (Figure 10).

Looking in detail at the C 1s and N 1s core-level spectra, we found that the main lines have a complex shape that mirrors the different chemical environments of each atom in the radical. The carbon atoms have two main different chemical environments: the emitted photoelectrons have different binding energies depending on whether they are bound to other carbon atoms and hydrogen atoms or to a nitrogen atom (see; the molecular structure in Figure 2, the fit analysis in Figure 10, and the corresponding Tables S8 and S9, SI). This is signaled by the C 1s spectroscopic line showing two contributions, the one at higher binding energy being the component due to photoemission of electrons from carbon atoms bound to nitrogen atoms. In a very simplified model, this can be understood in terms of electronegativity. Nitrogen atoms are more electronegative than carbon atoms. This moves the electronic cloud toward them, requiring more energy to emit an electron. A similar argument also holds for the N 1s spectroscopic line that, with its complex shape, mirrors the presence of the tetrazole ring, with four different chemical environments of the nitrogen atoms and the presence of the cyano groups (see the molecular structure in Figure 2, the fit analysis in Figure 10, and Tables S10 and S11, SI). The fit assignment is also in very good agreement with previously investigated radical and closed-shell thin films.[1,61,82] In addition to the effects due to the different chemical environment, we also observe the presence of several satellite features, the so-called shake-up satellites, typical features in photoemission that appear as an effect of the relaxation processes, caused by the core hole left behind by the photoemitted electron. Taking into account their intensity is mandatory to gain reliable information on the stoichiometry of the investigated systems.[79,80,83]

The comparison of the spectra of the assembly with the spectra of the powder does not show new or different features (see Figure 10).

In the tetrazolinyl ring, the chemical environments of the four nitrogen atoms are very similar, thus, within the experimental resolution, we expect a single asymmetric line, as it is the actual case both for powders and assemblies. This is consistent with previously published results on the diamagnetic tetrazole-based systems.[84−88] The main line at around 400 eV shows a pronounced shoulder. This suggests a stronger delocalization/screening of the core hole created upon photoemission in one of the nitrogen atoms. Considering the crystal structure of radical **1** (Figure 3), we can infer that the intermolecular contact N1···C5 is short enough[42,89−91] to enhance the screening of the core hole in N1, pushing the binding energy of the N1 photoemitted electrons toward the lower-energy range. This behavior is the same for the assemblies and the powder (polycrystalline **1**). This observation suggests that the nanoneedles are characterized by an arrangement of the molecules similar to the one of polycrystalline **1**.

The result of this approach indicates that evaporation and deposition do not change the chemical structure of the

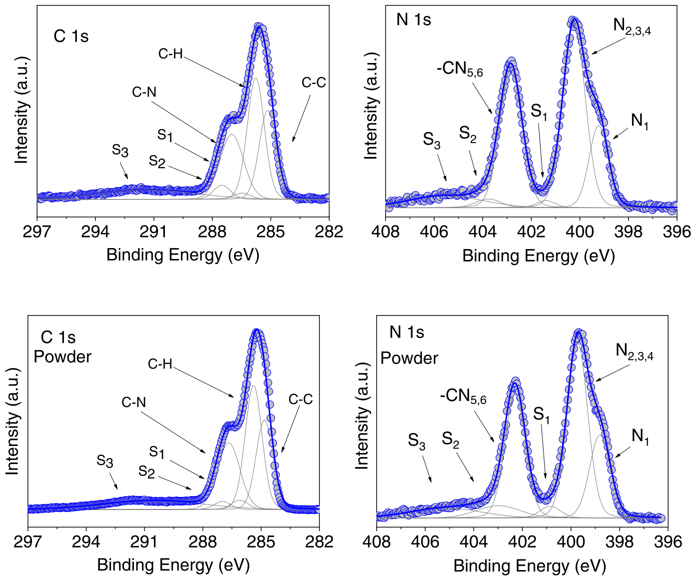

Figure 10. (Top) C 1s and N 1s core-level spectra of a thicker assembly of radical **1** deposited on SiO_2/Si(111) substrate compared to the (bottom) powder spectra, together with their fit components. For the fit details, see the Supporting Information.

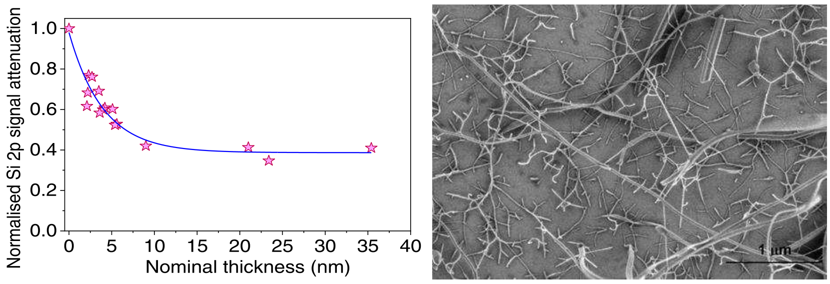

Figure 11. (Left) Attenuation of the Si 2p XPS signal, normalized to the corresponding substrate signal at zero adsorbate thickness as a function of radical **1** nominal thickness, during the deposition at room temperature of radical **1**. The exponential decay line is a guide to the eye. (Right) Typical SEM image showing the radical **1** nanoneedles (see also Figure S32 in the Supporting Information for additional SEM images).

molecules in the assemblies, i.e., the radical character and the molecules are wholly intact in the assembly, i.e., the deposition of radical **1** occurred without degradation. The assemblies were also investigated by using EPR spectroscopy that confirmed their radical character.

XPS is also a powerful spectroscopic method to assess the growth modes of adsorbates onto a substrate. An advantage of this method is that the investigation occurs in real time, without breaking the vacuum, by monitoring the decay of the substrate signal versus the nominal thickness of the adsorbate during evaporation (Figure 11). We note that the substrate signal, Si 2p in this case, follows an exponential decay with increasing the assembly nominal thickness, which indicates either Stranski−Krastanov (layer(s) + islands) or Volmer−Weber growth modes (islands). However, the decay at higher thickness is different in the two cases: for pure island nucleation and growth, the substrate signal intensity is still very high as in the present case. Thus, XPS hints at the Volmer−Weber growth mode. This growth mode is favored by weak molecule-substrate interactions and the selected thermodynamical conditions determined by substrate and evaporation temperatures. To shed light on the assembly morphology we used scanning electron microscopy (SEM). The SEM images (Figures 11 and S32, SI) are very surprising. On the one hand, they confirm the XPS finding of island growth, on the other hand, the islands have a specific morphology: they are needles. We have never observed this morphology in our previously investigated radical and multiradical systems. This specific morphology justifies, and it is the reason why, in this case, we prefer to use the word "assembly" rather than the word "film" to describe the adsorbate. In general, the needle morphology is generated by the asymmetry of the diffusion and traverse step-edge potential barriers seen by the molecules landing on the nucleated island during evaporation.[35] The diffusion barrier along the plane perpendicular to the needle axis is high, hindering the growth in those directions while the growth along the needle axis is facilitated. We also observe that in some cases the diffusion barrier relaxes giving rise to branches that follow a dendritic growth. The nanoneedles are stable when exposed to air: we monitored their core-level signals upon prolonged air exposure by using XPS and did not observe changes (see Figures S33 and S34, SI).

Persistence of Assemblies of Radical 1 on Silicon Surface by EPR Spectroscopy. We studied the nanoneedle assemblies of **1** on SiO_2/Si(111) by EPR spectroscopy. Their typical EPR spectra show two components, that is, a narrow $S = 1/2$ isotropic peak, which is superimposed on a broader anisotropic $S = 1/2$ peaks; these peaks correspond to radical **1** and the well-known paramagnetic defect site in the Si substrate, respectively (Figure 12A). This is confirmed by the spectra of empty SiO_2/Si(111) substrate (SI). Numerical fits of the spectra of the assemblies provide the ratios for the two components, which allow for a calculation of the molar fraction of radical **1**, x (Table S12, SI), assuming that the intensity of the spectrum for the Si-defect site is constant. Decay of x follows first-order kinetics with a half-life, $\tau_{1/2} = 50 \pm 4$ days (d) (Figure 12A).

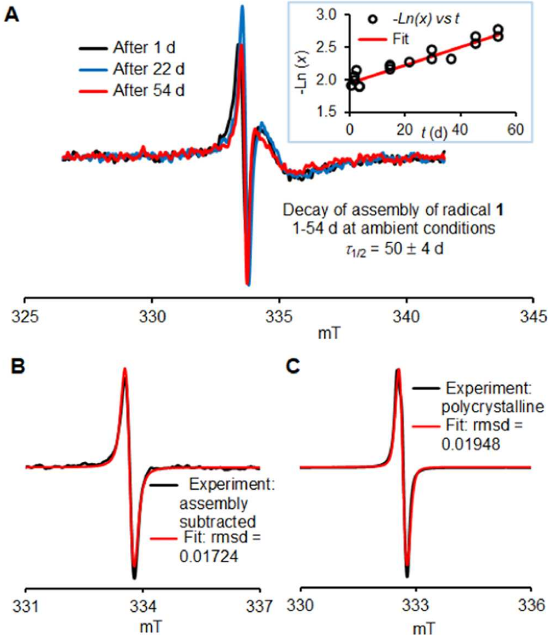

Figure 12. EPR spectroscopy of assemblies of radical **1** at ambient conditions: assemblies on SiO_2/Si(111) (A, B) and polycrystalline (C). Additional details may be found in the SI: Table S12 and Figures S35−S40.

For the freshly prepared assemblies on SiO_2/Si(111), the spectral subtraction (adsorbate minus the substrate), provides a narrow line spectrum with $g = 2.0036$ and a peak-to-peak linewidth (lwpp) of about 0.17 and 0.12 mT for Gaussian and Lorentzian components (Figure 12B). This spectrum may be compared to similar spectra of polycrystalline radical **1**, for which $g = 2.0034$ and lwpp = 0.18 mT (Gaussian) and 0.05 mT (Lorentzian) are obtained (Figure 12C). Since nanoneedle assemblies have a line-shape intermediate between Gaussian and Lorentzian, this may suggest an even more pronounced 1-D character for exchange coupling, compared to the polycrystalline solid.[92]

■ CONCLUSIONS

We successfully synthesized two new tetrazolinyl-based (BFTZ) radicals **1** and **2** with excellent spin concentrations. X-ray crystallography of **1** and **2** shows nearly perfectly planar structures. DFT computations reveal perfectly planar structures with C_{2v} (for **1**) and C_s (for **2**) point groups of symmetry. Dicyano-substituted radical **1** shows long electron spin coherence times in frozen solution. Polycrystalline **1** has an ultrarobust thermal stability as suggested by its onset of decomposition in TGA at >260 °C. We were able to evaporate radical **1** under controlled conditions to form nanoneedles with intact radical character. The nanoneedles are also stable under air. This specific morphology might enable using radical **1** with the purpose to achieve precise lateral control of deposition, growth, and positioning of radical nanostructures in nanodevices. Combination of ultrarobust thermal stability, nanoneedle morphology, low electrochemical band gap, and relatively long electron spin coherence times makes radical **1** exceptional.

We envisage tetrazolinyl-based (BFTZ) radicals as superior building blocks for the next generation of thermally and magnetically robust high-spin diradicals and triradicals.

■ EXPERIMENTAL SECTION

X-ray Crystallography. Crystals of **1** and **2** for X-ray studies were prepared by slow evaporation from organic solvents. Data collections were performed at Indiana University, using Mo Kα radiation. Final cell constants were calculated from the *xyz* centroids of strong reflections from the actual data collection after integration (SAINT);[93] intensity data were corrected for absorption (SADABS).[94] The space group, $P2_1/n$, was determined based on intensity statistics and systematic absences. The structures were solved and refined using the SHELX suite of programs.[95,96] Intrinsic-methods solutions were calculated, which provided most non-hydrogen atoms from the E-maps. Full-matrix least squares/difference Fourier cycles were performed, which located the remaining nonhydrogen atoms. All nonhydrogen atoms were refined with anisotropic displacement parameters. The hydrogen atoms were placed in ideal positions and refined as riding atoms with relative isotropic displacement parameters. Crystal and structure refinement data for **1** and **2** are in the Supporting Information and the CCDC deposited files in CIF format.

Synthesis. Standard techniques for synthesis under inert atmosphere (argon or nitrogen), using custom-made Schlenk glassware and custom-made double-manifold high-vacuum lines, were employed. Chromatographic separations were carried out using normal-phase neutral alumina or silica gel.

Electron Spin Relaxation. Pulse EPR data were recorded at X-band on a Bruker E580 spectrometer equipped with an MD4 dielectric resonator and a Bruker/ColdEdge cryogen-free sample cooling system. The sample in 4 mm O.D. was prepared in toluene with a concentration of 200 μM, validated by spin quantification. The sample was purged with argon for 3 minutes before freezing. Longitudinal relaxation times T_1 were determined from inversion recovery data recorded with a $\pi - T - \pi/2 - \tau - \pi - \tau -$echo sequence, with a constant $\tau = 200$ ns and four-step phase cycling. Phase memory times T_m were obtained from fitting a stretched exponential to Hahn echo decay curves, obtained with a $\pi/2 - \tau - \pi - \tau -$echo sequence, with an initial $\tau = 200$ ns and two-step phase cycling. All pulses are rectangular pulses. The length of the $\pi/2$ pulse ranges from 14 to 16 ns. A nutation experiment and an echo-detected field sweep were measured at each temperature for optimizing pulse length and magnetic field, respectively. The sample temperature was controlled via a Mercury iTC controller (Oxford Instruments) utilizing a Cernox sensor mounted on the resonator body.

Assemblies on SiO_2/Si(111) Wafers. The preparation of the radical assemblies and the XPS measurements were carried out under ultrahigh-vacuum conditions. A three-chamber UHV-System was used equipped with a monochromatic Al Kα source (SPECS Focus 500) and a SPECS Phoibos 150 MCD hemispherical electron analyzer, attached directly to the OMBD and sample preparation chambers. To grow the radical assemblies on SiO_2/n-Si(111) wafers, we followed our approach to film deposition by OMBD.[78,97] The substrate was cleaned in an ultrasonic bath in acetone and methanol for one hour each. After annealing at around 500 K for several hours, the wafer surface was examined for contaminants by XPS. The radical molecules were evaporated and deposited on the substrate kept at room temperature (evaporation rate: 0.1−0.7 nm/min). The evaporation rate was monitored by a quartz crystal microbalance. In parallel, the nominal thickness was estimated from the XPS data, investigating the attenuation of the substrate Si 2p signal after deposition. The XPS survey spectra were recorded at 50 eV pass energy and the high-resolution core-level spectra at 20 eV pass energy. All measured binding energies were calibrated by taking the substrate Si $2p_{3/2}$ signal at 99.8 eV as a reference.[98] The energy resolution was 0.4 eV. All photoemission measurements were performed in normal emission. The SEM images were acquired ex situ by using a Hitachi SU 8030 SEM.

■ ASSOCIATED CONTENT

Supporting Information

The Supporting Information is available free of charge at https://pubs.acs.org/doi/10.1021/jacs.3c03402.

General procedures and materials, additional experimental and computational details for **1** and **2**, including XPS fit parameters and stability investigations of assemblies of **1** (PDF)

Accession Codes

CCDC 2253237−2253239 contain the supplementary crystallographic data for this paper. These data can be obtained free of charge via www.ccdc.cam.ac.uk/data_request/cif, or by emailing data_request@ccdc.cam.ac.uk, or by contacting The Cambridge Crystallographic Data Centre, 12 Union Road, Cambridge CB2 1EZ, UK; fax: +44 1223 336033.

■ AUTHOR INFORMATION

Corresponding Authors

Stefan Stoll − *Department of Chemistry, University of Washington, Seattle, Washington 98195, United States;* orcid.org/0000-0003-4255-9550; Email: stst@uw.edu

Maria Benedetta Casu − *Institute of Physical and Theoretical Chemistry, University of Tübingen, Tübingen 72076, Germany;* orcid.org/0000-0002-5659-7040; Email: benedetta.casu@uni-tuebingen.de

Andrzej Rajca − *Department of Chemistry, University of Nebraska, Lincoln, Nebraska 68588-0304, United States;* orcid.org/0000-0002-8856-1536; Email: arajca1@unl.edu

Authors

Zhimin Yang − *Department of Chemistry, University of Nebraska, Lincoln, Nebraska 68588-0304, United States;* Present Address: Element Biosciences, Inc., 10055 Barnes Canyon Rd, Suite 100, San Diego, California 92121, United States

Maren Pink − *IUMSC, Department of Chemistry, Indiana University, Bloomington, Indiana 47405-7102, United States;* orcid.org/0000-0001-9049-4574

Ewa Malgorzata Nowik-Boltyk − *Institute of Physical and Theoretical Chemistry, University of Tübingen, Tübingen 72076, Germany;* orcid.org/0000-0003-3136-4870

Shutian Lu − *Department of Chemistry, University of Washington, Seattle, Washington 98195, United States*

Tobias Junghoefer − *Institute of Physical and Theoretical Chemistry, University of Tübingen, Tübingen 72076, Germany*

Suchada Rajca − *Department of Chemistry, University of Nebraska, Lincoln, Nebraska 68588-0304, United States*

Complete contact information is available at: https://pubs.acs.org/10.1021/jacs.3c03402

Notes

The authors declare no competing financial interest.

■ ACKNOWLEDGMENTS

The authors thank Haoxin Guo and Dr. Chan Shu, University of Nebraska, for their help with the characterization of the radicals and synthetic intermediates. They also thank Alexander Batelaan for his synthesis of **4**-Br and **5**-Br, and acknowledge UCARE program at University of Nebraska for his support. They further thank Elke Nadler, Institute of Physical and Theoretical Chemistry, University of Tübingen, for the SEM measurements. The authors are grateful to the National Science Foundation (NSF), Chemistry Division, for support of this research under Grants CHE-1955349 and CHE-2247170 (A.R.), and CHE-2154302 (S.S.). The upgrade of the EPR spectrometer at Nebraska was funded by the National Institutes of Health (NIH) (NIGMS #R01GM124310-01 to S.R. and A.R.). The upgrade of the EPR spectrometer at Washington was funded by NIH (S10OD021557). Support for the acquisition of the Bruker Venture D8 diffractometer through the Major Scientific Research Equipment Fund from the President of Indiana University and the Office of the Vice President for Research is gratefully acknowledged. The SEM was funded by the DFG under the contract INST 37/829-1 FUGG. Financial support from the German Research Foundation (DFG, contract CA852/11-3, project number: 394233453) is gratefully acknowledged. This work was partly supported by the European Union's Horizon 2020 Research and Innovation programme under grant agreement no. 965046, FET-Open project Interfast (Gated INTERfaces for FAST information processes).

■ REFERENCES

(1) Ciccullo, F.; Gallagher, N. M.; Geladari, O.; Chasse, T.; Rajca, A.; Casu, M. D. A Derivative of the Blatter Radical as a Potential Metal-Free Magnet for Stable Thin Films and Interfaces. *ACS Appl. Mater. Interfaces* **2016**, *8*, 1805−1812.

(2) Zheng, Y.; Miao, M.-S.; Kemei, M. C.; Seshadri, R.; Wudl, F. The Pyreno-Triazinyl Radical—Magnetic and Sensor Properties. *Isr. J. Chem.* **2014**, *54*, 774−778.

(3) Gallagher, N. M.; Bauer, J. J.; Pink, M.; Rajca, S.; Rajca, A. High-Spin Organic Diradical with Robust Stability. *J. Am. Chem. Soc.* **2016**, *138*, 9377−9380.

(4) Gallagher, N.; Zhang, H.; Junghoefer, T.; Giangrisostomi, E.; Ovsyannikov, R.; Pink, M.; Rajca, S.; Casu, M. B.; Rajca, A. Thermally and Magnetically Robust Triplet Ground State Diradical. *J. Am. Chem. Soc.* **2019**, *141*, 4764−4774.

(5) Shu, C.; Pink, M.; Junghoefer, T.; Nadler, E.; Rajca, S.; Casu, M. B.; Rajca, A. Synthesis and Thin Films of Thermally Robust Quartet ($S = 3/2$) Ground State Triradical. *J. Am. Chem. Soc.* **2021**, *143*, 5508−5518.

(6) Zhang, S.; Pink, M.; Junghoefer, T.; Zhao, W.; Hsu, S.-N.; Rajca, S.; Calzolari, A.; Boudouris, B. W.; Casu, M. B.; Rajca, A. High-Spin

(S = 1) Blatter-Based Diradical with Robust Stability and Electrical Conductivity. *J. Am. Chem. Soc.* **2022**, *144*, 6059−6070.

(7) Junghoefer, T.; Calzolari, A.; Baev, I.; Glaser, M.; Cicculло, F.; Giangrisostomi, E.; Ovsyannikov, R.; Kielgast, F.; Nissen, M.; Schwarz, J.; Gallagher, N. M.; Rajca, A.; Martins, M.; Casu, M. B. Magnetic behavior in metal-free radical thin films. *Chem* **2022**, *8*, P801−814.

(8) Rogers, F. J. M.; Norcott, P. L.; Coote, M. L. Recent advances in the chemistry of benzo[*e*][1,2,4]triazinyl radicals. *Org. Biomol. Chem.* **2020**, *18*, 8255−8277.

(9) Jasiński, M.; Szczytko, J.; Pociecha, D.; Monobe, H.; Kaszyński, P. Substituent-dependent magnetic behavior of discotic benzo[*e*]-[1,2,4]triazinyls. *J. Am. Chem. Soc.* **2016**, *138*, 9421−9424.

(10) Cigl, M.; Pociecha, D.; Jakubowski, R.; Kapuściński, S.; Kaszyński, P. Paramagnetic Liquid Crystals with Close $\pi-\pi$ Packing: The Effect of Blatter Radical Planarization on Behavior of Bent-Core Mesogens. *Chem. - Eur. J.* **2023**, *29*, No. e202203288.

(11) Steen, J. S.; Nuismer, J. L.; Eiva, V.; Wiglema, A. E. T.; Daub, N.; Hjelm, J.; Otten, E. Blatter Radicals as Bipolar Materials for Symmetrical Redox-Flow Batteries. *J. Am. Chem. Soc.* **2022**, *144*, 5051−5058.

(12) Poryvaev, A. S.; Gjuzi, E.; Polyukhov, D. M.; Hoffmann, F.; Frçba, M.; Fedin, M. V. Blatter-Radical-Grafted Mesoporous Silica as Prospective Nanoplatform for Spin Manipulation at Ambient Conditions. *Angew. Chem., Int. Ed.* **2021**, *60*, 8683−8688.

(13) Neugebauer, F. A. Hydrazidinyl Radicals: 1,2,4,5-Tetraazapentenyls, Verdazyls, and Tetrazolinyls. *Angew. Chem., Int. Ed.* **1973**, *12*, 455−464.

(14) Ovchinnikov, A. A. Multiplicity of the ground state of large alternant organic molecules with conjugated bonds. *Theor. Chim. Acta* **1978**, *47*, 297−304.

(15) Rajca, A. Organic diradicals and polyradicals: from spin coupling to magnetism? *Chem. Rev.* **1994**, *94*, 871−893.

(16) Gallagher, N. M.; Olankitwanit, A.; Rajca, A. High-Spin Organic Molecules. *J. Org. Chem.* **2015**, *80*, 1291−1298.

(17) Zhang, H.; Pink, M.; Wang, Y.; Rajca, S.; Rajca, A. High-Spin S = 3/2 Ground-State Aminyl Triradicals: Toward High-Spin Oligo-Aza Nanographenes. *J. Am. Chem. Soc.* **2022**, *144*, 19576−19591.

(18) McConnell, H. M.; Chesnut, D. B. Theory of Isotropic Hyperfine Interactions in π-Electron Radicals. *J. Chem. Phys.* **1958**, *28*, 107−117.

(19) Neugebauer, F. A. Elektronenspinsesonanz substituierter Kuhn-Jerchel-Radikale. *Chem. Ber.* **1969**, *102*, 1339−1346.

(20) Neugebauer, F. A.; Umminger, I. Uber 1,4-Dihydro-l,2,4-benzotriazinyl-Radikale. *Chem. Ber.* **1980**, *113*, 1205−1225.

(21) Neugebauer, F. A.; Rimmler, G. Endor and Triple Resonance Studies of 1,4-Dihydro-1,2,4-Benzotriazinyl Radicals and 1,4-Dihydro-1,2,4-Benzotriazine Radical Cations. *Magn. Reson. Chem.* **1988**, *26*, 595−600.

(22) Neugebauer, F. A.; Fischer, H.; Krieger, C. V. Part 33. EPR and ENDOR studies of 6-oxo- and 6-thioxoverdazyls. X-Ray molecular structure of 1,3,5-triphenyl-6-oxoverdazyl and 3-*tert*-butyl-1,5-diphenyl-6-thioxoverdazyl. *J. Chem. Soc., Perkin Trans 2* **1993**, 535−544.

(23) Neugebauer, F. A.; Brunner, H.; Hausser, K. H. Spin densities in 1,3,5-triphenylverdazyl: an NMR study. *Tetrahedron* **1971**, *27*, 3623−3628.

(24) Neugebauer, F. A. Substituted 5-*t*-butyl tetrazolinyl and phototetrazolinyl radicals. *Tetrahedron* **1970**, *26*, 4843−4851.

(25) Jerchel, D.; Fischer, H. 2,3-Diphenylen-tetrazoliumsalze und daraus entstehende Radicale. *Justus Liebigs Ann. Chem.* **1954**, *590*, 216−231.

(26) Kuhn, R.; Jerchel, D. Kristallisiertes 2,3-Diphenylen-5-phenyl-tetrazolium-Radikal. *Justus Liebigs Ann. Chem.* **1952**, *578*, 1−5.

(27) Kanal, F.; Schleier, D.; Nuernberger, P. Ultrafast Photogeneration of a Tetrazolinyl Radical. *ChemPhysChem* **2015**, *16*, 3143−3146.

(28) Bolze, T.; Were, J.-L.; Kanal, F.; Schleier, D.; Nuernberger, P. Ultrafast Dynamics of a Fluorescent Tetrazolium Compound in Solution. *ChemPhysChem* **2018**, *19*, 138−147.

(29) Cademartiri, L.; Ozin, G. A. Ultrathin Nanowires—A Materials Chemistry Perspective. *Adv. Mater.* **2009**, *21*, 1013−1020.

(30) Yavuz, C. T.; Mayo, J. T.; Yu, W. W.; Prakash, A.; Falkner, J. C.; Yean, S.; Cong, L.; Shipley, H. J.; Kan, A.; Tomson, M.; Natelson, D.; Colvin, V. L. Low-Field Magnetic Separation of Monodisperse Fe_3O_4 Nanocrystals. *Science* **2006**, *314*, 964−967.

(31) Yuan, J.; Liu, X.; Akbulut, O.; Hu, J.; Suib, S. L.; Kong, J.; Stellacci, F. Superwetting nanowire membranes for selective absorption. *Nat. Nanotechnol.* **2008**, *3*, 332−336.

(32) Hasegawa, M.; Iyoda, M. Conducting supramolecular nanofibers and nanorods. *Chem. Soc. Rev.* **2010**, *39*, 2420−2427.

(33) Briseno, A. L.; Mannsfeld, S. C. B.; Jenekhe, S. A.; Bao, Z.; Xia, Y. Introducing organic nanowire transistors. *Mater. Today* **2008**, *11*, 38−47.

(34) Savu, S.-A.; Sonström, A.; Bula, R.; Bettinger, H. F.; Chassé, T.; Casu, M. B. Intercorrelation of Electronic, Structural, and Morphological Properties in Nanorods of 2,3,9,10-Tetrafluoropentacene. *ACS Appl. Mater. Interfaces* **2015**, *7*, 19774−19780.

(35) Savu, S. A.; Abb, S.; Schundelmeier, S.; Saathoff, J. D.; Stevenson, J. M.; Toenshoff, C.; Bettinger, H. F.; Clancy, P.; Casu, M. B.; Chassé, T. Pentacene-based nanorods on Au(111) single crystals: Charge transfer, diffusion, and step-edge barriers. *Nano Res.* **2013**, *6*, 449−459.

(36) Kowarik, S.; Gerlach, A.; Hinderhofer, A.; Milita, S.; Borgatti, F.; Zontone, F.; Suzuki, T.; Biscarini, F.; Schreiber, F. Structure, morphology, and growth dynamics of perfluoro-pentacene thin films. *Phys. Status Solidi RRL* **2008**, *2*, 120−122.

(37) Günder, D.; Diez-Cabanes, V.; Huttner, A.; Breuer, T.; Lemaur, V.; Cornil, J.; Witte, G. F-Center-Mediated Growth of Patterned Organic Semiconductor Films on Alkali Halides. *ACS Appl. Mater. Interfaces* **2022**, *14*, 46086−46094.

(38) Gutiérrez, D.; Riera-Galindo, S.; Ajayakumar, M. R.; Veciana, J.; Rovira, C.; Mas-Torrent, M.; Crivillers, N. Self-Assembly of an Organic Radical Thin Film and Its Memory Function Investigated Using a Liquid-Metal Electrode. *J. Phys. Chem. C* **2018**, *122*, 17784−17791.

(39) Katritzky, A. A.; Belyakov, S. A.; Cheng, D.; Durst, H. D. Syntheses of Formazans Under Phase-Transfer Conditions. *Synthesis* **1995**, *1995*, 577−581.

(40) Hegarty, A. F.; Scott, F. L. Kinetics and Mechanism of the Formation of Formazans by Diazonium Ion Attack on Hydrazones. *J. Org. Chem.* **1967**, *32*, 1957−1963.

(41) Nineham, A. W. The chemistry of formazans and tetrazolium salts. *Chem. Rev.* **1955**, *55*, 355−483.

(42) Bondi, A. Van der Waals Volumes and Radii. *J. Phys. Chem. A* **1964**, *68*, 441−451.

(43) Frisch, M. J.; Trucks, G. W.; Schlegel, H. B.; Scuseria, G. E.; Robb, M. A.; Cheeseman, J. R.; Scalmani, G.; Barone, V.; Petersson, G. A.; Nakatsuji, H.; Li, X.; Caricato, M.; Marenich, A. V.; Bloino, J.; Janesko, B. G.; Gomperts, R.; Mennucci, B.; Hratchian, H. P.; Ortiz, J. V.; Izmaylov, A. F.; Sonnenberg, J. L.; Williams-Young, D.; Ding, F.; Lipparini, F.; Egidi, F.; Goings, J.; Peng, B.; Petrone, A.; Henderson, T.; Ranasinghe, D.; Zakrzewski, V. G.; Gao, J.; Rega, N.; Zheng, G.; Liang, W.; Hada, M.; Ehara, M.; Toyota, K.; Fukuda, R.; Hasegawa, J.; Ishida, M.; Nakajima, T.; Honda, Y.; Kitao, O.; Nakai, H.; Vreven, T.; Throssell, K.; Montgomery, J. A., Jr.; Peralta, J. E.; Ogliaro, F.; Bearpark, M. J.; Heyd, J. J.; Brothers, E. N.; Kudin, K. N.; Staroverov, V. N.; Keith, T. A.; Kobayashi, R.; Normand, J.; Raghavachari, R.; Rendell, A. P.; Burant, J. C.; Iyengar, S. S.; Tomasi, J.; Cossi, M.; Millam, J. M.; Klene, M.; Adamo, C.; Cammi, R.; Ochterski, J. W.; Martin, R. L.; Morokuma, K.; Farkas, O.; Foresman, J. B.; Fox, D. J. *Gaussian 16*, revision A.03; Gaussian, Inc.: Wallingford, CT, 2016.

(44) Grimme, S.; Antony, J.; Ehrlich, S.; Krieg, H. A consistent and accurate ab initio parametrization of density functional dispersion correction (DFT-D) for the 94 elements H-Pu. *J. Chem. Phys.* **2010**, *132*, 154104−154118.

(45) Grimme, S.; Ehrlich, S.; Goerigk, L. Effect of the damping function in dispersion corrected density functional theory. *J. Comput. Chem.* **2011**, *32*, 1456−1465.

(46) Gryn'ova, G.; Marshall, D. L.; Blanksby, S. J.; Coote, M. L. Switching radical stability by pH-induced orbital conversion. *Nat. Chem.* **2013**, *5*, 474−481.

(47) Wang, Y.; Zhang, H.; Pink, M.; Olankitwanit, A.; Rajca, S.; Rajca, A. Radical Cation and Neutral Radical of Aza-thia[7]helicene with SOMO−HOMO Energy Level Inversion. *J. Am. Chem. Soc.* **2016**, *138*, 7298−7304.

(48) Shu, C.; Zhang, H.; Olankitwanit, A.; Rajca, S.; Rajca, A. High-Spin Diradical Dication of Chiral π-Conjugated Double Helical Molecule. *J. Am. Chem. Soc.* **2019**, *141*, 17287−17294.

(49) Kasemthaveechok, S.; Abella, L.; Jean, M.; Cordier, M.; Roisnel, T.; Vanthuyne, N.; Guizouarn, T.; Cador, O.; Autschbach, J.; Crassous, J.; Favereau, L. Axially and Helically Chiral Cationic Radical Bicarbazoles: SOMO-HOMO Level Inversion and Chirality Impact on the Stability of Mono- and Diradical Cations. *J. Am. Chem. Soc.* **2020**, *142*, 20409−20418.

(50) Abella, L.; Crassous, J.; Favereau, L.; Autschbach, J. Why is the Energy of the Singly Occupied Orbital in Some Radicals below the Highest Occupied Orbital Energy? *Chem. Mater.* **2021**, *33*, 3678−3691.

(51) Kasemthaveechok, S.; Abella, L.; Jean, M.; Cordier, M.; Vanthuyne, N.; Guizouarn, T.; Cador, O.; Autschbach, J.; Crassous, J.; Favereau, L. Carbazole Isomerism in Helical Radical Cations: Spin Delocalization and SOMO−HOMO Level Inversion in the Diradical State. *J. Am. Chem. Soc.* **2022**, *144*, 7253−7263.

(52) Kasemthaveechok, S.; Abella, L.; Crassous, J.; Autschbach, J.; Favereau, L. Organic radicals with inversion of SOMO and HOMO energies and potential applications in optoelectronics. *Chem. Sci.* **2022**, *13*, 9833−9847.

(53) Neugebauer, F. A.; Russell, G. A. Tetrazolinyl Radicals. *J. Org. Chem.* **1968**, *33*, 2744−2746.

(54) Stoll, S.; Schweiger, A. EasySpin, a comprehensive software package for spectral simulation and analysis in EPR. *J. Magn. Reson.* **2006**, *178*, 42−55.

(55) Dzuba, S. A.; Maryasov, A. G.; Salikhov, K. M.; Tsvetkov, Y. D. Superslow rotations of nitroxide radicals studied by pulse EPR spectroscopy. *J. Magn. Reson.* **1984**, *58*, 95−117.

(56) Zecevic, A.; Eaton, G. R.; Eaton, S. S.; Lindgren, M. Dephasing of electron spin echoes for nitroxyl radicals in glassy solvents by non-methyl and methyl protons. *Mol. Phys.* **1998**, *95*, 1255−1263.

(57) Kveder, M.; Rakvin, B.; You, J. A quantum many body model for the embedded electron spin decoherence in organic solids. *J. Chem. Phys.* **2019**, *151*, No. 164124.

(58) Huang, S.; Pink, M.; Ngendahimana, T.; Rajca, S.; Eaton, G. R.; Eaton, S. S.; Rajca, A. Bis-Spiro-Oxetane and Bis-Spiro-Tetrahydrofuran Pyrroline Nitroxide Radicals: Synthesis and Electron Spin Relaxation Studies. *J. Org. Chem.* **2021**, *86*, 13636−13643.

(59) Zadrozny, J. M.; Niklas, J.; Poluektov, O. G.; Freedman, D. E. Millisecond Coherence Time in a Tunable Molecular Electronic Spin Qubit. *ACS Cent. Sci.* **2015**, *1*, 488−492.

(60) Yu, C.-J.; von Kugelgen, S.; Laorenza, D. W.; Freedman, D. E. A Molecular Approach to Quantum Sensing. *ACS Cent. Sci.* **2021**, *7*, 712−723.

(61) Cicciullo, F.; Calzolari, A.; Bader, K.; Neugebauer, P.; Gallagher, N. M.; Rajca, A.; van Slageren, J.; Casu, M. B. Interfacing a Potential Purely Organic Molecular Quantum Bit with a Real-Life Surface. *ACS Appl. Mater. Interfaces* **2019**, *11*, 1571−1578.

(62) Kahn, O. *Molecular Magnetism*; Wiley-VCH: New York, 1993; Chapter 11, p 272.

(63) Xiang, T. Thermodynamics of quantum Heisenberg spin chains. *Phys. Rev. B* **1998**, *58*, 9142−9149.

(64) Breunig, O.; Garst, M.; Klümper, A.; Rohrkamp, J.; Turnbull, M. M.; Lorenz, T. Quantum criticality in the spin-1/2 Heisenberg chain system copper pyrazine dinitrate. *Sci. Adv.* **2017**, *3*, No. eaao3773.

(65) Rajca, A.; Takahashi, M.; Pink, M.; Spagnol, G.; Rajca, S. Conformationally constrained, stable, triplet ground state ($S = 1$) nitroxide diradicals: antiferromagnetic chains of $S = 1$ diradicals. *J. Am. Chem. Soc.* **2007**, *129*, 10159−10170.

(66) Wang, W.; Chen, C.; Shu, C.; Rajca, S.; Wang, X.; Rajca, A. $S = 1$ Tetraazacyclophane Diradical Dication with Robust Stability: a Case of Low Temperature One-Dimensional Antiferromagnetic Chain. *J. Am. Chem. Soc.* **2018**, *140*, 7820−7826.

(67) Connelly, N. G.; Geiger, W. E. Chemical Redox Agents for Organometallic Chemistry. *Chem. Rev.* **1996**, *96*, 877−910.

(68) Hutchison, K. A.; Srdanov, G.; Menon, R.; Gabriel, J.-C. P.; Knight, B.; Wudl, F. A Pressure Sensitive Two-Dimensional Tetracyanoquinodimethane (TCNQ) Salt of a Stable Free Radical. *J. Am. Chem. Soc.* **1996**, *118*, 13081−13082.

(69) Bartos, P.; Anand, B.; Pietrzak, A.; Kaszyński, P. Functional Planar Blatter Radical through Pschorr-Type Cyclization. *Org. Lett.* **2020**, *22*, 180−184.

(70) Gilroy, J. B.; McKinnon, S. D. J.; Koivisto, B. D.; Hicks, R. G. Electrochemical Studies of Verdazyl Radicals. *Org. Lett.* **2007**, *9*, 4837−4840.

(71) Tretyakov, E. V.; Petunin, P. V.; Zhivetyeva, S. I.; Gorbunov, D. E.; Gritsan, N. P.; Fedin, M. V.; Stass, D. V.; Samoilova, R. I.; Bagryanskaya, I. Y.; Shundrina, I. K.; Bogomyakov, A. S.; Kazantsev, M. S.; Postnikov, P. S.; Trusova, M. E.; Ovcharenko, V. I. Platform for High-Spin Molecules: A Verdazyl-Nitronyl Nitroxide Triradical with Quartet Ground State. *J. Am. Chem. Soc.* **2021**, *143*, 8164−8176.

(72) Pal, S. K.; Itkis, M. E.; Tham, F. S.; Reed, R. W.; Oakley, R. T.; Haddon, R. C. Resonating valence-bond ground state in a phenalenyl-based neutral radical conductor. *Science* **2005**, *309*, 281−284.

(73) Mailman, A.; Wong, J. W. L.; Winter, S. M.; Claridge, R. C. M.; Robertson, C. M.; Assoud, A.; Yong, W.; Steven, E.; Dube, P. A.; Tse, J. S.; Desgreniers, S.; Secco, R. A.; Oakley, R. T. Fine tuning the performance of multiorbital radical conductors by substituent effects. *J. Am. Chem. Soc.* **2017**, *139*, 1625−1635.

(74) Joo, Y.; Agarkar, V.; Sung, S. H.; Savoie, B. M.; Boudouris, B. W. A nonconjugated radical polymer glass with high electrical conductivity. *Science* **2018**, *359*, 1391−1395.

(75) Tan, Y.; Casetti, N. C.; Boudouris, B. W.; Savoie, B. M. Molecular Design Features for Charge Transport in Nonconjugated Radical Polymers. *J. Am. Chem. Soc.* **2021**, *143*, 11994−12002.

(76) Junghoefer, T.; Gallagher, N. M.; Kolanji, K.; Giangrisostomi, E.; Ovsyannikov, R.; Chassé, T.; Baumgarten, M.; Rajca, A.; Calzolari, A.; Casu, M. B. Challenges in controlled thermal deposition of organic diradicals. *Chem. Mater.* **2021**, *33*, 2019−2028.

(77) Savu, S.-A.; Casu, M. B.; Schundelmeier, S.; Abb, S.; Tonshoff, C.; Bettinger, H. F.; Chassé, T. Nanoscale assembly, morphology and screening effects in nanorods of newly synthesized substituted pentacenes. *RSC Adv.* **2012**, *2*, 5112−5118.

(78) Casu, M. B. Nanoscale Studies of Organic Radicals: Surface, Interface, and Spinterface. *Acc. Chem. Res.* **2018**, *51*, 753−760.

(79) Siegbahn, K.; Nordling, C.; Fahlman, A.; Nordberg, R.; Hamrin, K.; Hedman, J.; Johansson, G.; Bergmark, T.; Karlsson, S.-E.; Lindgren, I.; Lindberg, B. *ESCA, Atomic, Molecular and Solid State Structure Studied by Means of Electron Spectroscopy*; Almqvist and Wiksells: Uppsala, 1967.

(80) Siegbahn, K. M. Nobel Lecture: Electron Spectroscopy for Atoms, Molecules and Condensed Matter. http://www.nobelprize.org/nobel_prizes/physics/laureates/1981/siegbahn-lecture.html (accessed Mar 20, 2023).

(81) Junghoefer, T.; Nowik-Boltyk, E. M.; de Sousa, J. A.; Giangrisostomi, E.; Ovsyannikov, R.; Chassé, T.; Veciana, J.; Mas-Torrent, M.; Rovira, C.; Crivillers, N.; Casu, M. B. Stability of radical-functionalized gold surfaces by self-assembly and on-surface chemistry. *Chem. Sci.* **2020**, *11*, 9162−9172.

(82) Dobler, C.; Tönshoff, C.; Bettinger, H. F.; Chassé, T.; Casu, M. B. Cyano-Functional Group as an Anchoring Tool for Organic Small Molecules on Gold. *J. Phys. Chem. C* **2017**, *121*, 13660−13665.

(83) Travnikova, O.; Børve, K. J.; Patanen, M.; Söderström, J.; Miron, C.; Sæthre, L. J.; Mårtensson, N.; Svensson, S. The ESCA molecule—Historical remarks and new results. *J. Electron Spectrosc. Relat. Phenom.* **2012**, *185*, 191−197.

(84) Du, X.; Wang, S.-Y.; Wei, M.; Zhang, J.-R.; Ge, G.; Hua, W. A theoretical library of N1s core binding energies of polynitrogen

molecules and ions in the gas phase. *Phys. Chem. Chem. Phys.* **2022**, *24*, 8196−8207.

(85) Dietrich, M.; Delaittre, G.; Blinco, J. P.; Inglis, A. J.; Bruns, M.; Barner-Kowollik, C. Photoclickable Surfaces for Profluorescent Covalent Polymer Coatings. *Adv. Funct. Mater.* **2012**, *22*, 304−312.

(86) Wu, Z.; Luo, J.; Liang, Y.; Yu, X.; Zhao, Y.; Li, Y.; Wang, W.; Sui, Z.; Tian, X.; Chen, Q. Tetrazole functionalized benzoquinoline-linked covalent organic frameworks with efficient performance for electrocatalytic H_2O_2 production and Li-S batteries. *Mater. Chem. Front.* **2023**, *7*, 1650−1658.

(87) Knecht, P.; Suryadevara, N.; Zhang, B.; Reichert, J.; Ruben, M.; Barth, J. V.; Klyatskaya, S.; Papageorgiou, A. C. The self-assembly and metal adatom coordination of a linear bis-tetrazole ligand on Ag(111). *Chem. Commun.* **2018**, *54*, 10072−10075.

(88) Szőcs, E.; Bakó, I.; Kosztolányi, T.; Bertóti, I.; Kálmán, E. EC-STM study of 5-mercapto-1-phenyl-tetrazole adsorption on Cu(1 1 1). *Electrochim. Acta* **2004**, *49*, 1371−1378.

(89) Henze, S. K. M.; Bauer, O.; Lee, T. L.; Sokolowski, M.; Tautz, F. S. Vertical bonding distances of PTCDA on Au(111) and Ag(111): Relation to the bonding type. *Surf. Sci.* **2007**, *601*, 1566−1573.

(90) Zou, Y.; Kilian, L.; Schöll, A.; Schmidt, T.; Fink, R.; Umbach, E. Chemical bonding of PTCDA on Ag surfaces and the formation of interface states. *Surf. Sci.* **2006**, *600*, 1240−1251.

(91) Kröger, I.; Stadtmüller, B.; Kleimann, C.; Rajput, P.; Kumpf, C. Normal-incidence x-ray standing-wave study of copper phthalocyanine submonolayers on Cu(111) and Au(111). *Phys. Rev. B* **2011**, *83*, No. 195414.

(92) Hennessy, M. J.; McElwee, C. D.; Richards, P. M. Effect of interchain coupling on electron-spin resonance in nearly one-dimensional systems. *Phys. Rev. B* **1973**, *7*, 930−947.

(93) *SAINT V8.40A*; Bruker AXS: Madison, WI, 2018.

(94) Krause, L.; Herbst-Irmer, R.; Sheldrick, G. M.; Stalke, D. Comparison of silver and molybdenum microfocus X-ray sources for single-crystal structure determination. *J. Appl. Crystallogr.* **2015**, *48*, 3−10.

(95) Sheldrick, G. M. SHELXT—Integrated space-group and crystal-structure determination. *Acta Crystallogr., Sect. A: Found. Adv.* **2015**, *71*, 3−8.

(96) Sheldrick, G. M. Crystal structure refinement with SHELXL. *Acta Crystallogr., Sect. C: Struct. Chem.* **2015**, *71*, 3−8.

(97) Savu, S.-A.; Biswas, I.; Sorace, L.; Mannini, M.; Rovai, D.; Caneschi, A.; Chassé, T.; Casu, M. B. Nanoscale Assembly of Paramagnetic Organic Radicals on Au(111) Single Crystals. *Chem. - Eur. J.* **2013**, *19*, 3445−3450.

(98) Moulder, J. F.; Stickle, W. F.; Sobol, P. E.; Bomben, K. D. *Handbook of X-ray Photoelectron Spectroscopy*; Chastain, J., Ed.; Perkin-Elmer Corp., Physical Electronics Division: Minnesota, United States of America, 1992.

https://doi.org/10.1021/jacs.3c03402
J. Am. Chem. Soc. 2023, 145, 13335−13346

Supporting Information

Thermally Ultra-Robust $S = ½$ Tetrazolinyl Radicals: Synthesis, Electronic Structure, Magnetism, and Nanoneedle Assemblies on Silicon Surface.

Zhimin Yang,[†,⊥] Maren Pink,[‡] Ewa Malgorzata Nowik-Boltyk,[§] Shutian Lu,[#] Tobias Junghoefer,[§] Suchada Rajca,[†] Stefan Stoll,[#] Maria Benedetta Casu,*[§] and Andrzej Rajca*[†]*

[†]Department of Chemistry, University of Nebraska, Lincoln, Nebraska 68588-0304, United States

[‡]IUMSC, Department of Chemistry, Indiana University, Bloomington, Indiana 47405-7102, United States

[§] Institute of Physical and Theoretical Chemistry, University of Tübingen, 72076 Tübingen, Germany

[#]Department of Chemistry, University of Washington, Seattle, Washington 98195, United States

[⊥] Present address: Element Biosciences Inc., 1278 Reamwood Ave, Sunnyvale, CA 94089, USA.

*Andrzej Rajca: e-mail, arajca1@unl.edu

*Maria Benedetta Casu: e-mail, benedetta.casu@uni-tuebingen.de

*Stefan Stoll: e-mail, stst@uw.edu

Table of Contents

1. Experimental Section: Synthesis and Measurements.

1.a General procedures and materials.

Throughout the following paragraphs labels “ZY831” and alike correspond to sample or experiment code directly traceable to the laboratory notebooks or raw data.

All solvents used in reactions are directly from supplier without further purification. Per-deuterated solvents for NMR spectroscopy were obtained from Cambridge Isotope Laboratories. All other commercially available chemicals were obtained from either Millipore Sigma or Acros, unless indicated otherwise. Standard techniques for synthesis under inert atmosphere, using vaccum lines and Schlenk vessels, were employed.

Column chromatography (0–20 psig pressure) was performed by using Sorbtech silica gel (60 Å, 40-75 μm). Analytical TLC plates were carried out on 0.25 mm MilliporeSigma silica plates (60F-254) using UV light as the visualizing agent. Photochemical reactions were carried out using a reactor employing multiple Analytik Jena 6 mW 254 nm lamps UVP UVG-54. Centrifugation was conducted using Fisher Scientific microcentrifuge Model 59A. IR spectra were obtained using a commercial instrument, equipped with an ATR sampling accessory. MS analyses were carried out at local facilities for mass spectrometry.

NMR spectra were obtained using Bruker spectrometers (^{1}H, 400, 600, and 700 MHz) using chloroform-*d* ($CDCl_3$), water-d_2, acetone-d_6, or DMSO-d_6, as solvent. The 700 MHz instrument was equipped with a cryoprobe. The chemical shift references were as follows: (^{1}H) chloroform-*d*, 7.26 ppm; (^{1}H) acetone-d_5, 2.05 ppm; (^{13}C) acetone-d_6, 30.23 ppm; (^{1}H) water-d_1, 4.79 ppm; (^{1}H) DMSO-d_5, 2.50 ppm; (^{13}C) DMSO-d_6, 39.51 ppm. Typical 1D FID was subjected to exponential multiplication with an exponent of 0.1 Hz (for ^{1}H) and 1.0 – 2.0 Hz (for ^{13}C).

1.b X-ray crystallography.

Crystallographic data for **1** and **2** were deposited in the Cambridge Crystallographic Data Centre (**CCDC 2253237, 2253238, and 2253239**). The data can be obtained free of charge from the Cambridge Crystallographic Data Centre via www.ccdc.cam.ac.uk/data_request/cif.

The single crystals of radicals **1** and **2** were obtained by slow solvent evaporation from solvent mixtures; the solvent mixture was obtained by a slow diffusion of pentane into a solution of **1** in benzene (sample label: ZY831, X-ray label: 20110) and solution of **2** in toluene (sample label: ZY985#2, X-ray label: 21234). Also, another crystal of **2**, obtained from pentane/ethyl acetate solvent mixture (sample label: ZY985#5) gave the identical structure (X-ray label: 21236).

Data collection for radical 1 (X-ray label: 20110). A black, needle-shaped crystal (approximate dimensions 0.34 × 0.06 × 0.05 mm^3) was placed onto the tip of a MiTeGen loop and mounted on a Bruker Venture D8 diffractometer equipped with a PhotonIII detector at 100(2) K. The data collection was carried out using Mo Kα radiation (graphite monochromator) with a frame time of 6 or 18 seconds and a detector distance of 13.00 cm. A collection strategy was calculated and complete data to a resolution of 0.80 Å with a redundancy of 8.9 were collected. Nine major sections of frames were collected with 0.50° ω and ϕ scans. A total of 3012 frames were collected. The total exposure time was 12.46 hours. The frames were integrated with the Bruker SAINT software package[S1] using a narrow-frame algorithm. The integration of the data using a monoclinic unit cell yielded a total of 38752 reflections to a maximum θ angle of 26.38° (0.80 Å resolution), of which 4244 were independent (average redundancy 9.131, completeness = 99.9%, R_{int} = 11.81%, R_{sig} = 6.60%) and 2670 (62.91%) were greater than $2\sigma(F^2)$. The final cell constants of $\underline{a}$ = 6.3017(3) Å, $\underline{b}$ = 12.8306(6) Å, $\underline{c}$ = 25.7727(12) Å, β = 90.4037(19)°, volume = 2083.79(17) Å^3, are based upon the refinement of the XYZ-centroids of 2805 reflections above 20 σ(I) with 4.48° < 2θ < 46.17°. Data were corrected for absorption effects using the Multi-Scan method (SADABS).[S2] The ratio of minimum to maximum apparent transmission was 0.876. The calculated minimum and maximum transmission coefficients (based on crystal size) are 0.9720 and 0.9960. Please refer to Table S1 for additional crystal and refinement information.

Data collection for radical 2 from pentane/toluene (X-ray label: 21234). A dark, needle-like crystal (approximate dimensions 0.165 × 0.075 × 0.036 mm^3) was placed onto the tip of a MiTeGen loop and mounted on a Bruker Venture D8 diffractometer equipped with a PhotonIII detector at 153(2) K. The data collection was carried out using Mo Kα radiation (graphite monochromator) with a frame time of 20 seconds and a detector distance of 4.00 cm. A collection strategy was calculated and complete data to a resolution of 0.77 Å with a redundancy of 16 were collected as ten major sections of frames with 1° ω and ϕ scans. A total of 1336 frames were collected. The total exposure time was 4.64 hours. The frames were integrated with the Bruker SAINT software package[S1] using a narrow-frame algorithm. The integration of the data using a monoclinic unit cell yielded a total of 62182 reflections to a maximum θ angle of 27.49° (0.77 Å resolution), of which 3740 were independent (average redundancy 16.626, completeness = 100.0%, R_{int} = 10.95%, R_{sig} = 3.58%) and 2662 (71.18%) were greater than $2\sigma(F^2)$. The final cell constants of $\underline{a}$ = 6.4403(2) Å, $\underline{b}$ = 12.2739(4) Å, $\underline{c}$ = 20.8170(8) Å, β = 97.1020(10)°, volume = 1632.91(10) Å^3, are based upon the refinement of the XYZ-centroids of 8614 reflections above 20 σ(I) with 5.154° < 2θ < 52.62°. Data were corrected for absorption effects using the Multi-Scan method (SADABS).[S2] The ratio of minimum to maximum apparent transmission was 0.889. The calculated minimum and maximum transmission coefficients (based on crystal size) are 0.6800 and 0.9140. Please refer to Table S2 for additional crystal and refinement information.

Data collection for radical 2 from pentane/ethyl acetate (X-ray label: 21236). A dark, long, needle-like crystal (approximate dimensions 0.873 × 0.067 × 0.033 mm^3) was placed onto the tip of a MiTeGen loop and mounted on a Bruker Venture D8 diffractometer equipped with a PhotonIII detector at room temperature. The data collection was carried out using Mo Kα radiation (graphite monochromator) with a frame time of 50 and 20 seconds and a detector distance of 4.00 cm. A collection strategy was calculated and complete data to a resolution of 0.84 Å with a redundancy of at least 13.04 were collected. Two major sections of frames were collected with 1° ϕ scans. A total of 720 frames were collected. The total exposure time was 7.00 hours. The frames were integrated with the Bruker SAINT software package[S1] using a narrow-frame algorithm. The integration of the data using a monoclinic unit cell yielded a total of 40167 reflections to a maximum θ angle of 25.04° (0.84 Å resolution), of which 2961 were independent (average redundancy 13.565, completeness = 99.9%, R_{int} = 6.65%, R_{sig} = 2.56%) and 2239 (75.62%) were greater than $2\sigma(F^2)$. The final cell constants of $\underline{a}$ = 6.4595(6) Å, $\underline{b}$ = 12.3137(14) Å, $\underline{c}$ = 21.149(3) Å, β = 96.254(3)°, volume = 1672.2(3) $Å^3$, are based upon the refinement of the XYZ-centroids of 7175 reflections above 20 $\sigma(I)$ with 5.095° < 2θ < 47.53°. Data were corrected for absorption effects using the Multi-Scan method (SADABS).[S2] The ratio of minimum to maximum apparent transmission was 0.908. The calculated minimum and maximum transmission coefficients (based on crystal size) are 0.2210 and 0.9230. Please refer to Table S3 for additional crystal and refinement information.

Structure solution and refinement for radical 1 (X-ray label: 20110). The space group $P2_1/n$ was determined based on intensity statistics and systematic absences. The structure was solved and refined using the SHELX suite of programs.[S3,S4] An intrinsic-methods solution was calculated, which provided most non-hydrogen atoms from the E-map. Full-matrix least squares / difference Fourier cycles were performed, which located the remaining non-hydrogen atoms. All non-hydrogen atoms were refined with anisotropic displacement parameters. The hydrogen atoms were placed in ideal positions and refined as riding atoms with relative isotropic displacement parameters. The final anisotropic full-matrix least-squares refinement on F^2 with 298 variables converged at R1 = 5.39%, for the observed data and wR2 = 14.98% for all data. The goodness-of-fit was 1.062. The largest peak in the final difference electron density synthesis was 0.289 $e^-/Å^3$ and the largest hole was -0.266 $e^-/Å^3$ with an RMS deviation of 0.059 $e^-/Å^3$. On the basis of the final model, the calculated density was 1.356 g/cm^3 and F(000), 884 e^-.

Structure solution and refinement for radical 2 at 153 K (X-ray label: 21234). The space group $P2_1/n$ was determined based on intensity statistics and systematic absences. The structure was solved and refined using the SHELX suite of programs.[S3,S4] An intrinsic-methods solution was calculated, which provided most non-hydrogen atoms from the E-map. Full-matrix least squares / difference Fourier cycles were performed, which located the remaining non-hydrogen atoms. All non-hydrogen atoms were refined with anisotropic displacement parameters. The hydrogen atoms were placed in ideal positions and refined as riding atoms with relative isotropic displacement parameters. Disorder was refined for the Br CN moieties; a set of restraints was applied. The final anisotropic full-matrix least-squares refinement on F^2 with 239 variables converged at R1 = 4.70%, for the observed data and wR2 = 11.06% for all data. The goodness-of-fit was 1.074. The largest peak in the final difference electron density synthesis was 0.337 $e^-/Å^3$ and the largest hole was -0.389 $e^-/Å^3$ with an RMS deviation of 0.065 $e^-/Å^3$. On the basis of the final model, the calculated density was 1.632 g/cm^3 and F(000), 804 e^-.

Structure solution and refinement for radical 2 at 296 K (X-ray label: 21236). The space group $P2_1/c$ was determined based on intensity statistics and systematic absences. The structure was solved and refined using the SHELX suite of programs.[S3,S4] An intrinsic-methods solution was calculated, which provided most non-hydrogen atoms from the E-map. Full-matrix least squares / difference Fourier cycles were performed, which located the remaining non-hydrogen atoms. All non-hydrogen atoms were refined with anisotropic displacement parameters. The hydrogen atoms were placed in ideal positions and refined as riding atoms with relative isotropic displacement parameters. Disorder was refined for the Br CN moieties; a set of restraints was applied. The final anisotropic full-matrix least-squares refinement on F^2 with 239 variables converged at R1 = 5.07%, for the observed data and wR2 = 10.61% for all data. The goodness-of-fit was 1.139. The largest peak in the final difference electron density synthesis was 0.198 $e^-/Å^3$ and the largest hole was -0.370 $e^-/Å^3$ with an RMS deviation of 0.050 $e^-/Å^3$. On the basis of the final model, the calculated density was 1.594 g/cm^3 and F(000), 804 e^-.

Table S1. Crystal data and structure refinement for radical **1** (X-ray label: 20110).

Empirical formula	$C_{27}\ H_{17}\ N_6$	
Formula weight	425.46	
Crystal color, shape, size	black needle, 0.34 × 0.06 × 0.05 mm^3	
Temperature	100(2) K	
Wavelength	0.71073 Å	
Crystal system, space group	Monoclinic, $P2_1/n$	
Unit cell dimensions	a = 6.3017(3) Å	$\alpha = 90°$.
	b = 12.8306(6) Å	$\beta = 90.4037(19)°$.
	c = 25.7727(12) Å	$\gamma = 90°$.
Volume	2083.79(17) $Å^3$	
Z	4	
Density (calculated)	1.356 Mg/m^3	
Absorption coefficient	0.084 mm^{-1}	
F(000)	884	

Data collection

Diffractometer	Venture D8, Bruker
Source	IμS 3.0, Incoatec
Theta range for data collection	2.240 to 26.382°.
Index ranges	-7<=h<=7, -16<=k<=16, -32<=l<=32
Reflections collected	38752
Independent reflections	4244 [R_{int} = 0.1181]
Observed Reflections	2670
Completeness to *theta* = 25.242°	99.9 %

Solution and Refinement

Absorption correction	Semi-empirical from equivalents
Max. and min. transmission	0.7454 and 0.6527
Solution	Intrinsic methods
Refinement method	Full-matrix least-squares on F^2
Weighting scheme	$w = [\sigma^2Fo^2 + AP^2]^{-1}$, with $P = (Fo^2 + 2\ Fc^2)/3$, A = 0.0746
Data / restraints / parameters	4244 / 0 / 298
Goodness-of-fit on F^2	1.062
Final R indices [$I>2\sigma(I)$]	R1 = 0.0539, wR2 = 0.1319
R indices (all data)	R1 = 0.0902, wR2 = 0.1498
Largest diff. peak and hole	0.289 and -0.266 e.$Å^{-3}$

Goodness-of-fit = $[\Sigma[w(F_o^2 - F_c^2)^2]/N_{observns} - N_{params})]^{1/2}$, all data.

$R1 = \Sigma(|F_o| - |F_c|) / \Sigma |F_o|$. $wR2 = [\Sigma[w(F_o^2 - F_c^2)^2] / \Sigma [w(F_o^2)^2]]^{1/2}$.

Table S2. Crystal data and structure refinement for **2** (X-ray label: 21234).

Empirical formula	C_{20} H_{11} Br N_5	
Formula weight	401.25	
Crystal color, shape, size	black needle, 0.165 × 0.075 × 0.036 mm^3	
Temperature	153(2) K	
Wavelength	0.71073 Å	
Crystal system, space group	Monoclinic, $P2_1/n$	
Unit cell dimensions	a = 6.4403(2) Å	α = 90°.
	b = 12.2739(4) Å	β = 97.1020(10)°.
	c = 20.8170(8) Å	γ = 90°.
Volume	1632.91(10) $Å^3$	
Z	4	
Density (calculated)	1.632 Mg/m^3	
Absorption coefficient	2.532 mm^{-1}	
F(000)	804	

Data collection

Diffractometer	Venture D8, Bruker
Source	IμS 3.0, Incoatec
Theta range for data collection	1.930 to 27.490°.
Index ranges	-8<=h<=8, -15<=k<=15, -27<=l<=27
Reflections collected	62182
Independent reflections	3740 [R_{int} = 0.1095]
Observed Reflections	2662
Completeness to theta = 25.242°	100.0 %

Solution and Refinement

Absorption correction	Semi-empirical from equivalents
Max. and min. transmission	0.7325 and 0.6628
Solution	Intrinsic methods
Refinement method	Full-matrix least-squares on F^2
Weighting scheme	$w = [\sigma^2 Fo^2 + AP^2 + BP]^{-1}$, with $P = (Fo^2 + 2\ Fc^2)/3$, A = 0.0328, B = 2.2763
Data / restraints / parameters	3740 / 85 / 239
Goodness-of-fit on F^2	1.074
Final R indices [I>2□(I)]	R1 = 0.0470, wR2 = 0.1010
R indices (all data)	R1 = 0.0758, wR2 = 0.1106
Largest diff. peak and hole	0.337 and -0.389 e.$Å^{-3}$

Goodness-of-fit = $[\Sigma[w(F_o^2 - F_c^2)^2]/N_{observns} - N_{params})]^{1/2}$, all data.

R1 = $\Sigma(|F_o| - |F_c|) / \Sigma |F_o|$. $wR2 = [\Sigma[w(F_o^2 - F_c^2)^2] / \Sigma [w(F_o^2)^2]]^{1/2}$.

Table S3. Crystal data and structure refinement for **2** (X-ray label: 21236).

Empirical formula	$C_{20} H_{11} Br N_5$	
Formula weight	401.25	
Crystal color, shape, size	black needle, 0.873 × 0.067 × 0.033 mm^3	
Temperature	296(2) K	
Wavelength	0.71073 Å	
Crystal system, space group	Monoclinic, $P2_1/n$	
Unit cell dimensions	a = 6.4595(6) Å	$\alpha = 90°$.
	b = 12.3137(14) Å	$\beta = 96.254(3)°$.
	c = 21.149(3) Å	$\gamma = 90°$.
Volume	1672.2(3) $Å^3$	
Z	4	
Density (calculated)	1.594 Mg/m^3	
Absorption coefficient	2.472 mm^{-1}	
F(000)	804	
Data collection		
Diffractometer	Venture D8, Bruker	
Source	IμS 3.0, Incoatec	
Detector	Photon III	
Theta range for data collection	1.917 to 25.039°.	
Index ranges	-7<=h<=7, -14<=k<=14, -25<=l<=25	
Reflections collected	40167	
Independent reflections	2961 [$R_{int} = 0.0665$]	
Observed Reflections	2239	
Completeness to theta = 25.039°	99.9 %	
Solution and Refinement		
Absorption correction	Semi-empirical from equivalents	
Max. and min. transmission	0.7452 and 0.6770	
Solution	Intrinsic methods	
Refinement method	Full-matrix least-squares on F^2	
Weighting scheme	$w = [\sigma^2 Fo^2 + AP^2 + BP]^{-1}$, with $P = (Fo^2 + 2 Fc^2)/3$, A = 0.0094, B = 2.6649	
Data / restraints / parameters	2961 / 85 / 239	
Goodness-of-fit on F^2	1.139	
Final R indices [$I>2\sigma(I)$]	R1 = 0.0507, wR2 = 0.0995	
R indices (all data)	R1 = 0.0688, wR2 = 0.1061	
Largest diff. peak and hole	0.198 and -0.370 e.$Å^{-3}$	

Goodness-of-fit = $[\Sigma[w(F_o^2 - F_c^2)^2]/N_{observns} - N_{params})]^{1/2}$, all data.
$R1 = \Sigma(|F_o| - |F_c|) / \Sigma |F_o|$. $wR2 = [\Sigma[w(F_o^2 - F_c^2)^2] / \Sigma [w(F_o^2)^2]]^{1/2}$.

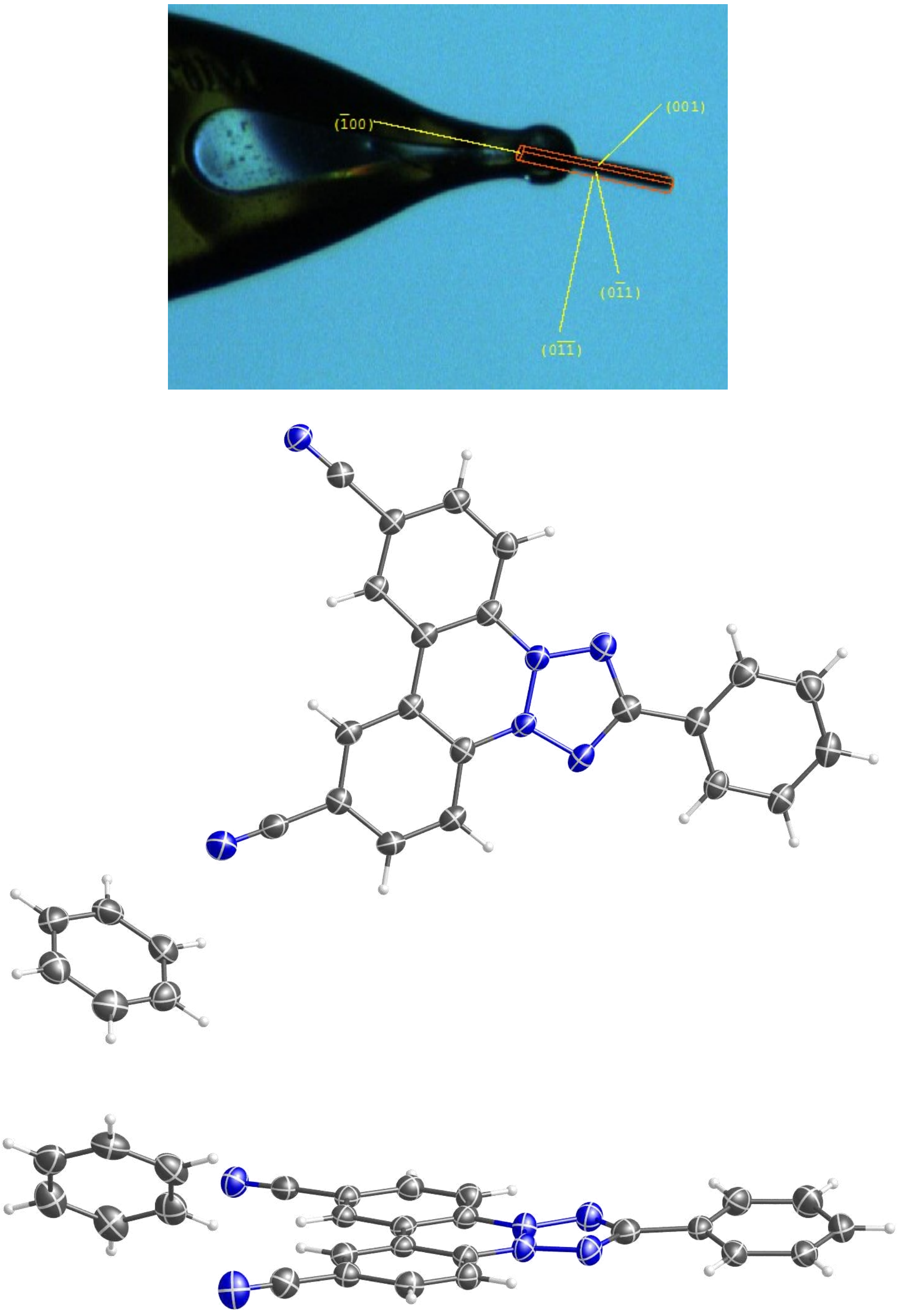

Fig. S1. Top: Selected specimen of **1** with face index. Bottom: Two views of formula unit of **1**.

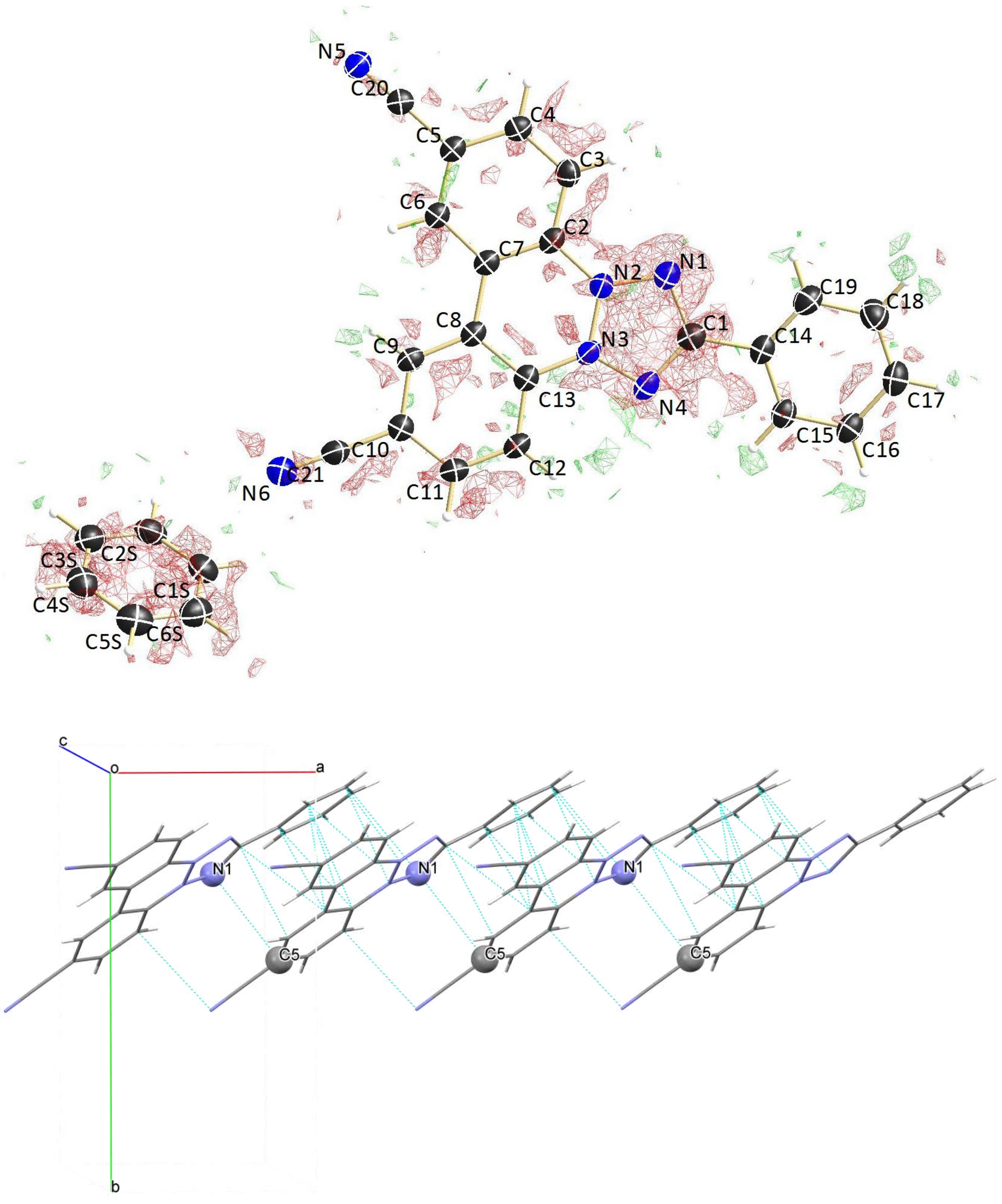

Fig. S2. Top plot: formula unit of **1** with electron density difference map; in green positive and in red negative difference e-density. Bottom: Tetramer of molecules **1**, showing packing into one-dimensional *S* = 1/2 antiferromagnetic chain along crystallographic *a*-axis; multiple C···C and N···C contacts within the sum of van der Waals radii plus 0.1 Å, including the N1…C5 = 3.346 Å contact emphasized in ball-and-stick, are shown.

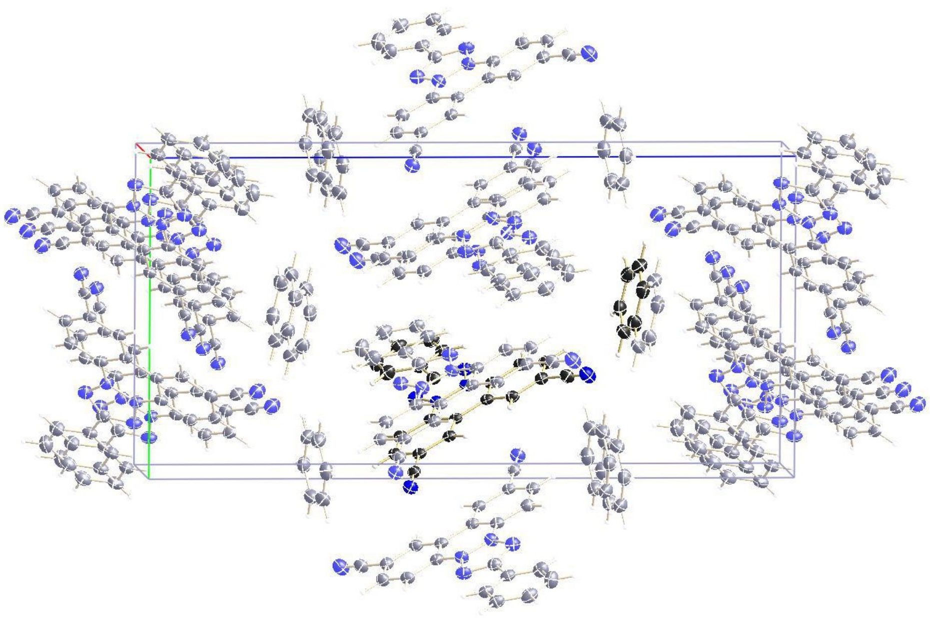

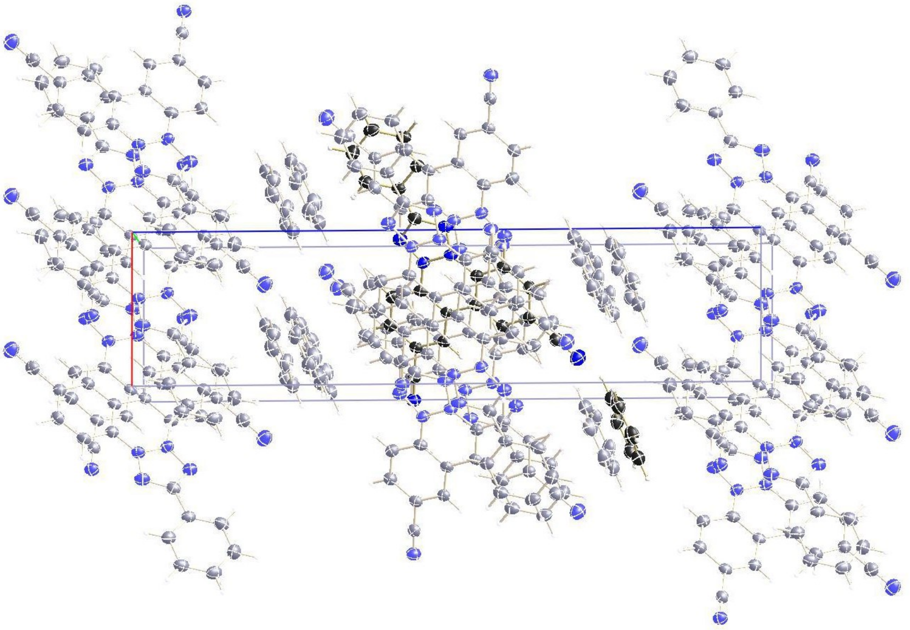

Fig. S3. Cell plots of **1** with a view along the *a*- and *b*-axes, top and bottom, respectively.

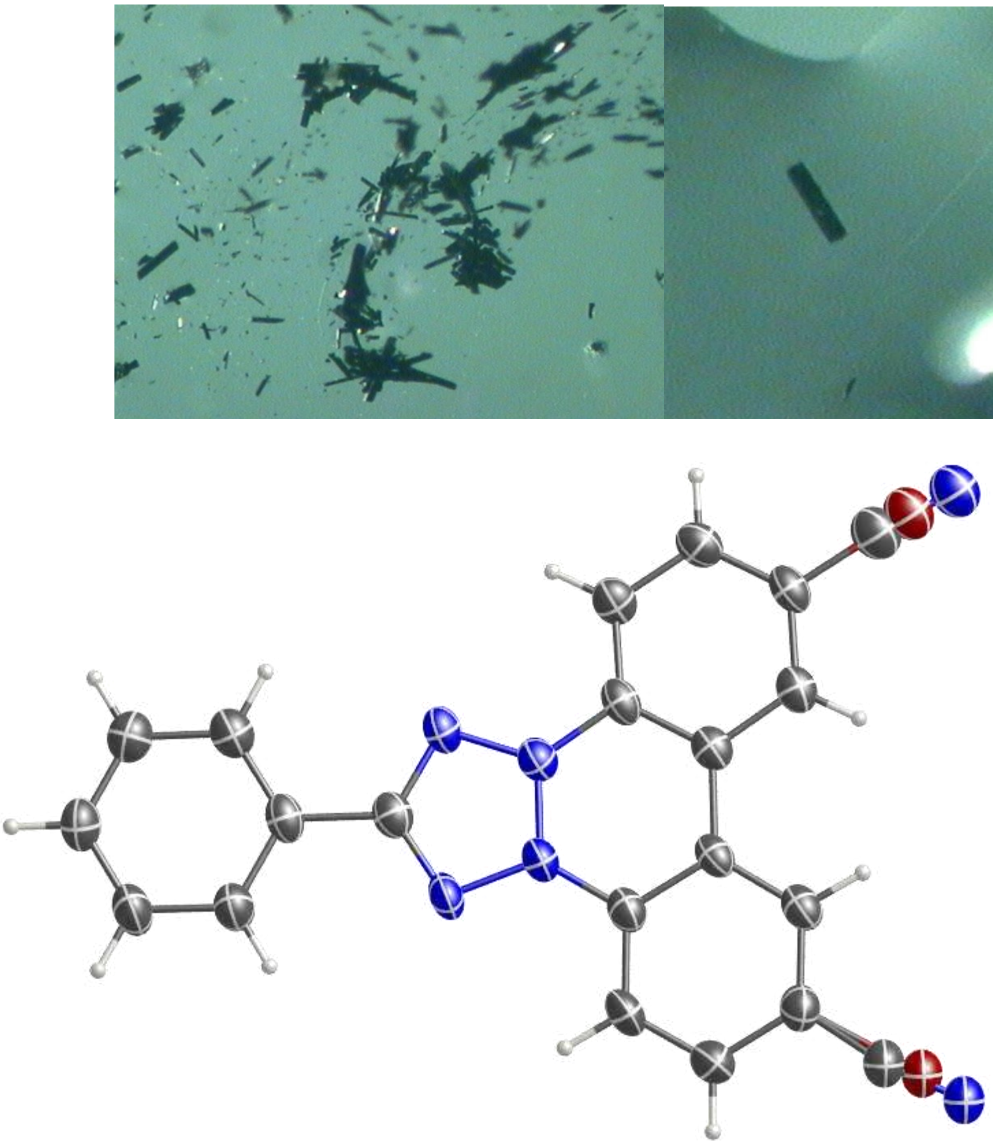

Fig. S4A. Top: Bulk material and selected specimen of **2** (from pentane/toluene). Bottom plot: Formula unit of **2**, with Br/CN disorder shown (X-ray label: 21234).

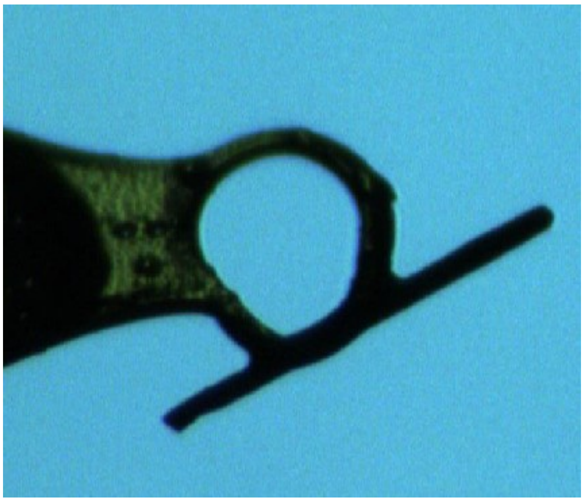

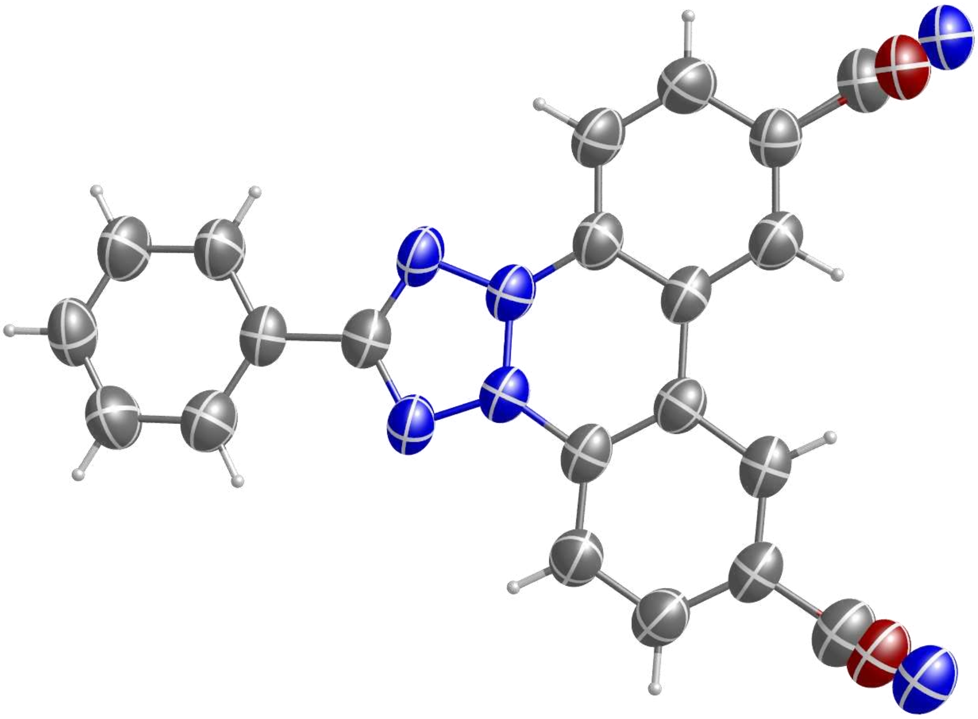

Fig. S4B. Top: Mounted crystal of **2** (from pentane/ethyl acetate). Bottom plot: Formula unit of **2**, with Br/CN disorder shown (X-ray label: 21236).

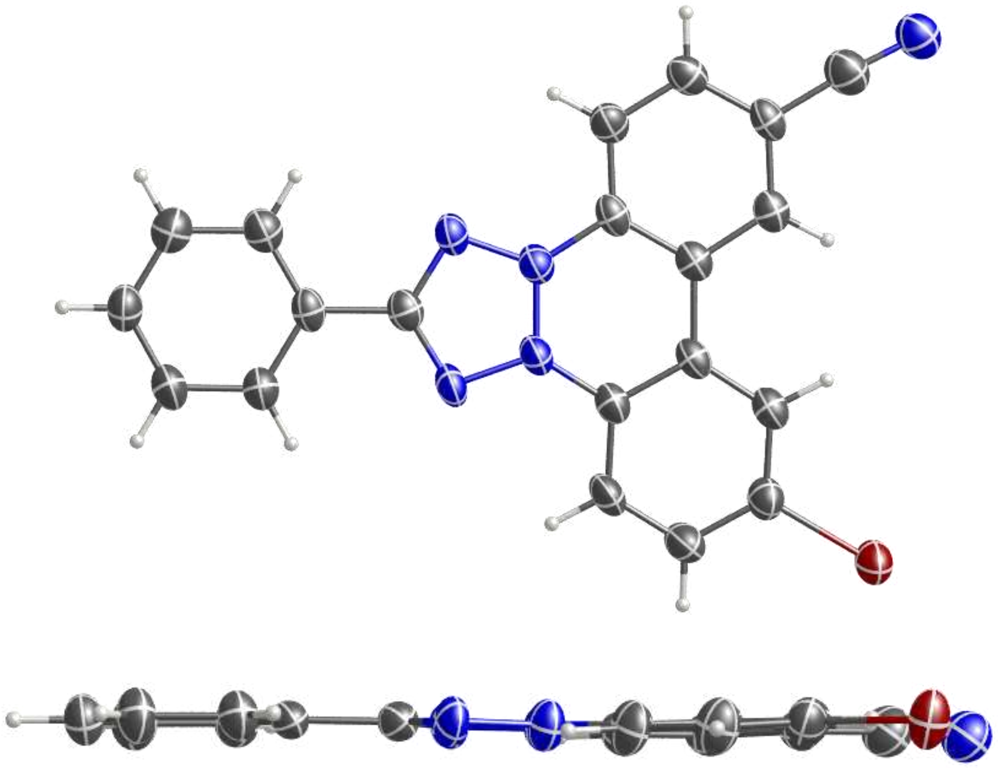

Fig. S5A. Two views of formula unit of **2** (from pentane/toluene), with disorder omitted (X-ray label: 21234).

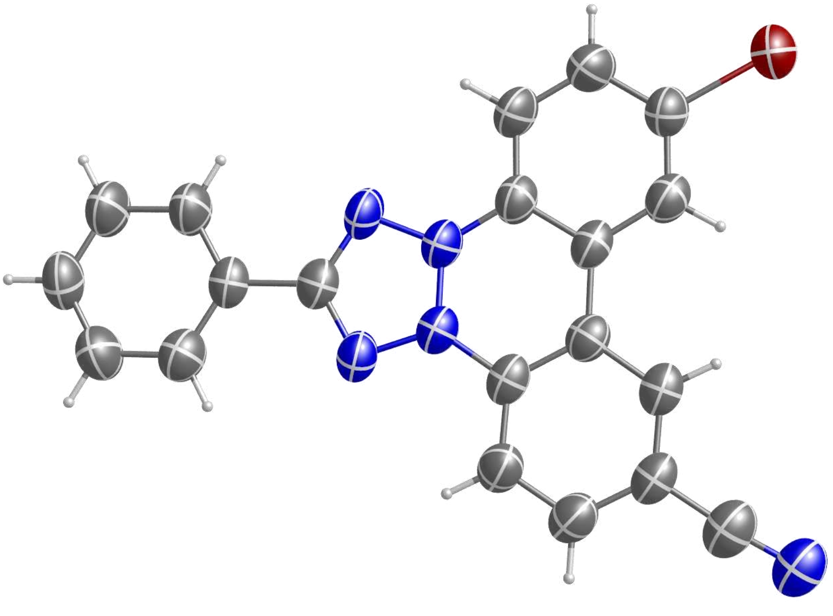

Fig. S5B. Formula unit of **2** (from pentane/ethyl acetate), with disorder omitted (X-ray label: 21236).

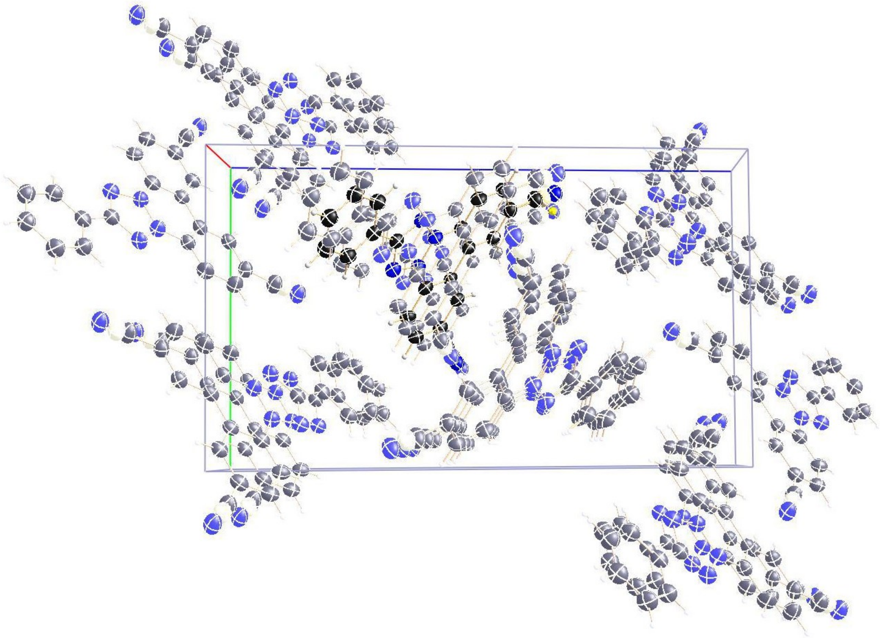

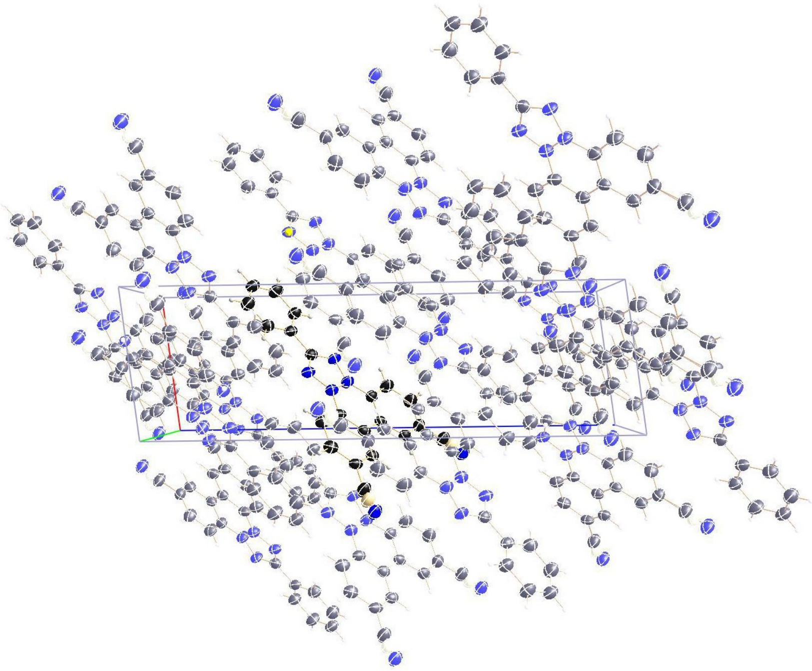

Fig. S6A. Cell plots of **2** (from pentane/toluene) with a view along the *a*- and *b*-axes, top and bottom, respectively (X-ray label: 21234).

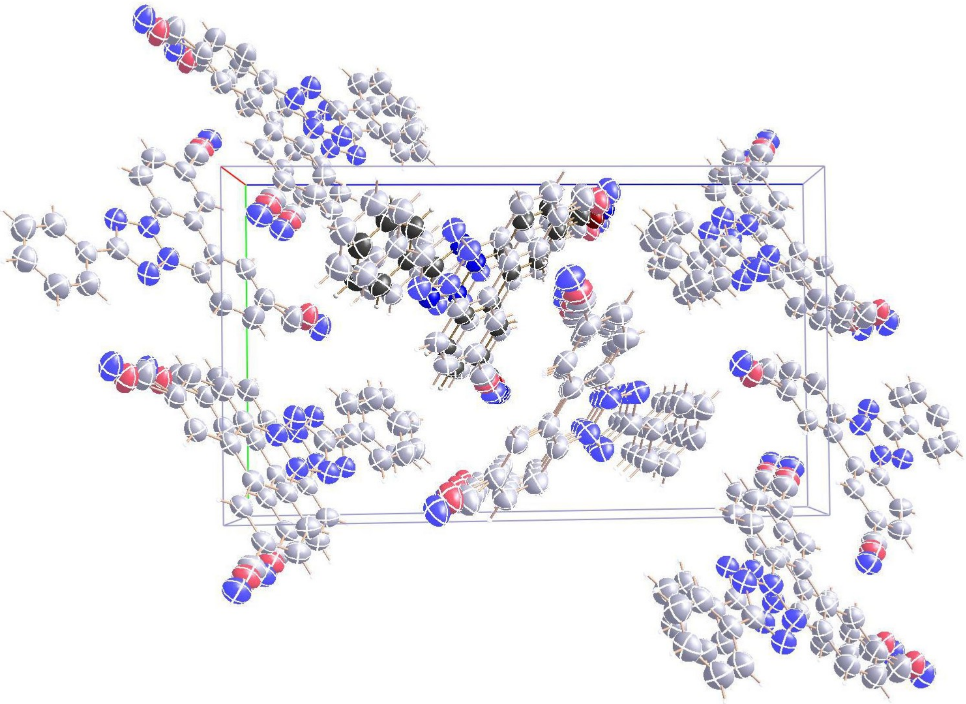

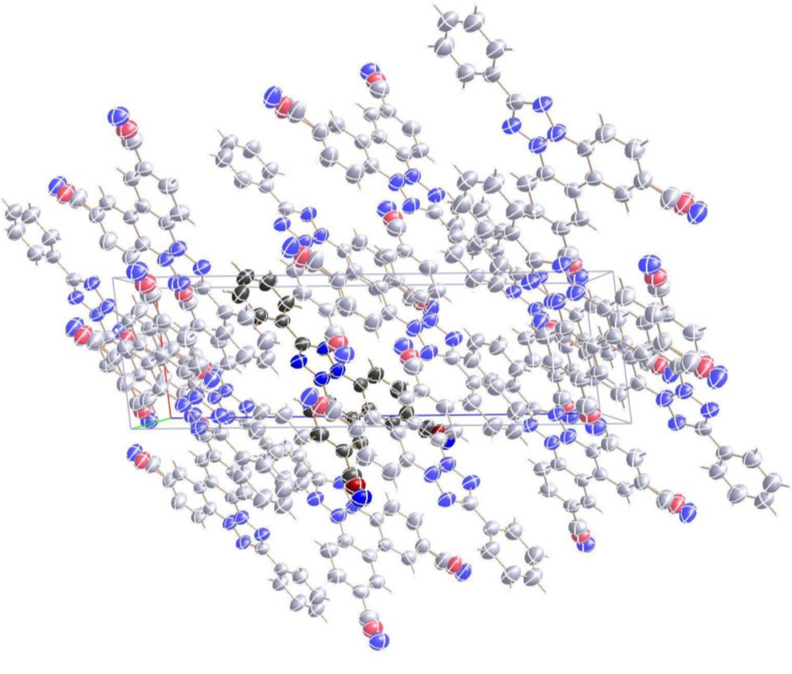

Fig. S6B. Cell plots of **2** (from pentane/ethyl acetate) with a view along the *a*- and *b*-axes, top and bottom, respectively (X-ray label: 21236).

1.c Synthesis of dicyano tetrazolinyl radical 1.

Scheme S1. Synthesis of dicyano phototetrazolinyl radical **1**.

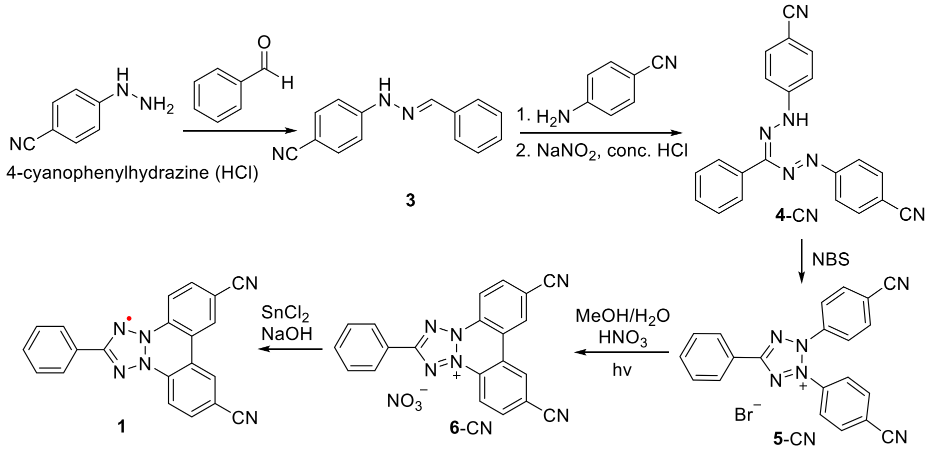

Procedure for compounds 3 and 4-CN. Formazan **4**-CN could be synthesized through one-pot reaction or stepwise reaction through compound **3** according to the reported literature.[S5] Here, stepwise reaction was used to prepare **4**-CN.

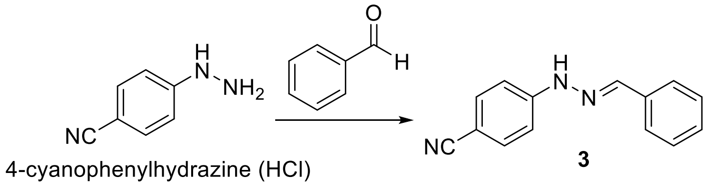

Run	4-Cyanophenylhydrazine (HCl)/ (g/mmol)	Benzaldehyde (g/mL)	NaOH (g/mmol)	TM (g)	Yield (%)	TM label
ZY814	3.17/18.69	1.77/1.69	0.69/18.69	3.92	94	ZY814
ZY815	10/58.96	6.26/6.00	2.36/58.96	12.62	97	ZY 815
Zy844	15/88.44	9.38/9.00	3.54/88.44	18.60	95	ZY844

ZY815. Benzaldehyde (6.26 g, 6.0 mL, 58.96 mmol) was added into the solution of 4-cyanophenylhydrazine hydrochloride (10 g, 58.96 mmol), NaOH (2.36 g, 58.96 mmol) in H_2O (56.6 mL) and MeOH (224 mL) under N_2 atmosphere, the yellow solution was heated at 75 °C for 2 hours to give yellow suspension. After cooling to room temperature, the yellow suspension was filtered and obtained solid dried under high vacuum line overnight to give hydrazone **3** (12.62 g, yield 97%) as a fluffy yellow solid. M.p. 160 °C. IR (powder, cm^{-1}): 3286, 2210, 1605, 1593, 1568, 1525, 1496, 1425, 1328, 1305, 1268, 1133, 1100, 1070, 933, 907. ^1H NMR (400 MHz, $CDCl_3$): δ 7.13-7.15 (m, 2H), 7.36-7.42 (m, 3H), 7.53-7.55 (m, 2H), 7.67-7.69 (m, 2H), 7.76 (s, 1H), 7.87 (br, 1H). ^{13}C NMR (176 MHz, $CDCl_3$): 102.1, 112.8, 120.1, 126.7, 128.9, 129.5, 133.9, 134.5, 140.4, 147.9. HR-MS (m/z): $[M+Na]^+$ calcd for $C_{14}H_{11}N_3Na$ 244.08452, found 244.08436 (0.6 ppm, RA = 100%).

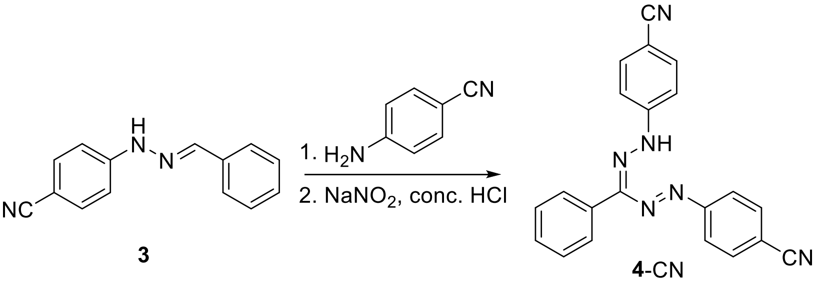

Run	SM label	**3** (g/mmol)	$Na_2CO_3 \cdot 10H_2O$ (g/mmol)	$NaNO_2$ (g/mmol)	Bu_4NBr (mg/mmol)	4-Cyanoaniline (g/mmol)	Conc. HCl (mL)	TM (g)	Yield (%)	TM label
ZY816	Zy814	0.50/2.26	3.23/11.3	0.214/3.10	74/0.23	0.307/2.60	0.59	0.25	31	ZY814 col
ZY817	Zy815	5/22.6	32.3/113	2.14/31	728.6/2.26	3.07/26.3	5.9	1.5	19	ZY817 col
Zy835	Zy814/815	10/45.2	64.6/226	4.28/62	1460/4.52	6.14/52	11.8	5.1	30	Zy835 col

ZY835. $Na_2CO_3 \cdot 10H_2O$ (64.6, 226 mmol) and tetrabutylammonium bromide (1.46 g, 4.52 mmol) were added into yellow suspension of compound **3** (zy814 and zy815, 10 g, 45.2 mmol) in H_2O (180 mL) and DCM (452 mL), the resulting non-homogeneous mixture was stirred for 1 h at 0 °C. In another round-bottom flask (500 mL), concentrated HCl solution (36.5-38%, 11.8 mL) was slowly added into the suspension of 4-cyanoaniline (6.14 g, 52 mmol) and $NaNO_2$ (4.28 g, 620 mmol) in H_2O (260 mL) at 0 °C for 1 h to give a yellow suspension. Above freshly prepared suspension of diazonium salt was added into the mixture of hydrazone **3**. Upon addition, the organic phase in the biphasic reaction mixture became blood red. After stirring at room temperature for 3 days, the red-dark organic phase was collected, aqueous phase was extracted with DCM (3×150 mL). Combined organic phase was dried over Na_2SO_4 and concentrated. Subsequently, obtained crude was purified by flash column chromatography on deactivated silica gel using hexane: DCM=1: 1 (R_f= 0.3) to give compound **4**-CN as red-purple spot on TLC plate and fluffy dark solid (5.1 g) after drying, yield 30%. M.p. 189-191 °C. IR (powder, cm^{-1}): 3059, 2220, 1600, 1577, 1496, 1443, 1411, 1348, 1315, 1221, 1147, 1103, 1015, 847, 834, 770, 741, 693. ^{1}H NMR (400 MHz, $CDCl_3$): δ 7.47-7.50 (m, 3H), 7.77 (s, 8H), 8.07-8.09 (m, 2H), 14.93 (s, 1H). ^{13}C NMR (176 MHz, $CDCl_3$): δ 110. 9, 118. 8, 119.4, 126.5, 128.82, 128.98, 133.8, 136.0, 143.1, 150.5. HR-MS (m/z): [M+Na]$^+$ calcd for $C_{21}H_{14}N_6Na$ 373.11722, found 373.11791 (-1.9 ppm, RA = 100%).

Procedure for tetrazolium salt **5**-CN:

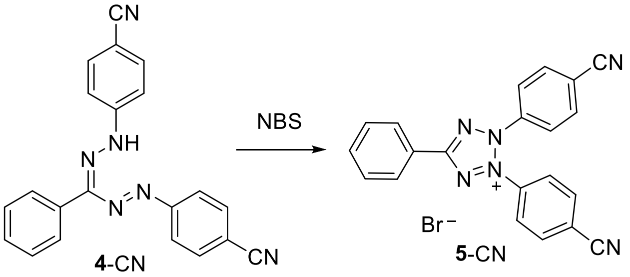

Run	S.M label	**4**-CN (mg/mmol)	**NBS** (mg/mmol)	TM (mg)	Yield (%)	TM label
ZY818	Zy816 col	247.7/0.71	143.4/0.81	169.6	56	ZY818
ZY822	ZY817 col	1150/3.83	777/4.37	846	51	ZY822
Zy837	Zy835 col	3500/9.99	2030/11.39	2307	54	Zy837
ZY1035	ZY835	1230/3.51	712.3/4.00	1194	79	ZY1035

Zy822. Red-dark mixture of formazan **4**-CN (zy817 col, 1.15 g, 3.83 mmol) and *N*-bromosuccinimide (NBS, 669.6 mg, 3.76 mmol) in ethyl acetate (106 mL) was stirred at room temperature for 3 hours to give yellow suspension. Reaction suspension was filtered off and the yellow solid was collected. After drying under high vacuum overnight, yellow solid was sufficiently pure for further use; tetrazolium salt **5**-CN overall mass is 846 mg, yield 51.4%. M.p. 236 °C. IR (powder, cm^{-1}): 3033, 2235, 1705, 1608, 1528, 1496, 1455, 1404, 1303, 1288, 1237, 1167, 1145, 1021, 998, 840. ^{1}H NMR (400 MHz, methanol-*d*$_4$): δ 7.76 (t, $J \approx 8$ Hz, 2H), 7.83 (t, $J \approx 8$ Hz, 1H), 8.00 (bd, $J \approx 8$ Hz, 4H), 8.15 (d, $J \approx 8$ Hz, 4H), 8.39 (d, $J \approx 8$ Hz, 2H). ^{13}C NMR (176 MHz, methanol-*d*$_4$): δ 117.5, 119.8, 123.9, 128.24, 128.90, 131.2, 135.28, 136.07, 137.06. HR-MS (m/z): [M]$^+$ calcd for $C_{21}H_{13}N_6$ 349.11962, found 349.11933 (0.8 ppm, RA = 100%).

Procedure for tetrazolium salt **6**-CN:[S6]

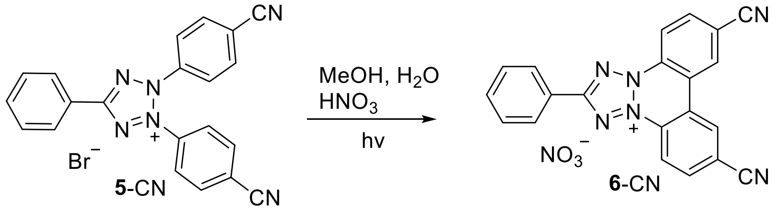

Run	S.M label	**5**-CN (mg/mmol)	MeOH (mL)	H_2O	2M HNO_3 (mL)	TM (mg)	Yield (%)	TM label
ZY823	Zy818	12.4/0.029	1.75	4.08	0.23	7.37	62	ZY823
ZY829	Zy818	37.2/0.087	5.25	14.4	0.69	28	79	ZY829
Zy833	Zy822	49.6/0.12	1.75	3.39	0.92	37.4	79	ZY647
Zy841	Zy822	347.2/0.81	12.2	23.7	6.3	165.1	50	Zy841
Zy846	Zy837	396.8/0.92	14	27.1	7.4	234.5	62	Zy846
Zy848	Zy837	347.2/0.81	12.2	23.7	6.3	224.9	68	Zy848
Zy852	Zy837	446.4/1.04	15.8	30.5	8.3	311	73	Zy852

Zy833. Tetrazolium salt **5**-CN (zy822, 49.6 mg, 0.12 mmol) suspension in MeOH (1.75 mL), H_2O (3.39 mL) and 2 M HNO_3 (0.92 mL) was irradiated by 254 nm UV lamp (4w×2) for 7 days to give brick-red suspensions. Subsequently, reaction mixture was concentrated and redissolved in MeOH (0.2 mL) and Et_2O (1.2 mL) mixture, the suspension was centrifuged at 3000 rpm for 5 mins. The brick-red precipitates of tetrazolium salt **6**-CN were collected and dried under high vacuum line overnight before further use (37.4 mg, yield 79%). M.p. > 300 °C. IR (powder, cm^{-1}): 3063, 2235, 1708, 1603, 1576, 1527, 1505, 1412, 1365, 1336, 1273, 1181, 1136, 1076, 1024, 996, 930, 828. ^{1}H NMR (400 MHz, methanol-*d*$_4$): δ 7.80-7.87 (m, 3H), 8.58 (d, $J \approx 7$ Hz, 2H), 8.63 (dd, $J_1 = 8.8$ Hz, $J_2 \approx 1$ Hz, 2H), 9.22 (d, $J_1 = 8.8$ Hz, 2H), 9.69 (s, 2H). ^{1}H NMR (400 MHz, DMSO-*d*$_6$): δ 7.86-7.91 (m, 3H), 8.53-8.54 (d, 2H, $J \approx 7$ Hz), 8.76 (dd, $J_1 = 8.8$ Hz, $J_2 \approx 1$ Hz, 2H), 9.22 (d, 2H, $J_1 = 8.8$ Hz), 9.90 (bs, 2H). ^{13}C NMR (176 MHz, methanol-*d*$_4$): 117.6, 119.4, 121.3, 123.8, 129.47, 131.28, 131.77, 132.42, 135.6, 137.3. ^{13}C NMR (150 MHz, DMSO-*d*$_6$): 116.69, 117.00, 119.8, 121.84, 122.34, 128.0, 130.43, 131.00, 131.16, 134.5, 136.3, 163.8. HR-MS (m/z): [M]$^+$ calcd for $C_{21}H_{11}N_6$ 347.10397, found 347.10415 (0.5 ppm, RA = 100%).

Procedure for radical **1**:[S7]

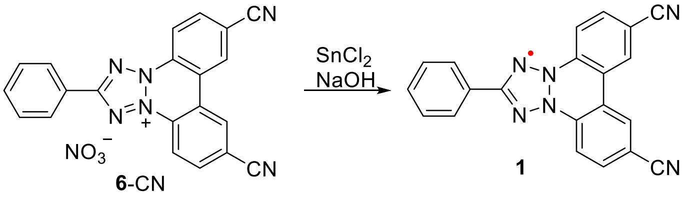

Run	S.M label	**6**-CN (mg/mmol)	$SnCl_2·2H_2O$ (mg/mmol)	2M NaOH (mL/mmol)	TM (mg)	Yield (%)	Spin Conc. (%)	TM label
ZY828	Zy823	5.1/0.013	49.6/0.22	2.17/4.33	0.58	12.8	59	Zy828
*Zy831	Zy823	5.0/0.013	49.6/0.22	2.17/4.33	/	/	/	Zy831
*Zy840	Zy833	37/0.09	337.1/1.49	15/30	/	/	/	Zy840
Zy843	Zy833	60.5/0.15	553.6/2.45	24.6/49.2	22.6	44	71	Zy843
Zy847	Zy841	60/0.15	546.9/2.42	24.3/48.6	16.2	32	82	Zy847
Zy849	Zy846	164/0.4	1500/6.65	66.6/133.3	63.1	45	94	Zy849
ZY904	ZY848	150/0.37	1370/6.08	61/122.1	51.3	40	94	ZY904
ZY1032	ZY846	102/0.25	933/4.14	42/83.3	24.0	28	96	ZY1032
ZY1036	ZY852	120/0.29	1100/4.87	48.8/97.7	51.0	51	100	ZY1036

*dark needle crystals in benzene/pentane were sent for X-ray crystallography, without spin concentration measurement.

ZY828. Reducing reagent, $SnCl_2·2H_2O$ (49.6 mg, 0.22 mmol, 10.2 mL H_2O) and 2M NaOH (2.17 mL) were added into the suspension of tetrazolium salt **6**-CN (ZY823, 5.3 mg, 0.013 mmol) in H_2O (2.41 mL) and benzene (14.9 mL). After stirring for 80 min, while argon gas passing through the suspension, the brown organic phase was separated, washed with water (3×5 mL), dried over Na_2SO_4 and then crystalized by pentane vapor diffusion, to give dark needle solid of radical **1** (0.58 mg, yield 12.8%). M.p. >300 °C (dec, under air); note that at 260 °C, the crystals turn to pink color. IR (powder, cm^{-1}): 3064, 2215, 1737, 1603, 1583, 1560, 1523, 1487, 1453, 1423, 1414, 1376, 1343, 1268, 1283, 1240, 1213, 1196, 1176, 1164, 1141, 1044, 911, 812. 807. LR-ESI (0.1 % HCOOH in MeOH, m/z): 347.4 (100%). HR-ESI (m/z): $[M]^+$ calcd for $C_{21}H_{11}N_6·$ 347.10397, found 347.10496 (2.9 ppm, RA = 87%).

1.d Synthesis of bromo-cyano tetrazolinyl radical 2.

Scheme S2. Synthesis of bromo-cyano phototetrazolinyl radical **2**.

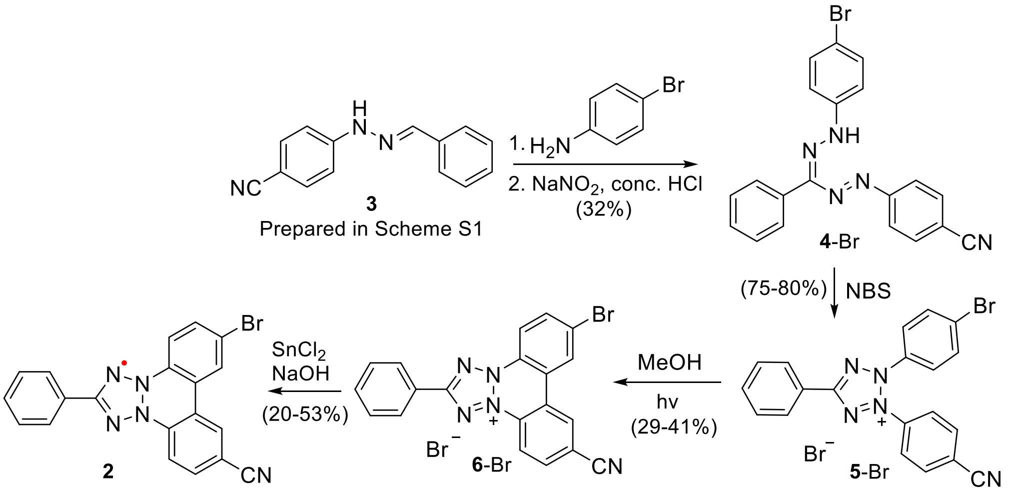

Preparation of formazan **4**-Br:[S5]

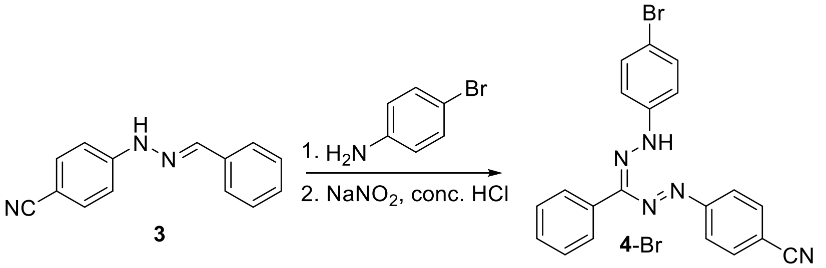

Run	SM label	**3** (g/mmol)	$Na_2CO_3 \cdot 10H_2O$ (g/mmol)	$NaNO_2$ (g/mmol)	Bu_4NBr (mg/mmol)	4-Bromoaniline (g/mmol)	Conc. HCl (mL)	TM (g)	Yield (%)	TM label
Zy964	Zy844	5/22.6	32.3/113	2.14/31	728.6/2.26	4.47/26	5.9	2.96	32	Zy964 rec

ZY964: $Na_2CO_3 \cdot 10H_2O$ (32.3, 113 mmol) and tetrabutylammonium bromide (728.6 mg, 2.26 mmol) were added into yellow suspension of hydrazone **3** (zy844, 10g, 22.6 mmol) in H_2O (90 mL) and DCM (226 mL), the resulting non-homogeneous mixture was stirred for 1 hour at room temperature. In another round-bottom flask (500 mL), concentrated HCl solution (36.5-38%, 5.9 mL) was added into the suspension of 4-bromoaniline (4.47 g, 26 mmol) and $NaNO_2$ (2.14 g, 31 mmol) in H_2O (130 mL) at 0 °C for 1 h to give a yellow suspension. Above freshly made suspension of diazonium salt was added into the mixture of hydrazone **3**. Upon addition, the organic phase in the biphasic reaction mixture became blood red. After stirring at room temperature for 3 days, the red-dark organic phase was collected, the aqueous phase was extracted with DCM (3×150 mL). Combined organic phase was dried over Na_2SO_4 and concentrated and purified by flash column chromatography on deactivated silica gel using hexane/DCM = 1:1 (R_f = 0.37) to give formazan target material **4**-Br as red spot at TLC plate; dark solid after recrystallization from MeOH (2.96 g, yield 32.4%). M.p. 180 °C. ^1H NMR (400 MHz, $CDCl_3$): δ 7.43-7.51 (m, 5H), 7.64-7.70 (m, 4H), 7.79 (d, $J \approx 8$ MHz, 2H), 8.08 (d, $J \approx 7$ MHz, 2H). ^{13}C NMR (150 MHz, $CDCl_3$): 106.5, 115.8, 119.4, 123.6, 126.29, 126.54, 128.71, 128.76, 132.97, 133.86, 136.3, 142.7, 147.5, 150.7. HR-ESI (m/z): calcd 402.0354 for $C_{20}H_{13}N_5{}^{79}Br$, found 402.0329 (-6.2 ppm, RA = 100%); calcd 404.0334 for $C_{20}H_{13}N_5{}^{81}Br$, found 404.0331 (-0.7 ppm, RA = 92%) (sample label: ZY964). Most likely under the ESI conditions, formazan **4**-Br gets oxidized to tetrazolium cation **5**-Br.

Preparation of tetrazolium salt **5**-Br:[S6]

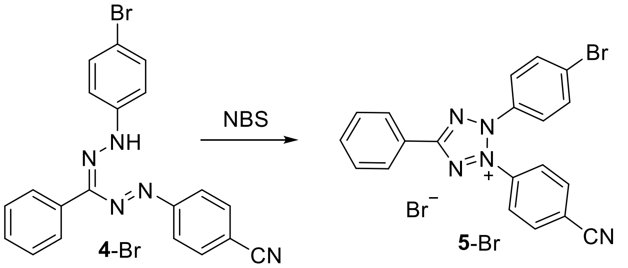

Run	SM label	**4**-Br (mg/mmol)	**NBS** (mg/mmol)	TM (mg)	Yield (%)	TM label
Zy687	AB-2	243/0.6	107/0.6	217.9	75	Zy687 crd
Zy855	AB-2	500/1.24	242.2/1.36	482.2	80	ZY855 crd
ZY868	AB-2	570/1.41	576/1.55	545.5	80	ZY868 crd
ZY968	Zy964 rec	2000/4.95	924.5/5.19	1900	79	ZY968 crd

Zy968: Red-dark mixture of formazan **4**-Br (zy964 rec, 2.0 g, 4.95 mmol, 1.0 equiv) and *N*-bromosuccinimide (NBS, 924.5 mg, 5.19 mmol, 1.05 equiv) in ethyl acetate (120 mL) was stirred at

room temperature overnight to give yellow suspension. Reaction suspension was filtered off and the yellow solid was collected. After drying under high vacuum overnight, yellow solid was sufficiently pure for further use, with target material **5**-Br overall mass is 1.9 g, yield 79%. M.p. 260–261 °C. ^{1}H NMR (700 MHz, DMSO-d_6): δ 7.78-7.80 (m, 4H), (t, $J \approx 8$ MHz, 1H), 8.00 (d, $J = 9.1$ MHz, 2H), 8.06 (d, $J = 9.1$ MHz, 2H), 8.27 (d, $J = 9.1$ MHz, 2H), 8.35 (d, $J \approx 8$ MHz, 2H). ^{13}C NMR (176 MHz, DMSO-d_6): 116.96, 117.01, 122.4, 127.40, 127.45, 128.19, 128.49, 130.4, 131.7, 133.89, 134.00, 134.88, 135.6, 164.6. HR-MS (m/z): calcd 402.0354 for $C_{20}H_{13}N_5{}^{79}Br$, found 402.0351 (-0.7 ppm, RA = 100%); calcd 404.0334 for $C_{20}H_{13}N_5{}^{81}Br$, found 404.0324 (-2.5 ppm, RA = 91%) (sample label: ZY968).

Preparation of phototetrazolium salt **6**-Br:[S6]

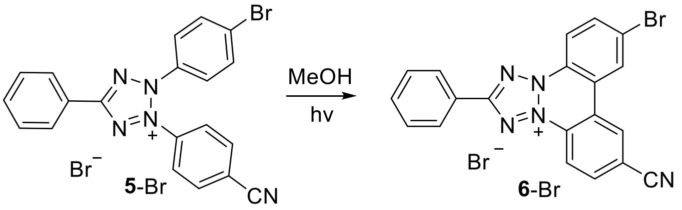

5-Br

6-Br

Run	S.M label	**5**-Br (mg/mmol)	MeOH (mL)	**6**-Br (mg/mmol)	Yield (%)
ZY688	Zy687	50/0.10	5	20/0.04	41
ZY869	ZY855/AB-3	200/0.41	20	66.9/0.14	34
ZY877	AB-3	300/0.62	36	89.5/0.186	30
ZY911	AB-3	350/0.72	42	97/0.20	29
ZY954	AB-3	100/0.21	12	38.6/0.08	38
ZY961	ZY868 crd	300/0.62	36	111/0.23	37
ZY970	ZY968	400/0.83	48	150/0.31	37
ZY974	ZY968	500/1.04	60	188/0.39	38
ZY980	ZY968	550/1.14	60	213.7/0.44	39

ZY961. Tetrazolium salt **5**-Br (300 mg, 0.62 mmol) solution in MeOH (6 mL × 6 test tubes) was irradiated with 254 nm (6W*2) for 9 days to give yellow suspension. After drying the mixture solid, small amount of MeOH (0.6 mL) was added to give concentrated suspension. Subsequently, mixture was centrifuged for minutes at 3000 rpm, dark liquid was removed, and yellow solid was kept and dried under high vacuum line overnight to give phototetrazolium salt **6**-Br as a yellow solid (111 mg, 37%). M.p. >300 °C. ^{1}H NMR (400 MHz, methanol-d_4): δ 7.78-7.85 (m, 3H), 8.49 (dd, $J_1 \approx 9$ Hz, $J_2 \approx 2$ Hz, 1H), 8.54-8.59 (m, 3H), 8.97 (d, $J_1 = 9$ Hz, 1H), 9.17 (d, $J = 8.8$ Hz, 1H), 9.47 (d, $J_2 = 2$ Hz, 1H), 9.66 (d, $J \approx 1$ Hz, 1H). ^{13}C NMR (176 MHz, methanol-d_4): 117.8, 119.2, 121.30, 121.72, 123.84, 124.39, 124.82, 129.52, 129.75, 129.99, 130.97, 131.36, 131.85, 132.5, 135.6, 137.0, 138.4, 166.5. HR-ESI (m/z): calcd 400.0198 for $C_{20}H_{11}N_5{}^{79}Br$, found 400.0210 (3.0 ppm, RA = 100%); calcd 402.0177 for $C_{20}H_{11}N_5{}^{81}Br$, found 402.0174 (0.7 ppm, RA = 89%) (sample label: ZY974).

Preparation of phototetrazolinyl radical **2**:[S7]

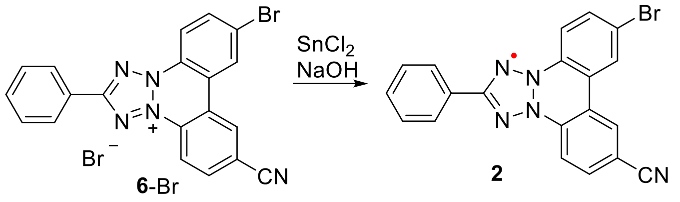

6-Br

2

Run	S.M label	**6**-Br (mg/mmol)	$SnCl_2 \cdot 2H_2O$ (mg/mmol)	2M NaOH (mL/mmol)	TM (mg)	Yield (%)	Spin Conc. (%)	TM label
ZY876	Zy869	20/0.042	155.7/0.69	7/14	6.18	37	93	Zy876
Zy972	Zy961	133/0.28	1040/4.59	46/92.1	22.6	20	97	Zy972
Zy973	Zy877	80/0.166	622.7/2.76	27.6/55.3	29.3	44	97	Zy973
Zy976	Zy970	20/0.042	155.7/0.69	7/14	5.2	31	100	Zy976
Zy978	Zy970	50/0.104	389.2/1.72	17.3/34.6	15	36	83	Zy978
Zy981	Zy970	70/0.14	543.8/2.41	24.2/48.3	29.8	53	94	Zy981

Zy876. Reducing reagent, $SnCl_2 \cdot 2H_2O$ (155.7 mg, 0.69 mmol, 31.8 mL H_2O, 16.6 equiv) and 2M NaOH (7 mL, 14 mmol, 333.2 equiv) were added into the suspension of phototetrazolium salt **6**-Br (ZY869, 20.0 mg, 0.042 mmol, 1.0 equiv) in H_2O (7.6 mL) and benzene (23.2 mL). After stirring for 10 min, while argon gas passing through the suspension, the brown-dark organic phase was separated, washed with water (3×7 mL), dried over Na_2SO_4, and then crystalized by pentane vapor diffusion, to give dark solid **2** (6.18 mg, yield 37%). M.p. >300 °C (dec, under air); note that at 235 °C, the crystals turn to purple color. HR-ESI (m/z): calcd 400.0198 for $C_{20}H_{11}N_5{}^{79}Br$, found 400.0210 (3.0 ppm, RA = 100%); calcd 402.0177 for $C_{20}H_{11}N_5{}^{81}Br$, found 402.0174 (0.7 ppm, RA = 99%) (sample label: ZY876).

1.e Acidification of dicyano phototetrazolinyl radical 1.

Procedure for compound **6**-CN:

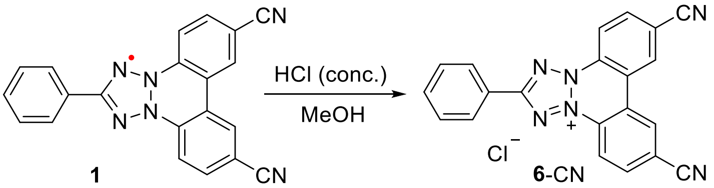

Run	S.M label	**1** (mg/mmol)	Conc. HCl (µL/mmol)	TM (mg)	Yield (%)	TM label
ZY896	Zy849	1.88/0.005	12/0.15	2.1	100	ZY896
Zy969	Zy849	10.98/0.032	64/0.88	11.1	92	Zy969

Zy969. A dark suspension of radical **1** (10.98 mg, 0.032 mmol, sample label: ZY849, spin conc. = 94%) in MeOH (9 mL) was stirred at 0 °C. Subsequently, concentrated HCl (36.5–38%, 0.88 mmol, 27.8 equiv) was added dropwise to the above dark suspension, which was stirred for another 30 min at 0 °C. After warming to room temperature for 1.5 h, initial dark suspension became yellow clear solution, and then solvents were removed by nitrogen gas flow. The resultant solid was dried under high vacuum line overnight, to give tetrazolium cation **6**-CN as a yellow solid (11.10 mg, 92% yield). ^{1}H NMR (400 MHz, methanol-d_4): δ 7.81-7.89 (m, 3H), 8.58 (d, $J \approx 7$ Hz, 2H), 8.63 (dd, $J_1 = 8.8$ Hz, $J_2 \approx 1$ Hz, 2H), 9.22 (d, $J_1 = 8.8$ Hz, 2H), 9.69 (d, $J_2 \approx 1$ Hz, 2H) (Fig. S54).

1.f DFT computations. DFT (UB3LYP/6-31G(d,p)/PCM-UFF) optimized geometries for **1** and **2** in benzene were obtained using Gaussian 16 (G16).[S8] Dispersion was taken into account using G16 keyword, empiricaldispersion=gd3bj, corresponding to Grimme's empirical dispersion correction (D3)[S9] with Becke–Johnson damping function (BJ).[S10] For geometry optimizations of radicals **1** and **2**, RMS forces in Cartesian coordinates are 1.3 and 6.4×10^{-6} a.u., respectively, and they are significantly lower in internal coordinates, i.e., typically better than the "tight" criterion for RMS forces in geometry optimization in Gaussian 16. Vibrational frequency computations confirm the minima on the potential energy surface for C_{2v}-symmetric **1** and C_s-symmetric **2**. Using these geometries hyperfine couplings were obtained for **1** and **2** (Table S4).

Spin density surfaces for radicals were calculated at the UB3LYP/6-31G(d,p)/PCM-UFF level in benzene, using the D3BJ correction. Cube files were obtained using "medium" setting in Gaussian 16 (cubegen utility), and surfaces were plotted with isodensity of 0.002 electron Bohr^{-3} (Table S3).

Using the optimized C_{2v}-symmetric geometry in DCM, UV-vis-NIR spectrum for radical **1** was computed at the TD-DFT/UCAM-UB3LYP-6-31G(d,p) level of theory, using PCM-UFF solvent model for DCM (G16 default); 40 excited states were calculated. For computed UV-vis-NIR absorption spectrum, the electronic UV-vis data (*f*) in the Gaussian 16 output file was converted to stick spectra in the text file format and then convoluted with the Gaussian functions with half-width of 0.20 eV, using graphical user interface Gabedit (version 2.5.0).[S11] The resultant UV-vis-NIR spectrum of **1** was imported to SigmaPlot, its horizontal axis shifted by –0.60 eV, and then re-plotted with the wavelength (nm) axis. Vertical axes were scaled to fit the experimental spectra (simulated spectra multiplied by a factor of 3). Computed spectrum for **1** is plotted in Figure 8 (main text) and Fig. S7 (SI).

Table S4. DFT computed hyperfine couplings (in MHz) for radicals **1** and **2** at the UB3LYP/6-31G(d,p)/D3BJ (in PCM-UFF benzene, G16 default) level of theory vs experimental values (EPR).

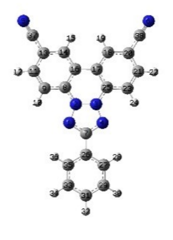		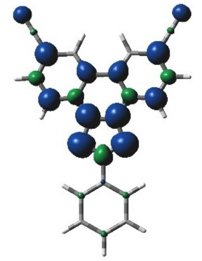			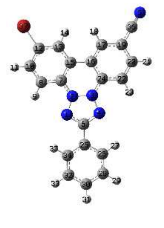		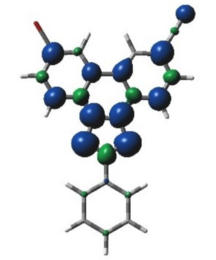	
1					**2**			
		DFT	EPR[a]				DFT	EPR[a]
1	N(14)	11.87764	10.51		1	N(14)	11.58357	10.40
2	N(14)	10.91878	15.79		2	N(14)	13.83312	20.10
3	N(14)	10.91878	15.79		3	N(14)	9.96029	14.79
4	N(14)	11.87764	10.51		4	N(14)	11.88359	10.40
5	N(14)	**1.60841**			5	N(14)	**1.84157**	
6	N(14)	**1.60841**			6	C(13)	-17.15207	
7	C(13)	-17.35183			7	C(13)	-13.81668	
8	C(13)	-12.75616			8	C(13)	11.7882	
9	C(13)	12.26007			9	H(1)	-7.05614	5.64
10	H(1)	-7.21296	5.74		10	C(13)	-7.36343	
11	C(13)	-9.40771			11	H(1)	**1.9522**	
12	H(1)	**2.7767**			12	C(13)	13.0372	
13	C(13)	13.057			13	C(13)	-5.75708	
14	C(13)	-4.5673			14	H(1)	1.23804	
15	H(1)	0.17643			15	C(13)	7.16194	
16	C(13)	6.72155			16	C(13)	6.65467	
17	C(13)	6.72155			17	C(13)	-4.49368	
18	C(13)	-4.5673			18	H(1)	-0.09412	
19	H(1)	0.17643			19	C(13)	14.53542	
20	C(13)	13.057			20	C(13)	-10.38678	
21	C(13)	-9.40771			21	H(1)	**3.03828**	
22	H(1)	**2.7767**			22	C(13)	13.38595	
23	C(13)	12.26007			23	H(1)	-7.90157	6.01
24	H(1)	-7.21296	5.74		24	C(13)	-12.46314	
25	C(13)	-12.75616			25	C(13)	2.89038	
26	C(13)	2.94527			26	C(13)	-2.7413	
27	C(13)	-2.77165			27	H(1)	1.25902	
28	H(1)	1.29764			28	C(13)	1.74991	
29	C(13)	1.76528			29	H(1)	-0.68158	
30	H(1)	-0.68045			30	C(13)	-2.2789	
31	C(13)	-2.30609			31	H(1)	1.18543	
32	H(1)	1.20335			32	C(13)	1.75839	
33	C(13)	1.76528			33	H(1)	-0.67814	
34	H(1)	-0.68045			34	C(13)	-2.75983	
35	C(13)	-2.77165			35	H(1)	1.30275	
36	H(1)	1.29764			36	C(13)	-8.18293	
37	C(13)	-7.331			37	Br(79)	**1.72061**	[b]
38	C(13)	-7.331						

[a] Figure 4 (main text). [b] Fig. S21, $A(^{79}\mathrm{Br}) = 0.78$ MHz.

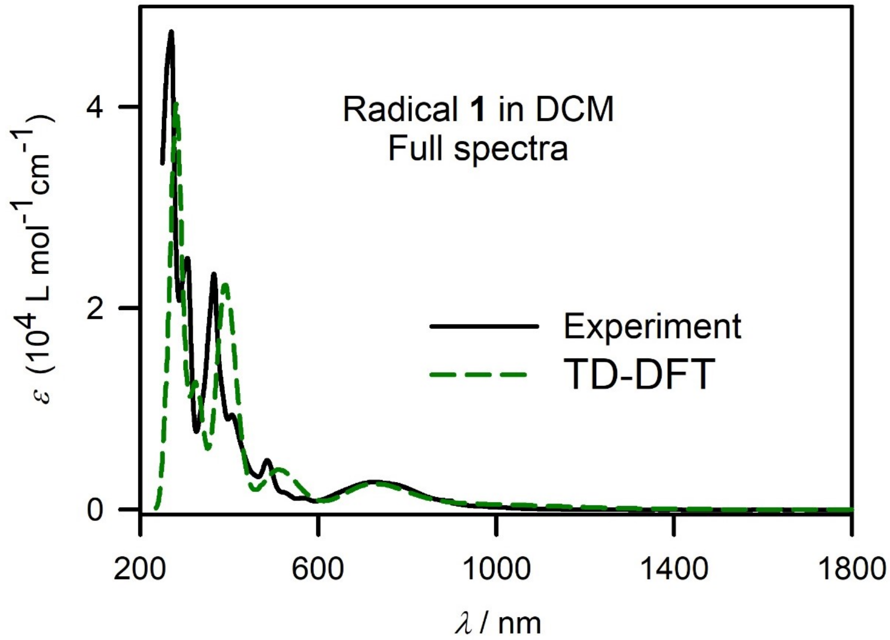

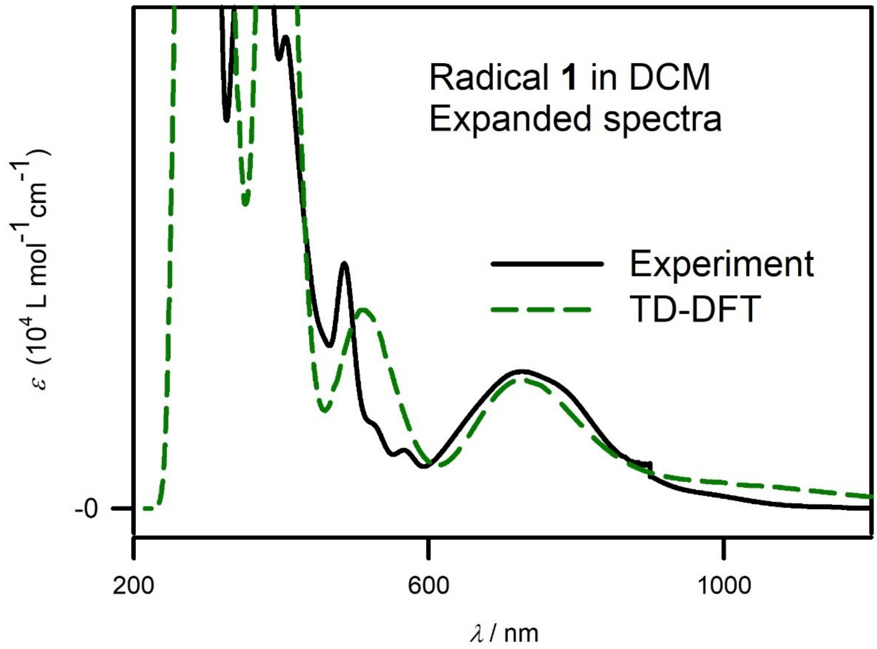

Fig. S7. UV-vis-NIR absorption spectra for **1** in DCM. Simulated spectrum (TD-DFT) was obtained at the UCAM-UB3LYP-6-31G(d,p) level of theory, using PCM-UFF solvent model for DCM (G16 default).

1.g UV-vis-NIR spectroscopy of radicals 1 and 2 at room temperature. UV-vis-NIR absorption spectra of radicals **1** and **2**, and its cationic precursors were obtained using JASCO (model V-670) spectrophotometer in the $\lambda = 250–1800$ nm range, using either benzene or dichloromethane (DCM), or, for cationic precursors, acetonitrile as a solvent. The values of ε are not corrected for spin concentration of the radicals.

For radical **1** in benzene vs DCM, plots of molar absorbance, ε, vs wavenumber, $\tilde{\nu}$, show that the longest wavelength band at $\lambda_{\text{max}} \approx 730$ nm (the lowest wavenumber band at $\tilde{\nu}_{\text{max}} \approx 13700$ cm^{-1}) is symmetrical and it shows little solvent dependence (Fig. S8).

For radical **1**, band gap, $E_{\text{g}} = 1.12 \pm 0.002$ eV, was determined using 3 different samples of **1** (two in DCM and one in benzene), as illustrated in Figs. S9 – S11. For radical **2** in dichloromethane, a somewhat smaller $E_{\text{g}} = 1.09$ eV was found (Fig. S12); this is in spite of the fact that $\lambda_{\text{max}} = 717$ nm for **2** corresponds to hypsochromic shift, when compared to $\lambda_{\text{max}} = 726–729$ nm for **1** in DCM. Diamagnetic cations (salts) **6**-CN and **6**-Br, precursors to **1** and **2**, possess much larger $E_{\text{g}} = 2.50$ and 2.00 eV, respectively (Figs. S13 and S14).

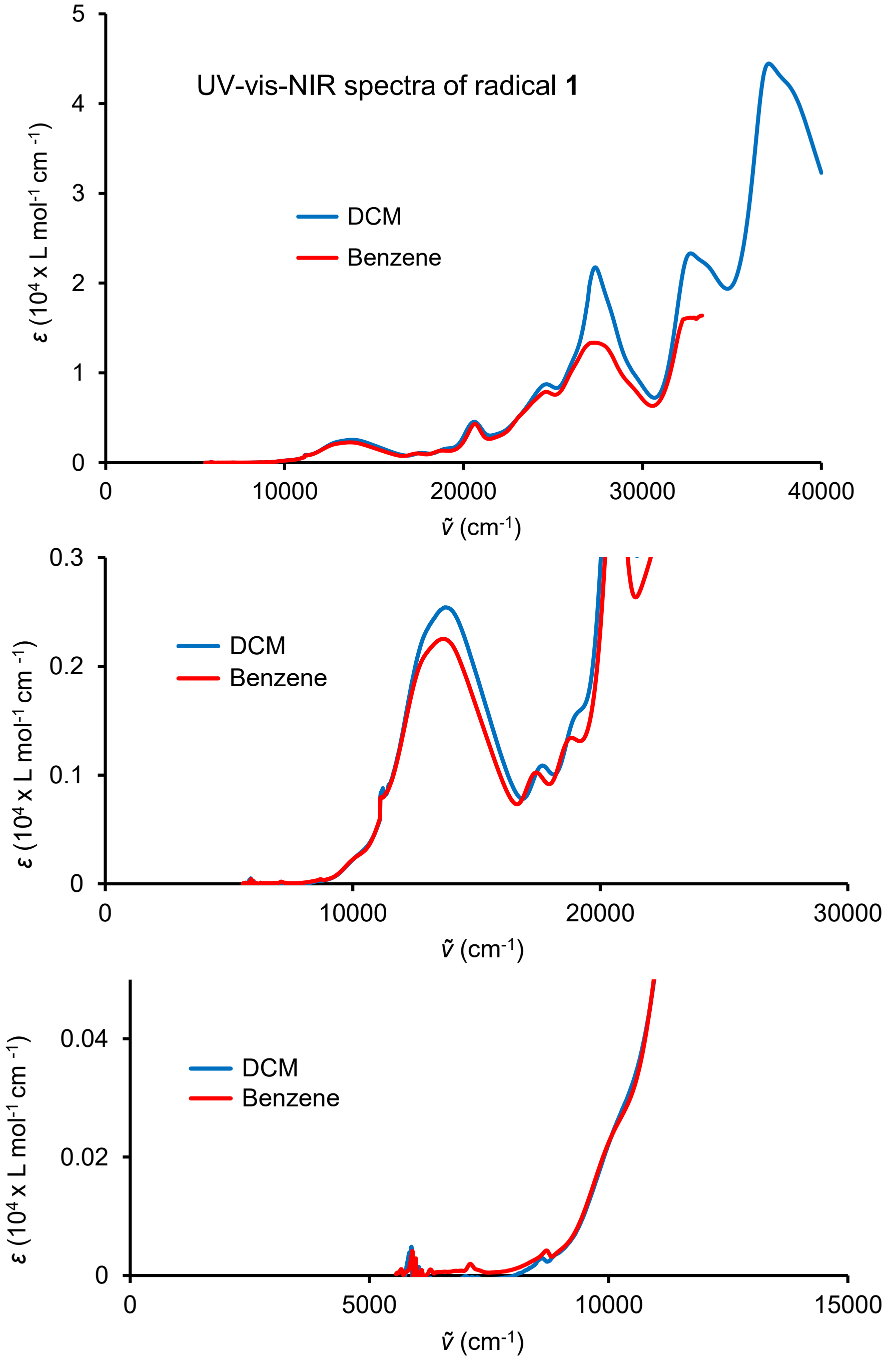

Fig. S8. UV-vis-NIR spectra of 0.27 mM radical **1** in benzene (label: ZY902) and 0.31 mM radical **1** in DCM (label: ZY903). The wavelength plots for these two samples are shown below.

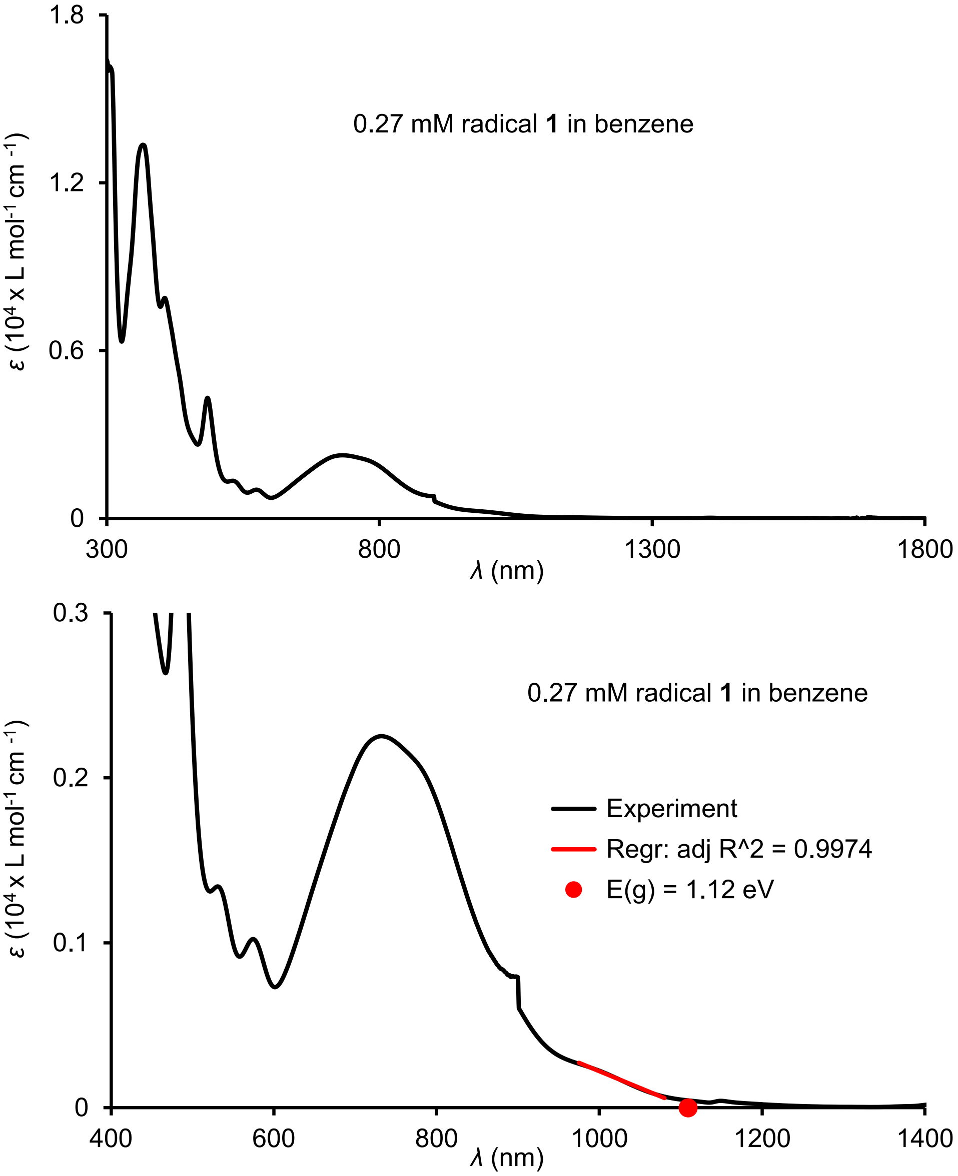

Fig S9. UV-vis-NIR spectra of 0.27 mM radical **1** (spin conc. = 94%, label: label ZY849fr1) in benzene (λ = 300–1800 nm range, label ZY902). UV-vis-NIR, λ_{max}/nm (ε_{max}/L mol^{-1} cm^{-1}): 366 (1.34×10^4), 406 (7.88×10^3), 485 (4.31×10^3), 732 (2.25×10^3). Band gap, E_g = 1.1180 eV (1109.0 nm), was determined using linear regression in the λ = 975–1080 nm range.

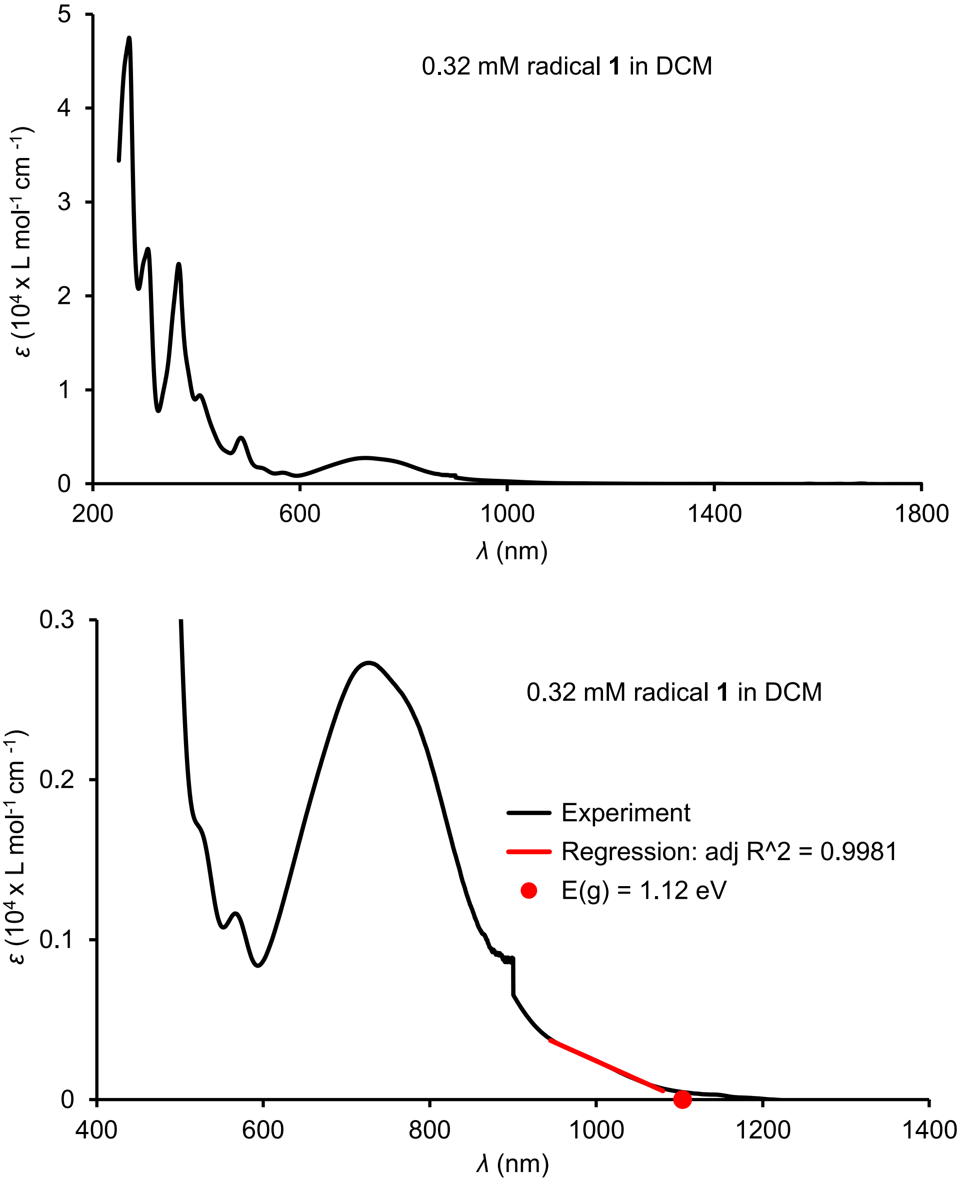

Fig S10. UV-vis-NIR spectra of 0.32 mM radical **1** (sample label: ZY849fr2, spin conc. 92%) in dichloromethane (λ = 250–1800 nm range, label ZY905). UV-vis-NIR, $\lambda_{\max}$/nm ($\varepsilon_{\max}$/L mol^{-1} cm^{-1}): 270 (4.75×10^4), 306 (2.50×10^4), 366 (2.34×10^4), 406 (9.40×10^3), 486 (4.89×10^3), 726 (2.73×10^3). Band gap, E_g = 1.1237 eV (1103.4 nm), was determined using linear regression in the λ = 950–1080 nm range.

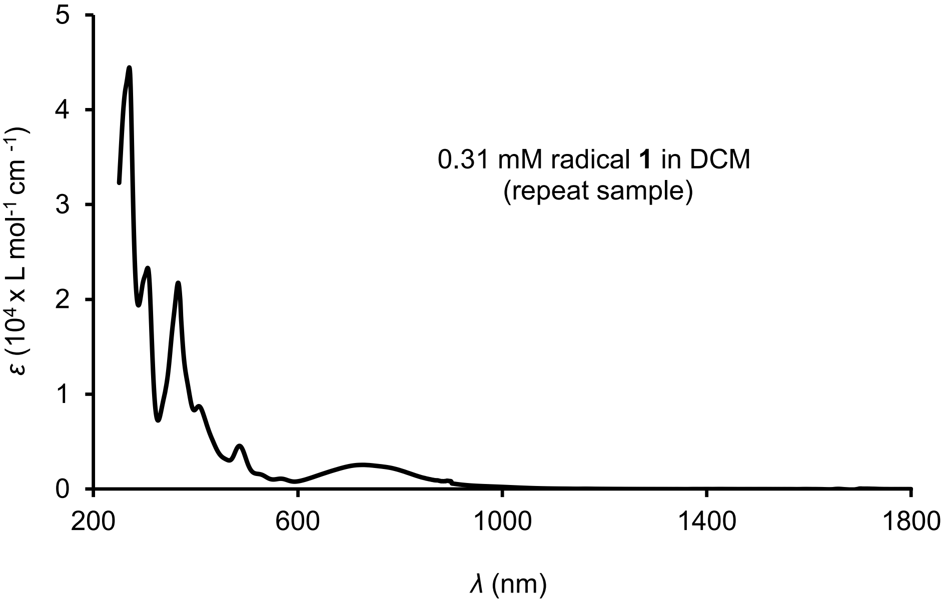

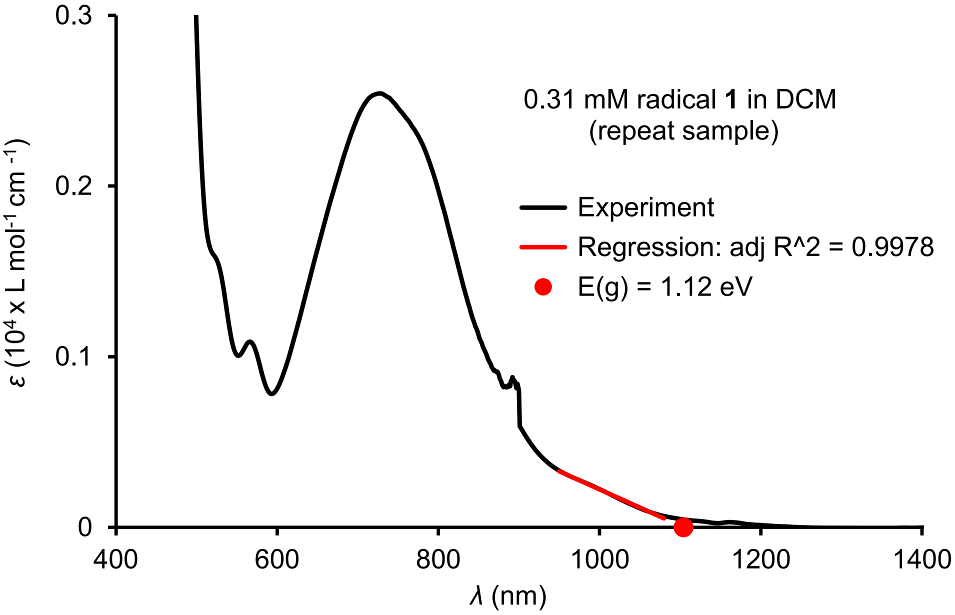

Fig S11. Repeat UV-vis-NIR spectra of 0.31 mM radical **1** (spin conc. = 92%, sample label: zy849fr2) in dichloromethane (λ = 250–1800 nm range, label ZY903). UV-vis-NIR, λ_{max}/nm (ε_{max}/L mol^{-1} cm^{-1}): 270 (4.45×10^4), 306 (2.33×10^4), 365 (2.17×10^4), 406 (8.73×10^3), 485 (4.55×10^3), 729 (2.54×10^3). Band gap, E_g = 1.1229 eV (1104.2 nm), was determined using linear regression in the λ = 950–1080 nm range.

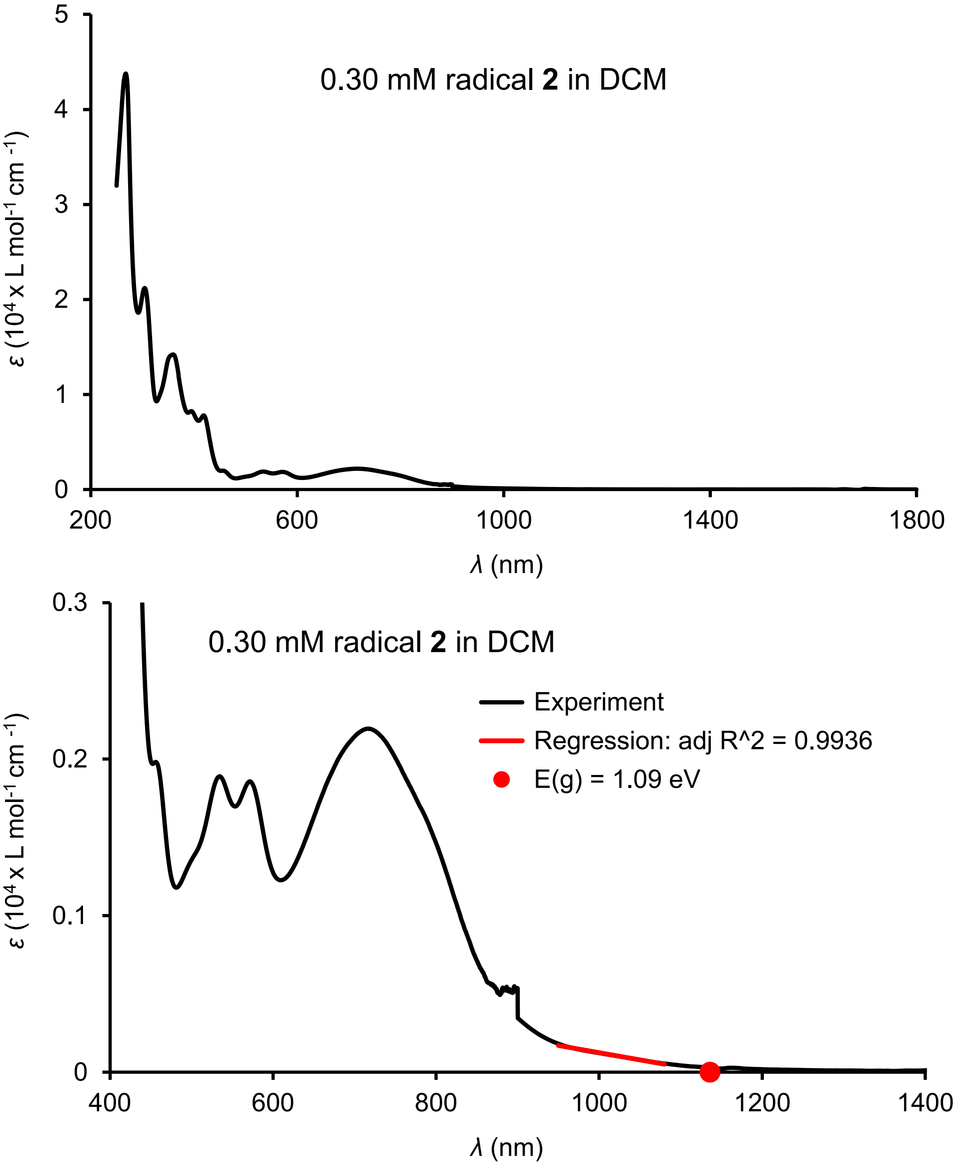

Fig S12. UV-vis-NIR spectra of 0.30 mM radical **2** (sample label: ZY972again, spin conc. = 97%) in dichloromethane (λ = 250–1800 nm range, label ZY1003). UV-vis-NIR, λ_{max}/nm ($\varepsilon_{\mathrm{max}}$/L mol^{-1} cm^{-1}): 268 (4.38×10^4), 304 (2.12×10^4), 359 (1.42×10^4), 395 (8.25×10^3), 419 (7.80×10^3), 535 (1.89×10^3), 572 (1.86×10^3), 717 (2.19×10^3). Band gap, E_g = 1.09 eV (1136.0 nm), was determined using linear regression in the λ = 950–1080 nm range.

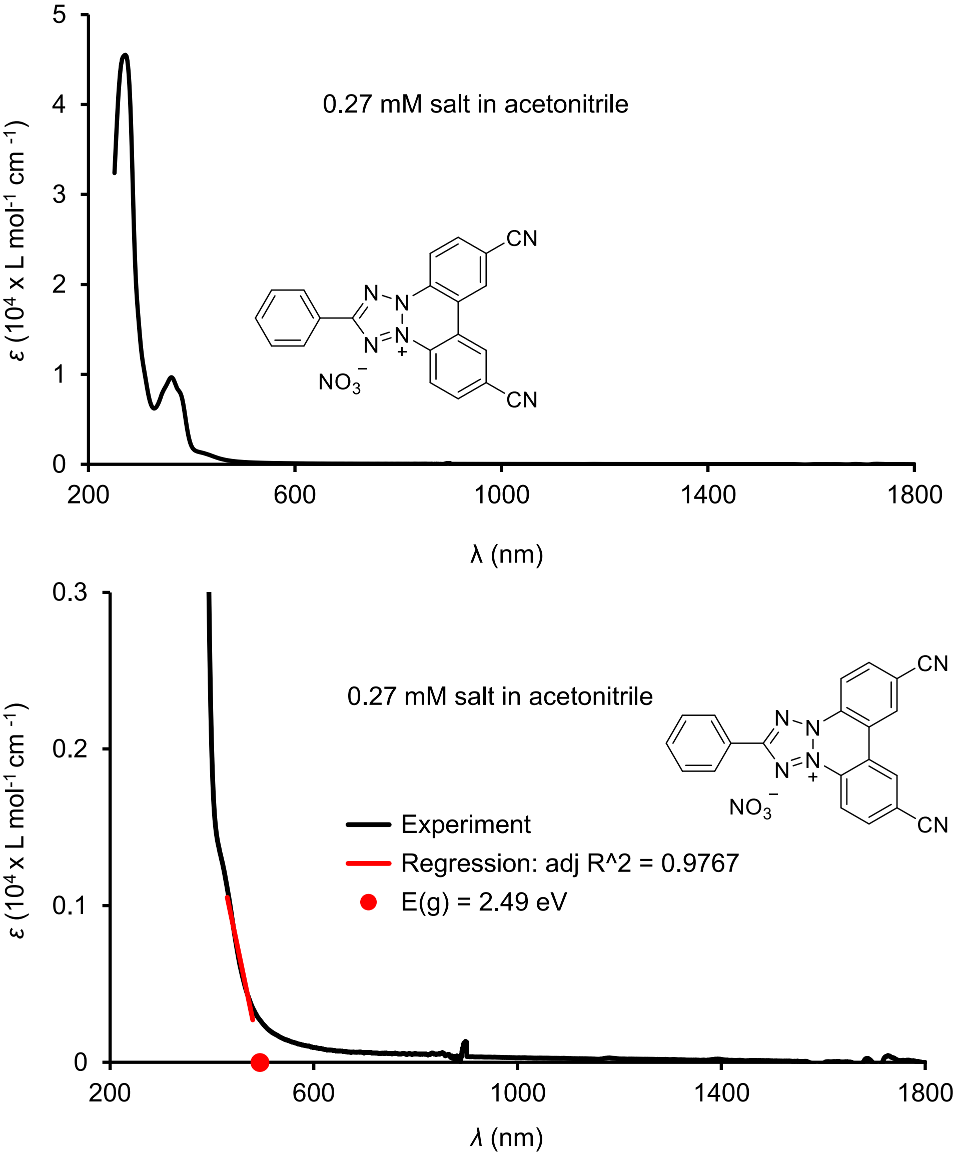

Fig S13. UV-vis-NIR spectra of 0.27 mM dicyano-substituted tetrazolium salt **6**-CN (precursor to radical **1**) in acetonitrile (λ = 250–1800 nm range, sample label ZY848). UV-vis-NIR, $\lambda_{\max}$/nm ($\varepsilon_{\max}$/L mol^{-1} cm^{-1}): 271 (4.54×10^4), 360 (9.61×10^3). Band gap, $E_g = 2.49$ eV (497.3 nm), was determined using linear regression in the $\lambda = 430$–480 nm range.

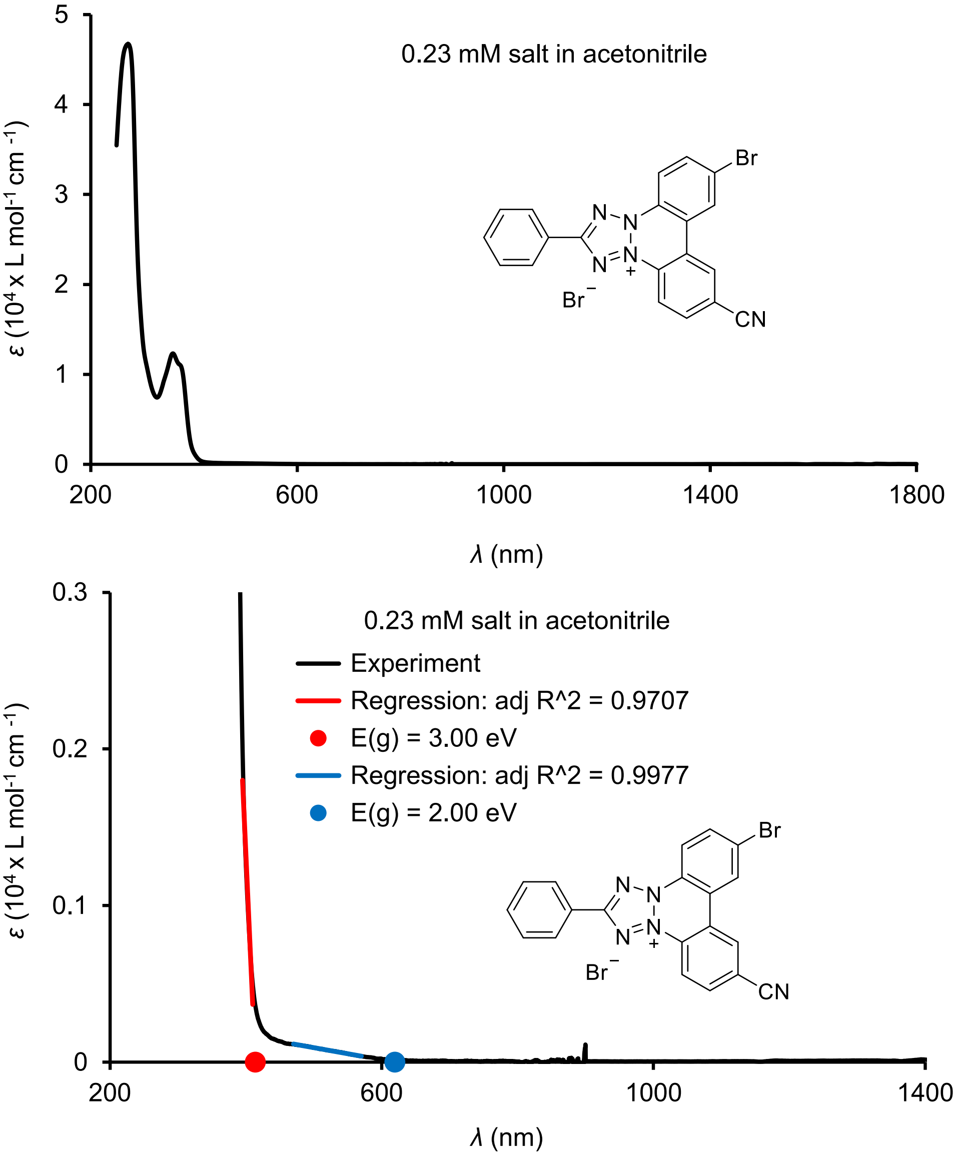

Fig S14. UV-vis-NIR spectra of 0.23 mM bromo-cyano-substituted tetrazolium salt **6**-Br (precursor to radical **2**) in acetonitrile (λ = 250–1800 nm range, sample label ZY974). UV-vis-NIR, λ_{max}/nm ($\varepsilon_{\mathrm{max}}$/L mol^{-1} cm^{-1}): 272 (4.67 × 10^4), 359 (1.23×10^4). Band gaps, E_g = 3.00 eV (413.9 nm) and E_g = 2.00 eV (619.5 nm), were determined using linear regressions in the λ = 395–410 and 470–570 nm ranges, respectively.

1.h. Voltammetry. Cyclic, differential pulse, and square wave voltammetry data for radicals **1** and **2** were obtained at room temperature in a glovebag under argon gas atmosphere. (The supply gas was a commercial ultra-high purity argon, certified to contain <1 ppm of O_2 and <1 ppm of H_2O.) The custom-made electrochemical cell with electrodes, all solid reagents, syringes, needles, etc. were extensively evacuated in Schlenk vessels (typical pressure 1 mTorr, temperature 20–70 °C), prior to the transfer to the glovebag. Dichloromethane (DCM) was obtained from commercial solvent purification system, then distilled from calcium hydride under nitrogen, and stored in the absence of light in a Schlenk vessel on a vacuum line; just prior to the use, the solvent was vacuum transferred as needed. Commercial potentiostat/galvanostat was used. Three electrodes were employed: quasi-reference (Ag-wire), counter (Pt-foil), and working (100-μm Pt-disk). Radical **1** (1.20 mg, spin conc. 94%, sample label: ZY904) and radical **2** (1.00 mg, spin conc 93%, sample label: ZY876) were used as electroactive solutes. Concentration of the tetrabutylammonium hexafluorophosphate supporting electrolyte ($[n\text{-}Bu_4N]^+[PF_6]^-$) was about 100 mM. The solution volume was about 2.2 – 2.8 mL. After a series of cyclic differential pulse and square wave voltammograms with potential increments of 2 – 4 mV, a small amount (ca. 8 – 15 drops) of solution of ferrocene (2.15 – 2.18 mg of Cp_2Fe, loaded to a Schlenk vessel in a glovebox under an argon atmosphere in the supporting electrolyte, ca. 0.6 – 0.8 mL) was added to the cell, to provide reference potentials (0.46 V vs. SCE for the Cp_2Fe/Cp_2Fe^+ couple in DCM).[S12] Cyclic voltammograms with the scanning rates in the 50–1000 mV/s range and square wave voltammograms with frequencies in the 2 – 10 Hz range (pulse height 25 mV) were obtained.

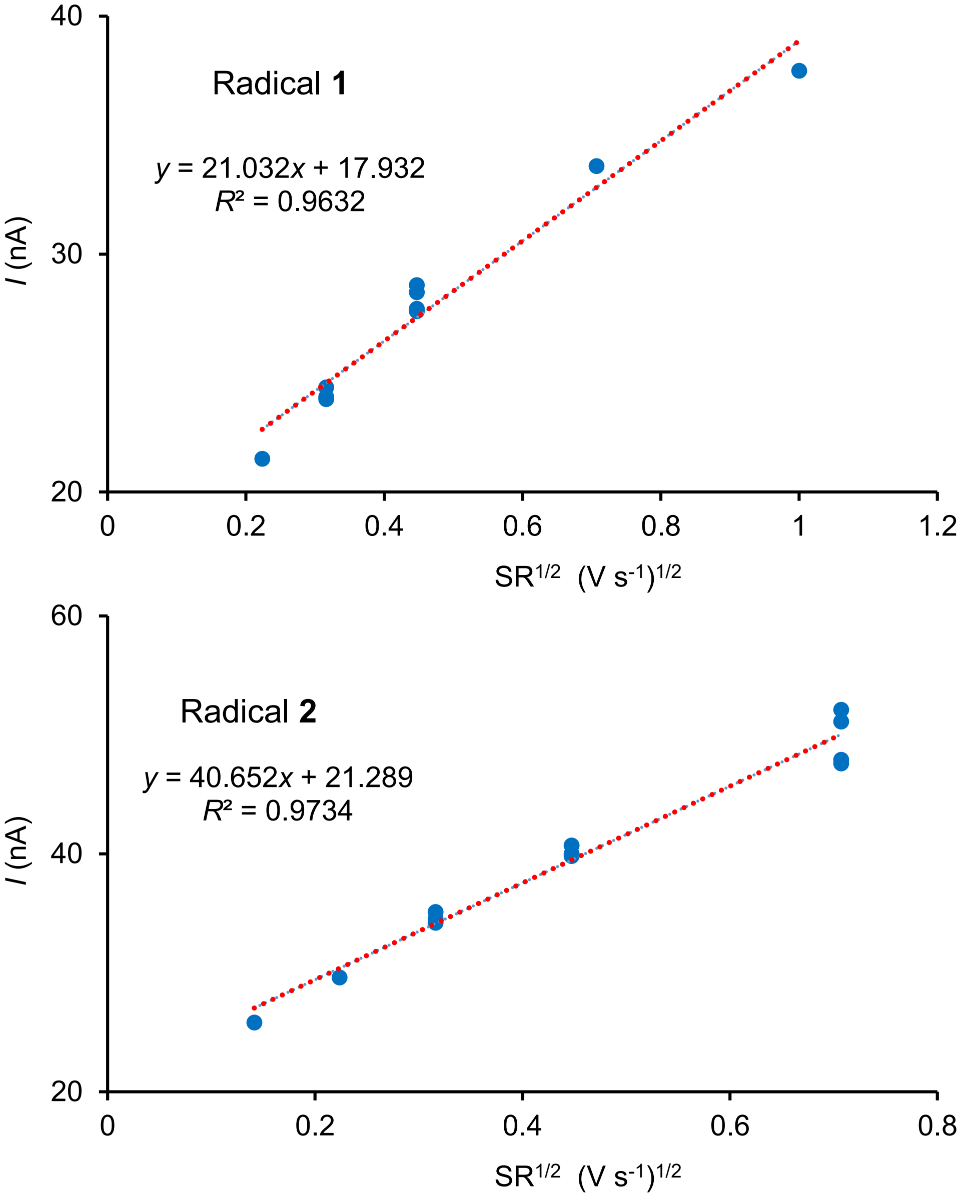

Fig. S15. Cyclic voltammetry (CV) of radicals **1** and **2** in 0.1 M tetrabutylammonium hexafluorophosphate in dichloromethane at room temperature. Plots of peak current (*I*) for the oxidation wave vs square root of scan rate (SR).

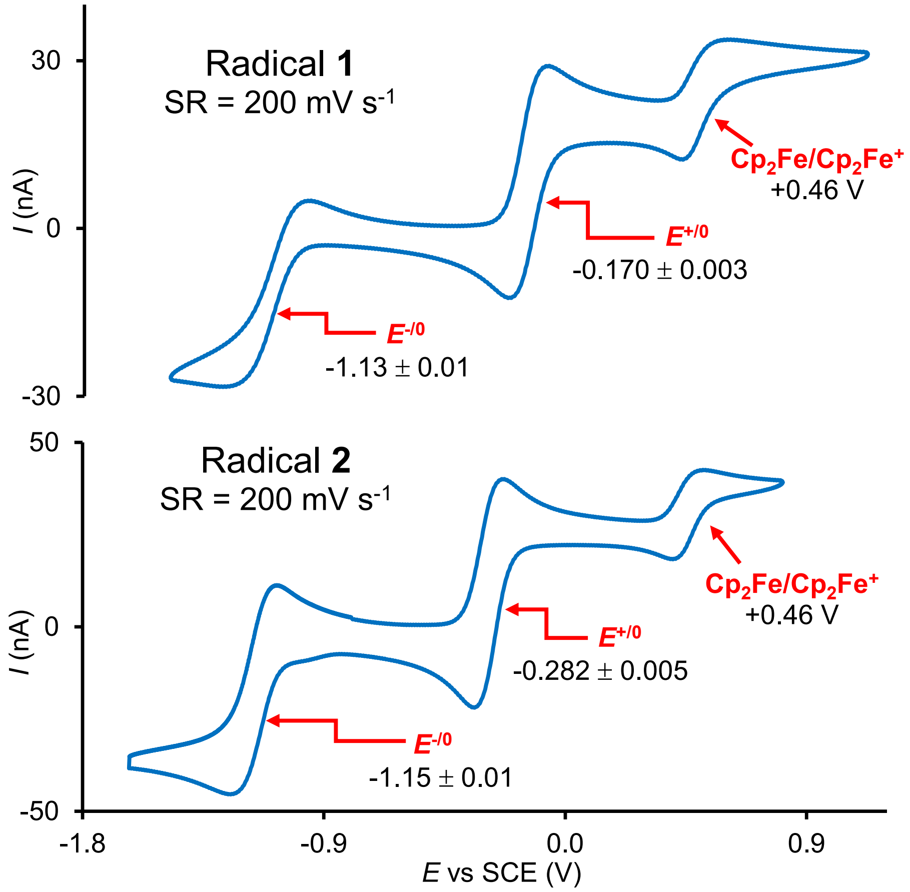

Fig. S16. Cyclic voltammetry (CV) of radicals **1** and **2** in 0.1 M tetrabutylammonium hexafluorophosphate in dichloromethane at room temperature. Redox potentials are given as mean ± stddev with $n = 6–7$ (**1**) and 10 (**2**). Scans were started and ended at ca. –0.6 – (–0.8) V. CV labels: ZY947ccv12 (**1**) and ZY971ccv4 (**2**).

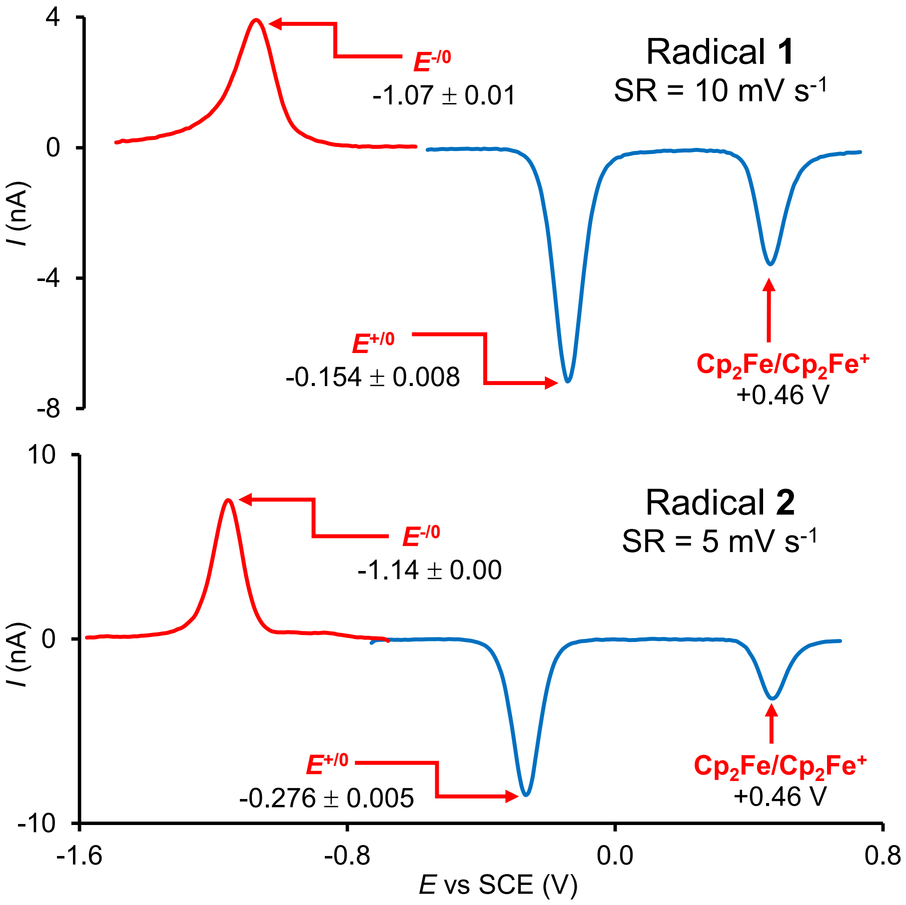

Fig. S17. Differential pulse voltammetry (DPV) of radicals **1** and **2** in 0.1 M tetrabutylammonium hexafluorophosphate in dichloromethane at room temperature. Redox potentials are given as mean ± stddev with $n = 3–7$ (**1**) and 4–5 (**2**). Oxidation scans (blue lines) and reduction scans (red lines) started at ca. –0.6 – (–0.7) V. DPV labels: ZY947dppv9 (**1**), ZY947dppv11 (**1**), ZY971dppv1 (**2**), and ZY971ddpv2 (**2**).

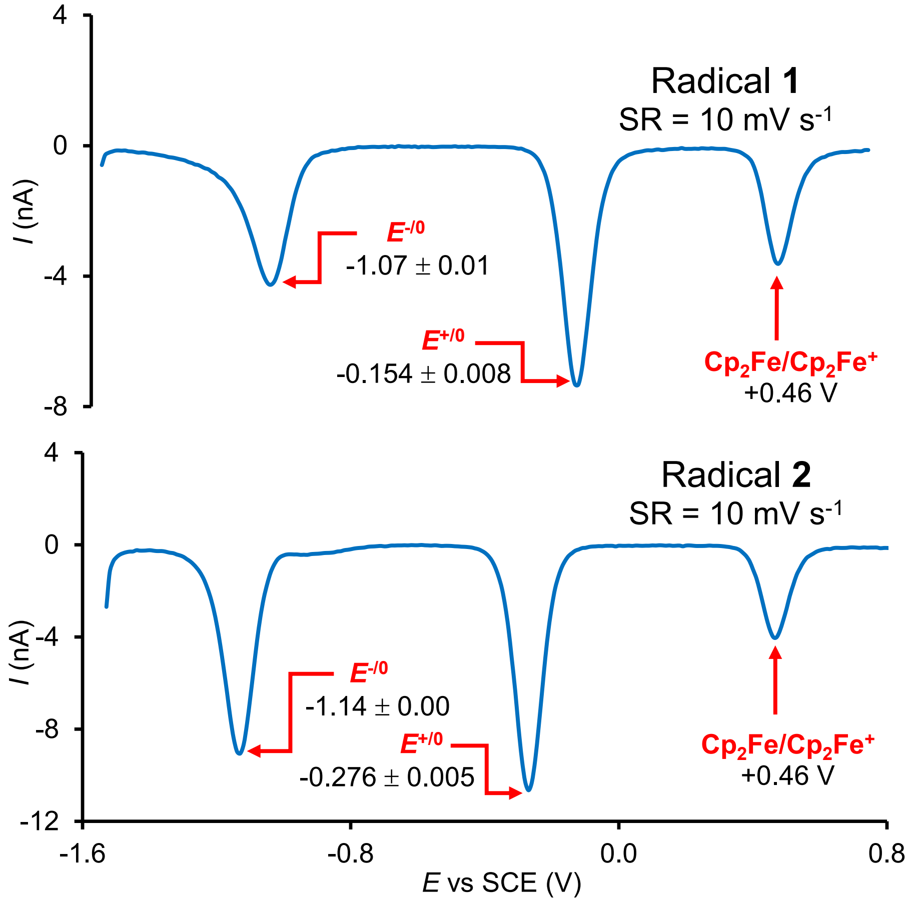

Fig. S18. Differential pulse voltammetry (DPV) of radicals **1** and **2** in 0.1 M tetrabutylammonium hexafluorophosphate in dichloromethane at room temperature. Redox potentials are given as mean ± stddev with $n = 3$–7 (**1**) and 4–5 (**2**). Oxidation scans (blue lines) started at ca. –1.5 – (–1.6) V. DPV labels: ZY947dppv8 (**1**) and ZY971ddpv6 (**2**).

1.i Pulse and CW EPR spectroscopy. Pulse X-band EPR experiments (at University of Washington) on radical **1** in toluene glass were carried out as described in the main text (Experimental Section). Below, we provide summary electron spin relaxation rates (Table S5), as well as the measured inversion recovery traces and Hahn echo decays (Figs. S22 and S23).

CW X-band EPR spectra for radicals were acquired on Bruker EMX-plus instrument at Nebraska, equipped with a frequency counter and nitrogen flow temperature control (100–400 K). The spectra were obtained using a single mode high sensitivity Bruker cavity, with an oscillating magnetic field perpendicular (TE_{102}) to the swept magnetic field. Temperatures were verified using an independently calibrated thin wire thermocouple inserted into the EPR sample tube (containing the solvent) and positioned in the cavity at the same place as in the variable temperature studies. The samples were typically contained in 4-mm EPR sample tubes, equipped with high-vacuum stopcocks (Kontes). DPPH powder ($g = 2.0037$) was used as a g-value reference for selected spectra.[S13] Spin concentrations were determined using ca. 1 mM 4-oxy-TEMPO (TEMPONE) in benzene with the radicals **1** or **2** in the same solvent.

Typical parameters for high-resolution CW EPR spectra of **1** and **2** in degassed benzene at room temperature were: MW power attenuation = 30 or 20 dB, modulation amplitude = 0.01 – 0.04 mT, conversion time = 5.0 ms, time constant = 0.32 ms, number of points = 2,500 – 10,000. Selected EPR spectra of **1** and **2** were numerically simulated in the fast-motion limit using EasySpin 5.2.33 software (*garlic* function).[S14] Simulations were started with a guess based on the DFT computations (Table S4); after initial optimization using default simplex algorithm, global optimizations using genetic algorithm (10k generations) provided good inputs for final simplex optimizations. Although the spectra contained a considerable number of lines, it was found that the best fits were obtained with target = fcn (i.e., the derivative spectrum as is) and quadratic baseline correction (lsq2).

EPR spectra of assemblies of **1** on SiO_2/Si(111) wafers were simulated in the rigid limit using EasySpin 5.2.33 (*pepper* function) by employing two components (for more details, see: Section 3).[S14]

Table S5. The fitted values of $1/T_1$, $1/T_\mathrm{m}$, ξ and their 95% confidence intervals bounds.

Temperature (K)	$1/T_1$ (ms^{-1})			$1/T_\mathrm{m}$ (μs^{-1})			ξ		
	low	fit	up	low	fit	up	low	fit	up
19	0.027	0.031	0.04	0.19	0.21	0.23	1.5	1.7	1.8
30	0.094	0.11	0.13	0.16	0.17	0.18	1.7	1.9	2.1
40	0.15	0.17	0.20	0.14	0.15	0.15	1.8	2.1	2.3
50	0.20	0.24	0.28	0.14	0.14	0.15	1.9	2.2	2.4
60	0.25	0.31	0.40	0.13	0.14	0.14	1.8	2.0	2.2
70	0.34	0.40	0.47	0.13	0.14	0.14	1.8	2.0	2.2
80	0.43	0.52	0.62	0.14	0.15	0.16	1.7	2.0	2.3
90	0.55	0.66	0.78	0.16	0.18	0.19	1.4	1.6	1.8
100	0.75	0.93	1.2	0.22	0.24	0.28	1.3	1.5	1.8
110	0.74	0.97	1.3	0.26	0.30	0.36	1.1	1.4	1.7
120	0.73	1.1	1.5	0.48	0.64	0.87	0.95	1.4	1.8
130	1.3	1.6	2.0	0.93	4.9	26	0.30	0.46	0.62
140	1.2	1.5	1.9	1.7	18	20e2	0.23	0.36	0.49
150	1.3	1.5	1.8	1.5	14	13e2	0.25	0.40	0.55
160	1.7	2.3	3.1	0.73	3.0	13	0.36	0.65	0.95

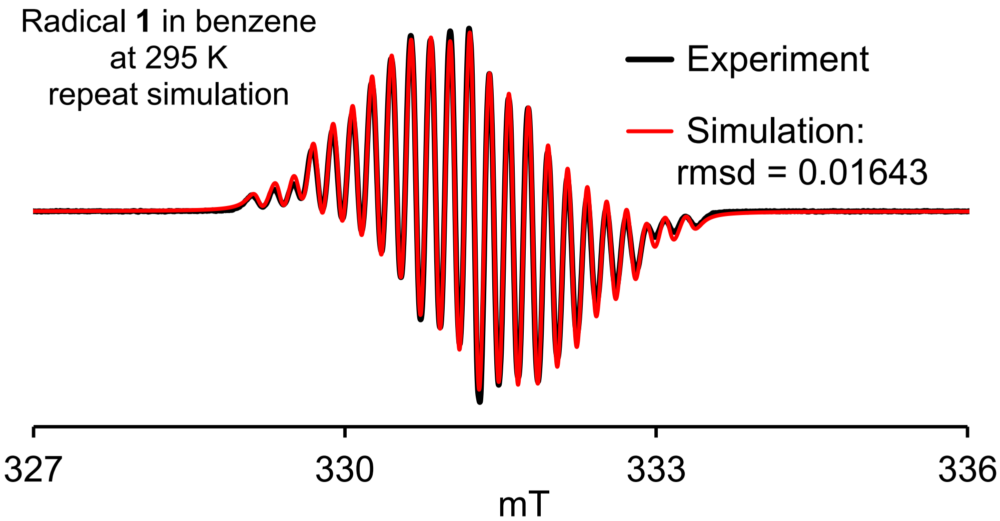

Fig. S19A. Re-simulated EPR (9.2918 GHz, modulation amplitude = 0.02 mT, label: ZY935R3, sample label: ZY904, spin conc. 94%) spectrum for 0.29 mM dicyano-substituted radical **1** in degassed benzene (same experimental data as in Figure 4, main text). Simulation (EasySpin, *garlic*): g = 2.0042, $A(^{14}\mathrm{N})$ = 15.79 MHz (n = 2), $A(^{14}\mathrm{N})$ = 10.51 MHz (n = 2), $A(^{1}\mathrm{H})$ = 5.74 MHz (n = 2), peak-to-peak linewidths, Gaussian = 0.000433 mT and Lorentzian = 0.1179 mT (all nuclei are at natural abundance); g-value is uncorrected.

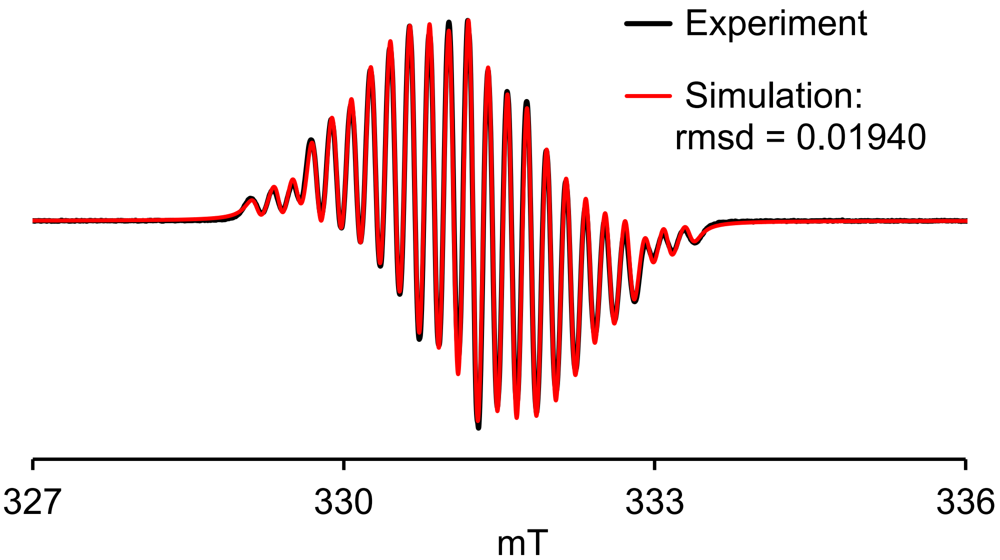

Fig. S19B. Repeat EPR (9.2918 GHz, modulation amplitude = 0.01 mT, label: ZY935R4, sample label: ZY904, spin conc. 94%) spectrum for 0.29 mM dicyano-substituted radical **1** in degassed benzene. Simulation (EasySpin, *garlic*): g = 2.0042, $A(^{14}\mathrm{N})$ = 15.75 MHz (n = 2), $A(^{14}\mathrm{N})$ = 10.55 MHz (n = 2), $A(^{1}\mathrm{H})$ = 5.85 MHz (n = 2), peak-to-peak linewidths, Gaussian = 0.000553 mT and Lorentzian = 0.11945 mT (all nuclei are at natural abundance); g-value is uncorrected.

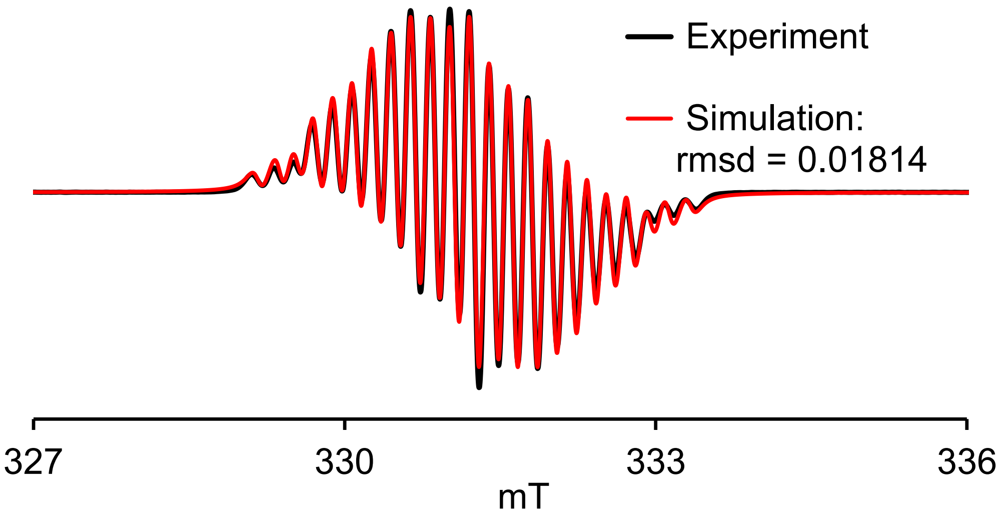

Fig. S19C. Second repeat EPR (9.2918 GHz, modulation amplitude = 0.05 mT, label: ZY935R2, sample label: ZY904, spin conc. 94%) spectrum for 0.29 mM dicyano-substituted radical **1** in degassed benzene. Simulation (EasySpin, *garlic*): g = 2.0042, $A(^{14}N)$ = 15.81 MHz (n = 2), $A(^{14}N)$ = 10.50 MHz (n = 2), $A(^{1}H)$ = 5.83 MHz (n = 2), peak-to-peak linewidths, Gaussian = 0.000669 mT and Lorentzian = 0.12167 mT (all nuclei are at natural abundance); g-value is uncorrected.

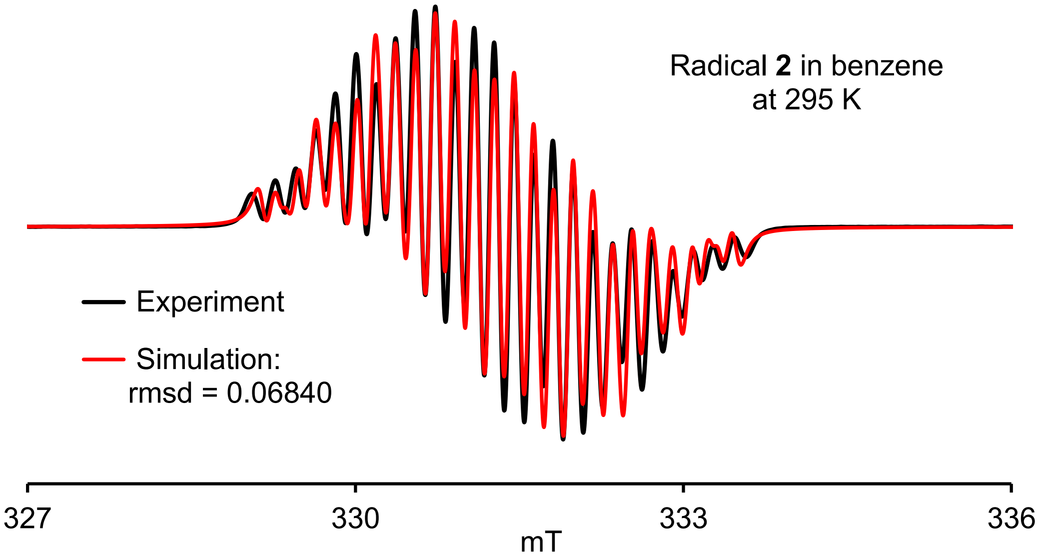

Fig. S20. EPR (9.2956 GHz, modulation amplitude = 0.04 mT, label: ZY973R7, sample label: ZY973crp1, spin conc. 97%) spectrum for ~0.2-mM bromo-cyano-substituted radical **2** in degassed benzene. Initial simulation (EasySpin, *garlic*): g = 2.0046, hyperfine couplings in MHz, each for n = 1, $A(^{14}N)$ = 15.58, 15.25, 14.59, 10.05, $A(^{1}H)$ = 6.51, 3.98, peak-to-peak linewidths, Gaussian = 0.000992 mT and Lorentzian = 0.099283 mT (all nuclei are at natural abundance); g-value is uncorrected.

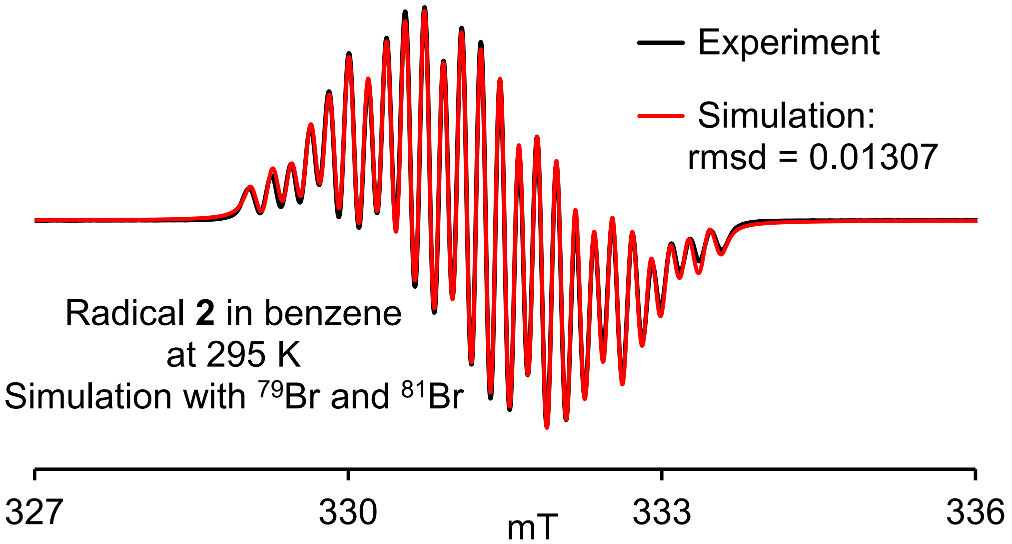

Fig. S21. EPR (9.2956 GHz, modulation amplitude = 0.04 mT, label: ZY973R7, sample label: ZY973crp1, spin conc. 97%) spectrum for ~0.2-mM bromo-cyano-substituted radical **2** in degassed benzene. 2nd repeat simulation including Br nuclei at natural abundance (additional genetic with 10,000 generations plus simplex simulations) (EasySpin, *garlic*): $g = 2.0046$, $A(^{14}\mathrm{N}) = 20.01$ MHz ($n = 1$), $A(^{14}\mathrm{N}) = 10.34$ MHz ($n = 2$), $A(^{14}\mathrm{N}) = 14.90$ MHz ($n = 1$), $A(^{1}\mathrm{H}) = 6.26$ MHz ($n = 1$), $A(^{1}\mathrm{H}) = 5.39$ MHz ($n = 1$), $A(^{79}\mathrm{Br}) = 0.776$ MHz plus $A(^{81}\mathrm{Br})$; lwpp, Gaussian = 0.00114 mT and Lorentzian = 0.09567 mT; *g*-value is uncorrected.

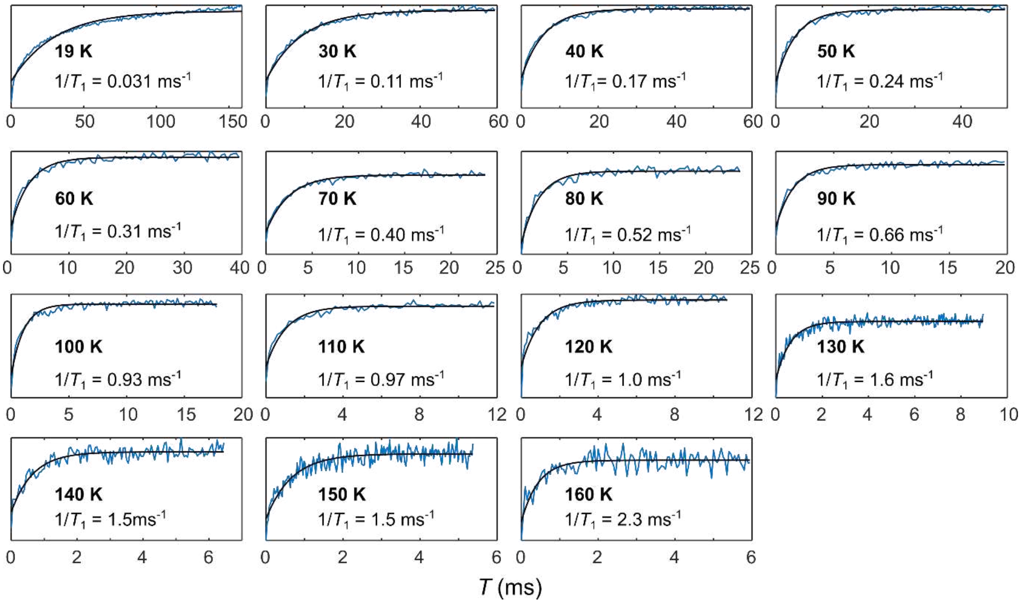

Fig. S22. Inversion recovery measurements of **1** (sample label: ZY1036, spin conc. ~100%). The phase-corrected data (blue) were fitted (black) with a three-parameter model, $V(T) = a - b\exp(-T/T_1)$, with fitting parameters a, b and $\log_{10} T_1$. For uncertainties, see: Table S5.

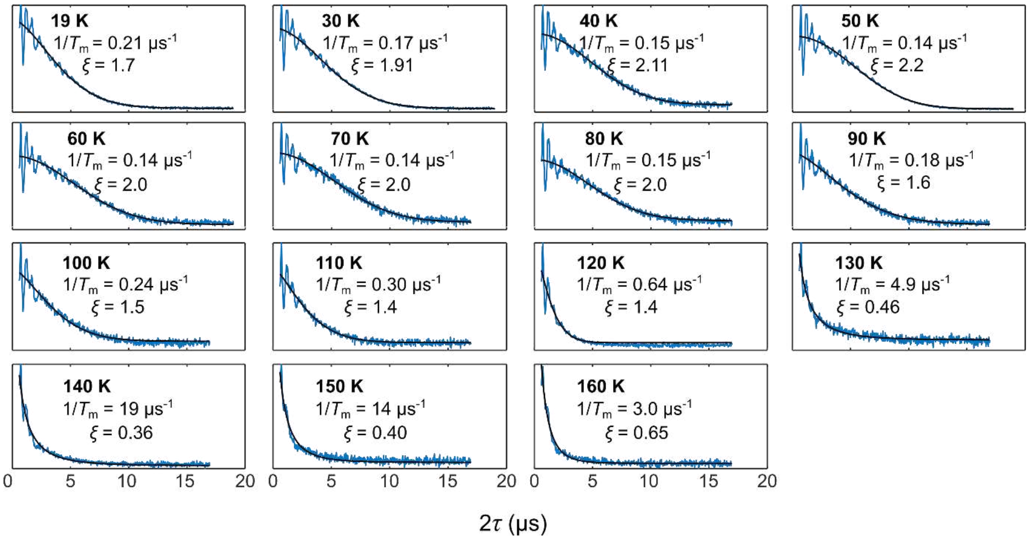

Fig. S23. Hahn echo measurements of **1** (sample label: ZY1036, spin conc. ~100%). The phase-corrected data (blue) were fitted (black) with a three-parameter model, $V(2\tau) = V(0)\exp(-(2\tau/T_\mathrm{m})^{\xi})$, with fitting parameters $V(0)$, ξ and $\log_{10} T_\mathrm{m}$. For uncertainties, see: Table S5.

1.j SQUID magnetometry of diradicals 1 and 2. Magnetic studies were carried out using 5-Tesla Quantum Design SQUID magnetometer at the applied magnetic fields H = 30000 and 5000 Oe at T = 1.80 – 320 K. The polycrystalline **1** and **2** were loaded to capsules and mounted in the colorless plastic straws. Primary correction for diamagnetism was implemented by point-by-point background subtraction, together with Pascal constants correction, as described in detail in the following paragraphs.

Selected models for numerical fitting of magnetic data for radical 1.

One-dimensional antiferromagnetic *S* = ½ chain model.[S15] This model is employing Heisenberg Hamiltonian model without the usual factor of 2. It is used to fit χ *vs* T or χT *vs* T data, in order to obtain the intra-chain antiferromagnetic exchange coupling constant, J'/k, in Kelvin. For all fits, mean-field correction parameter, $\theta = 0$.

$$\chi T = \{1.506 * N * [T/(T - \theta)] * [\mathrm{Num}/\mathrm{Den}]\} + \mathrm{Monorad} \qquad \text{(S1)}$$

$$\mathrm{Num} = 0.25 + (0.074975 * x) + (0.075235 * x^2)$$

$$\mathrm{Den} = 1 + (0.9931 * x) + (0.172135 * x^2) + (0.757825 * x^3)$$

$$x = -J'/T$$

$$\mathrm{Monorad} = \{T * 1.118 * N_\mathrm{imp} * \{\sinh(a)/[2 + 2\cosh(a)]\}\}/H$$

$$a = 1.345(H/(T - \theta))$$

***S* = ½ dimer model.**[S16] This model is employing Heisenberg Hamiltonian model with the usual factor of 2. It is used to fit χ *vs* T or χT *vs* T data, in order to obtain the singlet-triplet energy gap ($2J'/k$ in Kelvin) in the dimer or in other words, intra-dimer exchange (most likely antiferromagnetic) coupling constant, J'/k, in Kelvin. Diamagnetic impurities and inaccuracies in the mass balance are accounted for by the mass factor, N; free S = ½ radicals, i.e., crystal defects, are accounted with parameter N_imp. There is also a possibility of adding mean-field parameter θ, to account for relatively weak inter-molecular interactions (compared to intra-dimer J'/k) between radical molecules – however, this was not necessary for **1**, i.e., θ was set to 0. These models (Eq. S2 plus Monorad term from eq. S1) account for paramagnetic saturation.

$$\chi T = \{T * 1.118 * N * \{2\sinh(a)/[1 + 2\cosh(a) + \exp((-2J'/k)/T)]\}\}/H \qquad \text{(S2)}$$

$$a = 1.345(H/(T - \theta))$$

Details of numerical fitting of SQUID magnetic data. SigmaPlot for Windows software package is used for numerical curve fitting of the magnetic data. Standard error (*SE*) for each variable parameter is provided. The reliability of a fit is measured by the parameter dependence (*DEP*), which is defined for each variable parameter as follows: *DEP = 1 – ((variance of the parameter, other parameters constant)/(variance of the parameter, other parameters changing))*. Values close to 1 indicate an overparametrized fit.

The quality of fits may be measured by a coefficient of determination (R^2), which is defined for nonlinear numerical fits of the magnetic data as follows (Eq. S4):

$$R^2 = 1 - [(\Sigma(y_i - Y_i)^2)/(\Sigma(y_i - \langle y \rangle)^2)] \qquad \text{(S4)}$$

where y_i, Y_i , and $\langle y \rangle$ denote experimental values, fitted values, and the arithmetic mean of the experimental values. We list in Table S6 values of R^2 that are statistically adjusted, i.e., adj R^2; values close to 1 indicate a fit of high quality.

The quality of fits is more reliably measured by standard error of estimate (*SEE*), which is defined as follows (Eq. S5):

$$SEE = [\mathrm{SSE}/(n - 2)]^{1/2} \qquad \text{(S5)}$$

where, SSE is the sum of squared errors and *n* is the number of points. The perfect fit would imply *SEE* = 0.0000.

SQUID magnetometry of radicals 1 and 2 as polycrystalline powders. For radicals **1** and **2**, initial SQUID run involved samples of 19.32 mg (SQUID label: ZY902, sample label: ZY849, spin conc. = 94%) and 27.28 mg (SQUID label: ZY984, sample label: ZY973, spin conc. = 97%), respectively. For the background SQUID runs, a portion of the sample was removed from the holder, to leave 7.525 and 14.16 mg samples of **1** and **2**, respectively. (Also, for another sample of radical **2** (sample label: ZY973, after additional recrystallization), another set of SQUID runs (SQUID label: ZY999) was carried out to verify the absence of the maximum in the plot of χ vs T in the T = 1.8 – 300 K.) Following these runs, magnetization for the background, M_{bck}, was point-by-point subtracted from magnetization for the sample, M_{sample}, to provide corrected magnetization, M_{cr}, accounting for diamagnetism of sample holder. Thus, M_{cr} corresponded to mass of 11.795 and 13.12 mg for **1** and **2**, respectively.

Subsequently, the M_{cr} were converted to corresponding molar magnetic susceptibilities for **1** and **2**:

$$\chi_{\mathrm{cor}} = M_{\mathrm{cor}}/(H{*}n_{\mathrm{molsample}}),$$

where, H is the applied magnetic field in Oe and $n_{\mathrm{molsample}}$ is the number of moles of the radical sample.

Final molar magnetic susceptibility, χ, was obtained by subtraction of Pascal constant-derived correction P:[S17]

$$\chi = \chi_{\mathrm{cor}} - P$$

where, $P = -182.3 \times 10^{-6}$ emu/mol and $P = -202.2 \times 10^{-6}$ emu/mol for **1** and **2**, respectively.

In polycrystalline **1**, much stronger intermolecular antiferromagnetic interactions were found, compared to polycrystalline **2** (e.g., Fig. S26). For **1**, the χ *vs* T and χT *vs* T data, which were corrected for diamagnetism using point-by-point approach and Pascal constants, were fit in the T = 1.8 – 320 K range with two 3-parameter models (Eqs. S1 and S2). In the three-parameter models, three variable parameters were: J'/k – intra-chain or intra-dimer antiferromagnetic exchange coupling constant (in Kelvin), N – the weight factor (N = 1.00 for perfectly pure antiferromagnetically coupled S = 1/2 radicals), and N_{imp} – the mass factor for a “free” S = 1/2 radicals – i.e., crystal defects. The results of the fits for radical **1** are summarized in Table S6. One-dimensional intra-chain antiferromagnetic coupling constant J'/k, obtained from the fits to the χ *vs* T data at various magnetic fields and temperature changing modes (Table S6), was $J'/k = -21.85 \pm 0.70$ K (mean ± SE, n = 3).

Table S6. Complete set of fitting parameters for χT vs T and χ vs T data of polycrystalline radical **1** in the $T = 1.8 – 320$ K range.

Fit	χ or χT	H [Oe]	J'/k (SE, DEP)[a] [K]	N (SE, DEP)[b] [K]	N_{imp} (SE, DEP)[c]	SEE[d]	adj R^2[e]
1-D	χ	30000 (cool)	–21.09 (0.16, 0.8758)	1.017 (0.006, 0.7994)	0.040 (0.0005, 0.6988)	0.0002	0.9988
		30000 (warm)	–21.21 (0.13, 0.8793)	1.020 (0.005, 0.8132)	0.040 (0.0004, 0.6873)	0.0001	0.9990
		5000 (cool)	–23.24 (0.30, 0.8955)	1.058 (0.012, 0.8630)	0.057 (0.0005, 0.6277)	0.0003	0.9977
	χT	30000 (cool)	–17.46 (0.34, 0.7021)	0.973 (0.006, 0.8890)	0.020 (0.0062, 0.9313)	0.0065	0.9972
		30000 (warm)	–17.53 (0.31, 0.6922)	0.970 (0.005, 0.8642)	0.021 (0.0053, 0.9175)	0.0066	0.9974
		5000 (cool)	–19.24 (0.26, 0.6265)	0.987 (0.004, 0.6817)	0.043 (0.0031, 0.8045)	0.0057	0.9984
Dimer	χ	30000 (cool)	–11.26 (0.20, 0.5125)	0.778 (0.015, 0.4582)	0.101 (0.0012, 0.1513)	0.0007	0.9792
		30000 (warm)	–11.04 (0.18, 0.5095)	0.773 (0.015, 0.4698)	0.097 (0.0010, 0.1180)	0.0007	0.9769
	χT	30000 (cool)	–13.41 (0.12, 0.4674)	0.843 (0.003, 0.8323)	0.117 (0.0028, 0.8712)	0.0039	0.9990
		30000 (warm)	–13.27 (0.11, 0.4657)	0.845 (0.003, 0.8052)	0.113 (0.0025, 0.8520)	0.0041	0.9990

[a] *J'/k*, Heisenberg exchange coupling constant; *SE*, standard error; *DEP*, parameter dependence. [b] *N*, weight factor for exchange-coupled $S = 1/2$ radical. [c] N_{imp}, weight factor for isolated $S = 1/2$ radical. [d] *SEE*, standard error of estimate. [e] adj R^2, statistically adjusted coefficient of determination.

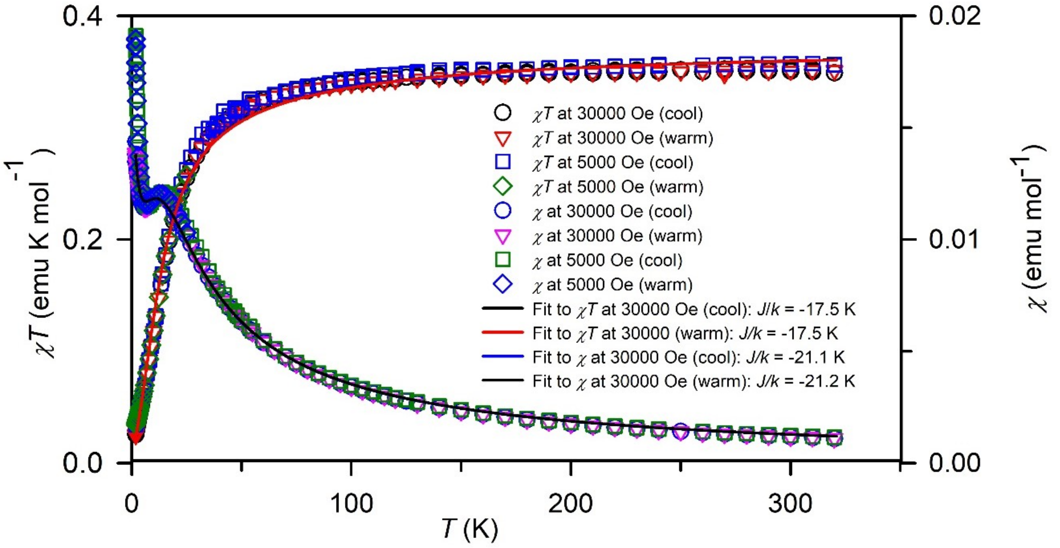

Fig. S24. SQUID magnetometry (label: ZY902) of polycrystalline radical **1** (sample label: label: ZY849fr1): experimental data plotted as χT vs T and χT vs T and the selected numerical fits to one-dimensional $S = ½$ antiferromagnetic Heisenberg chain (Eqs. S1A and S1B). Fitting parameters and relevant statistical parameters are summarized in Table S6.

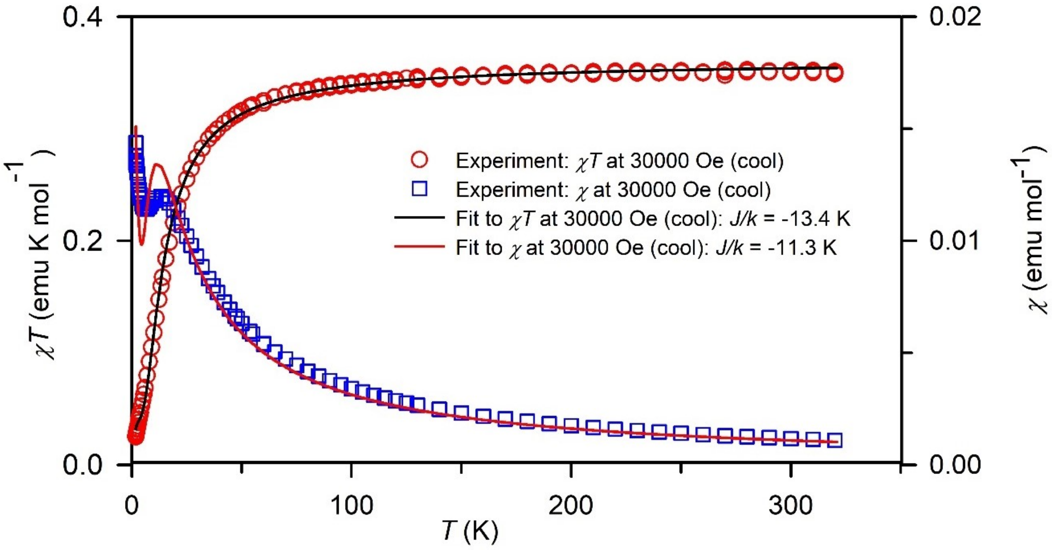

Fig. S25. SQUID magnetometry (label: ZY902) of polycrystalline radical **1** (sample label: label: ZY849fr1): selected experimental data plotted as χT vs T and χT vs T and the numerical fits to S = ½ dimer Heisenberg model with antiferromagnetic coupling (Eq. S2). Fitting parameters and relevant statistical parameters are summarized in Table S6.

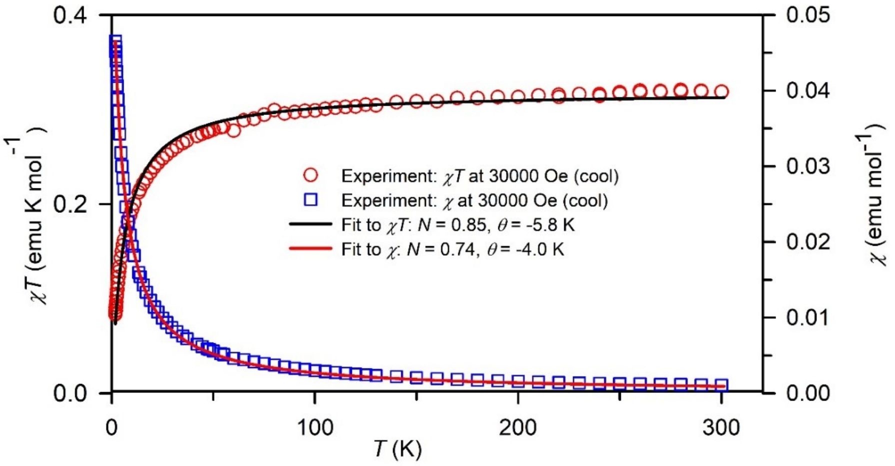

Fig. S26. SQUID magnetometry (label: ZY984) of polycrystalline radical **2**: selected experimental data plotted as χT vs T and χT vs T and the numerical fits to S = ½ with weight factor, N, and antiferromagnetic coupling described as a mean-field parameter, θ. Fitting parameters and relevant statistical parameters for radical **2** are as follows: fit to χT vs T, $N = 0.847 \pm 0.003$ and $\theta = -5.77 \pm 0.13$ K, DEP = 0.3649, SEE = 0.0070, adj $R^2 = 0.9921$; fit to χ vs T, $N = 0.774 \pm 0.005$ and $\theta = -4.00 \pm 0.05$ K, DEP = 0.9386, SEE = 0.0003, adj $R^2 = 0.9996$. For comparison fit to χT vs T for radical **1**: $N = 1.030 \pm 0.009$ and $\theta = -16.38 \pm 0.74$ K, DEP = 0.5755, SEE = 0.0177, adj $R^2 = 0.9790$.

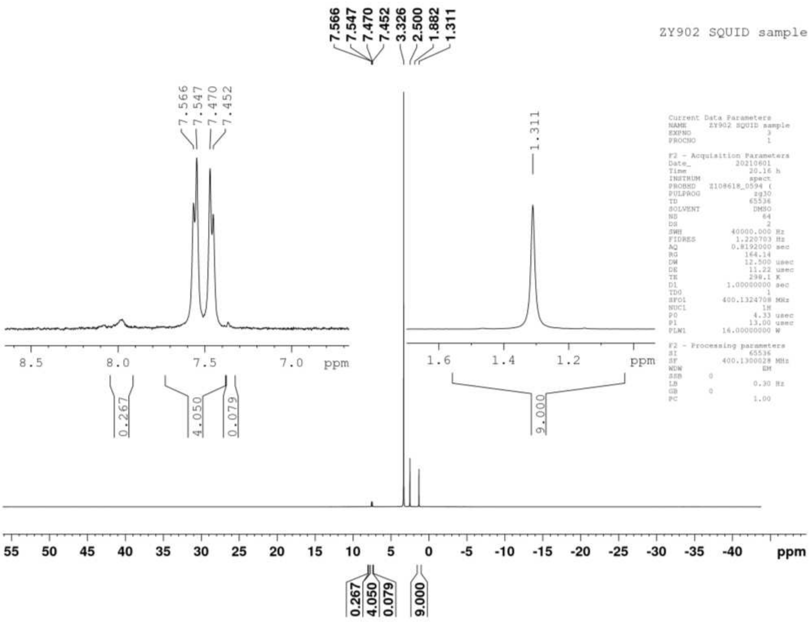

Fig S27. ^{1}H NMR (400 MHz, 0.54 mL of DMSO-d_6, label: ZY902) spectrum of radical **1** (SQUID sample, 0.48 mg, spin conc. 94%, label: ZY849fr1) with 4,4'-di-*tert*-butylbiphenyl (0.23 mg, 8.63×10^{-4} mmol) as a reference, to determine content of residual benzene; label: ZY902. Based on the integration of 0.079H for singlet at ~7.38 ppm, mass content of benzene in the sample of **1** is 0.37%, which corresponds to radical/benzene molar ratio of 61:1.

1.k Thermogravimetric analyses. TA Instruments TGA 550 was used for TGA of radicals **1** and **2**. Samples were obtained as dark solid from pentane penetrating to benzene, and they were dried on high vacuum line at 60 °C before measuring spin concentration. In a typical measurement, temperature was ramped from 25 °C to 390 °C (or 490 °C) at 5 °C min^{-1} and then held at 390 °C (or 490 °C) for 5 min.

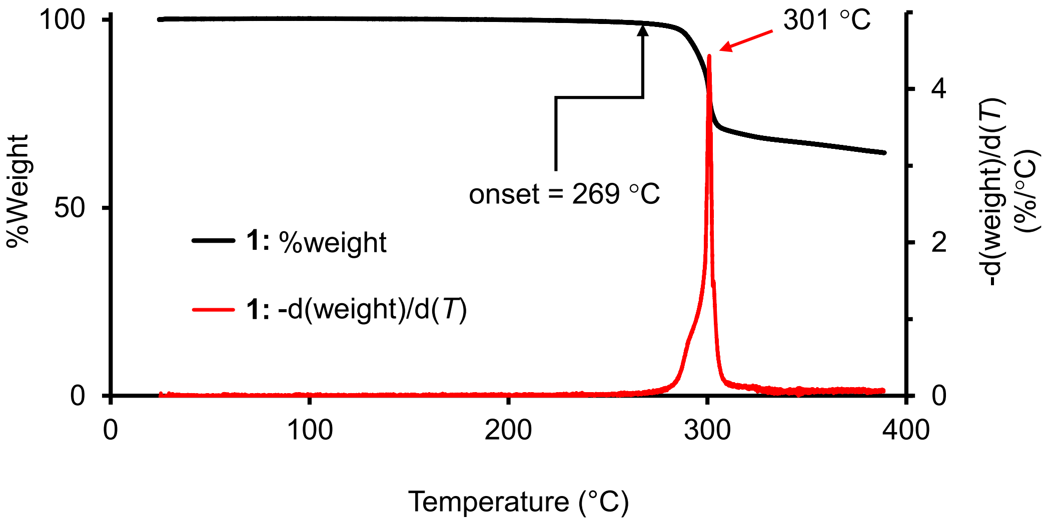

Fig. S28. Expanded version of Figure 9A (main text). TGA of dicyano radical **1** (1.162 mg, spin concentration 94%, sample label: ZY904). Temperature was ramped from 25 °C to 390 °C at 5 °C min^{-1} and held at 390 °C for 5 min. 1% mass loss was found at 269.35 °C.

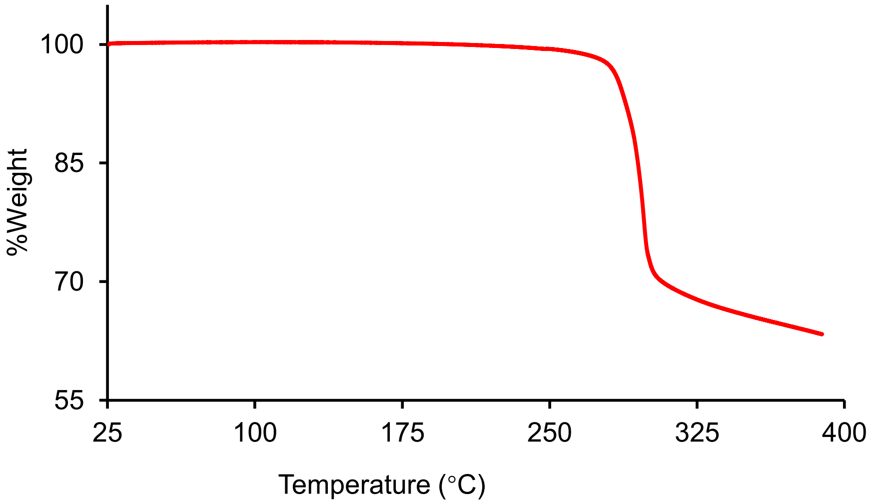

Fig. S29. TGA of dicyano radical **1** (1.857 mg, spin concentration 82%, sample label: ZY849). Temperature was ramped from 25 °C to 390 °C at 5 °C min^{-1} and held at 390 °C for 5 min. Sample changed from dark needle solid at room temperature to dark solid after heating. 1% mass loss was found at 262.98 °C and 18% was found at 296.37 °C.

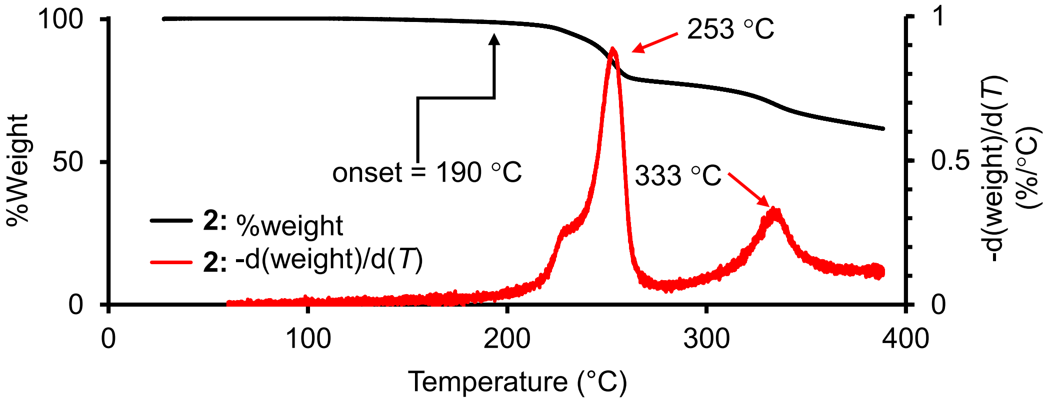

Fig. S30. TGA of monobromocyano radical **2** (1.375 mg, spin concentration 97%, sample label: ZY972again). Temperature was ramped from 25 °C to 390 °C at 5 °C min^{-1} and held at 390 °C for 5 min. 1% mass loss was found at 190.17 °C.

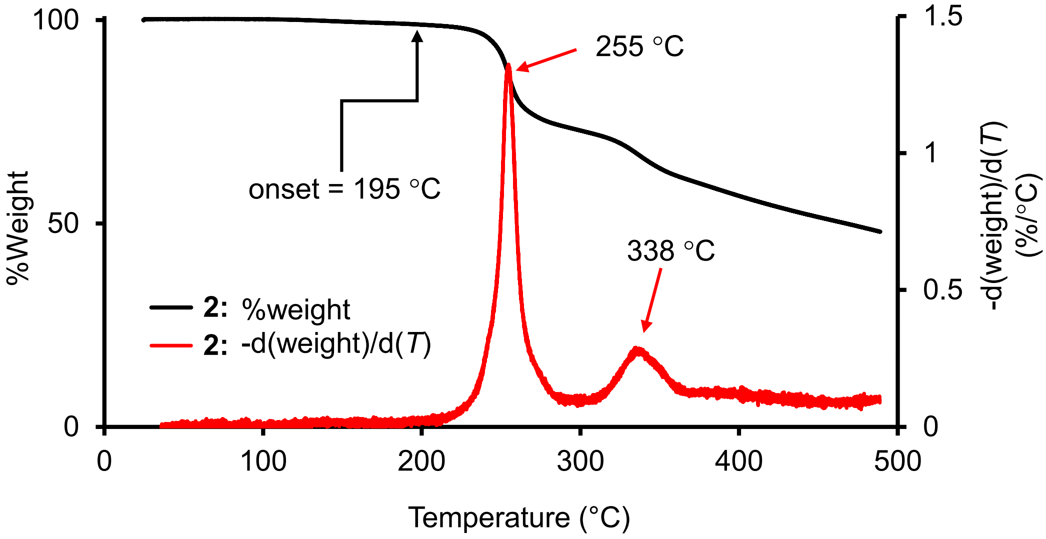

Fig. S31. Expanded version of Figure 9B (main text). TGA of monobromocyano radical **2** (1.186 mg, spin concentration 97%, sample label: ZY984, after SQUID measurement – first half of the SQUID sample). Temperature was ramped from 25 °C to 490 °C at 5 °C min^{-1} and held at 490 °C for 5 min. 1% mass loss was found at 194.96 °C.

2. Assemblies of Radical 1 on SiO_2/Si(111) Wafers.

Assembly stoichiometry. Quantitative information on assembly stoichiometry can be obtained by the analysis of the survey XPS spectra: the ratio of the integrated signal intensities of the spectroscopic lines in XPS curves of a film deposited with intact molecules is directly proportional to the theoretical percentages expected based on radical stoichiometry. This is a powerful tool to determine whether the deposition occurs without degradation.[S18] The results are given in Table S7.

Table S7. Stoichiometric and experimental elemental ratios for radical **1**.

	Theoretical value (%)	XPS values (%)
C	77.8	77.0 ± 2.5
N	22.2	23.0 ± 2.5
C/N	3.5	3.4 ± 0.6

The sensitivity factors (σ) are: $\sigma_{C\ 1s} = 0.25$ and $\sigma_{N\ 1s} = 0.42$.[S19]

We find that the integrated signal intensities obtained by analyzing the survey XPS curves agree with the theoretical elemental analyses. This means that the stoichiometry of the deposited assemblies corresponds to the quantitative composition of the molecule, indicating deposition without degradation.

Table S8. Assemblies: Fit results for the energy positions and relative intensities of the C 1s photoemission lines together with the molecular stoichiometry ratio in percent.

	Energy (eV)	Lorentzian Width (eV)	Gaussian Width (eV)	Intensity (%)	Theoretical values (%)
C-C	285.3	0.08	0.99	23.8	23.8
C-H	285.9	0.08	0.99	32.5	52.4
S_1	286.6	0.08	0.99	1.6	
C-N	287.1	0.08	1.38	23.8	23.8
S_2	287.6	0.08	1.00	3.8	
S_3	291.5	0.08	6.02	14.5	

Note that the cumulative intensity of the C-H feature and its satellites corresponds to the expected theoretical value (C-H + S_1 + S_2 + S_3 = 52.4 %).

Table S9. Powder: Fit results for the energy positions and relative intensities of the C 1s photoemission lines together with the molecular stoichiometry ratio in percent.

	Energy (eV)	Lorentzian Width (eV)	Gaussian Width (eV)	Intensity (%)	Theoretical values (%)
C-C	284.8	0.08	0.98	24.0	23.8
C-H	285.4	0.08	0.98	33.4	52.4
S_1	286.1	0.08	0.98	2.5	
C-N	286.7	0.08	1.32	23.8	23.8
S_2	287.0	0.08	0.98	2.2	
S_3	290.6	0.08	6.09	14.1	

Note that the cumulative intensity of the C-H feature and its satellites corresponds to the expected theoretical value (C-H + S_1 + S_2 + S_3 = 52.2 %).

Table S10. Assemblies: Fit results for the energy positions and relative intensities of the N 1s photoemission lines together with the molecular stoichiometry ratio in percent. Atom numbering refers to Figure 3 (main text, X-ray structure).

	Energy (eV)	Lorentzian Width (eV)	Gaussian Width (eV)	Intensity (%)	Theoretical values (%)
N_1	399.4	0.1	0.98	18.3	16.7
$N_{2,3,4}$	400.4	0.1	0.98	37.8	50.0
S_1	401.3	0.1	0.98	2.3	
$-CN_{5,6}$	402.9	0.1	0.98	29.5	33.3
S_2	403.7	0.1	1.10	3.9	
S_3	405.7	0.1	3.28	8.2	

Note that the cumulative intensity of the feature $N_{2,3,4}$ and $-CN_{5,6}$ and their satellites correspond to the expected theoretical value ($N_{2,3,4}+ S_1 + S_3 = 48.3$ % and $-CN_{5,6} + S_2 = 33.4$ %)

Table S11. Powder: Fit results for the energy positions and relative intensities of the N 1s photoemission lines together with the molecular stoichiometry ratio in percent. Atom numbering refers to Figure 3 (main text, X-ray structure).

	Energy (eV)	Lorentzian Width (eV)	Gaussian Width (eV)	Intensity (%)	Theoretical values (%)
N_1	398.8	0.1	0.95	18.4	16.7
$N_{2,3,4}$	399.7	0.1	0.95	38.9	50.0
S_1	400.9	0.1	0.95	2.6	
$-CN_{5,6}$	402.3	0.1	0.95	27.4	33.3
S_2	403.0	0.1	2.07	5.6	
S_3	405.1	0.1	3.38	7.1	

Note that the cumulative intensity of the feature $N_{2,3,4}$ and $-CN_{5,6}$ and their satellites correspond to the expected theoretical value ($N_{2,3,4}+ S_1 + S_3 = 48.6$ % and $-CN_{5,6} + S_2 = 33$ %)

We find that the integrated signal intensities obtained by analyzing the XPS lines by the fitting procedure agree with the theoretical elemental analyses and with the analogous values obtained from the powder line fit analyses. This further supports the conclusion that the deposition occurred without degradation.

SEM images. SEM images of a typical radical **1** assembly show that the substrate is homogeneously covered with nanoneedles. The lower panel in Figure S32 shows two images in high resolution. Typical diameters are also measured: they range from ~10 nm for small needles to ~100 nm for the bigger ones under the present preparation conditions (substrate kept at room temperature and evaporation rate: 0.1-0.7 nm/min).

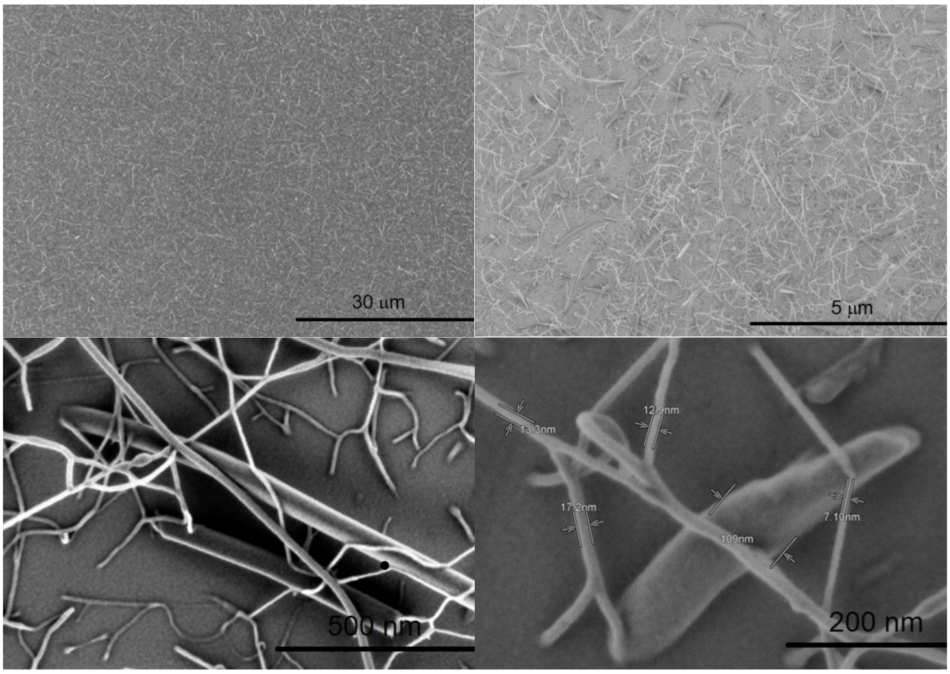

Fig. S32. Typical SEM images showing the radical **1** nanoneedles.

Assembly lifetime under air exposure. We also tested the lifetime of the assemblies of radical **1** taken out of the UHV and under air exposure. The assemblies are characterized by a long lifetime. In Fig. S33 a typical XPS N 1s core-level curve after 64 hours of air exposure is illustrated. There are no changes in the line shape or new features. We observe a shift of the curve towards higher binding energy and higher satellite intensity, upon air exposure. This hints at possible post-growth phenomena involving desorption and coalescence of the smaller nanoneedles in favor of the growth of bigger nanoneedles.
This is supported by the monitoring of the survey signals with time (Fig. S34). We observe a slight decrease of the C 1s and N 1s signals, concomitant to very slight desorption of the molecules, and the increase of the Si 2p signal that indicates desorption and nanoneedle reorganization that leaves free larger areas of the substrate.

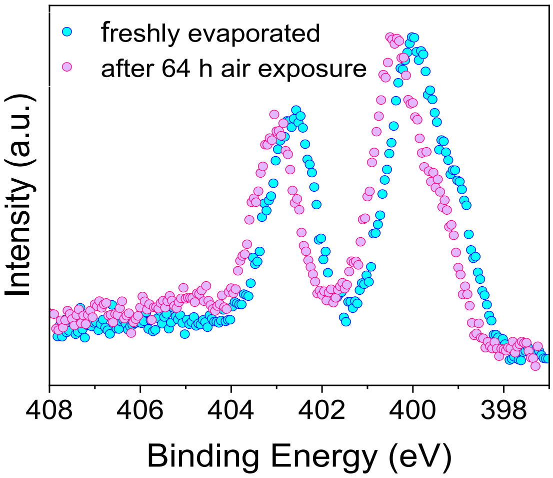

Fig. S33. Typical N 1s core-level spectra of the fresh assembly and after 64 h of air exposure.

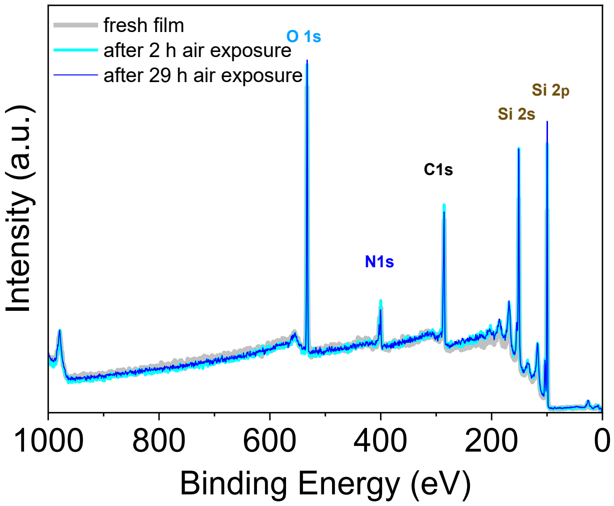

Fig. S34. Monitoring the survey core level spectra with increasing time of air exposure.

3. EPR Spectroscopy of Assemblies of Radical 1 on SiO_2/Si(111) Wafers.

EPR spectra of assemblies of **1** were obtained at the University of Nebraska, using Bruker CW EPR spectrometer (X-band EMXplus), as described in Section 1.e. The assemblies were shipped from the Casu lab to the Rajca lab via express mail in custom-made Schlenk vessels (under vacuum at ambient temperature). Upon arrival at Nebraska, the assemblies and empty substrate (SiO_2/Si(111) wafer) were rapidly transferred on air to custom made Schlenk 5-mm OD EPR tubes, and then placed under high vacuum (ca. 1×10^{-4} Torr).

Angular dependence of EPR spectra of freshly prepared assemblies of radical **1** on SiO_2/Si(111) wafers at room temperature (293 K) was found negligible (checked at 0, 45 , 90, … 315, 360 ° angles between the normal to the surface and the external magnetic field) (Fig. S35). Thus, all subsequent spectra were obtained at 90 ° angle.

The spectra of the assemblies of **1** were initially obtained while the assembly was kept under vacuum. First, the background spectra of empty SiO_2/Si(111) wafers were taken and simulated (Fig. S36). Second, the spectra of the assemblies were obtained and simulated with two $S = ½$ components (Fig. S37), as described in the following paragraph. Finally, the background spectra were subtracted from the spectra of the assemblies. To account for small differences in microwave frequencies between the two types of spectra (assembly vs background), prior to the subtraction, the background spectra were slightly shifted. The resultant difference spectra for **1** were simulated (Fig. S38); *g*-values for radical **1** were corrected with DPPH (powder sample).

In another experiment, stability (persistence) of the assemblies, after exposure to air for a total of 54 d, was followed by EPR spectroscopy. First, the spectra of empty SiO_2/Si(111) wafers were taken and simulated (Fig. S36). Then, the spectra of assemblies were obtained and simulated with two $S = ½$ components. The first component (weight = 1.000) corresponded to the background for which only the *g*-tensor was optimized; the values of *H*-strain, were fixed and taken from the simulation of the empty substrate spectra. The second component (weight = $w1$ = optimized) corresponded to isotropic, exchange narrowed, spectrum of radical **1** (Fig. S39). Using the weights $w1$, molar fraction of **1** (x) was computed, $x = w1/(w1 + 1)$. Linear regression, $-\ln(x)$ vs time (in days), gave half-life of **1** in the assemblies (Table S12, Fig. S40).

Finally, residue of radical **1**, following multiple cycles of evaporation under UHV was examined by quantitative EPR spectroscopy in benzene at room temperature; spin concentration of 92% was measured (label: ZY1012), compared to 94% for the original sample (label: ZY904).

Table S12. Summary of spectral simulations of the assemblies of **1** exposed to ambient conditions.

EPR label	Time (d)	Simulation label	Rmsd	Weight, *w1*	*x*	–ln(*x*)
ZY1025R7_T1d_bas	1	1891	0.023692	0.1754586	0.149268209	1.902010531
ZY1025R10_T2d_bas	2	1926	0.0273773	0.1486697	0.12942772	2.044632702
ZY1025R13_T2d_bas	2	1921	0.0228353	0.1595724	0.137613141	1.983308858
ZY1025R17_T3d_bas	3	1918	0.0213823	0.1339112	0.118096726	2.136251281
ZY1025R18_T4d_bas	4	1895	0.0184635	0.1799214	0.15248592	1.880683016
ZY1025R19_T4d_bas	4	1924	0.0195578	0.1777726	0.150939664	1.890875101
Zy1029R11_T15d_bas	15	1958	0.0215493	0.1254732	0.11148484	2.193866658
ZY1029R10_T15d_bas	15	1893	0.0210602	0.1324984	0.116996545	2.145610875
ZY1029R8_T15d_bas	15	1938	0.0193394	0.1225303	0.10915545	2.214982266
ZY1029R15_T22d_bas	22	1931	0.0224152	0.1155041	0.103544308	2.267755662
ZY1029R19_T30d_bas	30	1933	0.0189926	0.1109755	0.099890142	2.303684281
ZY1029R20_T30d_bas	30	1955	0.017995	0.09500452	0.086761761	2.444589301
ZY1029R23_T37d_bas	37	1929	0.0222802	0.1111941	0.100067216	2.301913159
ZY1044R3_T46d_bas	46	1953	0.029033	0.08468322	0.078071845	2.550125789
zY1044R5_T46d_bas	46	1951	0.0292153	0.07548823	0.070189731	2.656553255
ZY1044R8_T54d_bas	54	1949	0.0301573	0.07580686	0.07046512	2.652637437
ZY1044R9_T54d_bas	54	1947	0.031722	0.0669975	0.062790681	2.767948603

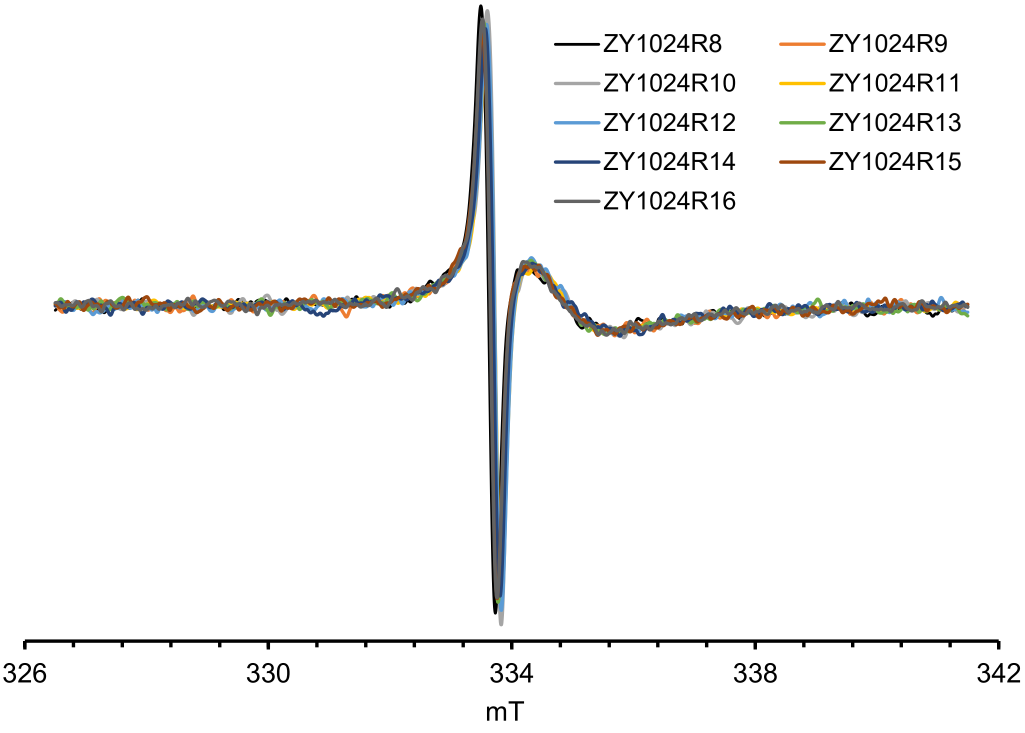

Fig. S35. EPR spectroscopy (ν ≈ 9.36 GHz, modulation amplitude = 0.1 mT, MW power attn = 33 dB, EPR labels: ZY1024R8–R16) of freshly prepared (time = 0 d) assemblies of radical **1** at 293 K; the spectra are obtained by incrementally changing the angle by 45 ° in the 0 – 360 ° range; no detectable angular dependence is found. Angles are between the normal to the surface and the external magnetic field.

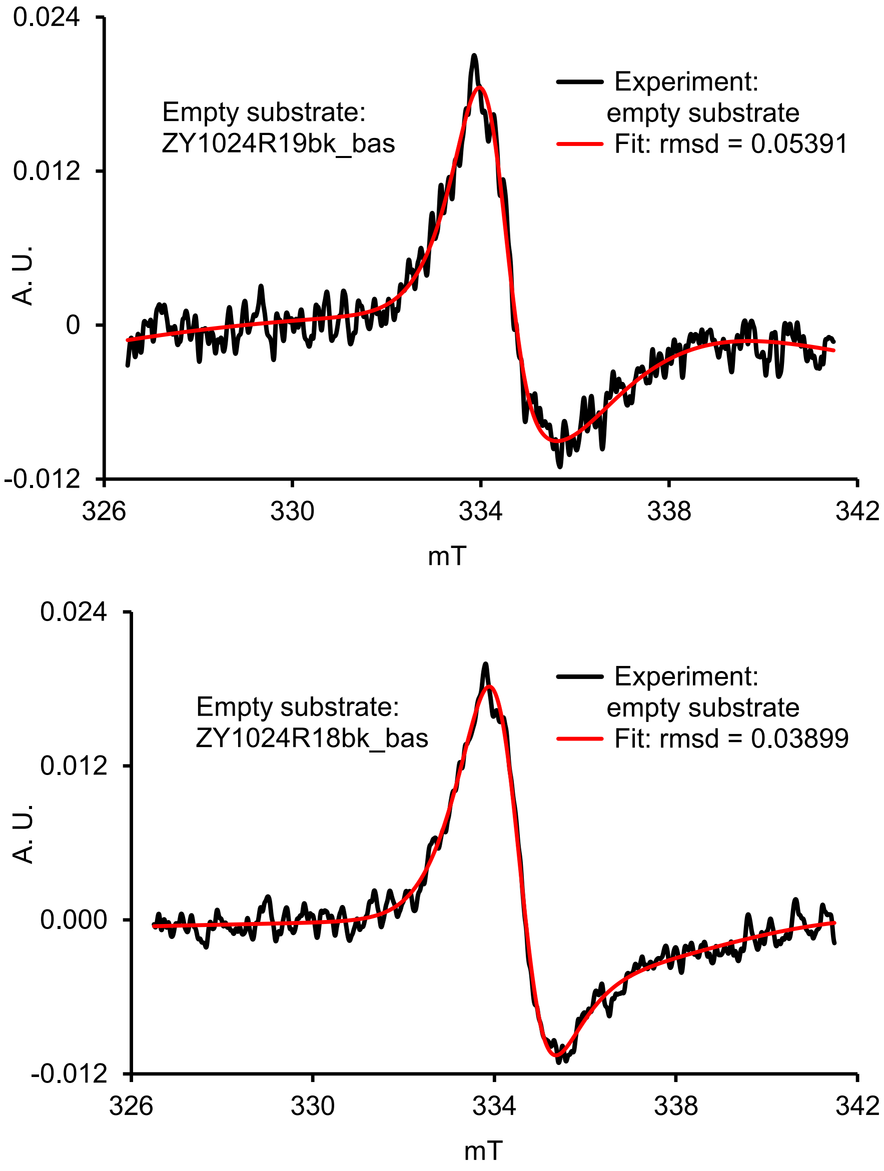

Fig. S36. EPR spectroscopy (ν = 9.3527 and 9.3547 GHz, EPR labels: ZY1024R18bk_bas and ZY1024R19bk_bas) of empty SiO_2/Si(111) substrate at 293 K. Top spectrum (number of scans = 8): simulation parameters: rmsd = 0.0539113, $S = ½$, $g_{xx} = 1.9986$, $g_{yy} = 1.9967$, $g_{zz} = 1.9865$, $H_{xx} = 25.0$ MHz, $H_{yy} = 68.7$ MHz, $H_{zz} = 105.3$ MHz. Bottom spectrum (number of scans = 16): simulation parameters: rmsd = 0.0389882, $S = ½$, $g_{xx} = 1.9976$, $g_{yy} = 1.9990$, $g_{zz} = 1.9769$, $H_{xx} = 28.6$ MHz, $H_{yy} = 59.5$ MHz, $H_{zz} = 147.2$ MHz.

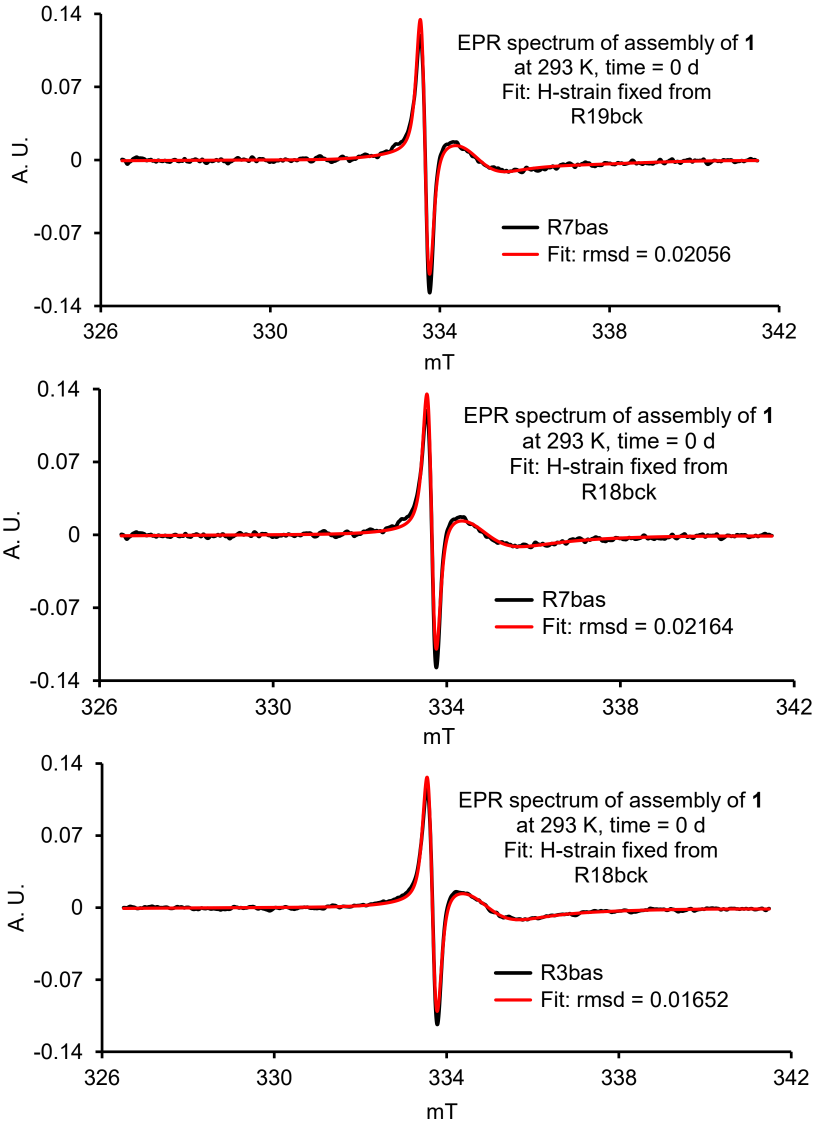

Fig. S37. EPR spectroscopy (ν = 9.3597 and 9.3592 GHz, EPR labels: ZY1024R3bas and ZY1024R7bas) of assemblies of **1** at 293 K (time = 0 d). Top spectrum (number of scans = 8, label: R7bas): simulation parameters: rmsd = 0.0205615, component 1, weight =1.000, $S = ½$, $g_{xx} = 1.9969$, $g_{yy} = 2.0026$, $g_{zz} = 1.9800$, **fixed H-strain (label: R19bck):** $H_{xx} = 25.0$ MHz, $H_{yy} = 68.7$ MHz, $H_{zz} = 105.3$ MHz; component 2, weight = 0.1474, $S = ½$, g(cor) = 2.0036, lwpp, Gaussian = 0.146 mT, Lorentzian = 0.122 mT. Middle spectrum (number of scans = 8, label: R7bas): simulation parameters: rmsd = 0.0216439, $S = ½$, $g_{xx} = 1.9974$, $g_{yy} = 1.9969$, $g_{zz} = 1.9866$, **fixed H-strain (label: R18bck):** $H_{xx} = 28.6$ MHz, $H_{yy} = 59.5$ MHz, $H_{zz} = 147.2$ MHz; component 2, weight = 0.1618, $S = ½$, g(cor) = 2.0036, lwpp, Gaussian = 0.143 mT, Lorentzian = 0.125 mT.. Bottom spectrum (number of scans = 16, label: R3bas): simulation parameters: rmsd = 0.0165215, $S = ½$, $g_{xx} = 1.9969$, $g_{yy} = 1.9982$, $g_{zz} = 1.9847$, **fixed H-strain (label: R18bck):** $H_{xx} = 28.6$ MHz, $H_{yy} = 59.5$ MHz, $H_{zz} = 147.2$ MHz; component 2, weight = 0.1559, $S = ½$, g(cor) = 2.0036, lwpp, Gaussian = 0.167 mT, Lorentzian = 0.119 mT.

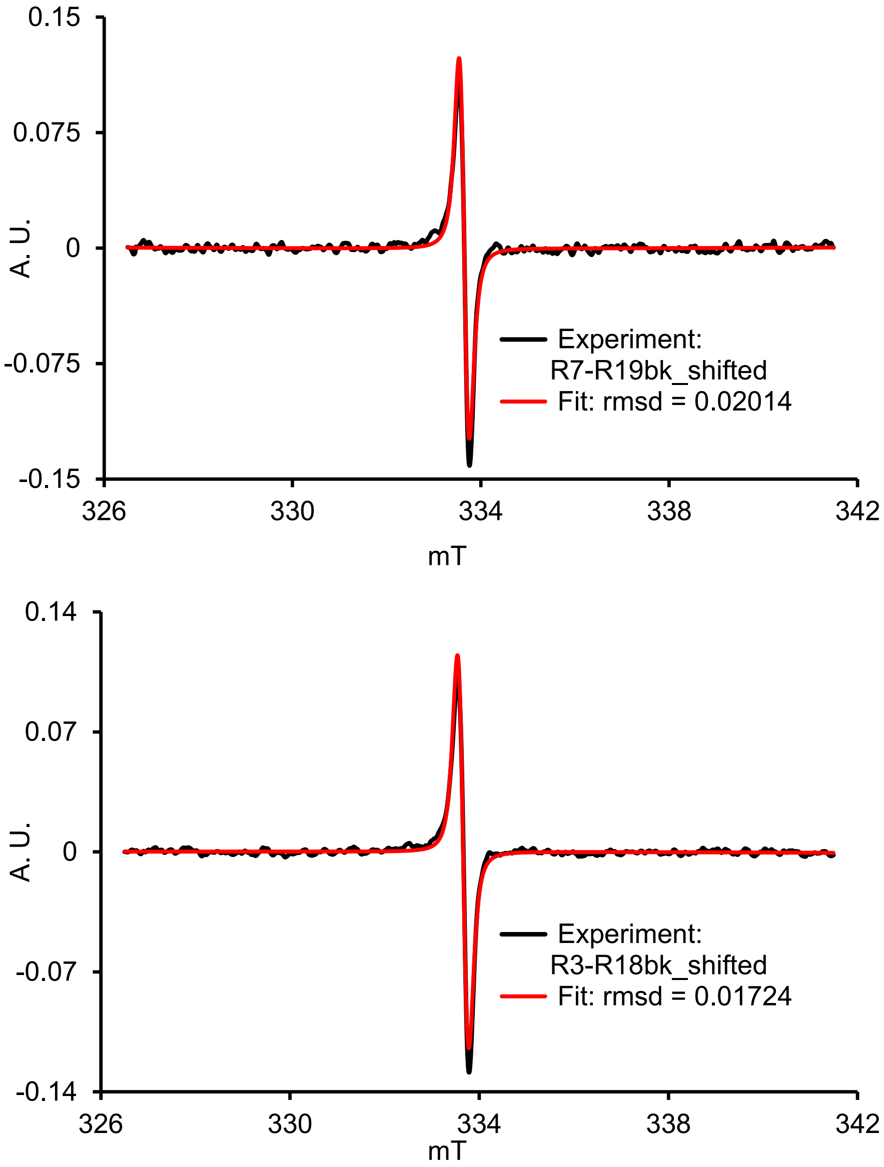

Fig. S38. EPR spectral differences: spectrum of the assemblies of **1** minus spectrum of the empty substrate. Because the spectra of the assemblies of **1** (ν = 9.3597 and 9.3592 GHz, EPR labels: ZY1024R3bas and ZY1024R7bas) and the empty substrate backgrounds (see: the Figs. S36 and S37, above) possess slightly different frequencies, the background spectra were slightly shifted prior to the subtraction of empty SiO_2/Si(111) substrate at 293 K. Top spectrum (number of scans = 8): simulation parameters: rmsd = 0.0201363, $S = ½$, g(cor) = 2.0036, line widths peak-to-peak (lwpp), Gaussian = 0.136 mT and Lorentzian = 0.134 mT. Bottom spectrum (number of scans = 16): simulation parameters: rmsd = 0.0172391, $S = ½$, g(cor) = 2.0036, lwpp, Gaussian = 0.167 mT and Lorentzian = 0.122 mT.

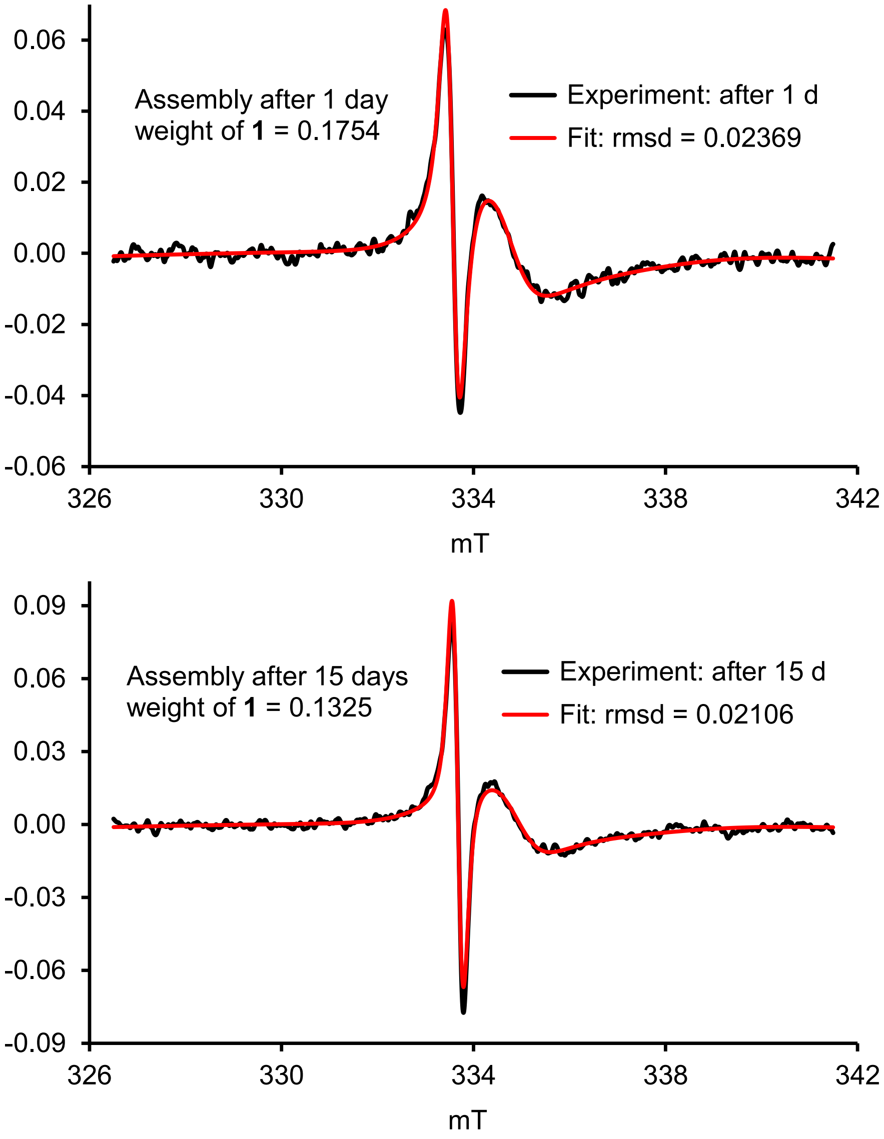

Fig. S39. EPR spectroscopy (ν = 9.3570 and 9.3601 GHz, EPR labels: ZY1025R7_T1d_bas and ZY1029R10_T15d_bas) of assemblies of **1** at 293 K. The spectra are taken after exposure of the film to ambient conditions for 1 and 15 days, respectively. Top spectrum (number of scans = 8, label: R7bas_T1d): simulation parameters: rmsd = 0.0236920, component 1, weight =1.000, $S = ½$, g_{xx} = 1.9974, g_{yy} = 1.9996, g_{zz} = 1.9835, **fixed H-strain (label: R19bck):** H_{xx} = 25.0 MHz, H_{yy} = 68.7 MHz, H_{zz} = 105.3 MHz; component 2, weight = 0.1755, $S = ½$, g(cor) = 2.0036, lwpp, Gaussian = 0.146 mT, Lorentzian = 0.233 mT. Bottom spectrum (number of scans = 8, label: R10bas_T15d): simulation parameters: rmsd = 0.0210602, $S = ½$, g_{xx} = 1.9969, g_{yy} = 2.0015, g_{zz} = 1.9836, **fixed H-strain (label: R19bck):** H_{xx} = 25.0 MHz, H_{yy} = 68.7 MHz, H_{zz} = 105.3 MHz; component 2, weight = 0.1325, $S = ½$, g(cor) = 2.0036, lwpp, Gaussian = 0.158 mT, Lorentzian = 0.137 mT.

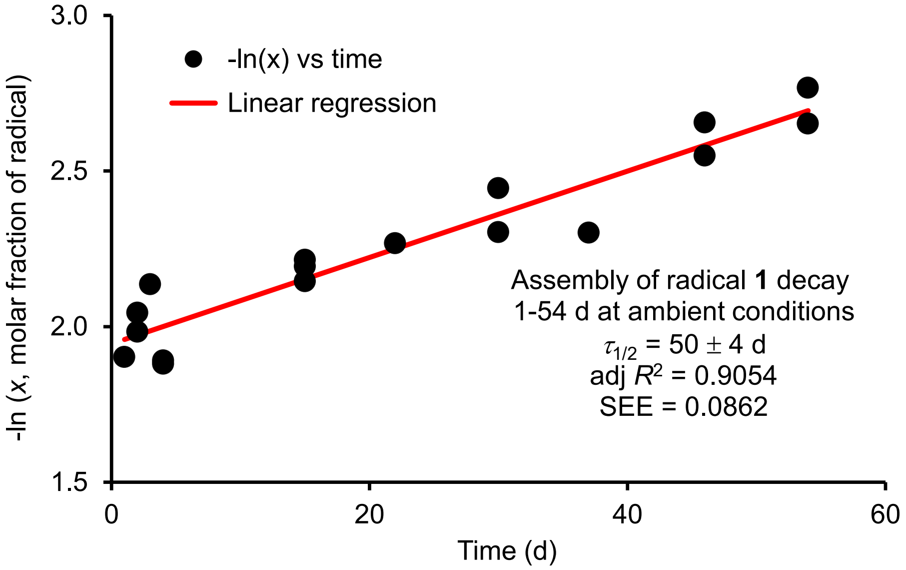

Fig. S40. Expanded version of inset plot Figure 12 (main text). Linear regression showing half-life of 50 d for assemblies of **1** at ambient conditions. The data for this figure are summarized in Table S12.

4. ^{1}H NMR, ^{13}C NMR, MS, IR Data for Radical 1 and Its Synthetic Intermediates

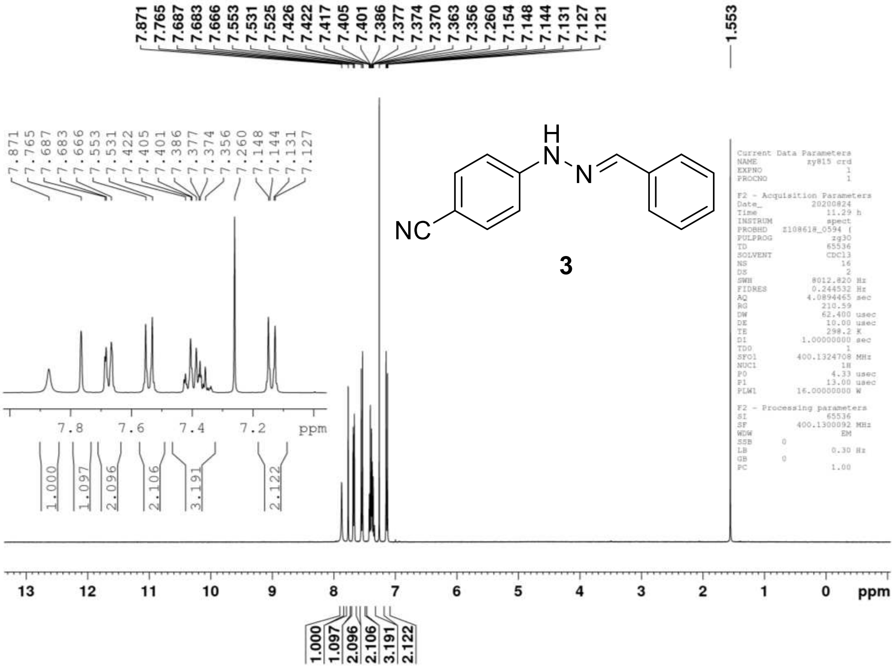

Fig. S41. ^{1}H-NMR spectrum for compound **3** (sample label: zy815, $CDCl_3$, 400 MHz).

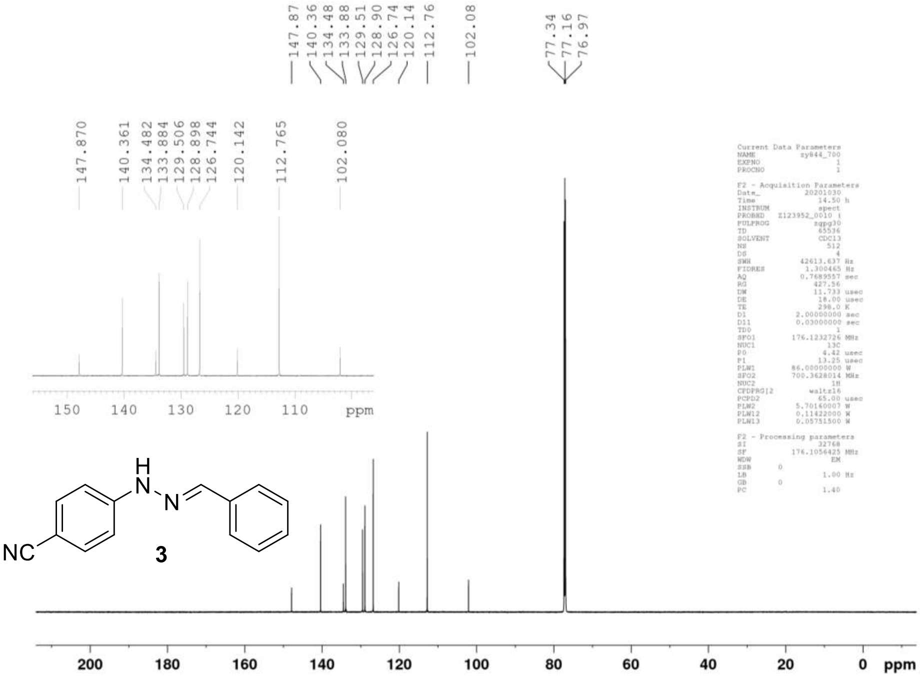

Fig. S42. ^{13}C-NMR spectrum for compound **3** (sample label: zy844, $CDCl_3$, 150 MHz).

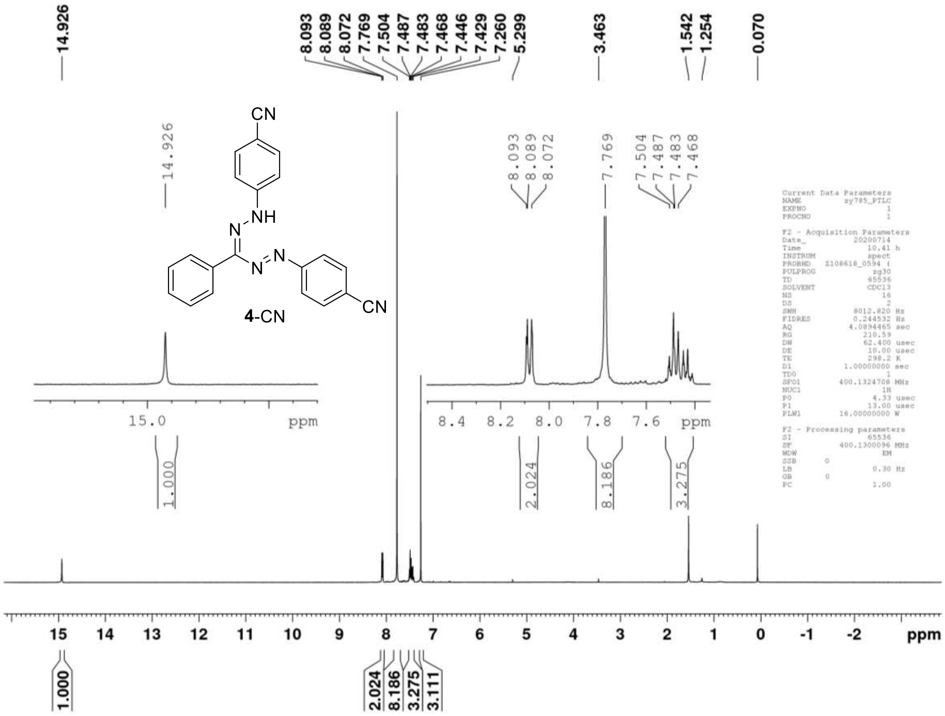

Fig. S43. ^{1}H-NMR spectrum for compound **4**-CN (sample label: zy817 col, $CDCl_3$, 400 MHz).

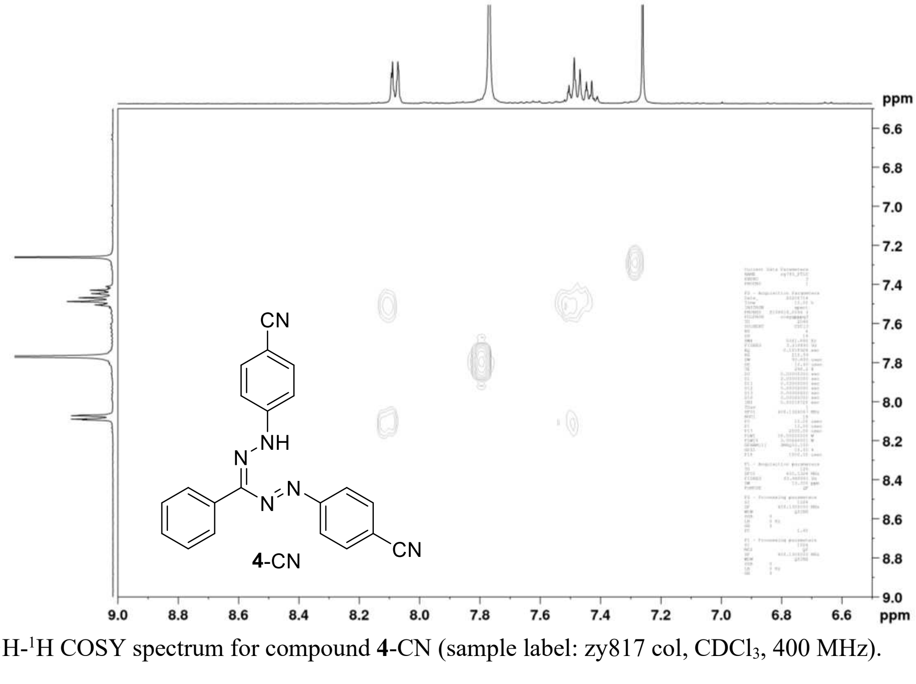

Fig. S44. ^{1}H-^{1}H COSY spectrum for compound **4**-CN (sample label: zy817 col, $CDCl_3$, 400 MHz).

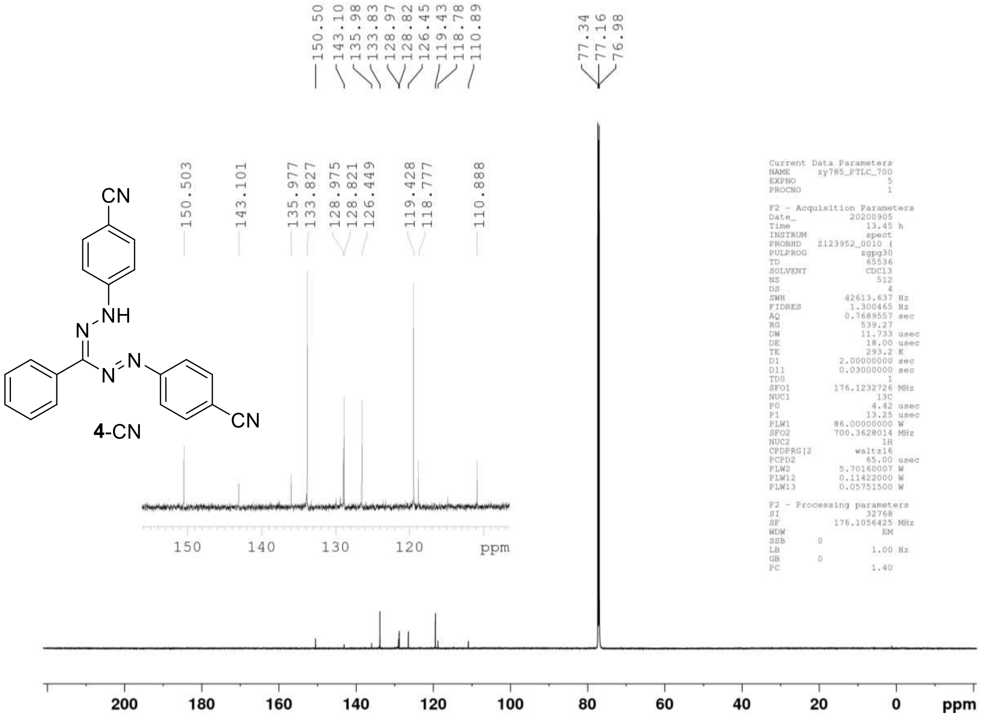

4-CN

```
Current Data Parameters
NAME       zy785_PTLC_700
EXPNO                   5
PROCNO                  1

F2 - Acquisition Parameters
Date_            20200905
Time                13.45 h
INSTRUM             spect
PROBHD   Z123952_0010 (
PULPROG           zgpg30
TD                 65536
SOLVENT            CDCl3
NS                   512
DS                     4
SWH            42613.637 Hz
FIDRES          1.300465 Hz
AQ             0.7689557 sec
RG                539.27
DW                11.733 usec
DE                 18.00 usec
TE                 293.2 K
D1            2.00000000 sec
D11           0.03000000 sec
TD0                    1
SFO1         176.1232726 MHz
NUC1                 13C
P0                  4.42 usec
P1                 13.25 usec
PLW1         86.00000000 W
SFO2         700.3628014 MHz
NUC2                  1H
CPDPRG[2         waltz16
PCPD2              65.00 usec
PLW2          5.70160007 W
PLW12         0.11422000 W
PLW13         0.05751500 W

F2 - Processing parameters
SI                 32768
SF           176.1056425 MHz
WDW                   EM
SSB       0
LB                  1.00 Hz
GB        0
PC                  1.40
```

Fig. S45. ^{13}C-NMR spectrum for compound **4**-CN (sample label: sample label: zy817 col, $CDCl_3$, 150 MHz)

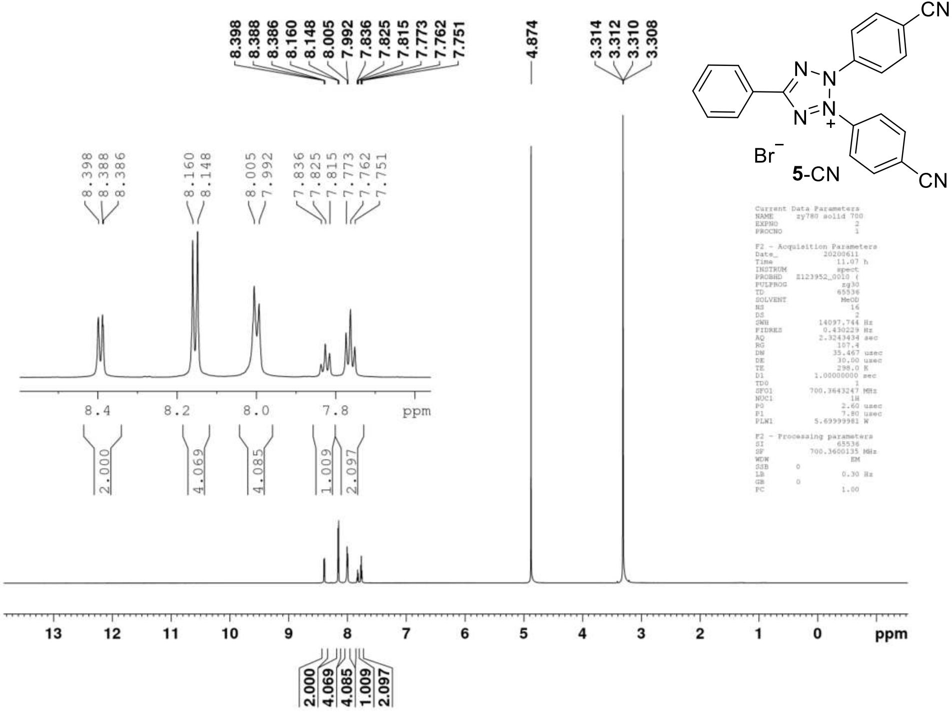

5-CN

```
Current Data Parameters
NAME       zy780 solid 700
EXPNO                   2
PROCNO                  1

F2 - Acquisition Parameters
Date_            20200611
Time                11.07 h
INSTRUM             spect
PROBHD   Z123952_0010 (
PULPROG             zg30
TD                 65536
SOLVENT             MeOD
NS                    16
DS                     2
SWH            14097.744 Hz
FIDRES          0.430229 Hz
AQ             2.3243434 sec
RG                 107.4
DW                35.467 usec
DE                 30.00 usec
TE                 298.0 K
D1            1.00000000 sec
TD0                    1
SFO1         700.3643247 MHz
NUC1                  1H
P0                  2.60 usec
P1                  7.80 usec
PLW1          5.69999981 W

F2 - Processing parameters
SI                 65536
SF           700.3600135 MHz
WDW                   EM
SSB       0
LB                  0.30 Hz
GB        0
PC                  1.00
```

Fig. S46. ^{1}H-NMR spectrum for compound **5**-CN (sample label: zy822, methanol-d_4, 400 MHz).

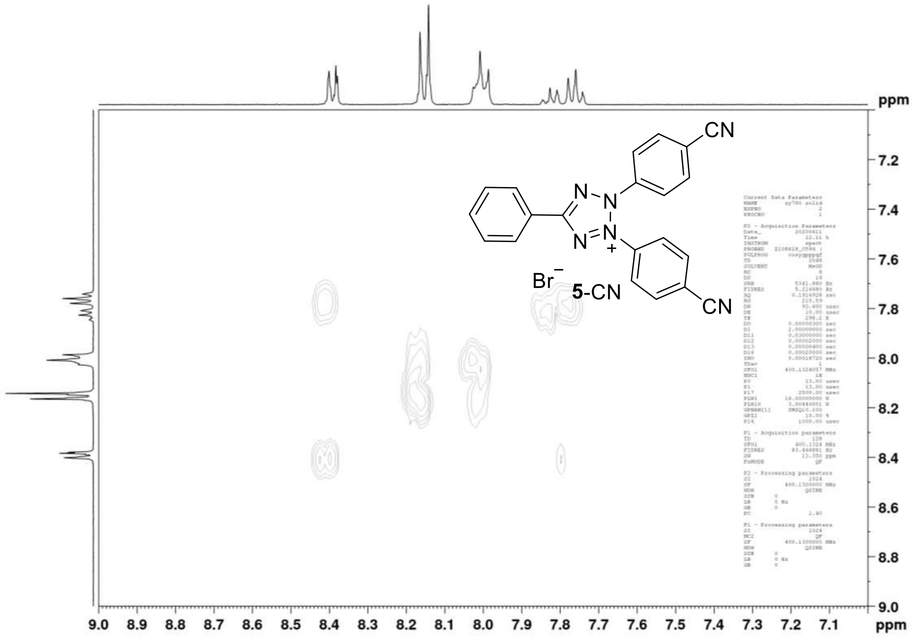

Fig. S47. ^{1}H-^{1}H COSY spectrum for compound **5**-CN (sample label: zy822, methanol-d_4, 400 MHz).

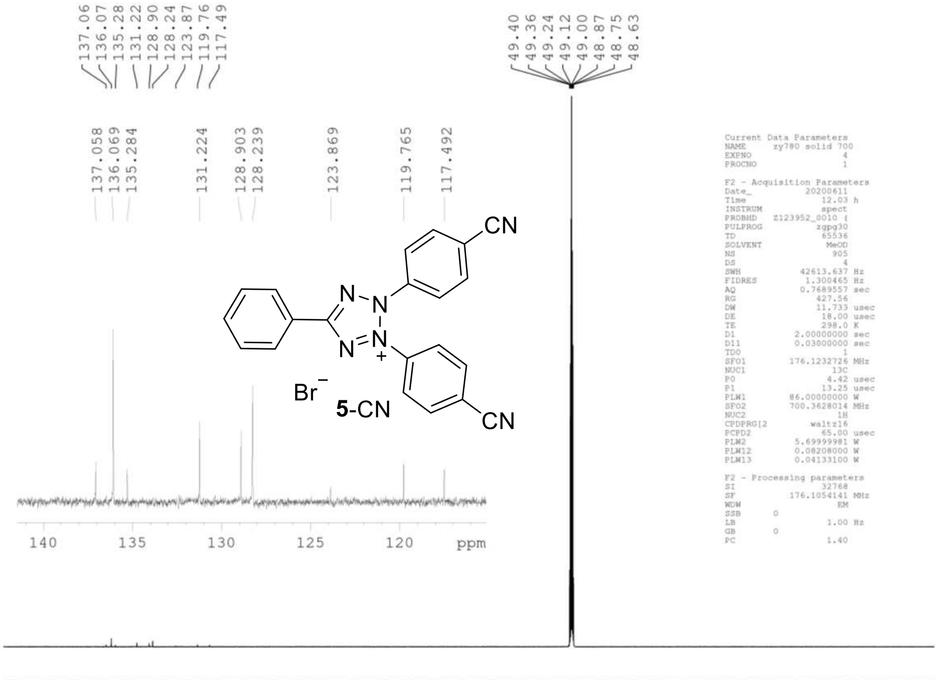

Fig. S48. ^{13}C-NMR spectrum for compound **5**-CN (sample label: zy822, methanol-d_4, 175 MHz).

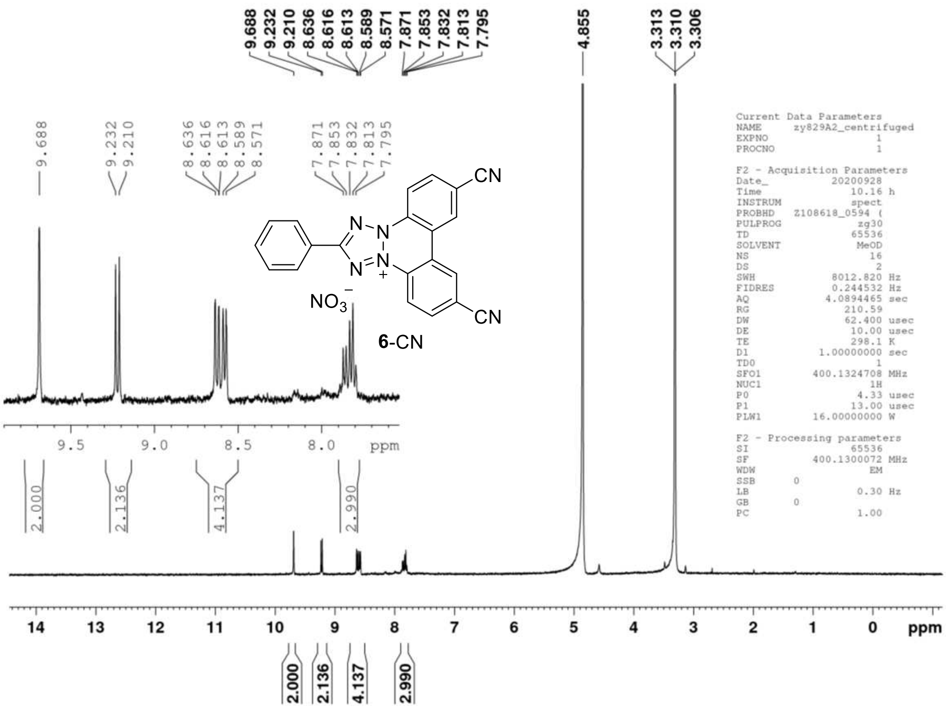

Fig. S49. ^{1}H-NMR spectrum for compound **6**-CN (sample label: zy829, methanol-d_4, 400 MHz).

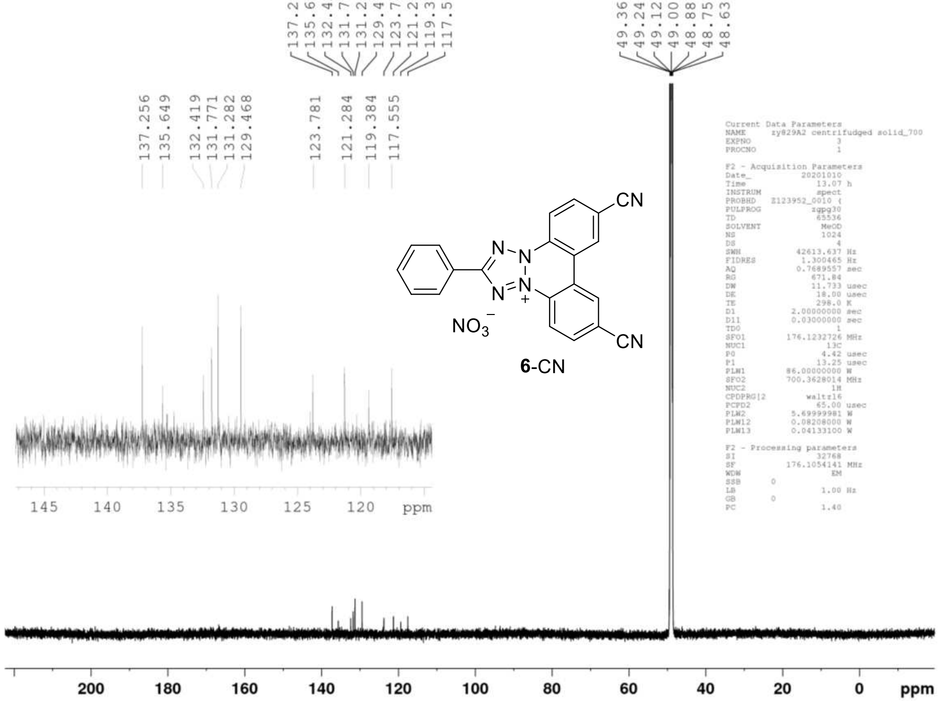

Fig. S50. ^{13}C-NMR spectrum for compound **6**-CN (sample label: zy829, methanol-d_4, 175 MHz).

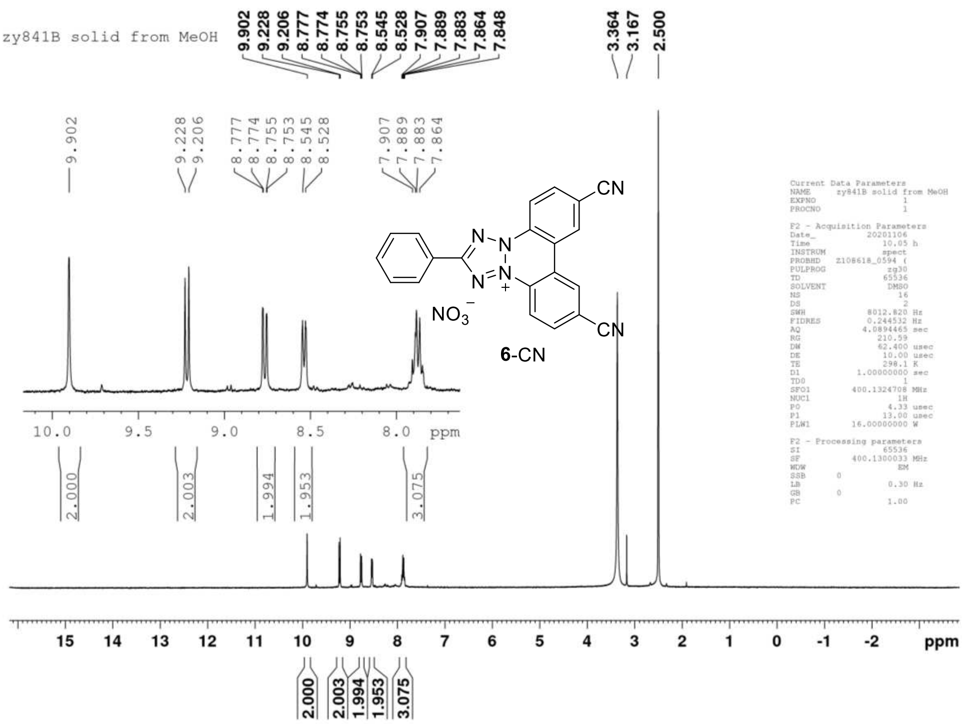

Fig. S51. ^{1}H-NMR spectrum for compound **6**-CN (sample label: zy841, DMSO-d_6, 400 MHz).

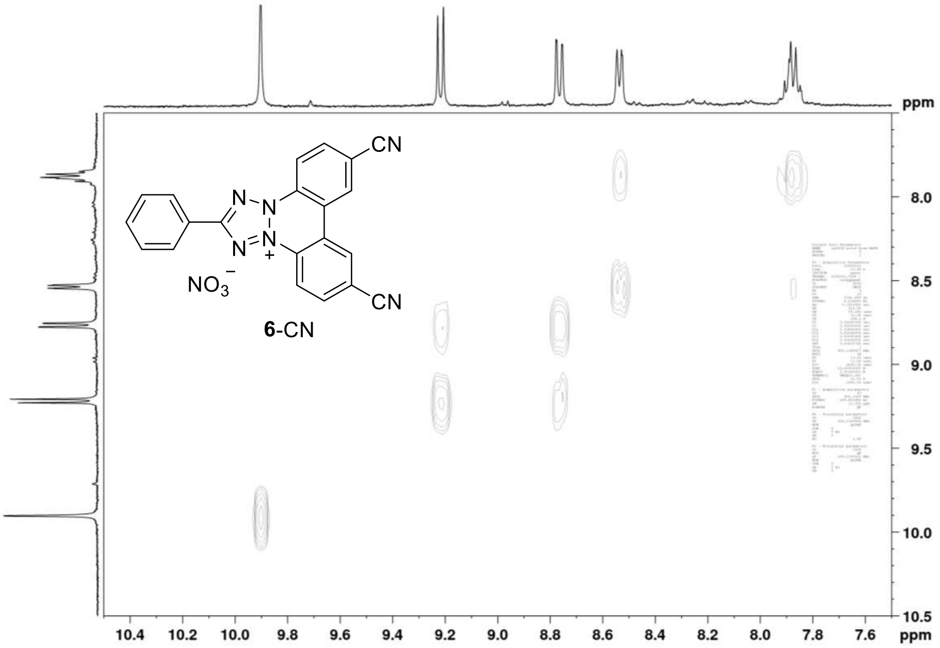

Fig. S52. ^{1}H-^{1}H COSY spectrum for compound **6**-CN (sample label: zy841, DMSO-d_6, 400 MHz).

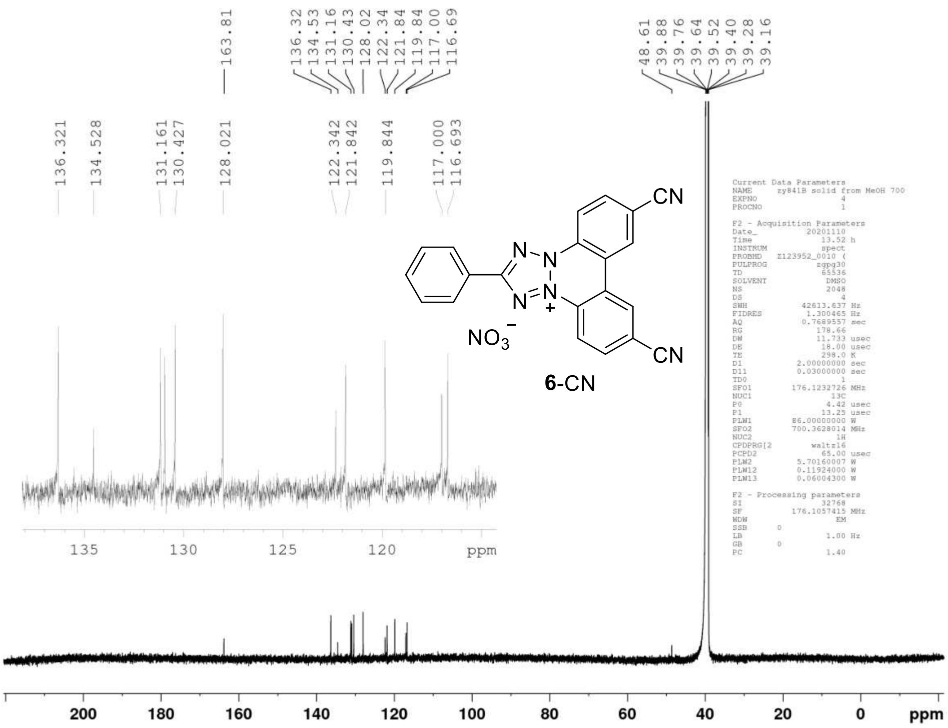

Fig. S53. ^{13}C-NMR spectrum for compound **6**-CN (sample label: zy841, DMSO-d_6, 174 MHz).

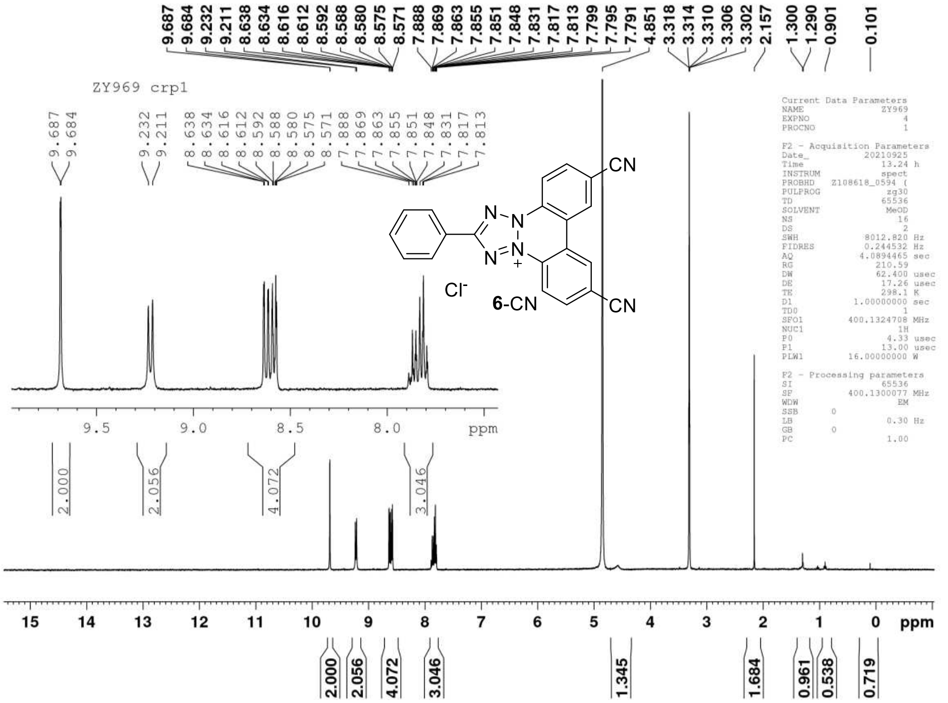

Fig. S54. ^{1}H-NMR spectrum for compound **6**-CN (sample label: zy969, methanol-d_4, 400 MHz), which was prepared by acidification of radical **1**.

Analysis Info

Analysis Name	D:\Kurt's stuff\Kurt's Data\61733 Zy815 crp1_000001.d	Acquisition Date	10/16/2020 3:23:28 PM
Method	New Shim 4_23_20	Operator	
Sample Name		Instrument	solariX XR
Comment			

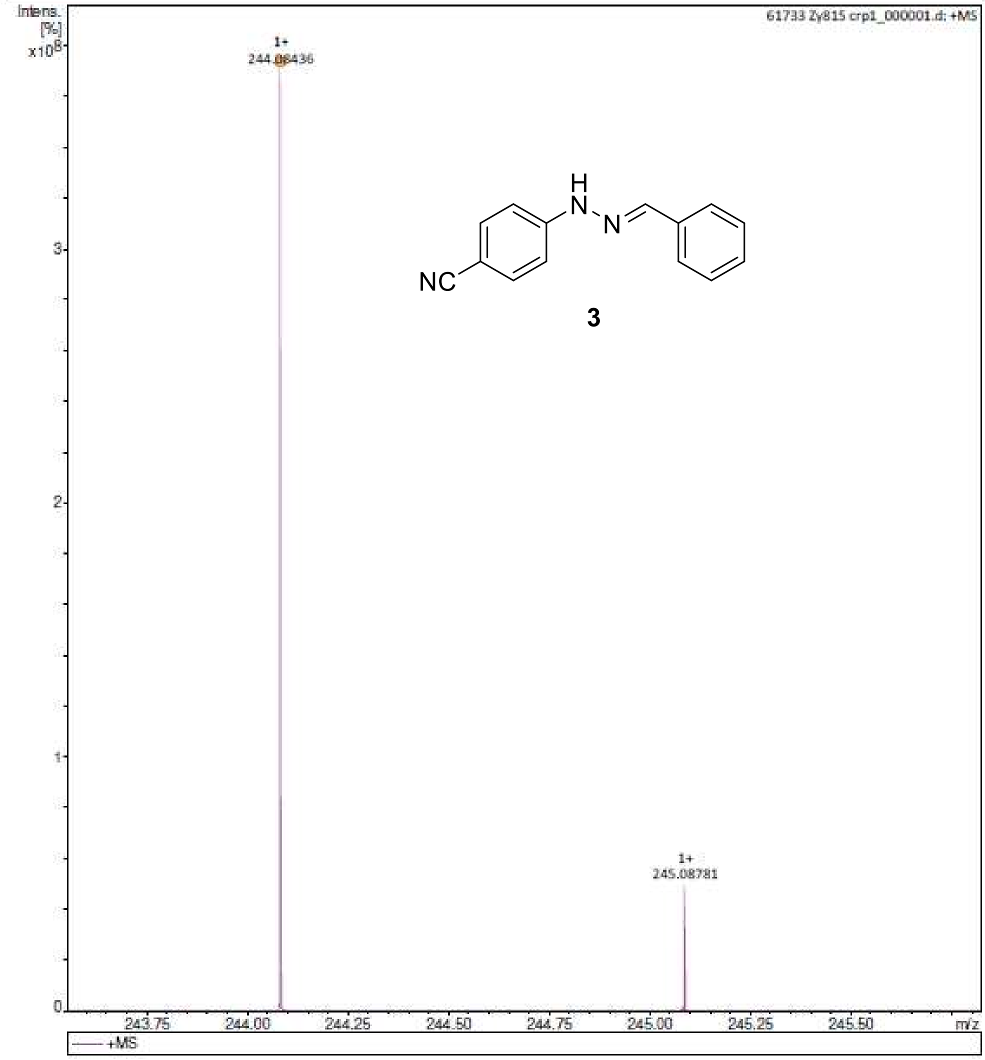

Bruker Compass DataAnalysis 5.0 printed: 10/16/2020 3:25:26 PM by: demo Page 1 of 1

Untitled

Meas. m/z	#	Ion Formula	Score	m/z	err [ppm]	Mean err [ppm]	mSigma	rdb	e¯ Conf	N-Rule	
244.084362	1	C14H11N3Na	100.00	244.084518	0.6	0.1		9.5	11.0	even	ok

Fig. S55. HR-ESI MS for compound **3** (sample label: zy815, calcd 244.08452 for $C_{14}H_{11}N_3Na$, found 244.08436).

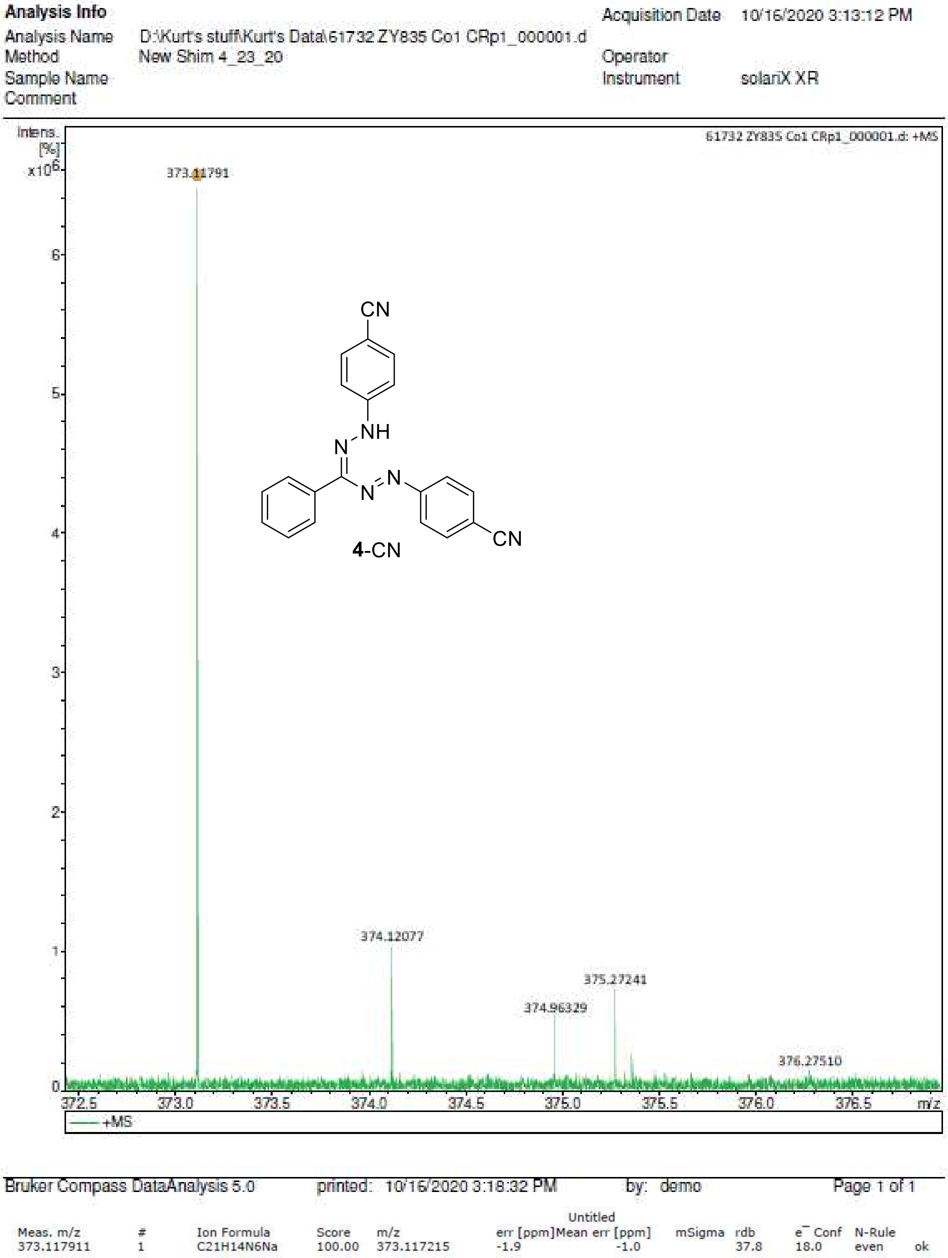

Analysis Info

Analysis Name D:\Kurt's stuff\Kurt's Data\61732 ZY835 Co1 CRp1_000001.d
Method New Shim 4_23_20
Sample Name
Comment

Acquisition Date 10/16/2020 3:13:12 PM
Operator
Instrument solariX XR

Bruker Compass DataAnalysis 5.0 printed: 10/16/2020 3:18:32 PM by: demo Page 1 of 1

Untitled

Meas. m/z	#	Ion Formula	Score	m/z	err [ppm]	Mean err [ppm]	mSigma	rdb	e⁻ Conf	N-Rule	
373.117911	1	C21H14N6Na	100.00	373.117215	-1.9	-1.0		37.8	18.0	even	ok

Fig. S56. HR-ESI MS for compound **4**-CN (sample label: zy835, calcd 373.11722 for $C_{21}H_{14}N_6Na$, found 373.11791).

Analysis Info

Analysis Name	D:\Kurt's stuff\Kurt's Data\61734 zy837 solid_000001.d	Acquisition Date	10/16/2020 3:58:39 PM
Method	New Shim 4_23_20	Operator	
Sample Name		Instrument	solariX XR
Comment			

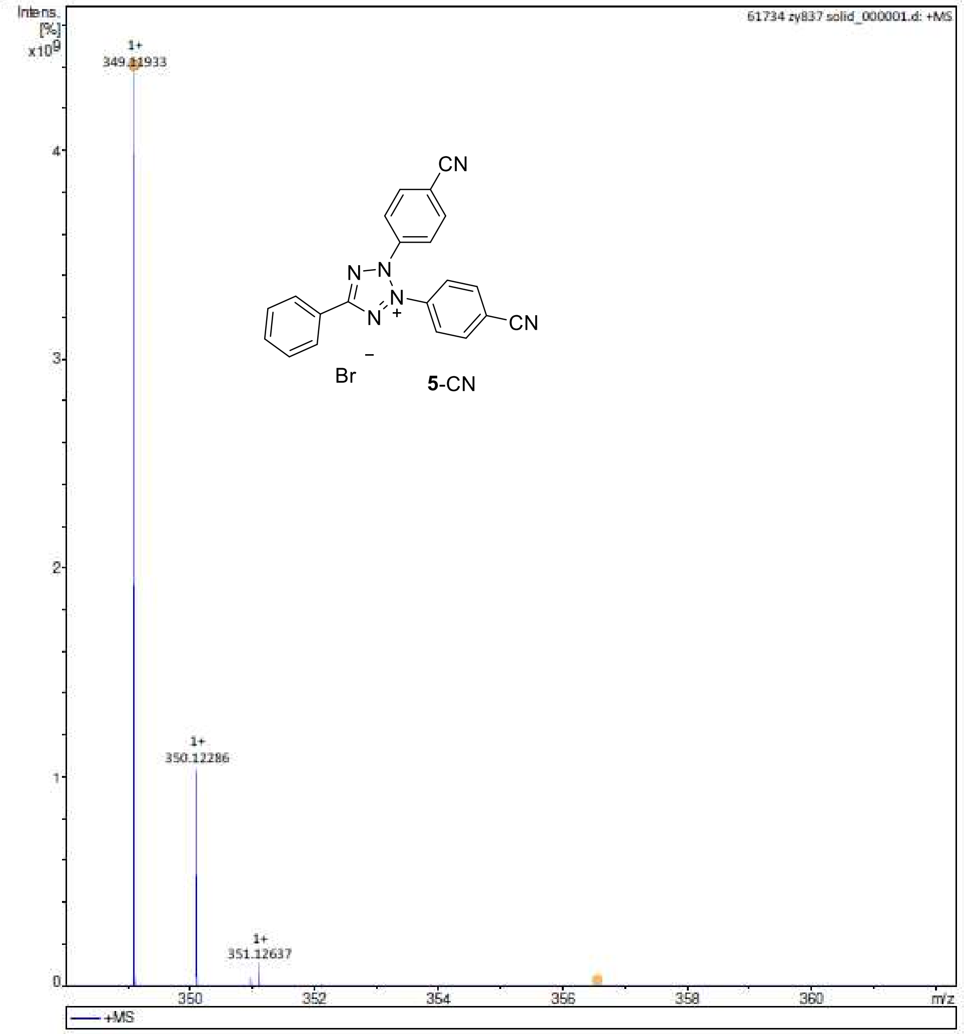

Bruker Compass DataAnalysis 5.0 printed: 10/16/2020 4:03:43 PM by: demo Page 1 of 1

Untitled

Meas. m/z	#	Ion Formula	Score	m/z	err [ppm]	Mean err [ppm]	mSigma	rdb	e⁻ Conf	N-Rule	
349.119331	1	C21H13N6	100.00	349.119621	0.8	0.2		6.9	19.0	even	ok

Fig. S57. HR-ESI MS for compound **5**-CN (sample label: zy837, calcd 349.11962 for $C_{21}H_{13}N_6$, found 349.11933).

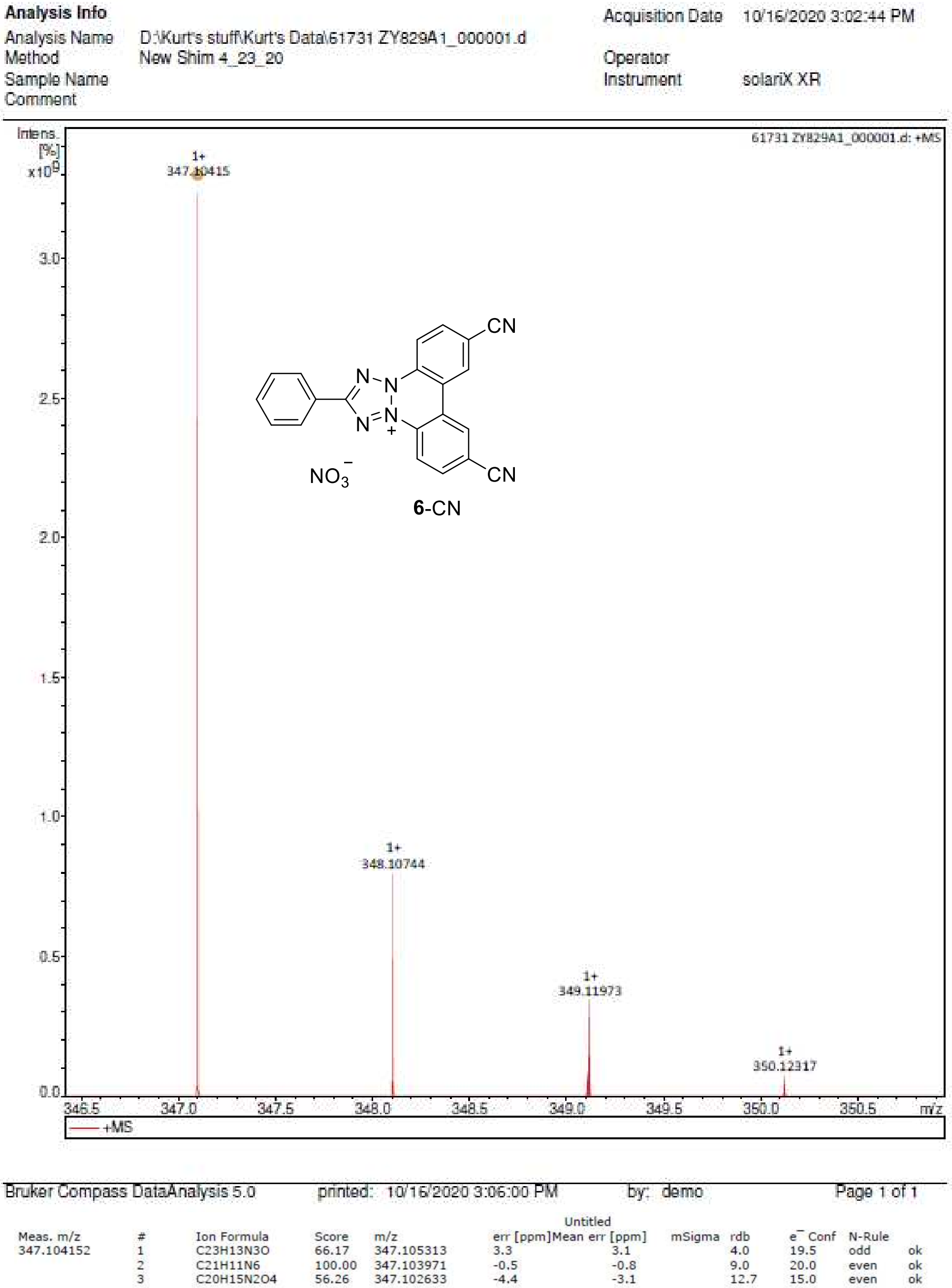

```
Analysis Info                                                   Acquisition Date   10/16/2020 3:02:44 PM
Analysis Name   D:\Kurt's stuff\Kurt's Data\61731 ZY829A1_000001.d
Method          New Shim 4_23_20                                Operator
Sample Name                                                     Instrument         solariX XR
Comment
```

```
Bruker Compass DataAnalysis 5.0        printed:  10/16/2020 3:06:00 PM        by:  demo                Page 1 of 1

                                                                Untitled
Meas. m/z      #    Ion Formula    Score    m/z           err [ppm]Mean err [ppm]   mSigma  rdb    e¯ Conf  N-Rule
347.104152     1    C23H13N3O      66.17    347.105313    3.3           3.1                 4.0    19.5     odd     ok
               2    C21H11N6       100.00   347.103971    -0.5          -0.8                9.0    20.0     even    ok
               3    C20H15N2O4     56.26    347.102633    -4.4          -3.1                12.7   15.0     even    ok
```

Fig. S58. HR-ESI MS for compound **6-**CN (sample label: zy829, calcd 347.10397 for $C_{21}H_{11}N_6$, found 347.10415).

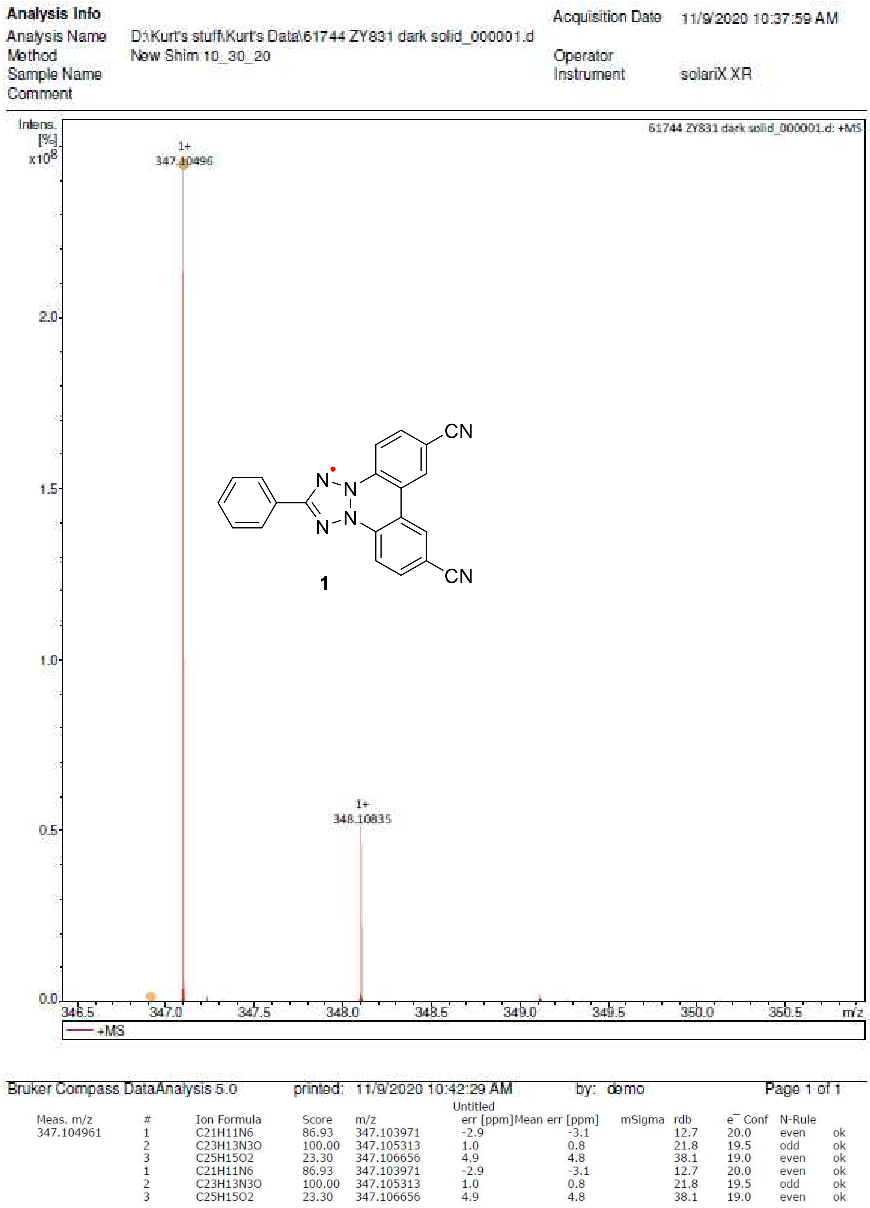

Analysis Info
Analysis Name D:\Kurt's stuff\Kurt's Data\61744 ZY831 dark solid_000001.d
Method New Shim 10_30_20
Sample Name
Comment

Acquisition Date 11/9/2020 10:37:59 AM
Operator
Instrument solariX XR

Bruker Compass DataAnalysis 5.0 printed: 11/9/2020 10:42:29 AM by: demo Page 1 of 1

Untitled

Meas. m/z	#	Ion Formula	Score	m/z	err [ppm]	Mean err [ppm]	mSigma	rdb	e⁻ Conf	N-Rule	
347.104961	1	C21H11N6	86.93	347.103971	-2.9	-3.1		12.7	20.0	even	ok
	2	C23H13N3O	100.00	347.105313	1.0	0.8		21.8	19.5	odd	ok
	3	C25H15O2	23.30	347.106656	4.9	4.8		38.1	19.0	even	ok
	1	C21H11N6	86.93	347.103971	-2.9	-3.1		12.7	20.0	even	ok
	2	C23H13N3O	100.00	347.105313	1.0	0.8		21.8	19.5	odd	ok
	3	C25H15O2	23.30	347.106656	4.9	4.8		38.1	19.0	even	ok

Fig. S59. HR-ESI MS for radical **1** (sample label: zy831, calc. 347.103971 for $C_{21}H_{11}N_6$, found 347.10496).

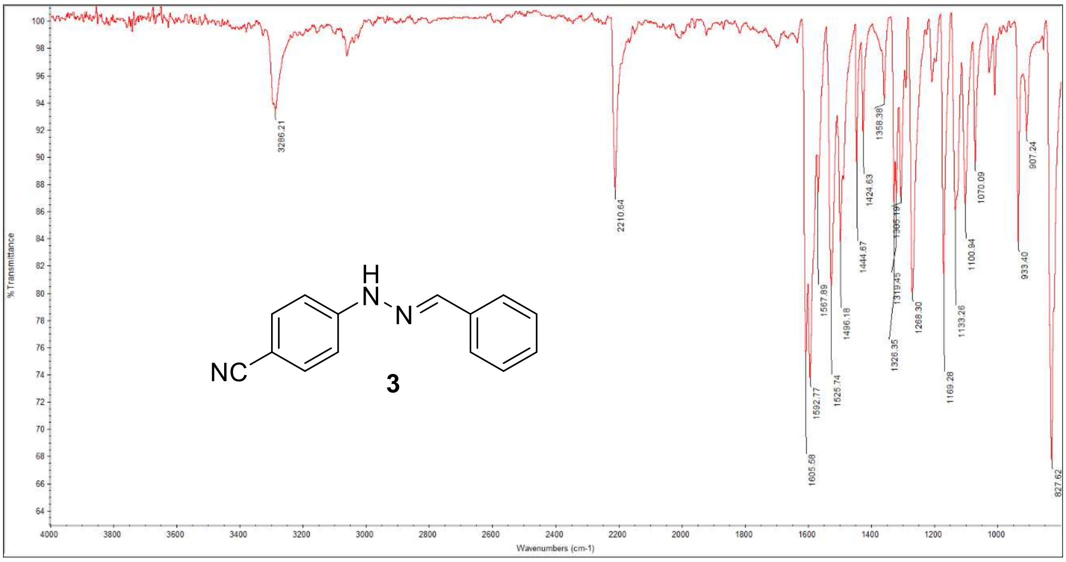

Fig. S60. IR spectrum (ATR, ZnSe) of compound **3** (sample label: zy815).

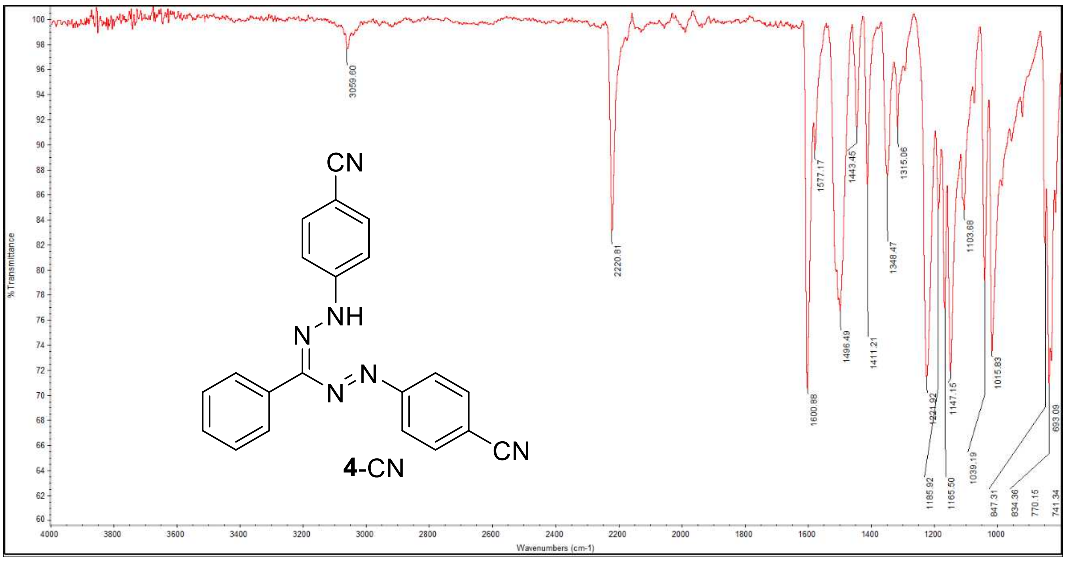

Fig. S61. IR spectrum (ATR, ZnSe) of compound **4**-CN (sample label: zy835).

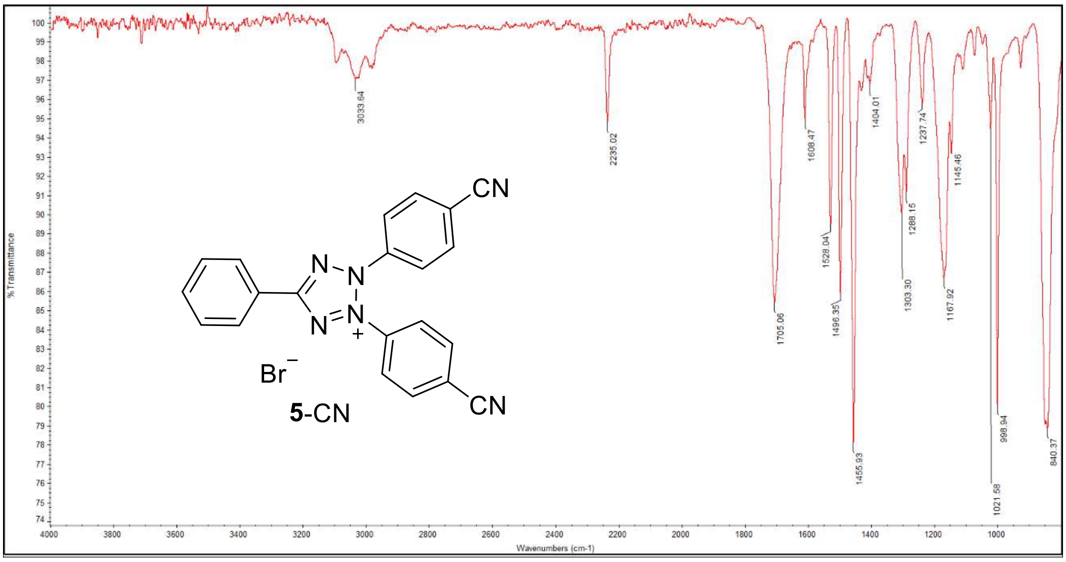

Fig. S62. IR spectrum (ATR, ZnSe) of compound **5**-CN (sample label: zy822).

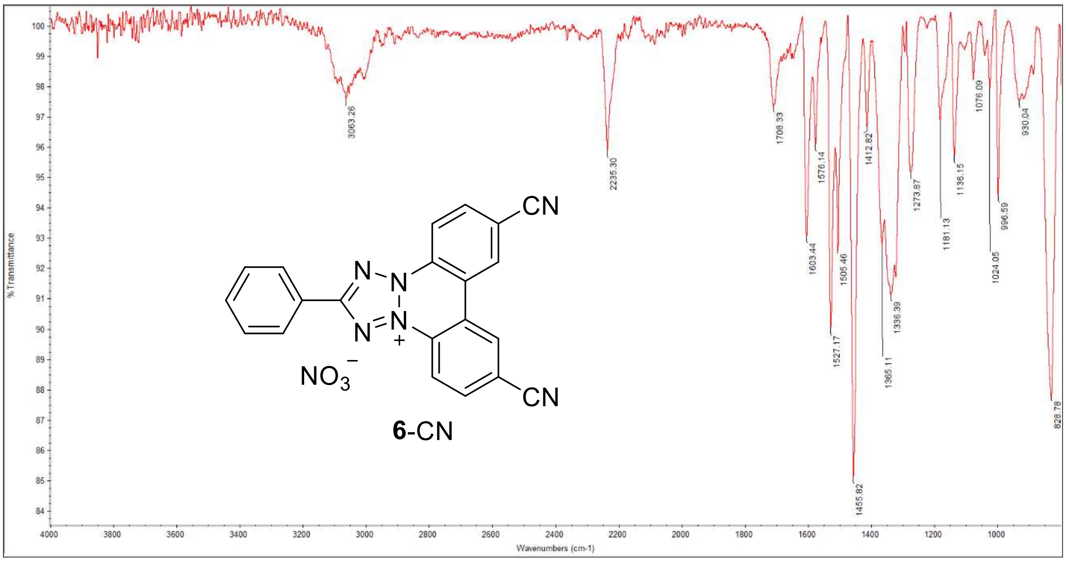

Fig. S63. IR spectrum (ATR, ZnSe) of compound **6**-CN (sample label: zy829)

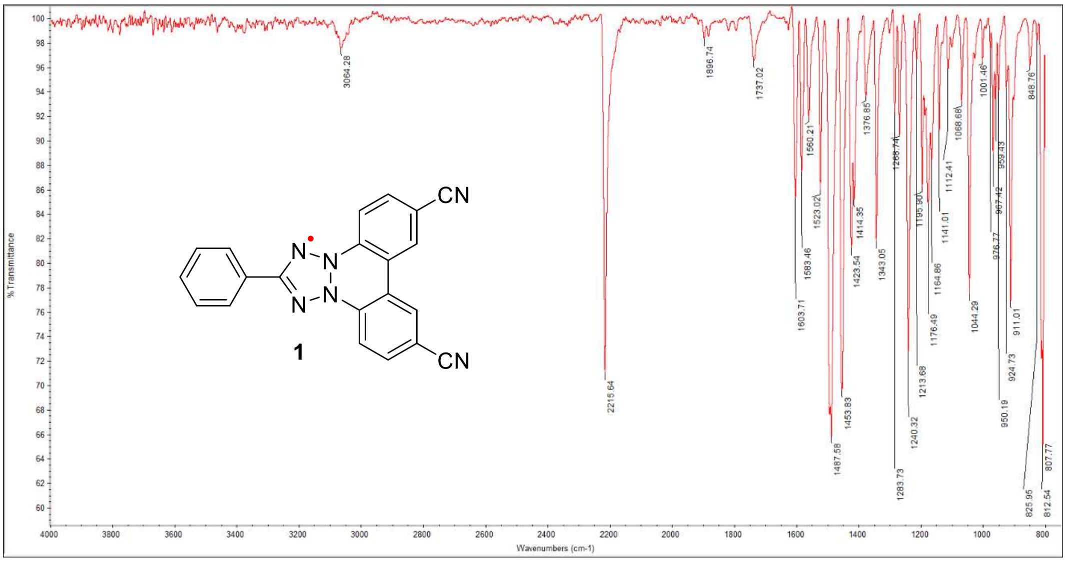

Fig. S64. IR spectrum (ATR, ZnSe) of radical **1** (sample label: zy986)

5. ^{1}H NMR, ^{13}C NMR, MS, IR Data for Radical 2 and Its Synthetic Intermediates

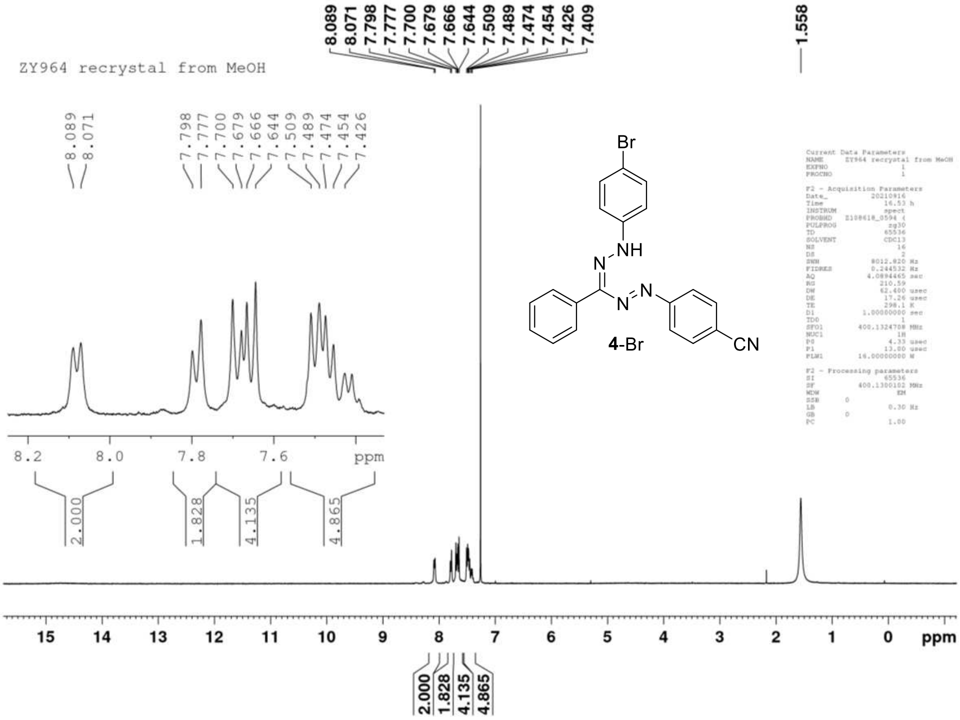

Fig. S65. ^{1}H-NMR spectrum for compound **4**-Br (sample label: zy964, $CDCl_3$, 400 MHz).

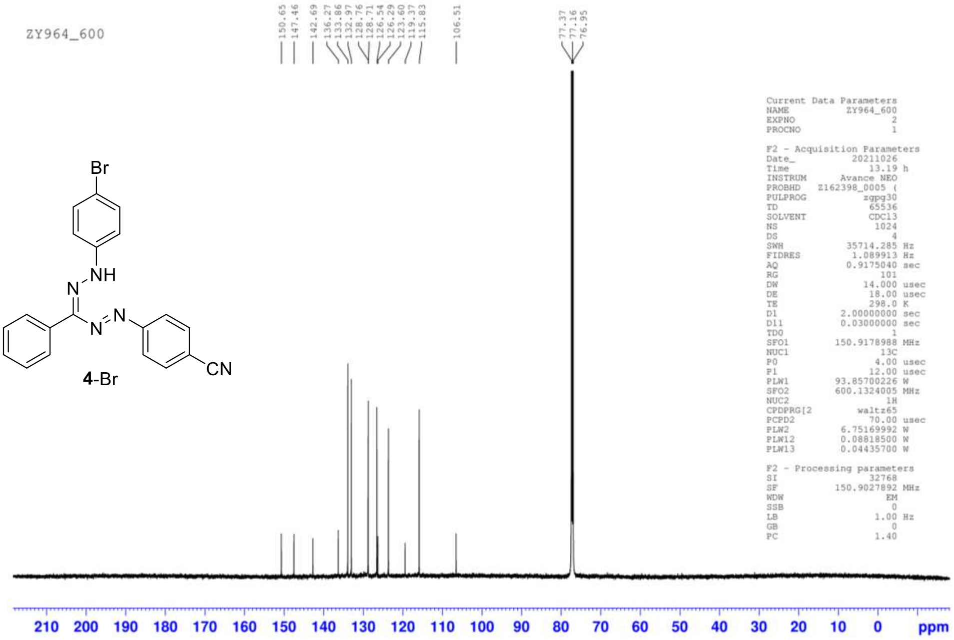

Fig. S66. ^{13}C-NMR spectrum for compound **4**-Br (sample label: zy964, $CDCl_3$, 150 MHz).

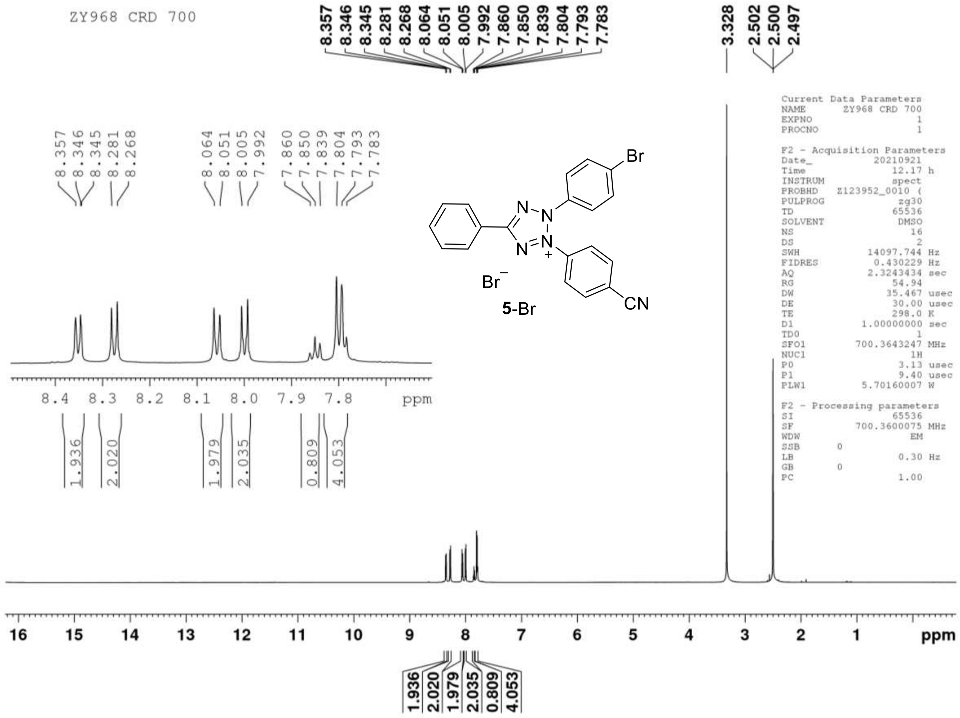

Fig. S67. ^{1}H-NMR spectrum for compound **5**-Br (sample label: zy968, DMSO-d_6, 400 MHz).

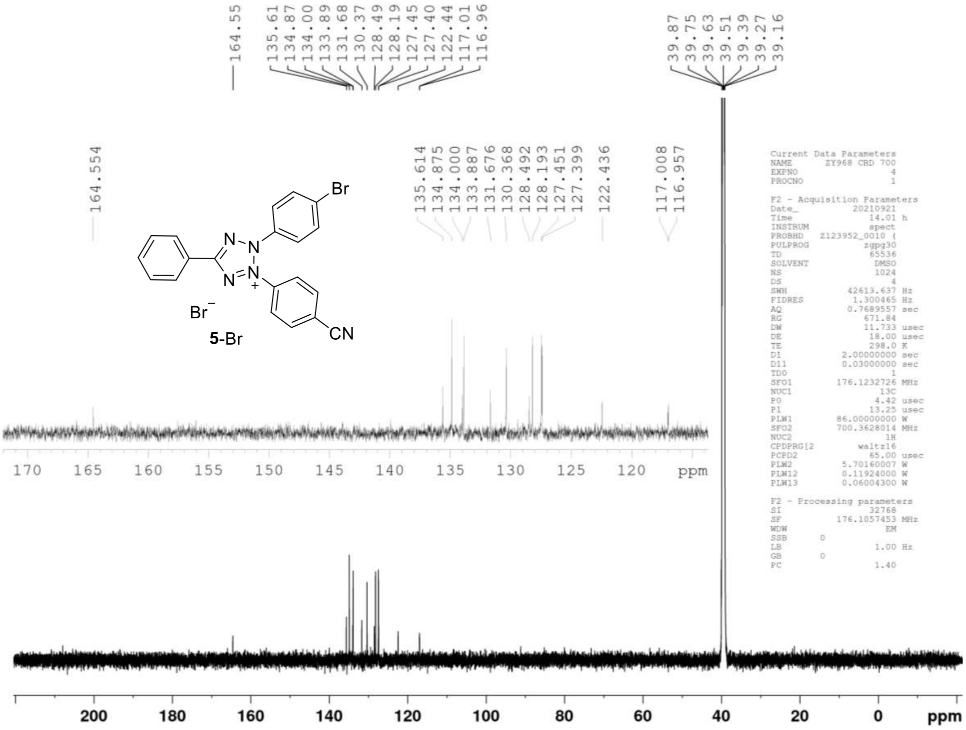

Fig. S68. ^{13}C-NMR spectrum for compound **5**-Br (sample label: zy968, DMSO-d_6, 176 MHz).

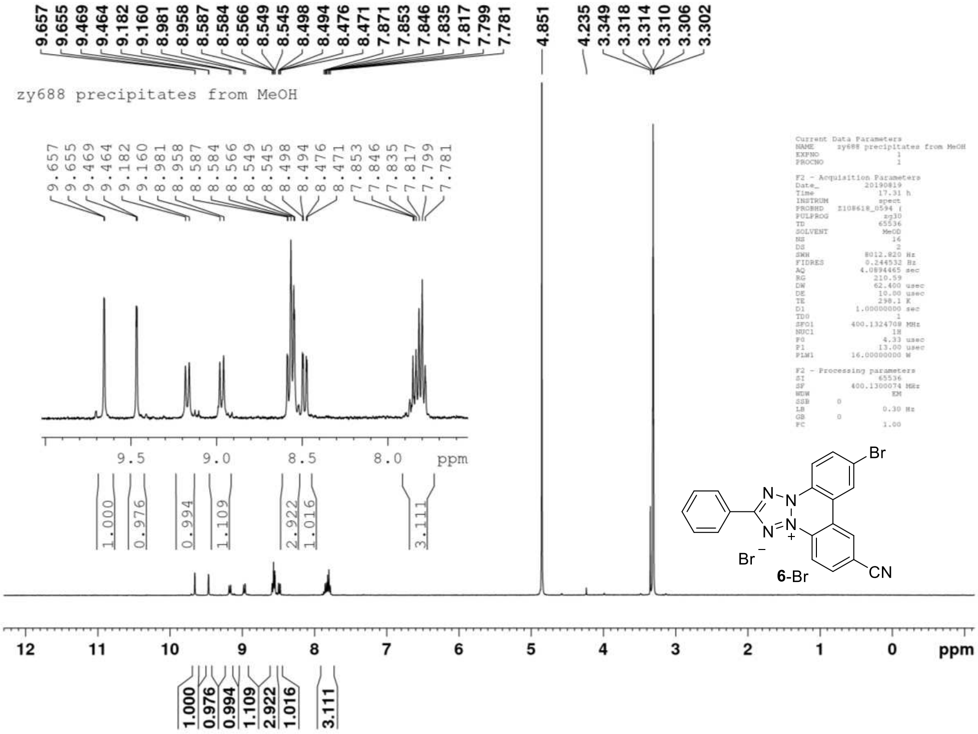

Fig. S69. ^{1}H-NMR spectrum for compound **6**-Br (sample label: zy688, methanol-d_4, 400 MHz).

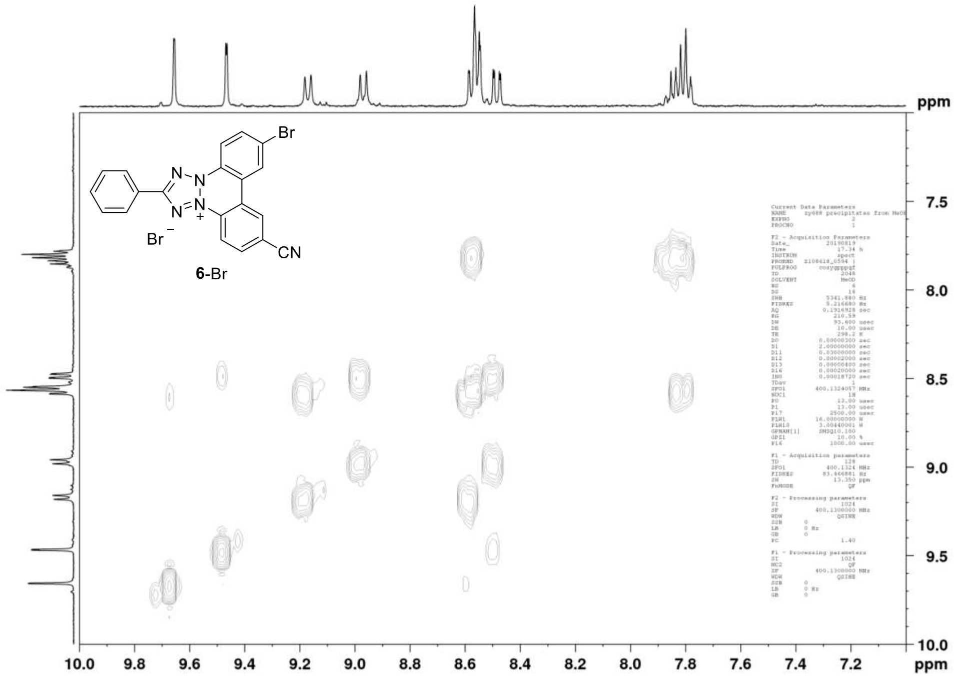

Fig. S70. ^{1}H-^{1}H COSY spectrum for compound **6**-Br (sample label: zy688, methanol-d_4, 400 MHz).

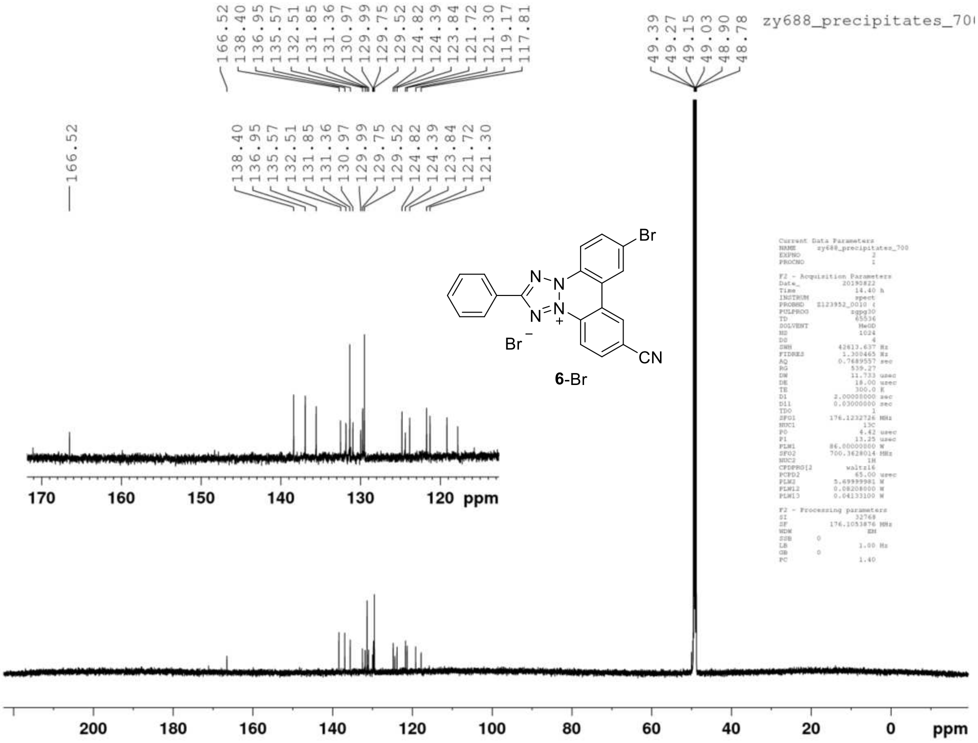

Fig. S71. ^{13}C-NMR spectrum for compound **6**-Br (sample label: zy688, methanol-d_4, 176 MHz).

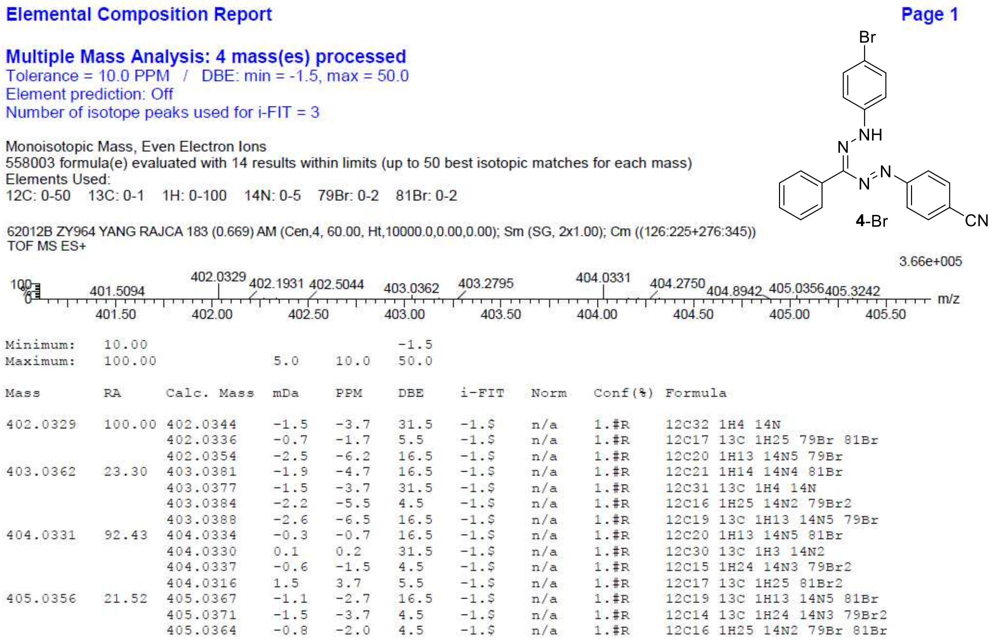

Elemental Composition Report

Page 1

Multiple Mass Analysis: 4 mass(es) processed
Tolerance = 10.0 PPM / DBE: min = -1.5, max = 50.0
Element prediction: Off
Number of isotope peaks used for i-FIT = 3

Monoisotopic Mass, Even Electron Ions
558003 formula(e) evaluated with 14 results within limits (up to 50 best isotopic matches for each mass)
Elements Used:
12C: 0-50 13C: 0-1 1H: 0-100 14N: 0-5 79Br: 0-2 81Br: 0-2

62012B ZY964 YANG RAJCA 183 (0.669) AM (Cen,4, 60.00, Ht,10000.0,0.00,0.00); Sm (SG, 2x1.00); Cm ((126:225+276:345))
TOF MS ES+

```
Minimum:    10.00                          -1.5
Maximum:    100.00              5.0   10.0  50.0

Mass        RA     Calc. Mass  mDa   PPM   DBE   i-FIT  Norm  Conf(%) Formula

402.0329    100.00 402.0344    -1.5  -3.7  31.5  -1.$   n/a   1.#R    12C32 1H4 14N
                   402.0336    -0.7  -1.7  5.5   -1.$   n/a   1.#R    12C17 13C 1H25 79Br 81Br
                   402.0354    -2.5  -6.2  16.5  -1.$   n/a   1.#R    12C20 1H13 14N5 79Br
403.0362    23.30  403.0381    -1.9  -4.7  16.5  -1.$   n/a   1.#R    12C21 1H14 14N4 81Br
                   403.0377    -1.5  -3.7  31.5  -1.$   n/a   1.#R    12C31 13C 1H4 14N
                   403.0384    -2.2  -5.5  4.5   -1.$   n/a   1.#R    12C16 1H25 14N2 79Br2
                   403.0388    -2.6  -6.5  16.5  -1.$   n/a   1.#R    12C19 13C 1H13 14N5 79Br
404.0331    92.43  404.0334    -0.3  -0.7  16.5  -1.$   n/a   1.#R    12C20 1H13 14N5 81Br
                   404.0330    0.1   0.2   31.5  -1.$   n/a   1.#R    12C30 13C 1H3 14N2
                   404.0337    -0.6  -1.5  4.5   -1.$   n/a   1.#R    12C15 1H24 14N3 79Br2
                   404.0316    1.5   3.7   5.5   -1.$   n/a   1.#R    12C17 13C 1H25 81Br2
405.0356    21.52  405.0367    -1.1  -2.7  16.5  -1.$   n/a   1.#R    12C19 13C 1H13 14N5 81Br
                   405.0371    -1.5  -3.7  4.5   -1.$   n/a   1.#R    12C14 13C 1H24 14N3 79Br2
                   405.0364    -0.8  -2.0  4.5   -1.$   n/a   1.#R    12C16 1H25 14N2 79Br 81Br
```

Fig. S72. HR-ESI MS for compound **4**-Br (sample label: ZY964): calcd 402.0354 for $C_{20}H_{13}N_5{}^{79}Br$, found 402.0329 (-6.2 ppm, RA = 100%); calcd 404.0334 for $C_{20}H_{13}N_5{}^{81}Br$, found 404.0331 (-0.7 ppm, RA = 92%). Most likely under the ESI conditions, formazan **4**-Br gets oxidized to tetrazolyl cation **5**-Br.

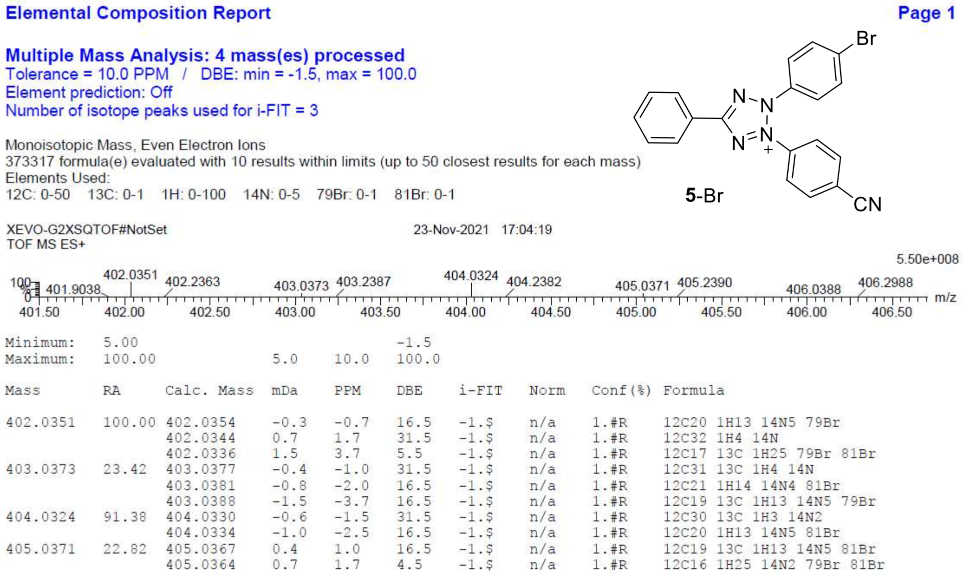

Elemental Composition Report **Page 1**

Multiple Mass Analysis: 4 mass(es) processed
Tolerance = 10.0 PPM / DBE: min = -1.5, max = 100.0
Element prediction: Off
Number of isotope peaks used for i-FIT = 3

Monoisotopic Mass, Even Electron Ions
373317 formula(e) evaluated with 10 results within limits (up to 50 closest results for each mass)
Elements Used:
12C: 0-50 13C: 0-1 1H: 0-100 14N: 0-5 79Br: 0-1 81Br: 0-1

5-Br

XEVO-G2XSQTOF#NotSet 23-Nov-2021 17:04:19
TOF MS ES+

```
Minimum:    5.00                          -1.5
Maximum:    100.00          5.0    10.0   100.0

Mass        RA     Calc. Mass mDa    PPM    DBE    i-FIT   Norm   Conf(%) Formula

402.0351    100.00 402.0354   -0.3   -0.7   16.5   -1.$    n/a    1.#R    12C20 1H13 14N5 79Br
                   402.0344   0.7    1.7    31.5   -1.$    n/a    1.#R    12C32 1H4 14N
                   402.0336   1.5    3.7    5.5    -1.$    n/a    1.#R    12C17 13C 1H25 79Br 81Br
403.0373    23.42  403.0377   -0.4   -1.0   31.5   -1.$    n/a    1.#R    12C31 13C 1H4 14N
                   403.0381   -0.8   -2.0   16.5   -1.$    n/a    1.#R    12C21 1H14 14N4 81Br
                   403.0388   -1.5   -3.7   16.5   -1.$    n/a    1.#R    12C19 13C 1H13 14N5 79Br
404.0324    91.38  404.0330   -0.6   -1.5   31.5   -1.$    n/a    1.#R    12C30 13C 1H3 14N2
                   404.0334   -1.0   -2.5   16.5   -1.$    n/a    1.#R    12C20 1H13 14N5 81Br
405.0371    22.82  405.0367   0.4    1.0    16.5   -1.$    n/a    1.#R    12C19 13C 1H13 14N5 81Br
                   405.0364   0.7    1.7    4.5    -1.$    n/a    1.#R    12C16 1H25 14N2 79Br 81Br
```

Fig. S73. HR-ESI MS for compound **5**-Br (sample label: ZY968): calcd 402.0354 for $C_{20}H_{13}N_5{}^{79}Br$, found 402.0351 (-0.7 ppm, RA = 100%); calcd 404.0334 for $C_{20}H_{13}N_5{}^{81}Br$, found 404.0324 (-2.5 ppm, RA = 91%)

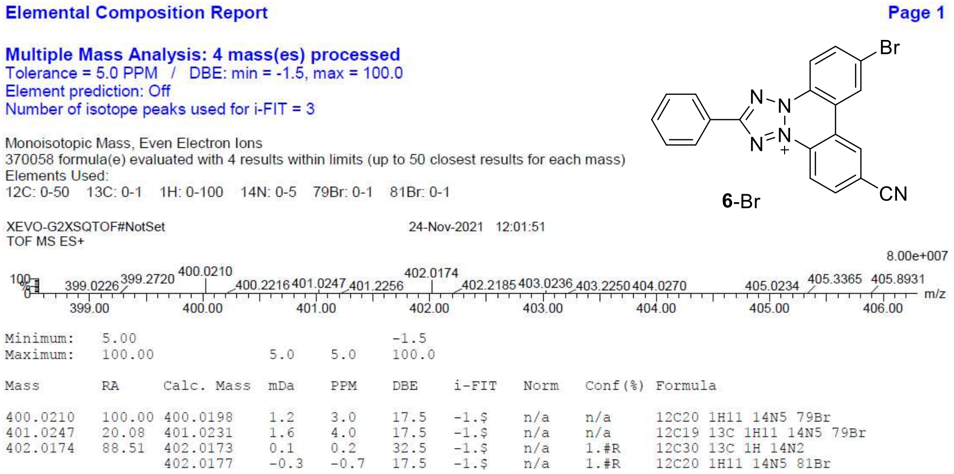

Elemental Composition Report **Page 1**

Multiple Mass Analysis: 4 mass(es) processed
Tolerance = 5.0 PPM / DBE: min = -1.5, max = 100.0
Element prediction: Off
Number of isotope peaks used for i-FIT = 3

Monoisotopic Mass, Even Electron Ions
370058 formula(e) evaluated with 4 results within limits (up to 50 closest results for each mass)
Elements Used:
12C: 0-50 13C: 0-1 1H: 0-100 14N: 0-5 79Br: 0-1 81Br: 0-1

6-Br

XEVO-G2XSQTOF#NotSet 24-Nov-2021 12:01:51
TOF MS ES+

```
Minimum:    5.00                          -1.5
Maximum:    100.00          5.0    5.0    100.0

Mass        RA     Calc. Mass mDa    PPM    DBE    i-FIT   Norm   Conf(%) Formula

400.0210    100.00 400.0198   1.2    3.0    17.5   -1.$    n/a    n/a     12C20 1H11 14N5 79Br
401.0247    20.08  401.0231   1.6    4.0    17.5   -1.$    n/a    n/a     12C19 13C 1H11 14N5 79Br
402.0174    88.51  402.0173   0.1    0.2    32.5   -1.$    n/a    1.#R    12C30 13C 1H 14N2
                   402.0177   -0.3   -0.7   17.5   -1.$    n/a    1.#R    12C20 1H11 14N5 81Br
```

Fig. S74. HR-ESI MS for compound **6**-Br (sample label: ZY974): calcd 400.0198 for $C_{20}H_{11}N_5{}^{79}Br$, found 400.0210 (3.0 ppm, RA = 100%); calcd 402.0177 for $C_{20}H_{11}N_5{}^{81}Br$, found 402.0174 (0.7 ppm, RA = 89%).

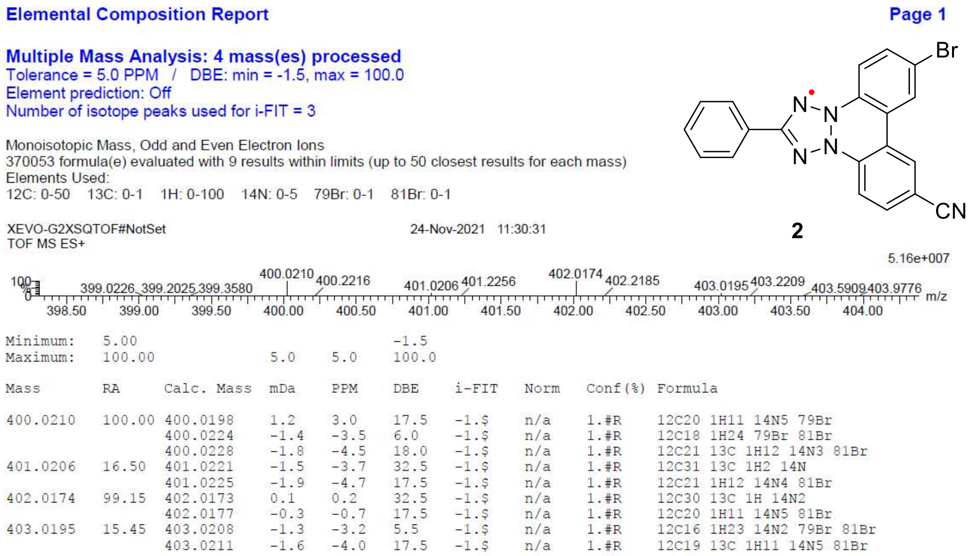

Elemental Composition Report **Page 1**

Multiple Mass Analysis: 4 mass(es) processed
Tolerance = 5.0 PPM / DBE: min = -1.5, max = 100.0
Element prediction: Off
Number of isotope peaks used for i-FIT = 3

Monoisotopic Mass, Odd and Even Electron Ions
370053 formula(e) evaluated with 9 results within limits (up to 50 closest results for each mass)
Elements Used:
12C: 0-50 13C: 0-1 1H: 0-100 14N: 0-5 79Br: 0-1 81Br: 0-1

XEVO-G2XSQTOF#NotSet 24-Nov-2021 11:30:31
TOF MS ES+

```
Minimum:    5.00                         -1.5
Maximum:    100.00            5.0   5.0   100.0

Mass        RA     Calc. Mass mDa   PPM   DBE    i-FIT   Norm   Conf(%) Formula

400.0210    100.00 400.0198   1.2   3.0   17.5   -1.$    n/a    1.#R    12C20 1H11 14N5 79Br
                   400.0224   -1.4  -3.5  6.0    -1.$    n/a    1.#R    12C18 1H24 79Br 81Br
                   400.0228   -1.8  -4.5  18.0   -1.$    n/a    1.#R    12C21 13C 1H12 14N3 81Br
401.0206    16.50  401.0221   -1.5  -3.7  32.5   -1.$    n/a    1.#R    12C31 13C 1H2 14N
                   401.0225   -1.9  -4.7  17.5   -1.$    n/a    1.#R    12C21 1H12 14N4 81Br
402.0174    99.15  402.0173   0.1   0.2   32.5   -1.$    n/a    1.#R    12C30 13C 1H 14N2
                   402.0177   -0.3  -0.7  17.5   -1.$    n/a    1.#R    12C20 1H11 14N5 81Br
403.0195    15.45  403.0208   -1.3  -3.2  5.5    -1.$    n/a    1.#R    12C16 1H23 14N2 79Br 81Br
                   403.0211   -1.6  -4.0  17.5   -1.$    n/a    1.#R    12C19 13C 1H11 14N5 81Br
```

Fig. S75. HR-ESI MS for radical **2** (sample label: ZY876): calcd 400.0198 for $C_{20}H_{11}N_5{}^{79}Br$, found 400.0210 (3.0 ppm, RA = 100%); calcd 402.0177 for $C_{20}H_{11}N_5{}^{81}Br$, found 402.0174 (0.7 ppm, RA = 99%)

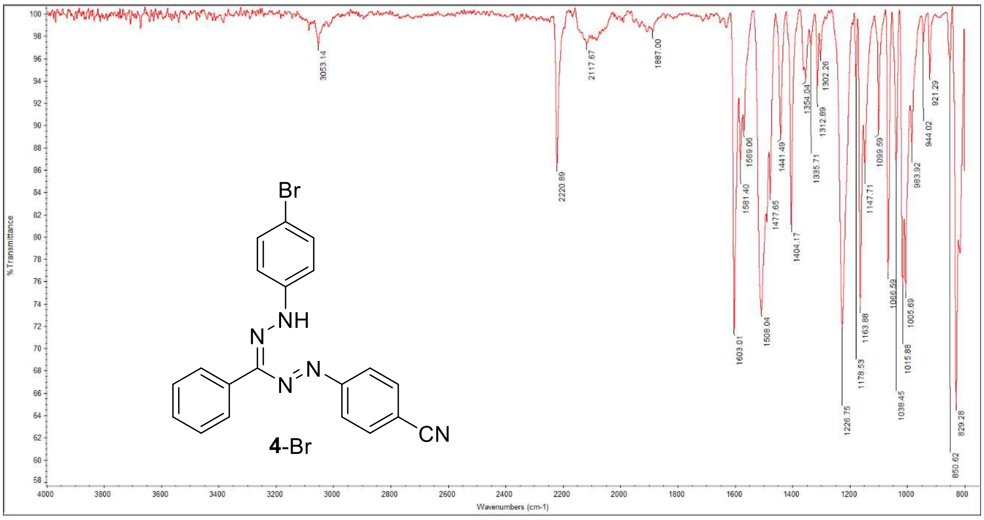

Fig. S76. IR spectrum of compound **4**-Br (ATR, ZnSe) (sample label: ZY964).

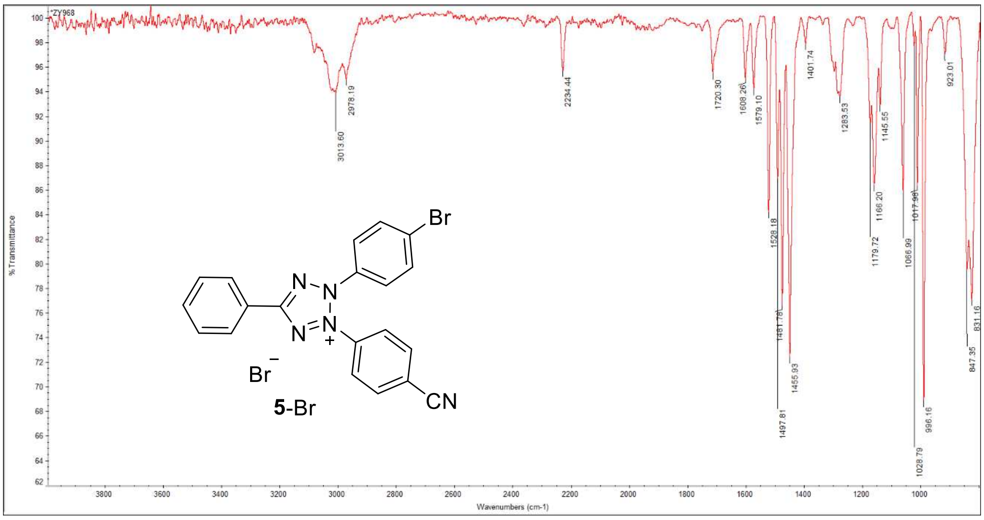

Fig. S77. IR spectrum of compound **5**-Br (ATR, ZnSe) (sample label: ZY968).

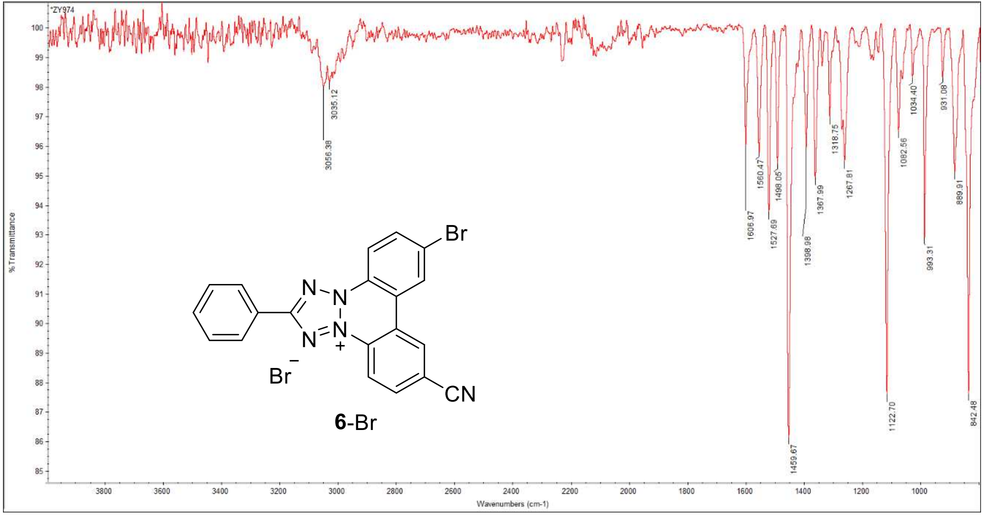

Fig. S78. IR spectrum of compound **6**-Br (ATR, ZnSe) (sample label: ZY974).

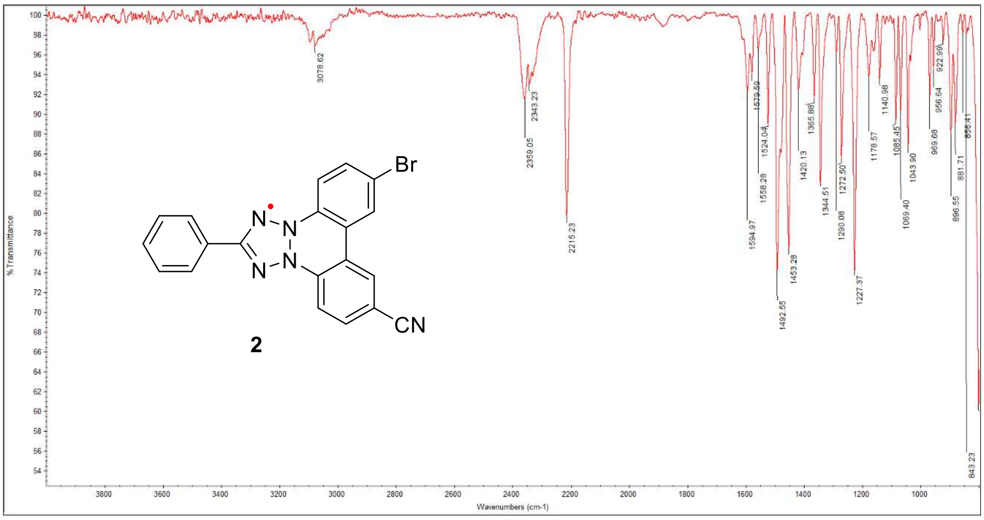

Fig. S79. IR spectrum of radical **2** (ATR, ZnSe) (sample label: ZY981).

6. DFT Optimized Geometries and Total Energies for 1 and 2.

Radical 1, C_{2v} at UB3LYP/6-31G(d,p)/D3BJ/PCM-UFF+ZPVE in benzene.

```
Stoichiometry    C21H11N6(2)
 Framework group  C2V[C2(CCCH),SGV(C18H10N6)]
 Deg. of freedom    37
 Full point group                 C2V     NOp   4
 Largest Abelian subgroup         C2V     NOp   4
 Largest concise Abelian subgroup C2      NOp   2
                         Standard orientation:
 ---------------------------------------------------------------------
 Center     Atomic      Atomic             Coordinates (Angstroms)
 Number     Number       Type             X           Y           Z
 ---------------------------------------------------------------------
      1          7           0        0.000000    1.136530    1.758561
      2          7           0        0.000000    0.694075    0.479547
      3          7           0       -0.000000   -0.694075    0.479547
      4          7           0       -0.000000   -1.136530    1.758561
      5          7           0       -0.000000    4.287215   -5.218572
      6          7           0       -0.000000   -4.287215   -5.218572
      7          6           0       -0.000000    0.000000    2.476756
      8          6           0       -0.000000    1.431309   -0.675410
      9          6           0        0.000000    2.835050   -0.605949
     10          1           0        0.000000    3.313664    0.364168
     11          6           0       -0.000000    3.568123   -1.777200
     12          1           0       -0.000000    4.651208   -1.740960
     13          6           0       -0.000000    2.910357   -3.022570
     14          6           0       -0.000000    1.506674   -3.076895
     15          1           0       -0.000000    1.029472   -4.048223
     16          6           0       -0.000000    0.737336   -1.915642
     17          6           0       -0.000000   -0.737336   -1.915642
     18          6           0       -0.000000   -1.506674   -3.076895
     19          1           0       -0.000000   -1.029472   -4.048223
     20          6           0       -0.000000   -2.910357   -3.022570
     21          6           0       -0.000000   -3.568123   -1.777200
     22          1           0       -0.000000   -4.651208   -1.740960
     23          6           0       -0.000000   -2.835050   -0.605949
     24          1           0       -0.000000   -3.313664    0.364168
     25          6           0       -0.000000   -1.431309   -0.675410
     26          6           0       -0.000000    0.000000    3.941872
     27          6           0        0.000000   -1.213081    4.644364
     28          1           0        0.000000   -2.146660    4.093323
     29          6           0        0.000000   -1.209324    6.036353
     30          1           0        0.000000   -2.150375    6.576830
     31          6           0       -0.000000    0.000000    6.734977
     32          1           0       -0.000000    0.000000    7.820408
     33          6           0        0.000000    1.209324    6.036353
     34          1           0        0.000000    2.150375    6.576830
     35          6           0        0.000000    1.213081    4.644364
     36          1           0        0.000000    2.146660    4.093323
     37          6           0       -0.000000    3.667957   -4.232534
     38          6           0       -0.000000   -3.667957   -4.232534
 ---------------------------------------------------------------------
 Rotational constants (GHZ):      0.2713214           0.1166230           0.0815641;  Standard basis: 6-31G(d,p) (6D, 7F)
The electronic state is 2-A2.   Error on total polarization charges =  0.01043
SCF Done:  E(UB3LYP) = -1135.39861371 A.U. after 1 cycles;  NFock=  1,  Conv=0.53D-08,  -V/T= 2.0095,  <Sx>= 0.0000 <Sy>= 0.0000  <Sz>=
0.5000, <S**2>= 0.7686 S= 0.5093;  <L.S>=  0.000000000000; Annihilation of the first spin contaminant: S**2 before annihilation 0.7686, after 0.7503
The lowest vibrational freqs. (cm-1): 16.3513 (A2),  30.1114 (B1), 39.6622 (A2) (all real, positive)
         Item                      Value      Threshold   Converged?
 Maximum Force              0.000004     0.000015      YES
 RMS     Force              0.000001     0.000010      YES
 Maximum Displacement   0.000015     0.000060      YES
 RMS     Displacement     0.000004     0.000040      YES
 Predicted change in Energy=-1.515573D-10. Optimization completed. Stationary point found.
 RMSF=1.336e-06; RMSD=3.833e-09
```

Radical 2, C_s at UB3LYP/6-31G(d,p)/D3BJ/PCM-UFF+ZPVE in benzene.

```
Stoichiometry    C20H11BrN5(2)
 Framework group  CS[SG(C20H11BrN5)]
 Deg. of freedom    71
 Full point group                 CS      NOp   2
 Largest Abelian subgroup         CS      NOp   2
 Largest concise Abelian subgroup C1      NOp   1
                         Standard orientation:
 ---------------------------------------------------------------------
 Center     Atomic      Atomic             Coordinates (Angstroms)
 Number     Number       Type             X           Y           Z
 ---------------------------------------------------------------------
      1          7           0       -0.081291   -2.372167    0.000000
      2          7           0       -0.000000   -1.020638    0.000000
      3          7           0        1.336527   -0.644331   -0.000000
      4          7           0        2.108637   -1.758861   -0.000000
      5          7           0        3.258410    5.812285   -0.000000
      6          6           0        1.205826   -2.755907   -0.000000
      7          6           0       -1.024381   -0.100293    0.000000
      8          6           0       -2.356181   -0.536503    0.000000
      9          1           0       -2.564409   -1.598400    0.000000
     10          6           0       -3.379360    0.401104    0.000000
     11          1           0       -4.413896    0.080633    0.000000
     12          6           0       -3.061374    1.759997    0.000000
     13          6           0       -1.740234    2.196312    0.000000
     14          1           0       -1.539879    3.259273    0.000000
     15          6           0       -0.686910    1.276221    0.000000
     16          6           0        0.732436    1.673508   -0.000000
     17          6           0        1.159497    2.998160   -0.000000
     18          1           0        0.436155    3.803193   -0.000000
     19          6           0        2.526773    3.326413   -0.000000
     20          6           0        3.495305    2.302934   -0.000000
     21          1           0        4.548191    2.560064   -0.000000
     22          6           0        3.106569    0.977579   -0.000000
     23          1           0        3.829631    0.172996   -0.000000
     24          6           0        1.734667    0.663282   -0.000000
     25          6           0        1.601232   -4.167281   -0.000000
     26          6           0        2.958645   -4.516877   -0.000000
     27          1           0        3.708510   -3.734006   -0.000000
     28          6           0        3.330831   -5.858373   -0.000000
     29          1           0        4.382926   -6.124721   -0.000000
     30          6           0        2.355198   -6.857601   -0.000000
     31          1           0        2.648119   -7.902802   -0.000000
     32          6           0        1.002263   -6.510882   -0.000000
     33          1           0        0.241835   -7.285224    0.000000
     34          6           0        0.623190   -5.171446    0.000000
     35          1           0       -0.424328   -4.892263    0.000000
     36          6           0        2.929262    4.694894   -0.000000
     37         35           0       -4.465382    3.050737    0.000000
 ---------------------------------------------------------------------
 Rotational constants (GHZ):           0.2176569           0.0920901           0.0647110;  Standard basis: 6-31G(d,p) (6D, 7F)
The electronic state is 2-A". Error on total polarization charges =  0.00996
 SCF Done:  E(UB3LYP) = -3614.25761126 A.U. after  1 cycles
  NFock=  1;  Conv=0.49D-08;   -V/T= 2.0071
 <Sx>= 0.0000 <Sy>= 0.0000 <Sz>= 0.5000 <S**2>= 0.7683 S= 0.5091;  <L.S>=  0.00000000000
 Annihilation of the first spin contaminant: S**2 before annihilation     0.7683,   after     0.7503
The lowest vibrational freqs. (cm-1): 22.3835 (A"), 28.6638 (A"), 44.0243 (A") (all real, positive).
         Item               Value     Threshold  Converged?
 Maximum Force            0.000015     0.000015     YES
 RMS     Force            0.000003     0.000010     YES
 Maximum Displacement     0.000045     0.000060     YES
 RMS     Displacement     0.000008     0.000040     YES
 Predicted change in Energy=-1.937348D-09.  Optimization completed.    -- Stationary point found.
RMSF=6.369e-06; RMSD=4.043e-09
```

7. Supporting References

S1. SAINT V8.40A (2020), Bruker AXS, Madison, WI, 2018.

S2. Krause, L.; Herbst-Irmer, R.; Sheldrick, G. M.; Stalke, D. Comparison of silver and molybdenum microfocus X-ray sources for single-crystal structure determination. *J. Appl. Cryst.* **2015**, *48*, 3–10. doi:10.1107/S1600576714022985.

S3. Sheldrick, G. M. SHELXT--Integrated space-group and crystal-structure determination. *Acta Cryst. A* **2015**, *71*, 3–8. doi:10.1107/S2053273314026370.

S4. Sheldrick, G. M. Crystal structure refinement with SHELXL. *Acta Cryst. C* **2015**, *71*, 3–8. doi:10.1107/S2053229614024218.

S5. Katritzky, A. A.; Belyakov, S. A.; Cheng, D.; Durst, H. D., Syntheses of Formazans Under Phase-Transfer Conditions. *Synthesis* **1995**, *1995* (05), 577-581.

S6. Neugebauer, F. A. Substituted 5-T-butyl tetrazolinyl and phototetrazolinyl radicals. *Tetrahedron* **1970**, *26* (20), 4843-4851.

S7. Kuhn, R.; Jerchel, D., Kristallisiertes 2,3-Diphenylen-5-phenyl-tetrazolium-Radikal. *Justus Liebigs Annalen der Chemie* **1952**, *578* (1), 1-5.

S8. Frisch, M. J.; Trucks, G. W.; Schlegel, H. B.; Scuseria, G. E.; Robb, M. A.; Cheeseman, J. R.; Scalmani, G.; Barone, V.; Petersson, G. A.; Nakatsuji, H.; Li, X.; Caricato, M.; Marenich, A. V.; Bloino, J.; Janesko, B. G.; Gomperts, R.; Mennucci, B.; Hratchian, H. P.; Ortiz, J. V.; Izmaylov, A. F.; Sonnenberg, J. L.; Williams-Young, D.; Ding, F.; Lipparini, F.; Egidi, F.; Goings, J.; Peng, B.; Petrone, A.; Henderson, T.; Ranasinghe, D.; Zakrzewski, V. G.; Gao, J.; Rega, N.; Zheng, G.; Liang, W.; Hada, M.; Ehara, M.; Toyota, K.; Fukuda, R.; Hasegawa, J.; Ishida, M.; Nakajima, T.; Honda, Y.; Kitao, O.; Nakai, H.; Vreven, T.; Throssell, K.; Montgomery, J. A., Jr.; Peralta, J. E.; Ogliaro, F.; Bearpark, M. J.; Heyd, J. J.; Brothers, E. N.; Kudin, K. N.; Staroverov, V. N.; Keith, T. A.; Kobayashi, R.; Normand, J.; Raghavachari, R.; Rendell, A. P.; Burant, J. C.; Iyengar, S. S.; Tomasi, J.; Cossi, M.; Millam, J. M.; Klene, M.; Adamo, C.; Cammi, R.; Ochterski, J. W.; Martin, R. L.; Morokuma, K.; Farkas, O.; Foresman, J. B.; Fox, D. J. *Gaussian 16*, revision A.03; Gaussian, Inc.: Wallingford, CT, 2016.

S9. Grimme, S.; Antony, J.; Ehrlich, S.; Krieg, H. A consistent and accurate ab initio parametrization of density functional dispersion correction (DFT-D) for the 94 elements H-Pu. *J. Chem. Phys.* **2010**, *132*, 154104−154118.

S10. Grimme, S.; Ehrlich, S.; Goerigk, L. Effect of the damping function in dispersion corrected density functional theory. *J. Comput. Chem.* **2011**, *32*, 1456−1465.

S11. Allouche, A.-R. Gabedit—A graphical user interface for computational chemistry softwares. *J. Comput. Chem.* **2011**, *32*, 174–182.

S12. Connelly, N. G.; Geiger, W. E. Chemical Redox Agents for Organometallic Chemistry. *Chem. Rev.* **1996**, *96*, 877–910.

S13. Yordanov, N. D.; Christova, A. G. DPPH as a primary standard for quantitative EPR spectrometry. *Appl. Magn. Reson*. **1996**, *10*, 339–350.

S14. Stoll, S.; Schweiger, A. EasySpin, a comprehensive software package for spectral simulation and analysis in EPR. *J. Magn. Reson.* **2006**, *178*, 42–55.

S15. Kahn, O. *Molecular magnetism*, Wiley-VCH, New York, 1993, Ch. 11, p. 272, Eq. 11.1.5.

S16. Rajca, A. Organic diradicals and polyradicals: from spin coupling to magnetism?. *Chem. Rev.* **1994**, *94*, 871–893.

S17. Kahn, O. *Molecular magnetism*, Wiley-VCH, New York, 1993, Table 1.1.

S18. Casu, M. B. Nanoscale Studies of Organic Radicals: Surface, Interface, and Spinterface. *Acc. Chem. Res.* **2018**, *51*, 753–760.

S19. Wagner, C. D., Sensitivity factors for XPS analysis of surface atoms. *J. Electron Spectrosc. Relat. Phenom.* **1983,** *32*, 99–102.

B. Unlocking the Electronic Structure and Morphology of Dicyano Tetrazolinyl Radical Assemblies on Polycrystalline Gold and Hybrid Surfaces.

This section provides the results obtained by performing a fit procedure on the N 1*s* and C 1*s* core-level spectra of dicyano tetrazolinyl radical assemblies grown on polycrystalline gold and hybrid substrates. Two systems of dicyano tetrazolinyl radical are discussed in section 4.2.

B.1. Assemblies of Dicyano Tetrazolinyl Radical on Polycrystalline Gold

Fit parameters and results for the N 1*s* and C 1*s* core-level spectra of radical assembly at the interface with gold are given in table 1 and 2.

	Energy (eV)	**Lorentzian Width (eV)**	**Gaussian Width (eV)**	**Intensity %**	**Theoretical Values %**
$N_{1,2,3,4}$	399.5	0.1	1.6	64.4	66.7
S_1	400.3	0.1	1.6	2.3	
$-CN_{5,6}$	401.4	0.1	1.6	22.4	33.3
S_2	402.4	0.1	1.6	2.9	
S_3	404.5	0.1	1.6	8.0	

Table 1.: Assembly at the interface (nominal 0.1 nm): fit results and parameters obtained for the N 1*s* core-level spectrum.

	Energy (eV)	**Lorentzian Width (eV)**	**Gaussian Width (eV)**	**Intensity %**	**Theoretical** Values %
C−C	284.3	0.08	1.2	22.4	23.8
C−H	284.7	0.08	1.2	29.9	52.4
S_1	285.5	0.08	1.2	3.1	
C−N	285.6	0.08	1.4	23.6	23.8
S_2	286.9	0.08	1.5	11.8	
S_3	289.2	0.08	2.2	9.2	

Table 2.: Assembly at the interface (nominally 0.1 nm) with gold: fit results and parameters obtained for the C 1*s* core-level spectrum.

Fit parameters and results for the N 1*s* and C 1*s* core-level spectra of a 0.3 nm thick radical assembly on gold are given in table 3 and 4.

	Energy (eV)	**Lorentzian Width (eV)**	**Gaussian Width (eV)**	**Intensity %**	**Theoretical Values %**
N_1	398.8	0.1	1.1	19.4	16.7
$N_{2,3,4}$	399.8	0.1	1.1	37.9	50.0
S_1	401.1	0.1	1.1	7.1	
$-CN_{5,6}$	402.4	0.1	1.1	27.7	33.3
S_2	404.1	0.1	1.4	6.2	
S_3	404.7	0.1	1.4	1.7	

Table 3.: A 0.3 nm thick assembly on gold: fit results and parameters obtained for the N 1*s* core-level spectrum.

	Energy (eV)	**Lorentzian Width (eV)**	**Gaussian Width (eV)**	**Intensity %**	**Theoretical** Values %
C−C	284.7	0.08	1.2	23.8	23.8
C−H	285.3	0.08	1.2	35.4	52.4
S_1	286.0	0.08	1.2	2.3	
C−N	286.5	0.08	1.6	23.1	23.8
S_2	287.0	0.08	1.5	8.1	
S_3	290.0	0.08	4.6	7.3	

Table 4.: A 0.3 nm thick assembly on gold: fit results and parameters obtained for the C 1*s* core-level spectrum.

Fit parameters and results for the N 1*s* and C 1*s* core-level spectra of a 2.9 nm thick radical assembly are given in table 5 and 6.

	Energy (eV)	**Lorentzian Width (eV)**	**Gaussian Width (eV)**	**Intensity %**	**Theoretical Values %**
N_1	399.1	0.1	1.1	20.0	16.7
$N_{2,3,4}$	400.1	0.1	1.1	40.0	50.0
S_1	401.2	0.1	1.1	4.1	
$-CN_{5,6}$	402.7	0.1	1.1	29.0	33.3
S_2	403.6	0.1	1.4	4.9	
S_3	405.1	0.1	1.4	2.0	

Table 5.: Thick assembly (nominally 2.9 nm) on gold: fit results and parameters obtained for the N 1*s* core-level spectrum.

	Energy (eV)	**Lorentzian Width (eV)**	**Gaussian Width (eV)**	**Intensity %**	**Theoretical** Values %
C−C	284.9	0.08	1.2	23.2	23.8
C−H	285.5	0.08	1.2	39.8	52.4
S_1	286.2	0.08	1.2	1.7	
C−N	286.7	0.08	1.6	23.5	23.8
S_2	287.2	0.08	1.3	5.8	
S_3	290.1	0.08	4.6	6.0	

Table 6.: Thick assembly (nominally 2.9 nm) on gold: fit results and parameters obtained for the C 1*s* core-level spectrum.

B.2. Assemblies of Dicyano Tetrazolinyl Radical on Hybrid Substrates

Fit parameters and results for the N 1s core-level spectra of radical assemblies deposited on a hybrid substrate consisting of polycrystalline gold and SiO_2/Si(111) surfaces are given in table 7 and 8.

	Energy (eV)	**Lorentzian Width (eV)**	**Gaussian Width (eV)**	**Intensity %**	**Theoretical Values %**
N_1	399.0	0.1	1.1	21.7	16.7
$N_{2,3,4}$	400.0	0.1	1.1	37.6	50.0
S_1	401.1	0.1	1.1	4.6	
$-CN_{5,6}$	402.6	0.1	1.1	26.6	33.3
S_2	403.5	0.1	1.4	5.9	
S_3	405.0	0.1	1.4	3.6	

Table 7.: Thick assembly on gold of a hybrid substrate: fit results and parameters obtained for the N 1*s* core-level spectrum.

	Energy (eV)	**Lorentzian Width (eV)**	**Gaussian Width (eV)**	**Intensity %**	**Theoretical Values %**
N_1	399.3	0.1	1.0	18.7	16.7
$N_{2,3,4}$	400.3	0.1	1.0	37.4	50.0
S_1	401.2	0.1	1.0	2.7	
$-CN_{5,6}$	402.9	0.1	1.0	27.9	33.3
S_2	403.6	0.1	1.2	4.6	
S_3	405.6	0.1	3.5	8.7	

Table 8.: Thick assembly on SiO_2/Si(111) of a hybrid substrate: fit results and parameters obtained for the N 1*s* core-level spectrum.

C. Long-Term Degradation Mechanisms in Application-Implemented Radical Thin Films

Reproduced from
E. M. Nowik-Boltyk, T. Junghoefer, M. Glaser, E. Giangrisostomi, R. Ovsyannikov, S. Zhang, C. Shu, A. Rajca, A. Calzolari, M. B. Casu, "Long-Term Degradation Mechanisms in Application-Implemented Radical Thin Films", *ACS Applied Materials & Interfaces* **2023**, *15*, 30935–30943, DOI `10.1021/acsami.3c02057`, `https://doi.org/10.1021/acsami.3c02057`

ACS APPLIED MATERIALS & INTERFACES

www.acsami.org Research Article

Long-Term Degradation Mechanisms in Application-Implemented Radical Thin Films

Ewa Malgorzata Nowik-Boltyk, Tobias Junghoefer, Mathias Glaser, Erika Giangrisostomi, Ruslan Ovsyannikov, Shuyang Zhang, Chan Shu, Andrzej Rajca, Arrigo Calzolari, and M. Benedetta Casu*

Cite This: *ACS Appl. Mater. Interfaces* 2023, 15, 30935−30943 Read Online

ACCESS | Metrics & More | Article Recommendations | Supporting Information

ABSTRACT: Blatter radical derivatives are very attractive due to their potential applications, ranging from batteries to quantum technologies. In this work, we focus on the latest insights regarding the fundamental mechanisms of radical thin film (long-term) degradation, by comparing two Blatter radical derivatives. We find that the interaction with different contaminants (such as atomic H, Ar, N, and O and molecular H_2, N_2, O_2, H_2O, and NH_2) affects the chemical and magnetic properties of the thin films upon air exposure. Also, the radical-specific site, where the contaminant interaction takes place, plays a role. Atomic H and NH_2 are detrimental to the magnetic properties of Blatter radicals, while the presence of molecular water influences more specifically the magnetic properties of the diradical thin films, and it is believed to be the major cause of the shorter diradical thin film lifetime in air.

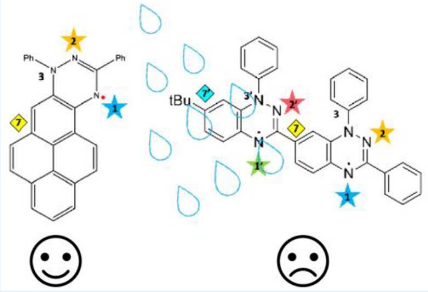

KEYWORDS: *organic radicals, Blatter radicals, thin films, photoemission, ab initio simulations, degradation*

INTRODUCTION

New technologies need new visions and materials and, specifically, sustainable materials. In this respect, organic small molecular compounds might offer feasible routes, in consideration of factors such as raw material availability, ease of synthesis, recyclability, and their potential role in a circular economy.

Inspired by these ideas, we pioneered the controlled growth of organic radical thin films and we introduced the use of soft X-rays to investigate this class of materials.[1,2] Materials with a radical site, i.e., with one or more unpaired electrons that give rise to a permanent magnetic moment,[3−5] are strong candidates for ground-breaking applications,[6−10] because of low-cost, energy saving technologies and eco-friendly production, holding the promise of social impact.[8,11−20] While the function and performance of devices are highly important, the material stability also needs to be addressed if these technologies are to find their way to industrial applications. In this respect, we chose chemically stable organic radicals to grow thin films. We identified the properties, such as high delocalization of the unpaired electrons and high-temperature onset of the thermal degradation that give rise to films stable in ultrahigh vacuum (UHV), under X-rays, and exposed to air.[21−24] Among the various chemically stable organic radical derivatives that are used in a variety of applications, the Blatter radical derivatives were revealed to be very successful.

In fact, the Blatter radical derivatives are very attractive due to their potential applications, ranging from batteries to quantum technologies,[25−33] making them a class of materials of paramount importance with the Blatter radical being an exceptionally chemically stable radical.[34]

We have shown in previous work that the Blatter radical fulfills the necessary conditions to be evaporated without degradation, leading to chemically and thermodynamically stable thin films in ultrahigh vacuum (UHV).[27,35] The stability is due to the large delocalization of the unpaired electron that makes it less prone to reactions.[2,27,35] Also, we found that Blatter radical derivative thin films have a longer life when exposed to air at room temperature[21,35] than other organic radical thin films, such as nitroxides, typically used in prototypical devices and applications.[12,36] Although their lifetime in air is significantly long considering their radical nature, also in comparison with the known values for open and closed shell organic thin films,[22,27,37,38] it is not indefinitely long.

Understanding (long-term) film degradation mechanisms, including their impact on the radical character and therefore on the magnetic properties, is necessary to implement the use

Received: February 13, 2023
Accepted: May 30, 2023
Published: June 15, 2023

ACS Publications

https://doi.org/10.1021/acsami.3c02057
ACS Appl. Mater. Interfaces 2023, 15, 30935−30943

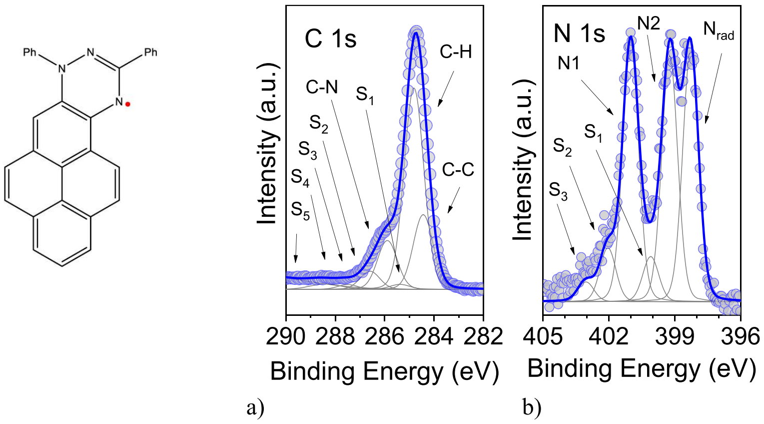

Figure 1. (Left) Molecular structure of the Blatter-pyr. C 1s (a) and N 1s (b) core level spectra of a nominally 6 nm thick film together with their fit analysis (photon energy: 1486.6 eV, for the fit parameters; see the Supporting Information).

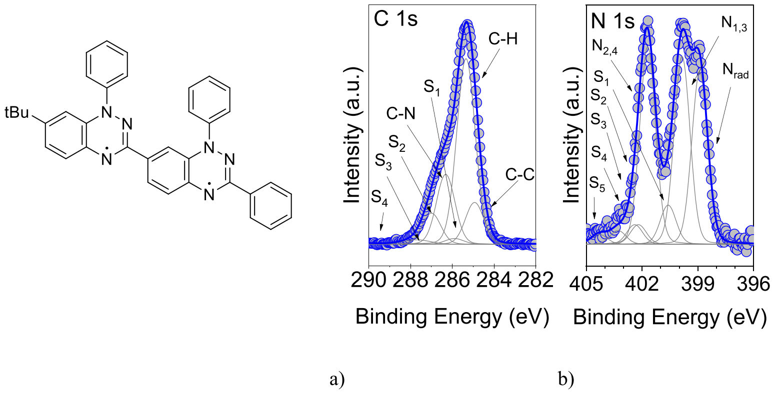

Figure 2. (Left) Molecular structure of diBlatter. C 1s (a) and N 1s (b) core level spectra of a nominally 1 nm thick film together with their fit analysis (photon energy: 1486.6 eV, for the fit parameters; see the Supporting Information).

of the Blatter radical derivatives in devices that could potentially reach the market.[25,26,28]

In this work, we focus on the latest insights regarding the fundamental mechanisms of radical thin film degradation, by comparing two Blatter radical[33,39] derivatives: Blatter-pyr[35] ($C_{29}H_{18}N_3$·, Figure 1) obtained fusing a Blatter radical to a pyrene substituent, and diBlatter[21] ($C_{36}H_{30}N_6$·, Figure 2) obtained fusing two Blatter radicals. The former has one unpaired electron ($S = 1/2$), and the latter has two unpaired electrons ($S = 1$). Our work is based on a complete characterization of the long-term degradation mechanisms shown by the thin films once exposed to air, by using X-ray-based investigations, a robust fit procedure, and ab initio calculations. In particular, X-ray photoelectron spectroscopy (XPS) is a powerful analytical method that allows the monitoring of chemical changes in thin films, also when the system is made of a very small number of molecules. XPS is element-sensitive; its signal is proportional to the element concentration in the investigated systems and coupled with ab initio calculations gives a precise insight into their electronic structure. Introducing this technique to investigate radical thin films revealed its ability to identify whether the unpaired electron of the radical is involved in charge transfer, or a chemical bond, losing its imparity and, consequently, the molecule losing its radical character.[1,40,41]

Ours represents a general approach to investigating the degradation mechanisms in thin films, including organic and inorganic closed-shell thin films.

■ METHODS

Experimental Section. The Blatter-pyr and the diBlatter were synthesized as in refs 35 and 21, respectively. Film deposition and XPS measurements were performed in a UHV system consisting of a substrate preparation chamber and an organic molecular beam deposition (OMBD) dedicated chamber, connected to an analysis chamber (base pressure of (4−9) × 10^{-10} mbar) equipped with a SPECS Phoibos 150 hemispherical electron analyzer and a monochromatic Al Kα source (SPECS Focus 500). Native SiO_2, grown on single-side polished n-Si(111) wafers, was used as a substrate. The substrates were prepared by cleaning in ultrasonic baths of acetone and ethanol, followed by multiple cycles of annealing at around 500 K (i.e., much below the temperature at which the oxide is removed) for several hours. Their cleanness was verified by XPS. Thin films were deposited in situ by OMBD using a Knudsen cell on the substrate kept at room temperature. The evaporation rate (evaporation rate = 0.2 nm/min) was measured with a quartz crystal microbalance, and the nominal thickness was cross-checked by using the attenuation of the XPS substrate signal (Si 2p) after the deposition of the radical. Film characterization and stoichiometry checks were done according to refs 21 and 35. Survey and detailed XPS spectra were measured with electron pass energy of 50 and 20 eV, respectively. The binding energy scale was calibrated by using the Si 2p XPS signal (Si 2p at 99.3 eV[42]). NEXAFS measurements were performed at the third-generation synchrotron radiation source BESSY II at the LowDosePES end station installed at the PM4 beamline ($E/\Delta E$ = 6000 at 400 eV).[43] This end-station was equipped with a similar setup as the one described above. The same calibrated Knudsen cells, used to grow the films for the XPS measurements, were mounted to a preparation chamber attached to the NEXAFS measuring chamber to reproduce the same preparation conditions. NEXAFS spectra were measured in total electron yield and normalized with the clean substrate signal as well as the ring current. Subsequently, they were scaled to give an equal absorption edge jump.[44,45] The reference spectra were measured on freshly prepared films. For measurements probing the film stability and lifetime after air exposure, the beam exposure was further limited, by using shorter acquisition times, to ascribe spectral changes exclusively to the degradation by air exposure. This is the reason for a worse signal-to-noise ratio in those spectra. The samples were kept under air in darkness under standard ambient temperature and pressure.

Calculation Details. Spin-unrestricted geometry optimizations for the Blatter-derived radicals were performed in the density functional theory framework by using the Quantum ESPRESSO software package.[46] All calculations employed the Perdew−Burke−Ernzerhof (PBE) exchange−correlation functional.[47] Single particle wave functions (charge) were expanded in plane waves up to a kinetic energy cutoff of 28 Ry (280 Ry). Ultrasoft pseudopotentials of the Vanderbilt type were used to simulate the ionic potentials.[48] Grimme's implementation of van der Waals corrections was included to improve the nonbonding interactions. A thick layer of vacuum (∼15 Å) in the three spatial directions was included in the simulation cell to avoid spurious interactions between adjacent replicas. Each structure was fully relaxed until the forces on all atoms became lower than 0.03 eV/Å. The core level spectra were calculated in the pseudopotential framework using the final state theory.[49]

■ RESULTS AND DISCUSSION

XPS C 1s core level spectra (Figure 1) of the thick films of Blatter-pyr are characterized by the main line at around 284.6 eV, which is attributed to photoelectrons emitted from the carbon atoms of the aromatic sites (C−C and C−H bound carbons), and a second feature at higher binding energies (285.8 eV) related to contributions from the carbon atoms bound to nitrogen atoms (C−N).[35] These results are mirrored by the N 1s core level spectra (Figure 1) that are characterized by three contributions that correspond to the three different nitrogen atom chemical environments, as expected for an intact Blatter-pyr.[35]

The spectra of the diBlatter films show analogous features (Figure 2). The C 1s main line shows two distinguishable contributions. The N 1s core level spectral main features are three, as expected. They stem from the signal due to photoelectrons emitted from carbon and nitrogen atoms having a similar chemical environment as in the Blatter-pyr (compare Figures 1 and 2). The stoichiometry of the films is further proved by using a well-established fit routine,[21,35,50] systematically correlated with electron paramagnetic resonance (EPR) results on a variety of different radicals,[1,21,27,51−53] which indicates that all components are stoichiometrically meaningful (Tables S1−S4 in the Supporting Information). They are typical of the Blatter-pyr and diBlatter films with the expected EPR pattern corresponding to an intact (di-)radical.[21,27,35]

Before investigating the stability of the films under air exposure, we need to define their time stability under the X-ray beam. Usually, XPS measurements are performed by scanning the sample surface to avoid radiation damage and always measuring a single spectrum on a fresh point of a freshly evaporated film. On the contrary, during this part of the experiment, we kept the beam focused on a single spot for several hours (see Supporting Information). The core level spectra do not show any evidence of chemical changes because we do not see any changes in the shape and intensity of the spectroscopy lines. After around 2 h, small changes are present (Figure S1). They can be ascribed to small morphological modifications, such as island reorganization.[53] This observation is also supported by the NEXAFS spectra that confirm the high stability of the films under the beam exposure with only minor changes in the intensity indicating small structural adjustments under the beam (Figures S2 and S3). The beam stability of the films is a prerequisite to investigating the film lifetime under air exposure without artifacts due to potential radiation damage.

We exposed the films to air keeping them at room temperature (Figures 3 and S4). The C 1s core level spectra are less prone to major changes (Figure S4). It is also interesting to note that there are no new features due to the possible oxidation of the Blatter radicals,[54] as observed in solution using either MnO_2 or $KMnO_4$ as oxidant.[34] The occurrence of a double bond between a carbon atom and an oxygen atom would give rise to an additional feature in the higher binding energy range, i.e., immediately following the C−N component. This feature is not present in our spectra (Figures 4 and S4). For this oxidation pattern to occur, the C7 carbon atom must be such that its position makes a bond with oxygen favorable, as in the Blatter radical.[34] It is sufficient to block it, and the Blatter radical stability toward oxidation is strongly enhanced.[34] In this work, the Blatter-pyr is protected, the Blatter radical being fused to the pyrene, and the diBlatter is protected by a *tert*-butyl group and the second Blatter radical.

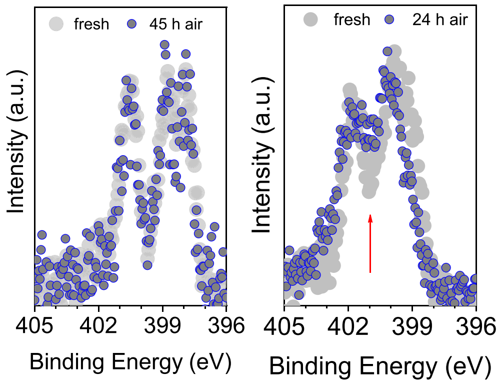

Figure 3. N 1s core level spectra before (light gray) and after (bluish) air exposure for thin films of Blatter-pyr (left panel, after 45 h in air) and diBlatter (right panel, after 24 h in air) (photon energy: 1486.6 eV). The arrow indicates the increased intensity in the 400−401 eV range upon air exposure.

Looking at the C 1s core level spectra, we note that diBlatter thin films show changes on a shorter time scale than the Blatter-pyr thin films (Figure S4). Those changes pertain to the

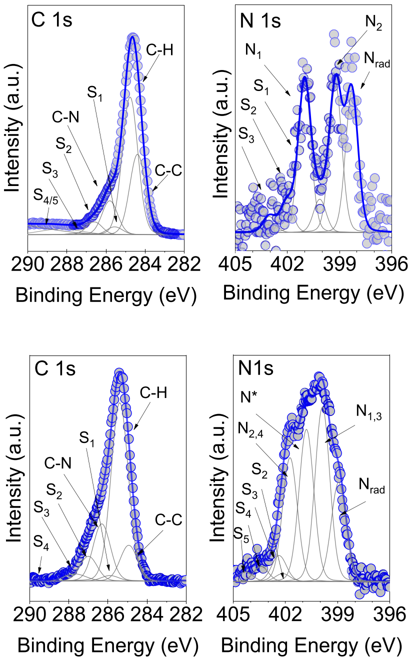

Figure 4. C 1s and N 1s core level spectra together with their fits after air exposure for thin films of Blatter-pyr (upper panel, after 45 h) and diBlatter (lower panel, after 72 h in air) (photon energy: 1486.6 eV, for the fit parameters; see the Supporting Information).

second feature at higher binding energies related to the carbon atoms bound to nitrogen atoms. Indeed, the N 1s core level spectra reveal clear changes (Figures 3 and 4). N 1s core level spectra are particularly important for the systems under investigation because they carry the information on the unpaired electrons and therefore on the radical character of the films, which is of interest for the goal of the present work. We observe changes in the shape of the N 1s core level curves for both Blatter-pyr and diBlatter thin films, although on a different time scale, as found for the C 1s core level spectra.

Electron paramagnetic resonance (EPR) spectroscopy investigations have shown that Blatter-pyr films are stable for up to three months under air[35] and diBlatter for at least 18 h.[21] Therefore, we have especially focused on the diBlatter thin films N 1s core level spectra, monitoring them and comparing the results to those obtained for the Blatter-pyr thin films. This enables understanding the chemical mechanisms playing a role and their impact on the thin film properties and assessing the role of the two radical sites versus one.

The major change that is observed is that the characteristic dip (at around 400 eV) between the first two components and the third one is progressively canceled within 24 h (see the arrow in Figure 3, right panel) and disappears after 72 h in diBlatter thin films, replaced by the increased signal intensity in this binding energy range (the N* feature in Figure 4). This is concomitant with the decrease of the signal of the first feature (Nrad) at lower binding energy (see also the fit parameters in the Supporting Information) that is correlated with the radical character of the films.[21,27,35] Blatter-pyr films show only a very small increase in intensity in the same binding energy range after 1 week in air.[35] This feature also emerges when evaporation is not fully successful.[40]

These results indicate the coexistence of two ongoing phenomena: (1) the new N* signal indicates a change in the chemical environment of the nitrogen atoms, and (2) a certain percentage of molecules have lost their radical character. This can be estimated by using the fit analysis comparing the relative fit contributions before and after air exposure. In the diBlatter films, the loss is around 38% after 72 h (see Tables S4 and S8). Note that we do not have any information on how the first satellite feature (S_1) might change under air exposure; thus, in the fit, we consider its intensity in N*.

The intensity in the binding energy range of N* is typically correlated with chemical interactions due to the hydrogenation or oxidation of the nitrogen atoms.[42] For example, a bond between oxygen and the nitrogen atom that emits photoelectrons contributing to the Nrad feature would move the binding energy of the photoemitted electrons to the higher binding energy range leading to an increased intensity where N* is identified. Also, the presence of molecular water might give rise to similar effects on the N 1s core level signals. Considering the oxidation pattern of the Blatter radical in solution,[34,54] we would exclude the occurrence of a bond between nitrogen atoms and oxygen in the Blatter radical derivatives investigated in this work.

To shed further light on the impact of air exposure on the electronic structure and the radical character of the two systems, we have performed ab initio calculations.

Air in the atmosphere is mostly composed of nitrogen, oxygen, argon, noble gases, and molecular water. By using simulations from first-principles, we considered the effect of the most relevant elements (H, Ar, N, O) and molecules (H_2, N_2, O_2, OH, H_2O, NH_2) that can react/adsorb on the radical films during air exposure. Several other gases and molecules, which stem from human activities, may be present, too, in urban environments (e.g., pollution).[55] The study of these contaminants goes beyond the aim of this work.

Because of the critical role of nitrogen in the Blatter radical derivatives, we considered different adsorption sites on the radical (S_i, with i = 1, 2, 1′, 2′, Figure 5). All adsorbed atoms and molecules are in their neutral charge state. For each radical, atom/molecule, and adsorption site, we fully relaxed

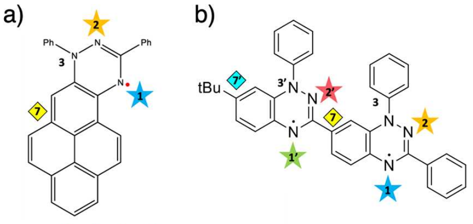

Figure 5. Sketch of selected impurities included in the calculations for (a) Blatter-pyr and (b) diBlatter. Numerical labels identify the chemically different nitrogen atoms within the molecules (N_1, N_2, N_1', N_2'). Colored symbols mark the adsorption sites and the adsorbed molecular species: stars indicate atoms/molecules attached to radical nitrogens (N_i), and diamonds indicate oxygen attached to carbon site C_7 or C_7'.

the atomic structure, and we studied the resulting electronic and magnetic properties. The results are summarized in Tables 1 and 2, where we reported the magnetic moment (μ) for the final systems, along with the formation energy (ΔE_f) calculated as $\Delta E_f = E_{tot} - E_{rad} - E_{mol}$, where E_{tot} is the ground state total energy after the impurity adsorption, E_{rad} is the total energy of the pristine radical, and E_{mol} is the total energy of the attached molecule.

Table 1. Magnetic Moment (μ) and Formation Energy (ΔE_f) of Blatter-pyr upon Adsorption of Characteristic Elements (H, H^+, Ar, N, O) and Molecules (H_2, N_2, O_2, OH, H_2O, NH_2) Present in Air in Standard Conditions as a Function of the Adsorption Sites (S_i)[a]

		Blatter-pyr	
★/◆	site	μ (Bohr mag)	ΔE_f (eV)
H	S1	0.00	−0.80
	S2	0.00	−0.29
H^+	S1	1.00	
	S2	1.00	
Ar	S1	1.00	0.00
	S2	1.00	0.00
N	**S1**	**0.00**	**+2.59**
	S2	**0.00**	**+1.62**
O	S1	1.00	−0.20
	S2	1.00	−0.19
	C7	**1.00**	**+0.15**
H_2	S1	1.00	0.00
	S2	1.00	0.00
N_2	S1	1.00	0.00
	S2	1.00	0.00
O_2	S1	1.00	0.00
	S2	1.00	0.00
OH	**S1**	**0.00**	**+1.75**
	S2	**0.00**	**+1.57**
H_2O	S1	1.00	−0.37
	S2	1.00	−0.33
NH_2	S1	0.00	−1.40
	S2	0.00	−1.38

[a] Labels and symbols refer to Figure 5. Boldfaced areas indicate energetically unfavored adsorption configurations.

In the case of Blatter-pyr, the adsorption of H, O, H_2O, and NH_2 is energetically favored, while the reaction is unfavored in the case of the atomic N and the OH fragment. We can thus exclude these two contaminant agents from those that have the highest probability to cause film degradation. The S1 adsorption site is generally energetically more favorable than the S2 one (see Figure 5 and Table 1). Noble gas (Ar) and divalent molecules (H_2, N_2, O_2) do not react with the radical (i.e., $\Delta E_f = 0$) moving away from the starting S_i sites and leaving the electronic and magnetic properties of the radical unperturbed (see Figure S5, Supporting Information). This excludes also these elements/molecules from the possible degradation causes. Among the interacting and energetically favored impurities, the inclusion of H, and NH_2 quenches the magnetic moment of the radical, restoring the double electron pairing. This is due to the formation of N−H bonds between atom N_1 or N_2 of the radical (depending on the adsorption site) and the contaminant H or NH_2. This saturates the initial charge unbalance, as demonstrated by the density of state (DOS) plot shown in Figure S5 of the Supporting Information.

Table 2. Magnetic Moment (μ) and Formation Energy (ΔE_f) of diBlatter upon Adsorption of Characteristic Elements and Molecules Present in Air in Standard Conditions as a Function of the Adsorption Sites (S_i)[a]

		diBlatter	
★/◆	site	μ (Bohr mag)	ΔE_f (eV)
H	S1	1.00	−0.80
	S2	1.00	−0.32
	S1′	1.00	−0.80
	S2′	1.00	−0.33
Ar	S1	2.00	0.00
	S2	2.00	0.00
	S1′	2.00	0.00
	S2′	2.00	0.00
N	**S1**	**1.00**	**+2.46**
	S2	**1.00**	**+1.73**
	S1′	**1.00**	**+2.51**
	S2′	**1.00**	**+1.79**
O	S1	2.00	−0.37
	S2	**1.00**	**+0.03**
	S1′	2.00	−0.36
	S2′	**1.00**	**−0.01**
	C7	**2.00**	**+0.72**
	C7′	**0.00**	**−0.01**
H2	S1	2.00	0.00
	S2	2.00	0.00
	S1′	2.00	0.00
	S2′	2.00	0.00
N2	S1	2.00	0.00
	S2	2.00	0.00
	S1′	2.00	0.00
	S2′	2.00	0.00
O2	S1	2.00	0.00
	S2	2.00	0.00
	S1′	2.00	0.00
	S2′	2.00	0.00
OH	**S1**	**1.00**	**+1.79**
	S2	**1.00**	**+1.62**
	S1′	**1.00**	**+1.81**
	S2′	**1.00**	**+1.60**
H_2O	S1	0.00	−0.40
	S2	2.00	−0.25
	S1′	0.00	−0.25
	S2′	0.00	−0.22
NH_2	S1	1.00	−1.46
	S2	1.00	−1.36
	S1′	1.00	−1.43
	S2′	1.00	−0.40

[a] Labels and symbols refer to Figure 5. Boldfaced areas indicate energetically unfavored adsorption configurations.

Different is the case of the O-based impurities (O and H_2O). Atomic oxygen forms covalent N−O bonds as well as H-bonds with the surrounding H atoms. This explains the energy gain upon adsorption. Yet, oxygen does not change the dipole moment of the radical because of the unpaired N−O electrons. In the case of H_2O, we do not find the formation of covalent bonds as for the other systems but of O−H···N hydrogen bonds between water and the radical. As a result, the radical maintains its initial spin configuration.

The different initial charge state of the impurities (i.e., ionized/radical impurities) could change the degradation effect

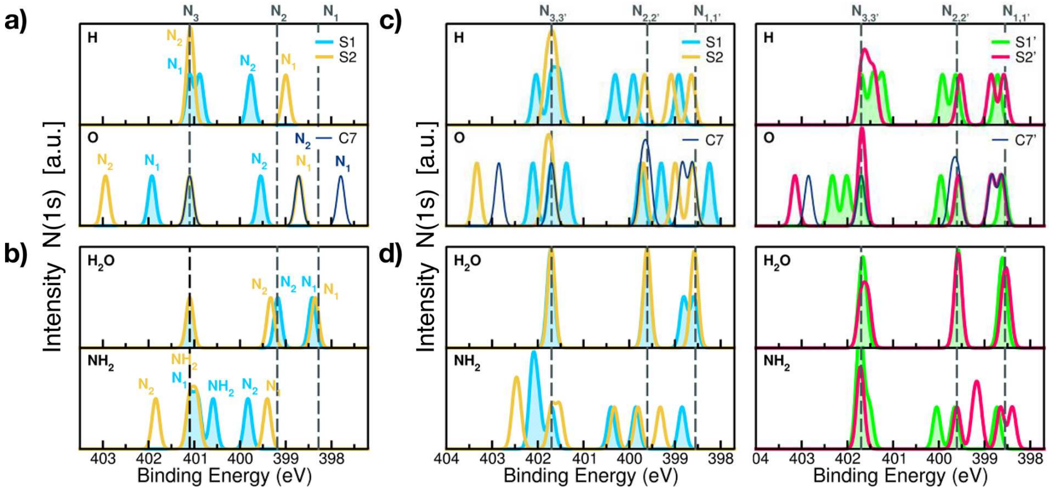

Figure 6. Simulated N 1s core level spectra of (a, b) Blatter-pyr and (c, d) diBlatter upon adsorption of characteristic (a, c) atoms (H, O) and (b, d) molecules (H_2O, NH_2) and as a function of the adsorption sites S1, S2, and C7 for Blatter-pyr and S1, S1′, S2, S2′, C7, and C7′ for diBlatter. Vertical dashed lines refer to the core-level features of the pristine molecules. The N_3 peak is assumed as the energy reference for all spectra and aligned to the experimental value for a direct comparison. Labels and colors refer to Figure 5.

on the radicals, as it modifies the total electron distribution of the system. For example, the adsorption of H^+ proton leaves the radical unperturbed (Table 1), since the lack of the valence electron impedes the electron pairing that quenches the magnetic moment, as in the case of the neutral H discussed above (Figure S5, Supporting Information).

Qualitatively similar results also hold for diBlatter: molecular contaminant adsorption is energetically favored in the case of H, O, H_2O, and NH_2, while it is unfavored in the case of atomic N and OH. S1 and S1′ sites are slightly more stable than the corresponding S2, and S2′ ones. The formation energies of equivalent sites on the two radical units (S1/S1′ and S2/S2′) are very similar but not identical as the diBlatter is not structurally symmetric. The adsorption of H, N, OH, or NH_2 saturates one of the two unpaired electrons, reducing the magnetic moment from two to one (i.e., total spin reduction from $S = 1$ to $S = 1/2$). Again, oxygen and water behave differently. When adsorbed in S1 and S1′, oxygen forms energetically stable bonds, but it does not change the magnetic moment of the radical, as for the Blatter-pyr case. When attached to S2 and S2′, the energy gain is negligible; thus the relative deterioration of the moment of the molecule ($\mu = 1.0$ Bohr mag) is thermodynamically unfavored.

In the case of water, although no covalent bonds are formed, the polarization effect due to the formation of H-bonds with the radical imparts an internal charge redistribution that couples and pairs the originally unpaired electron, zeroing the magnetic moment of the molecule ($\mu = 0$). This is confirmed by the DOS plot shown in Figure S6 (see the Supporting Information). In only one case (H_2O at S2) this polarization seems to be less effective, and the molecule maintains its initial spin. DiBlatter radical is not sensitive to the presence of Ar and diatomic molecules (H_2, N_2, O_2).

Atomic H and NH_2 molecules seem to have the same degradation effect on both radicals. Conversely, from the different interactions of Blatter-pyr and diBlatter with molecular water, we can infer that molecular water may have a stronger degradation effect on diBlatter thin films, causing the difference in film lifetime between Blatter-pyr and diBlatter films when exposed to air.

To investigate the possible formation of quinone terminations and their effect on the magnetic properties of the molecule, we further considered the adsorption of atomic O at C7 and C7′. In the former case, the adsorption is energetically unfavored for both radicals; adsorption in C7′ (for diBlatter only) is only slightly favored. The difference is due to the inequivalent atomic environment between C7 and C7′ which are connected to a phenyl or a butyl group, respectively. This agrees with the experimental observation that the formation of C−O bonds is not favored and, in general, atomic oxygen is not a source of magnetic degradation for these systems.

To have a direct comparison with the experimental data, we simulated the N 1s core level spectra after molecule adsorption, as shown in Figure 6. Panels a and c report the results for atomic H and O species, and panels b and d report those for H_2O, and NH_2 molecules.

Since the approach we used provides only the relative shift between the core level binding energies of inequivalent atoms, here we shifted the simulated spectra to the experimental value of the N_3 peaks of each radical (i.e., 401.1 eV for Blatter-pyr and 401.7 eV for diBlatter) for a direct comparison. The calculated spectra of both radicals have a three-peaked shape, where each peak is associated with the three inequivalent nitrogen atoms of the molecules (see Figures 1, 2, and 5). The numerical values (Blatter-pyr, N_1 = 398.3 eV, N_2 = 399.2 eV, N_3 = 401.1 eV; diBlatter, $N_{1,1}'$ = 401.1 eV, N_2 = 399.6 eV, $N_{3,3}'$ = 398.6 eV) are in excellent agreement with the experimental values and are marked as vertical dashed lines in Figure 6. The adsorption of contaminants modifies this plot, shifting the energy position of the peak as a function of the attached species and the adsorption site. Specifically, the adsorption of contaminants in position S1 gives rise, for both Blatter-pyr and diBlatter, to intensity in the binding energy range around 400−401 eV, as experimentally observed with XPS (Figures 3 and 4). Water, which weakly interacts with radicals, hardly modifies the original spectra. The adsorption of the other investigated element/molecules is energetically unfavored or has a neutral effect on the radicals; thus, they do not contribute significatively to the modification of the XPS spectra (Figure S7 in the Supporting Information). In particular, diatomic molecules and noble gas do not modify the three characteristic peaks of the Blatter radicals. Even though the adsorption of H^+ does not modify the magnetic properties of the radicals, it changes the local environment of the bonded nitrogen. This effect is detectable in the simulated XPS spectra. Yet, the low percentage of H^+ ions in air is expected to give a minor contribution to the experimental spectra. OH adsorption would generate a major degradation effect on the radicals, imparting relevant changes to the XPS spectra. However, the thermodynamical analysis does not predict this type of reaction, confirming the experimental findings.

This variety of contributions is the origin of the additional intensity and line broadening observed in the experimental spectra upon air exposure. Therefore, these features are the spectroscopic indication of the degradation of the magnetic properties of the radicals when they are exposed to air, that is, when exposed to molecular contaminant attaching/adsorption.

■ CONCLUSIONS

Stability and degradation mechanisms in materials that are candidates for new applications are of foremost importance. Our work focuses on the degradation mechanisms upon air exposure in two Blatter radical derivatives.

Our multitechnique investigations indicate that the Blatter radical derivative films are chemically very stable; however, they are affected by long-term degradation. In our previous work on understanding why diradical evaporation is challenging, we observed that the number of radical sites makes a difference. Also when comparing the same radical in a single or diradical configuration, the diradical evaporation is always more complicated.[22] We obtain analogous results comparing the film lifetime of Blatter-pyr and diBlatter in the present work.

We analyzed the degradation effect due to the adsorption of most chemical elements and molecules present in air. On a general ground, the long-term stability of Blatter radicals is justified by the low/selective reactivity to most air components. We found that the adsorption of contaminants such as H, H_2O, and NH_2 is energetically favorable, while noble gases and diatomic molecules do not react with radicals. For H, and NH_2, adsorption on both radical and diradical derivatives leads to the quenching of the pristine magnetic moment.

Our work indicates that the interaction with different contaminants affects the chemical and magnetic properties of the thin films upon air exposure but also the chemical structure of the radicals is important: the adsorption of contaminants on different sites affects the core levels in different ways.

Our calculations indicate that molecular water also plays a role; because we found that Blatter-pyr is molecular water resistant while diBlatter is not, diBlatter films degrade in a shorter time. From the experimental point of view, techniques such as near ambient pressure XPS, currently in development also in the soft X-ray range, allowing exposure in UHV of the investigated surface to selected gases or contaminants, including vapor and liquid water, are new opportunities to be pursued to further deepen the comprehension of these degradation patterns. Molecular water is ubiquitously present also in clean environments for device production. The presence of "intrinsic" molecular water is known to play a role in the degradation mechanisms in organic devices, such as organic light-emitting devices,[56] and hybrid perovskite-based devices.[57] Showing that Blatter-pyr is resistant in the presence of molecular water is a key result for the use of the Blatter radical in real devices.

■ ASSOCIATED CONTENT

Supporting Information

The Supporting Information is available free of charge at https://pubs.acs.org/doi/10.1021/acsami.3c02057.

> XPS fit parameters for the freshly evaporated films, time-dependent core level signals, time-dependent NEXAFS signals, C 1s core level spectra after air exposure, XPS fit parameters after air exposure, spin polarized density of states of the Blatter-pyr, spin polarized density of states (DOS) of the diBlatter, simulated N 1s core level spectra of Blatter-pyr upon adsorption of characteristic H^+, H_2, Ar, and OH species and as a function of the adsorption sites (S1) (PDF)

■ AUTHOR INFORMATION

Corresponding Author

M. Benedetta Casu − *Institute of Physical and Theoretical Chemistry, University of Tübingen, 72076 Tübingen, Germany*; orcid.org/0000-0002-5659-7040;
Email: benedetta.casu@uni-tuebingen.de

Authors

Ewa Malgorzata Nowik-Boltyk − *Institute of Physical and Theoretical Chemistry, University of Tübingen, 72076 Tübingen, Germany*; orcid.org/0000-0003-3136-4870
Tobias Junghoefer − *Institute of Physical and Theoretical Chemistry, University of Tübingen, 72076 Tübingen, Germany*
Mathias Glaser − *Institute of Physical and Theoretical Chemistry, University of Tübingen, 72076 Tübingen, Germany*
Erika Giangrisostomi − *Institute Methods and Instrumentation for Synchrotron Radiation Research, Helmholtz-Zentrum Berlin, 12489 Berlin, Germany*
Ruslan Ovsyannikov − *Institute Methods and Instrumentation for Synchrotron Radiation Research, Helmholtz-Zentrum Berlin, 12489 Berlin, Germany*
Shuyang Zhang − *Department of Chemistry, University of Nebraska, Lincoln, Nebraska 68588, United States*
Chan Shu − *Department of Chemistry, University of Nebraska, Lincoln, Nebraska 68588, United States*
Andrzej Rajca − *Department of Chemistry, University of Nebraska, Lincoln, Nebraska 68588, United States*; orcid.org/0000-0002-8856-1536
Arrigo Calzolari − *CNR-NANO Istituto Nanoscienze, 41125 Modena, Italy*; orcid.org/0000-0002-0244-7717

Complete contact information is available at:
https://pubs.acs.org/10.1021/acsami.3c02057

Author Contributions

E.M.N.-B., T.J., M.G., E.G., R.O, and M.B.C. performed the measurements. S.Z., C.S., and A.R. designed and synthesized the radicals. A.C. performed the calculations. E.M.N.-B. and T.J. performed the fits. M.B.C. conceived and supervised the project, interpreted the experimental data, and wrote the manuscript together with A.C. All authors contributed to the discussion and commented on the manuscript.

Notes

The authors declare no competing financial interest.

The data that support the findings of this study are available from the corresponding author upon reasonable request.

ACKNOWLEDGMENTS

The authors thank Helmholtz-Zentrum Berlin (HZB) for providing beamtime at BESSY II, E. Nadler for technical support, and Dr. M. Pink for the X-ray structures of the radicals. Financial support from HZB and the German Research Foundation (DFG, Contract CA852/11-3, Project Number 394233453) is gratefully acknowledged. The authors thank the Chemistry Division of the National Science Foundation for supporting this research under Grants CHE-1665256 and CHE-1955349 (A.R.). Computer resources were provided by the TACC supercomputing center (TX, USA) through QUANTRANS project. This work was partly supported by the European Union's Horizon 2020 Research and Innovation program under Grant Agreement 965046, FET-Open Project Interfast (Gated INTERfaces for FAST information processes).

REFERENCES

(1) Casu, M. B. Nanoscale Studies of Organic Radicals: Surface, Interface, and Spinterface. *Acc. Chem. Res.* **2018**, *51* (3), 753−760.

(2) Junghoefer, T.; Calzolari, A.; Baev, I.; Glaser, M.; Ciccullo, F.; Giangrisostomi, E.; Ovsyannikov, R.; Kielgast, F.; Nissen, M.; Schwarz, J.; Gallagher, N. M.; Rajca, A.; Martins, M.; Casu, M. B. Magnetic behavior in metal-free radical thin films. *Chem* **2022**, *8* (3), 801−814.

(3) Epifanov, G. I. *Solid State Physics*; Mir Publisher: Moscow, 1979.

(4) Gatteschi, D.; Sessoli, R.; Villain, J. *Molecular Nanomagnets*; Oxford University Press Inc.: New York, 2006.

(5) Getzlaff, M. *Fundamentals of Magnetism*; Springer-Verlag: Berlin, 2008.

(6) Nakazawa, S.; Nishida, S.; Ise, T.; Yoshino, T.; Mori, N.; Rahimi, R. D.; Sato, K.; Morita, Y.; Toyota, K.; Shiomi, D.; Kitagawa, M.; Hara, H.; Carl, P.; Höfer, P.; Takui, T. A Synthetic Two-Spin Quantum Bit: g-Engineered Exchange-Coupled Biradical Designed for Controlled-NOT Gate Operations. *Angew. Chem., Int. Ed.* **2012**, *51* (39), 9860−9864.

(7) Sproules, S. Molecules as electron spin qubits. In *Electron Paramagnetic Resonance: Volume 25*; The Royal Society of Chemistry, 2017; pp 61−97.

(8) Oyaizu, K.; Nishide, H. Radical Polymers for Organic Electronic Devices: A Radical Departure from Conjugated Polymers? *Adv. Mater.* **2009**, *21* (22), 2339−2344.

(9) Suga, T.; Konishi, H.; Nishide, H. Photocrosslinked nitroxide polymer cathode-active materials for application in an organic-based paper battery. *Chem. Commun.* **2007**, No. 17, 1730−1732.

(10) Wasielewski, M. R.; Forbes, M. D. E.; Frank, N. L.; Kowalski, K.; Scholes, G. D.; Yuen-Zhou, J.; Baldo, M. A.; Freedman, D. E.; Goldsmith, R. H.; Goodson, T.; Kirk, M. L.; McCusker, J. K.; Ogilvie, J. P.; Shultz, D. A.; Stoll, S.; Whaley, K. B. Exploiting chemistry and molecular systems for quantum information science. *Nat. Rev. Chem.* **2020**, *4* (9), 490−504.

(11) Domingo, N.; Bellido, E.; Ruiz-Molina, D. Advances on structuring, integration and magnetic characterization of molecular nanomagnets on surfaces and devices. *Chem. Soc. Rev.* **2012**, *41* (1), 258−302.

(12) Lee, J.; Lee, E.; Kim, S.; Bang, G. S.; Shultz, D. A.; Schmidt, R. D.; Forbes, M. D. E.; Lee, H. Nitronyl Nitroxide Radicals as Organic Memory Elements with Both n- and p-Type Properties. *Angew. Chem., Int. Ed.* **2011**, *50* (19), 4414−4418.

(13) Simão, C.; Mas-Torrent, M.; Crivillers, N.; Lloveras, V.; Artés, J. M.; Gorostiza, P.; Veciana, J.; Rovira, C. A robust molecular platform for non-volatile memory devices with optical and magnetic responses. *Nat. Chem.* **2011**, *3* (5), 359−364.

(14) Tomlinson, E. P.; Hay, M. E.; Boudouris, B. W. Radical Polymers and Their Application to Organic Electronic Devices. *Macromolecules* **2014**, *47* (18), 6145−6158.

(15) Huskinson, B.; Marshak, M. P.; Suh, C.; Er, S.; Gerhardt, M. R.; Galvin, C. J.; Chen, X.; Aspuru-Guzik, A.; Gordon, R. G.; Aziz, M. J. A metal-free organic-inorganic aqueous flow battery. *Nature* **2014**, *505* (7482), 195−198.

(16) Crivillers, N.; Mas-Torrent, M.; Rovira, C.; Veciana, J. Charge transport through unpaired spin-containing molecules on surfaces. *J. Mater. Chem.* **2012**, *22* (28), 13883−13890.

(17) Sugawara, T.; Komatsu, H.; Suzuki, K. Interplay between magnetism and conductivity derived from spin-polarized donor radicals. *Chem. Soc. Rev.* **2011**, *40* (6), 3105−3118.

(18) Davis, R. M.; Sowers, A. L.; DeGraff, W.; Bernardo, M.; Thetford, A.; Krishna, M. C.; Mitchell, J. B. A novel nitroxide is an effective brain redox imaging contrast agent and in vivo radioprotector. *Free Radical Biol. Med.* **2011**, *51* (3), 780−790.

(19) Sowers, M. A.; McCombs, J. R.; Wang, Y.; Paletta, J. T.; Morton, S. W.; Dreaden, E. C.; Boska, M. D.; Ottaviani, M. F.; Hammond, P. T.; Rajca, A.; Johnson, J. A. Redox-responsive branched-bottlebrush polymers for in vivo MRI and fluorescence imaging. *Nat. Commun.* **2014**, *5*, 5460.

(20) Rajca, A.; Wang, Y.; Boska, M.; Paletta, J. T.; Olankitwanit, A.; Swanson, M. A.; Mitchell, D. G.; Eaton, S. S.; Eaton, G. R.; Rajca, S. Organic Radical Contrast Agents for Magnetic Resonance Imaging. *J. Am. Chem. Soc.* **2012**, *134* (38), 15724−15727.

(21) Zhang, S.; Pink, M.; Junghoefer, T.; Zhao, W.; Hsu, S.-N.; Rajca, S.; Calzolari, A.; Boudouris, B. W.; Casu, M. B.; Rajca, A. High-Spin (S = 1) Blatter-Based Diradical with Robust Stability and Electrical Conductivity. *J. Am. Chem. Soc.* **2022**, *144* (13), 6059−6070.

(22) Junghoefer, T.; Gallagher, N. M.; Kolanji, K.; Giangrisostomi, E.; Ovsyannikov, R.; Chassé, T.; Baumgarten, M.; Rajca, A.; Calzolari, A.; Casu, M. B. Challenges in controlled thermal deposition of organic diradicals. *Chem. Mater.* **2021**, *33*, 2019−2028.

(23) Shu, C.; Pink, M.; Junghoefer, T.; Nadler, E.; Rajca, S.; Casu, M. B.; Rajca, A. Synthesis and Thin Films of Thermally Robust Quartet (S = 3/2) Ground State Triradical. *J. Am. Chem. Soc.* **2021**, *143*, 5508−5518.

(24) Calzolari, A.; Rajca, A.; Casu, M. B. From radical to triradical thin film processes: the Blatter radical derivatives. *J. Mater. Chem. C* **2021**, *9* (33), 10787−10793.

(25) Ji, Y.; Long, L.; Zheng, Y. Recent advances of stable Blatter radicals: synthesis, properties and applications. *Mater. Chem. Front.* **2020**, *4* (12), 3433−3443.

(26) Zhang, Y.; Zheng, Y.; Zhou, H.; Miao, M.-S.; Wudl, F.; Nguyen, T.-Q. Temperature Tunable Self-Doping in Stable Diradicaloid Thin-Film Devices. *Adv. Mater.* **2015**, *27* (45), 7412−7419.

(27) Ciccullo, F.; Calzolari, A.; Bader, K.; Neugebauer, P.; Gallagher, N. M.; Rajca, A.; van Slageren, J.; Casu, M. B. Interfacing a Potential Purely Organic Molecular Quantum Bit with a Real-Life Surface. *ACS Appl. Mater. Interfaces* **2019**, *11* (1), 1571−1578.

(28) Zheng, Y.; Miao, M.-s.; Dantelle, G.; Eisenmenger, N. D.; Wu, G.; Yavuz, I.; Chabinyc, M. L.; Houk, K. N.; Wudl, F. A Solid-State Effect Responsible for an Organic Quintet State at Room Temperature and Ambient Pressure. *Adv. Mater.* **2015**, *27* (10), 1718−1723.

(29) Häupler, B.; Schubert, U. S.; Wild, A.; Koutentis, P. A.; Zissimou, G. Verwendung benzotriazinyl-haltiger Polymere als Ladungsspeicher. Patent DE102017005924 (A1), Dec 27, 2018.

(30) Steen, J. S.; Nuismer, J. L.; Eiva, V.; Wiglema, A. E. T.; Daub, N.; Hjelm, J.; Otten, E. Blatter Radicals as Bipolar Materials for Symmetrical Redox-Flow Batteries. *J. Am. Chem. Soc.* **2022**, *144* (11), 5051−5058.

(31) Saal, A.; Elbinger, L.; Schreyer, K.; Fataj, X.; Friebe, C.; Schubert, U. S. Structural Improvement of the Blatter Radical for

High-Current Organic Batteries. *ACS Appl. Energy Mater.* **2022**, *5* (12), 15019−15028.

(32) Poryvaev, A. S.; Gjuzi, E.; Yazikova, A. A.; Polyukhov, D. M.; Albrekht, Y. N.; Efremov, A. A.; Kudriavykh, N. A.; Yanshole, V. V.; Hoffmann, F.; Fröba, M.; Fedin, M. V. Blatter Radical-Decorated Silica as a Prospective Adsorbent for Selective NO Capture from Air. *ACS Appl. Mater. Interfaces* **2023**, *15* (4), 5191−5197.

(33) Constantinides, C. P.; Berezin, A. A.; Manoli, M.; Leitus, G. M.; Zissimou, G. A.; Bendikov, M.; Rawson, J. M.; Koutentis, P. A. Structural, Magnetic, and Computational Correlations of Some Imidazolo-Fused 1,2,4-Benzotriazinyl Radicals. *Chem.—Eur. J.* **2014**, *20* (18), 5388−5396.

(34) Constantinides, C. P.; Koutentis, P. A.; Krassos, H.; Rawson, J. M.; Tasiopoulos, A. J. Characterization and Magnetic Properties of a "Super Stable" Radical 1,3-Diphenyl-7-trifluoromethyl-1,4-dihydro-1,2,4-benzotriazin-4-yl. *J. Org. Chem.* **2011**, *76* (8), 2798−2806.

(35) Ciccullo, F.; Gallagher, N. M.; Geladari, O.; Chasse, T.; Rajca, A.; Casu, M. B. A Derivative of the Blatter Radical as a Potential Metal-Free Magnet for Stable Thin Films and Interfaces. *ACS Appl. Mater. Interfaces* **2016**, *8* (3), 1805−1812.

(36) Poggini, L.; Cucinotta, G.; Sorace, L.; Caneschi, A.; Gatteschi, D.; Sessoli, R.; Mannini, M. Nitronyl nitroxide radicals at the interface: a hybrid architecture for spintronics. *Rendiconti Lincei. Scienze Fisiche e Naturali* **2018**, *29* (3), 623−630.

(37) Tesi, L.; Lucaccini, E.; Cimatti, I.; Perfetti, M.; Mannini, M.; Atzori, M.; Morra, E.; Chiesa, M.; Caneschi, A.; Sorace, L.; Sessoli, R. Quantum coherence in a processable vanadyl complex: new tools for the search of molecular spin qubits. *Chem. Sci.* **2016**, *7* (3), 2074−2083.

(38) Maliakal, A.; Raghavachari, K.; Katz, H.; Chandross, E.; Siegrist, T. Photochemical Stability of Pentacene and a Substituted Pentacene in Solution and in Thin Films. *Chem. Mater.* **2004**, *16* (24), 4980−4986.

(39) Blatter, H. M.; Lukaszewski, H. A new stable free radical. *Tetrahedron Lett.* **1968**, *9* (22), 2701−2705.

(40) Low, J. Z.; Kladnik, G.; Patera, L. L.; Sokolov, S.; Lovat, G.; Kumarasamy, E.; Repp, J.; Campos, L. M.; Cvetko, D.; Morgante, A.; Venkataraman, L. The Environment-Dependent Behavior of the Blatter Radical at the Metal−Molecule Interface. *Nano Lett.* **2019**, *19* (4), 2543−2548.

(41) Ajayakumar, M. R.; Moreno, C.; Alcón, I.; Illas, F.; Rovira, C.; Veciana, J.; Bromley, S. T.; Mugarza, A.; Mas-Torrent, M. Neutral Organic Radical Formation by Chemisorption on Metal Surfaces. *J. Phys. Chem. Lett.* **2020**, *11* (10), 3897−3904.

(42) Moulder, J. F. *Handbook of X-ray Photoelectron Spectroscopy*; Perkin-Elmer Corp., 1992.

(43) Giangrisostomi, E.; Ovsyannikov, R.; Sorgenfrei, F.; Zhang, T.; Lindblad, A.; Sassa, Y.; Cappel, U. B.; Leitner, T.; Mitzner, R.; Svensson, S.; Mårtensson, N.; Föhlisch, A. Low Dose Photoelectron Spectroscopy at BESSY II: Electronic structure of matter in its native state. *J. Electron Spectrosc. Relat. Phenom.* **2018**, *224*, 68−78.

(44) Casu, M. B.; Cosseddu, P.; Batchelor, D.; Bonfiglio, A.; Umbach, E. A high-resolution near-edge x-ray absorption fine structure investigation of the molecular orientation in the pentacene/poly(3,4-ethylenedioxythiophene):poly(styrenesulfonate) pentacene/system. *J. Chem. Phys.* **2008**, *128* (1), 014705.

(45) Casu, M. B. Nanoscale Order and Structure in Organic Materials: Diindenoperylene on Gold as a Model System. *Cryst. Growth Des.* **2011**, *11* (8), 3629−3635.

(46) Giannozzi, P.; Baroni, S.; Bonini, N.; Calandra, M.; Car, R.; Cavazzoni, C.; Ceresoli, D.; Chiarotti, G. L.; Cococcioni, M.; Dabo, I.; Dal Corso, A.; de Gironcoli, S.; Fabris, S.; Fratesi, G.; Gebauer, R.; Gerstmann, U.; Gougoussis, C.; Kokalj, A.; Lazzeri, M.; Martin-Samos, L.; Marzari, N.; Mauri, F.; Mazzarello, R.; Paolini, S.; Pasquarello, A.; Paulatto, L.; Sbraccia, C.; Scandolo, S.; Sclauzero, G.; Seitsonen, A. P.; Smogunov, A.; Umari, P.; Wentzcovitch, R. M. Quantum ESPRESSO: a modular and open-source software project for quantum simulations of materials. *J. Phys.: Condens. Matter* **2009**, *21* (39), 395502.

(47) Perdew, J. P.; Burke, K.; Ernzerhof, M. Generalized Gradient Approximation Made Simple. *Phys. Rev. Lett.* **1996**, *77* (18), 3865−3868.

(48) Vanderbilt, D. Soft self-consistent pseudopotentials in a generalized eigenvalue formalism. *Phys. Rev. B* **1990**, *41* (11), 7892−7895.

(49) Pehlke, E.; Scheffler, M. Evidence for site-sensitive screening of core holes at the Si and Ge (001) surface. *Phys. Rev. Lett.* **1993**, *71* (14), 2338−2341.

(50) Junghoefer, T.; Nowik-Boltyk, E. M.; de Sousa, J. A.; Giangrisostomi, E.; Ovsyannikov, R.; Chassé, T.; Veciana, J.; Mas-Torrent, M.; Rovira, C.; Crivillers, N.; Casu, M. B. Stability of radical-functionalized gold surfaces by self-assembly and on-surface chemistry. *Chem. Sci.* **2020**, *11* (34), 9162−9172.

(51) Kakavandi, R.; Ravat, P.; Savu, S. A.; Borozdina, Y. B.; Baumgarten, M.; Casu, M. B. Electronic Structure and Stability of Fluorophore−Nitroxide Radicals from Ultrahigh Vacuum to Air Exposure. *ACS Appl. Mater. Interfaces* **2015**, *7* (3), 1685−1692.

(52) Kakavandi, R.; Savu, S.-A.; Sorace, L.; Rovai, D.; Mannini, M.; Casu, M. B. Core-Hole Screening, Electronic Structure, and Paramagnetic Character in Thin Films of Organic Radicals Deposited on SiO2/Si(111). *J. Phys. Chem. C* **2014**, *118* (15), 8044−8049.

(53) Savu, S.-A.; Biswas, I.; Sorace, L.; Mannini, M.; Rovai, D.; Caneschi, A.; Chassé, T.; Casu, M. B. Nanoscale Assembly of Paramagnetic Organic Radicals on Au(111) Single Crystals. *Chem.—Eur. J.* **2013**, *19* (10), 3445−3450.

(54) Neugebauer, F. A.; Umminger, I. Über 1,4-Dihydro-1,2,4-benzotriazinyl-Radikale. *Chem. Ber.* **1980**, *113* (4), 1205−1225.

(55) Schlesinger, W. H.; Bernhardt, E. S. The Atmosphere. In *Biogeochemistry*, 4th ed.; Schlesinger, W. H., Bernhardt, E. S., Eds.; Academic Press, 2020; Chapter 3, pp 51−97.

(56) Scholz, S.; Kondakov, D.; Lüssem, B.; Leo, K. Degradation Mechanisms and Reactions in Organic Light-Emitting Devices. *Chem. Rev.* **2015**, *115* (16), 8449−8503.

(57) Deretzis, I.; Smecca, E.; Mannino, G.; La Magna, A.; Miyasaka, T.; Alberti, A. Stability and Degradation in Hybrid Perovskites: Is the Glass Half-Empty or Half-Full? *J. Phys. Chem. Lett.* **2018**, *9*, 3000−3007.

Supporting Information

Long-term degradation mechanisms in application-implemented radical thin films

Ewa Malgorzata Nowik-Boltyk,[†] *Tobias Junghoefer,*[†] *Mathias Glaser,*[†] *Erika Giangrisostomi,*[#] *Ruslan Ovsyannikov,*[#] *Shuyang Zhang,*[§] *Chan Shu,*[§] *Andrzej Rajca,*[§] *Arrigo Calzolari,*[‡] *M. Benedetta Casu*[†]*

[†]*Institute of Physical and Theoretical Chemistry, University of Tübingen, 72076 Tübingen, Germany*

[#]*Institute Methods and Instrumentation for Synchrotron Radiation Research, Helmholtz-Zentrum Berlin, 12489 Berlin, Germany*

[§]*Department of Chemistry, University of Nebraska, Lincoln, NE 68588, United States*

[‡]*CNR-NANO Istituto Nanoscienze, Centro S3, 41125 Modena, Italy*

Corresponding Author

*E-mail: benedetta.casu@uni-tuebingen.de, Tel. +49 7071 29 76252, Fax: +49 7071 29 5490 (M.B.C.).

Table of contents

1) Fit parameters for the freshly evaporated Blatter-pyr films as in Figure 1. The fit has been performed as described in references [1-5].

The expected stoichiometric values for the C 1s and N 1s elemental analyses are:

C-C = 24%, C-H = 62%, C-N = 14%, and $N_{radical} = N_{imino} = N_{amino} = 33\%$

Table S1

	Energy (eV)	Lorentzian Width (eV)	Gaussian Width (eV)	Intensity (%)
C-C	284.4	0.08	0.90	17.7
C-H	284.8	0.08	0.90	47.9
S_1	285.4	0.08	0.90	1.2
C-N	285.9	0.08	0.90	11.6
S_2	286.6	0.08	0.90	4.3
S_3	287.5	0.08	0.90	1.1
S_4	288.4	0.08	1.44	2.0
S_5	291.6	0.08	5.14	14.2

C-C + $S_1+S_3+S_4$=22.0%, C-H+ S_5=62.1%, C-N + S_2=15.9%

Table S2

	Energy (eV)	Lorentzian Width (eV)	Gaussian Width (eV)	Intensity (%)
N_{rad}	398.3	0.1	0.8	28.6
N_2	399.2	0.1	0.8	28.1
S_1	400.1	0.1	0.8	5.2
N_1	401.0	0.1	0.8	29.7
S_2	402.1	0.1	0.8	6.1
S_3	403.0	0.1	0.8	2.3

$N_{rad}+S_1= 33.8\%$, $N_2+S_2= 34.2\ \%$, $N_1+S_3=32.0\%$

Fit parameters for the freshly evaporated diBlatter films as in Figure 2.

The expected stoichiometric values for the C 1s and N 1s elemental analyses are:

C-C = 11.1%, C-H = 66.7%, C-N = 22.2%, and $N_{radical} = N_1 = N_2 = 33\%$

Table S3

	Energy (eV)	**Lorentzian Width (eV)**	**Gaussian Width (eV)**	**Intensity (%)**
C-C	284,9	0.08	1.0	11.9
C-H	285,3	0.08	1.0	52.7
S_1	285,9	0.08	1.0	1.6
C-N	286,3	0.08	1.0	19.9
S_2	287,0	0.08	1.0	8.8
S_3	287,7	0.08	1.5	1.8
S_4	292,2	0.08	3.1	3.3

C-C + S_1 =13.5%, C-H+½ $S_2+S_3+S_4$=62.2%, C-N + ½ S_2=24.3%

Table S4

	Energy (ev)	Lorentzian Width (eV)	Gaussian Width (eV)	Intensity (%)
N_{rad}	398.9	0.1	0.95	26.1
$N_{1,3}$	399.9	0.1	0.95	28.5
$N_{2,4}$	401.7	0.1	0.95	29.9
S_1	400.6	0.1	0.95	5.9
S_2	402.2	0.1	0.95	3.0
S_3	402.4	0.1	0.95	3.0
S_4	403.3	0.1	0.95	2.1
S_5	404.3	0.1	0.95	1.5

$N_{rad} + ½(S_1 + S_2) + S_4 + S_5 = 34.1$ %
$N_{1/3} + ½(S_1 + S_2) = 33.0$ %
$N_{2/4} + S_3 = 32.9$ %

2) Time dependent core level signals.

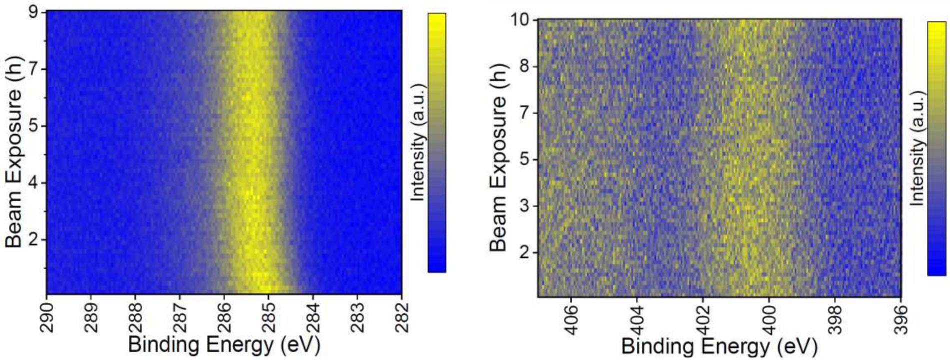

Figure S1. diBlatter thin films. (Left) Time-dependent C 1s and (right) N 1s core level signals. Color scale: Blue represents the background signal; yellow is the peak intensity (photon energy: 700 eV).

3) Time-dependent NEXAFS signals.

The unoccupied states and the molecular arrangement adopted by the molecules in the thin films can be investigated by NEXAFS spectroscopy. NEXAFS features and their intensities are sensitive to intermolecular interactions, and NEXAFS dichroism allows determining the orientation of the molecules with respect to the substrate.[6, 7] In particular, the main resonance at around 286.0 eV can be identified as due to the pyrene substituent, leading to a calculated average orientation of the pyrene plane of 30°. The observed dichroic behavior is the typically dichroic expected one for the herringbone structure,[8-10] due to the compromise between the strength of the C-H and the π–π interactions.[11]

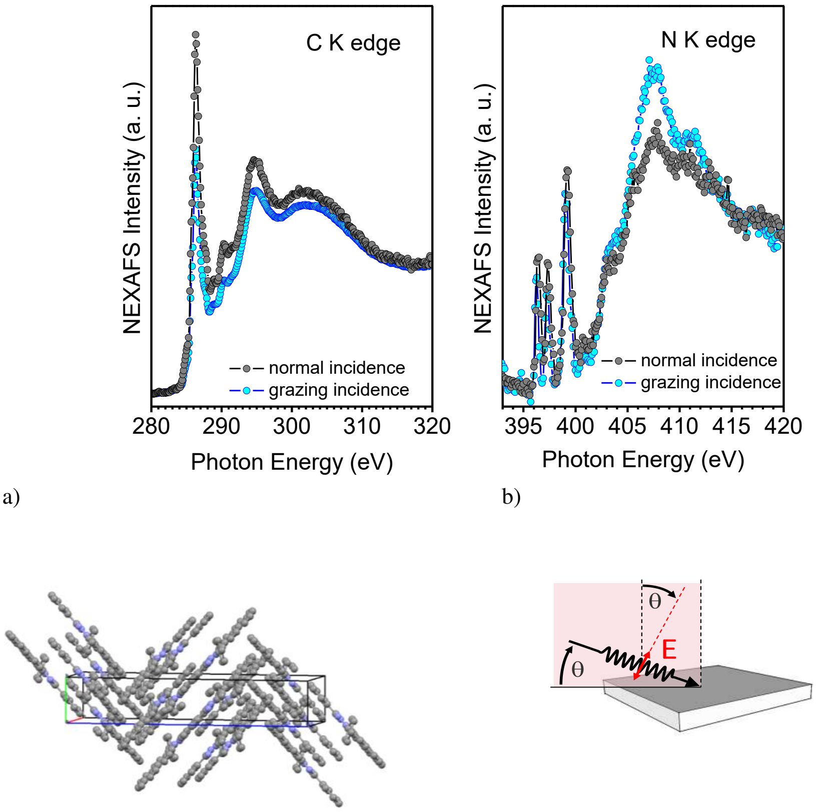

a)

b)

c)

d)

Figure S2. Blatter-pyr. a) C K edge and b) N K edge NEXAFS spectra of a nominally 3.5 nm thick film. c) Crystal structure. d) Geometry of the experiment.

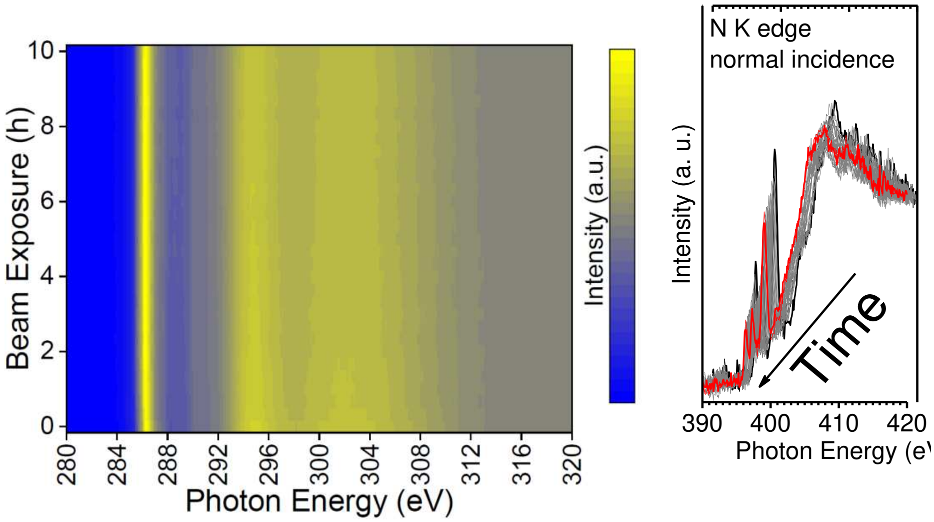

Figure S3. Blatter-pyr thin films. NEXAFS intensity versus beam exposure.

4) C 1s core level spectra after air exposure.

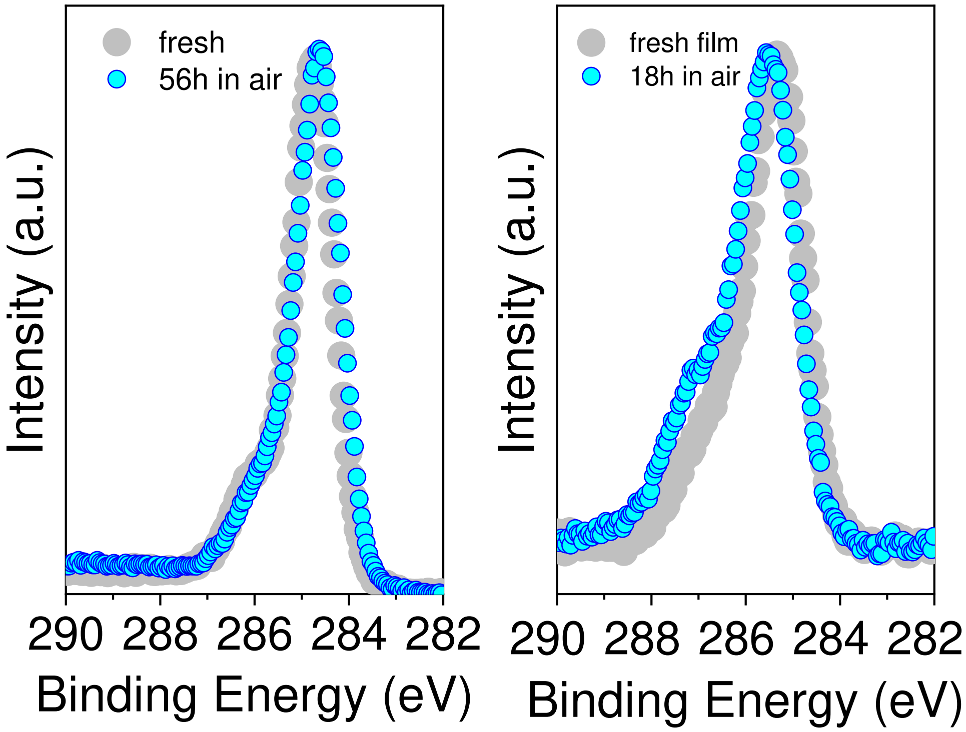

a) b)

Figure S4. C 1s core level spectra of a) Blatter-pyr and b) diBlatter thin films, after air exposure, as indicated. The fresh film core level curves (light grey) are also shown for comparison (photon energy: 1486.6 eV).

5) Fit parameters for Blatter-pyr films as in Figure 3 after 45 hours of air exposure

Table S5

	Energy (eV)	**Lorentzian Width (eV)**	**Gaussian Width (eV)**	**Intensity (%)**
C-C	284.4	0.08	0.90	23.9
C-H	284.8	0.08	0.90	41.0
S_1	285.6	0.08	0.90	2.3
C-N	285.8	0.08	0.90	10.1
S_2	286.6	0.08	0.90	3.8
S_3	287.5	0.08	0.90	0.5
S_4	288.3	0.08	2.45	4.4
S_5	291.6	0.08	5.14	14.0

Table S6

	Energy (eV)	**Lorentzian Width (eV)**	**Gaussian Width (eV)**	**Intensity (%)**
N_{rad}	398.3	0.1	0.8	27.0
N_2	399.2	0.1	0.8	28.6
S_1	400.1	0.1	0.8	6.4
N_1	401.0	0.1	0.8	29.1
S_2	402.0	0.1	0.8	5.8
S_3	403.0	0.1	0.8	3.1

Fit parameters for diBlatter films as in Figure 3 after 72 hours of air exposure.

Table S7

	Energy (eV)	Lorentzian Width (eV)	Gaussian Width (eV)	Intensity (%)
C-C	284.9	0.08	1.0	11.2
C-H	285.4	0.08	1.0	55.9
S_1	285.9	0.08	1.0	1.7
C-N	286.3	0.08	1.0	17.9
S_2	287.0	0.08	1.0	7.7
S_3	287.7	0.08	1.3	2.8
S_4	292.2	0.08	3.8	2.8

Table S8

	Energy (eV)	Lorentzian Width (eV)	Gaussian Width (eV)	Intensity (%)
N_{rad}	398.9	0.1	0.95	16.3
$N_{1,3}$	399.9	0.1	0.95	28.6
N*	400.8	0.1	0.95	25.0
$N_{2,4}$	401.7	0.1	0.95	20.4
S_2	402.2	0.1	0.95	1.3
S_3	402.4	0.1	0.95	4.3
S_4	403.4	0.1	0.95	2.5
S_5	404.3	0.1	0.95	1.6

6) Spin-polarized density of states of the Blatter-pyr.

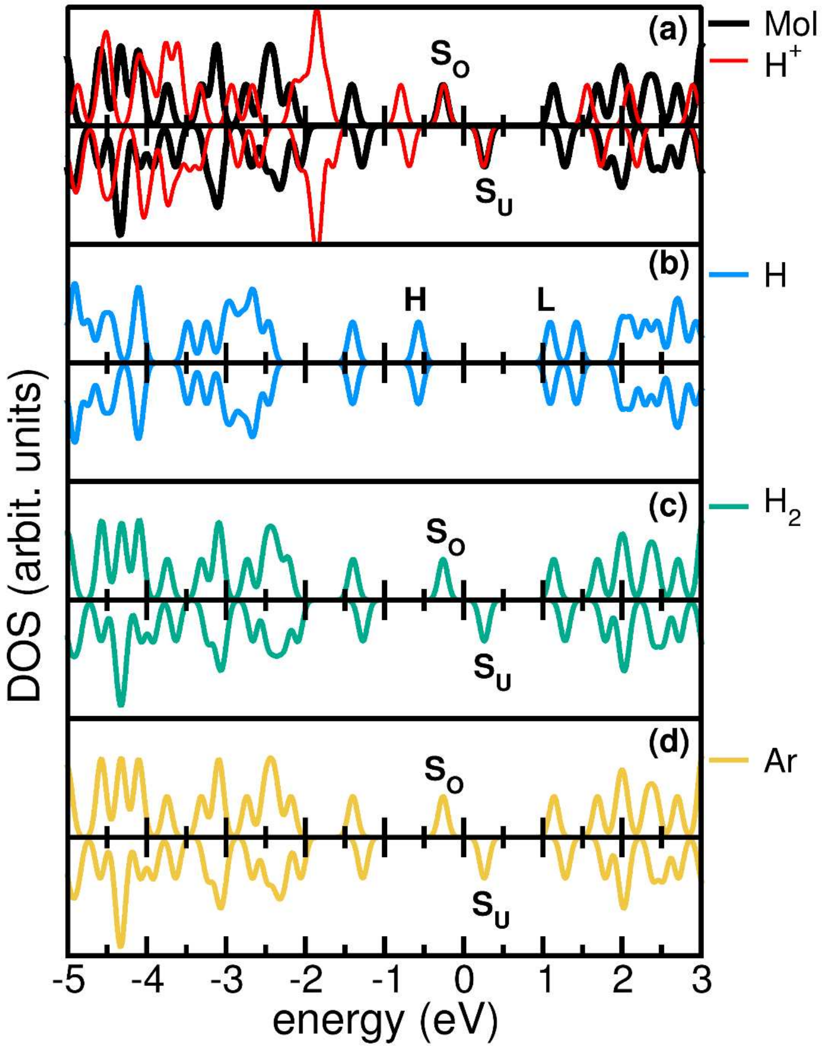

Figure S5. Spin-polarized density of states (DOS) of the Blatter-pyr without (black line, panel a) and with selected adsorbed impurities: H^+ (red line, panel a), H (cyan line, panel b), H_2 (green line panel c), and Ar (yellow line, panel d). Negative/positive energies indicate occupied/empty electronic states: highest Single Occupied (S_O) and lowest Single Unoccupied (S_U) molecular orbitals are indicated (panels a,c,d) , along with double occupied HOMO (H) and LUMO (L) states (panel b). All elements/molecules are adsorbed on site S1.

7) Spin-polarized density of states (DOS) of the diBlatter.

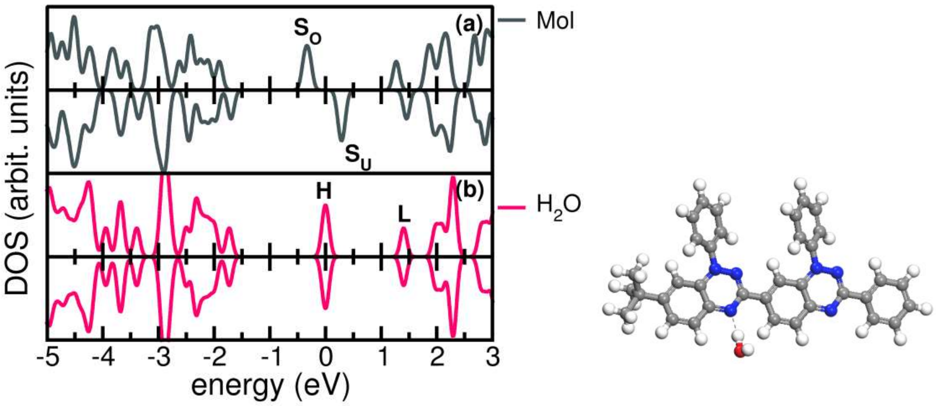

Figure S6. Spin-polarized density of states (DOS) of diBlatter radical (black line, panel a) and of the same molecule with H_2O molecule adsorbed in site S1’ (pink line, panel b). Negative/positive energies indicate occupied/empty electronic states: double degenerate highest Single Occupied (S_O) and lowest Single Unoccupied (S_U) molecular orbitals are indicated (panels a), along with double degenerate/double occupied HOMO (H) and LUMO (L) states (panel b). Relaxed geometry upon water molecule adsorption is shown on right.

8) Simulated N 1s core level spectra of Blatter-pyr upon adsorption of characteristic H^+, H_2, Ar, and OH species and as a function of the adsorption sites (S1).

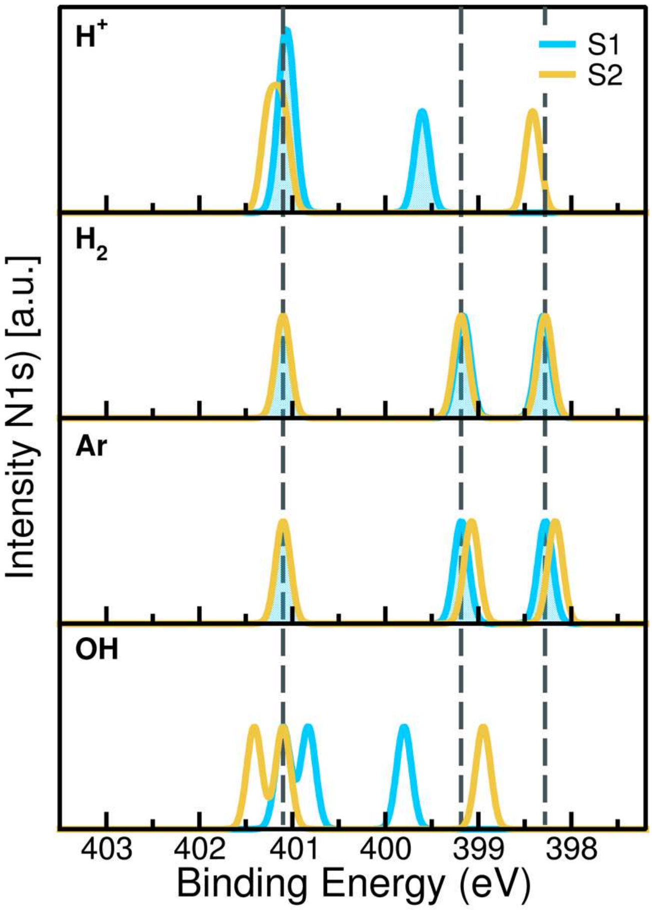

Figure S7. Simulated N 1s core level spectra of Blatter-pyr upon adsorption of characteristic H^+, H_2, Ar, and OH species and as a function of the adsorption sites (S1). Vertical dashed lines refer to the core-level features of the pristine molecules. The N_3 peak is assumed as the energy reference for all spectra and aligned to the experimental value for a direct comparison. Labels and colors refer to Figure 5, main text.

9) References

1. S. Zhang, M. Pink, T. Junghoefer, W. Zhao, S.-N. Hsu, S. Rajca, A. Calzolari, B. W. Boudouris, M. B. Casu and A. Rajca, *J. Am. Chem. Soc.*, 2022, **144**, 6059-6070.
2. T. Junghoefer, E. M. Nowik-Boltyk, J. A. de Sousa, E. Giangrisostomi, R. Ovsyannikov, T. Chassé, J. Veciana, M. Mas-Torrent, C. Rovira, N. Crivillers and M. B. Casu, *Chem. Sci.*, 2020, **11**, 9162-9172.
3. F. Ciccullo, N. M. Gallagher, O. Geladari, T. Chasse, A. Rajca and M. B. Casu, *ACS Appl. Mater. Interfaces*, 2016, **8**, 1805–1812.
4. S.-A. Savu, I. Biswas, L. Sorace, M. Mannini, D. Rovai, A. Caneschi, T. Chassé and M. B. Casu, *Chem.-Eur. J.* , 2013, **19**, 3445-3450.
5. S.-A. Savu, M. B. Casu, S. Schundelmeier, S. Abb, C. Tonshoff, H. F. Bettinger and T. Chassé, *RSC Adv.*, 2012, **2**, 5112-5118.
6. J. Stöhr, *NEXAFS Spectroscopy*, Springer, 2003.
7. J. Stöhr, K. Baberschke, R. Jaeger, R. Treichler and S. Brennan, *Phys. Rev. Lett.*, 1981, **47**, 381-384.
8. T. Breuer, M. Klues and G. Witte, *Journal of Electron Spectroscopy and Related Phenomena*, 2015, **204**, 102-115.
9. M. B. Casu, B.-E. Schuster, I. Biswas, C. Raisch, H. Marchetto, T. Schmidt and T. Chassé, *Adv. Mater.*, 2010, **22**, 3740-3744.
10. S.-A. Savu, A. Sonström, R. Bula, H. F. Bettinger, T. Chassé and M. B. Casu, *ACS Appl. Mater. Interfaces*, 2015, **7**, 19774-19780.
11. C. C. Mattheus, G. A. de Wijs, R. A. de Groot and T. T. M. Palstra, *J. Am. Chem. Soc.*, 2003, **125**, 6323-6330.

D. Radical-Induced Changes in Transition Metal Interfacial Magnetic Properties: A Blatter Derivative on Polycrystalline Cobalt

Reproduced from
E. M. Nowik-Boltyk, T. Junghoefer, E. Giangrisostomi, R. Ovsyannikov, C. Shu, A. Rajca, A. Droghetti, M. B. Casu, "Radical-Induced Changes in Transition Metal Interfacial Magnetic Properties: A Blatter Derivative on Polycrystalline Cobalt", *Angewandte Chemie International Edition* **2024**, *63*, e202403495, DOI `https://doi.org/10.1002/anie.202403495`

Check for updates

GDCh

Research Article

Angewandte Chemie International Edition
www.angewandte.org

How to cite: *Angew. Chem. Int. Ed.* **2024**, *63*, e202403495
doi.org/10.1002/anie.202403495

Magnetic Properties

Radical-Induced Changes in Transition Metal Interfacial Magnetic Properties: A Blatter Derivative on Polycrystalline Cobalt

Ewa Malgorzata Nowik-Boltyk, Tobias Junghoefer, Erika Giangrisostomi, Ruslan Ovsyannikov, Chan Shu[+]*, Andrzej Rajca, Andrea Droghetti, and Maria Benedetta Casu**

Abstract: In this work, we study the interface obtained by depositing a monolayer of a Blatter radical derivative on polycrystalline cobalt. By examining the occupied and unoccupied states at the interface, using soft X-ray techniques, combined with electronic structure calculations, we could simultaneously determine the electronic structure of both the molecular and ferromagnetic sides of the interface, thus obtaining a full understanding of the interfacial magnetic properties. We found that the molecule is strongly hybridized with the surface. Changes in the core level spectra reflect the modification of the molecule and the cobalt electronic structures inducing a decrease in the magnetic moment of the cobalt atoms bonded to the molecules which, in turn, lose their radical character. Our method allowed us to screen, beforehand, organic/ferromagnetic interfaces given their potential applications in spintronics.

Introduction

Organic/inorganic interfaces have been investigated for at least three decades[1] as they are at the core of the technological developments driven by the miniaturization of materials and devices towards the nanoscale limit. In particular, in the field of spintronics, the study of organic/ferromagnetic metal interfaces initially acquired importance in order to understand spin tunneling and spin injection from ferromagnetic electrodes into molecules.[2] Yet, the interest in these interfaces now encompasses many aspects of magnetism, with a variety of effects that have been reported to emerge when an organic layer is deposited on an ultra-thin ferromagnetic film.[2c,g,3]

The organic layer at an organic/ferromagnetic metal interface often acquires a spin polarization because of the chemical bond with the ferromagnetic film.[4] In turn, the electronic and magnetic properties of the ferromagnetic film are also significantly modified.[5] A paradigmatic example is the fullerene (C_{60})/cobalt interface. On one side of such an interface, the C_{60} layer can be used to spin filter electrons,[6] while, on the other side, the Co magnetic moments are reduced,[6] and the Co film's magnetic anisotropy and hardness are enhanced compared to the clean Co film.[7] Similar or even larger modifications of the magnetic properties of Co films have also been reported with tris(8-hydroxyquinoline) metal (Mq_3) molecules.[8]

The goal of our work is to go beyond the most studied molecules for spintronics, $C_{60,}$ and $Mq_{3,}$ by considering the yet unexplored interfaces formed between organic radicals and cobalt. To achieve this goal, we propose an original and powerful approach to characterize at the same time the electronic properties of both the molecular and the metallic side of interfaces, whereas most studies to date have focused on either of the two separately.

Thin films of purely organic radicals (i.e., organic molecules that carry an unpaired electron and, thus, a magnetic moment[9]) have attracted attention for many applications.[10] Recently, it was demonstrated that they can be evaporated under controlled conditions in ultra-high vacuum,[11] thus enabling the use of characterization techniques complementary to the ones traditionally employed in radical chemistry. For instance, soft X-ray spectroscopy, combined with concepts originally stemming from the surface science of closed-shell systems, make it possible to

---

[*] E. M. Nowik-Boltyk, Dr. T. Junghoefer, Prof. Dr. M. B. Casu
Institute of Physical and Theoretical Chemistry
University of Tübingen
72076 Tübingen, Germany
E-mail: benedetta.casu@uni-tebingen.de

Dr. E. Giangrisostomi, Dr. R. Ovsyannikov
Institute Methods and Instrumentation for Synchrotron Radiation Research
Helmholtz-Zentrum Berlin
12489 Berlin, Germany

Dr. C. Shu,[+] Prof. Dr. A. Rajca
Department of Chemistry
University of Nebraska
Lincoln, NE 68588, United States

Dr. A. Droghetti
School of Physics and CRANN,
Trinity College, the University of Dublin,
Dublin D02, Ireland

[+] Current address: Toyota Research Institute of North America, Ann Arbor, Michigan 48105, United States

access radical/inorganic interfaces and the therein occurring phenomena.[9c,11–12]

In this work, we study the cobalt/radical interface obtained by depositing a derivative of the Blatter radical[13] (Blatter-pyr, Figure 1) on polycrystalline cobalt. In the polycrystalline form, cobalt maintains its magnetic properties[14] broadly used in spintronic devices. Blatter-pyr, obtained by fusing a Blatter radical to a pyrene unit, is a chemically and thermodynamically stable purely organic radical[13] that can be evaporated in ultra-high vacuum (UHV), under controlled conditions.[12c]

We investigated the occupied and unoccupied states at the interface, by taking advantage of the element-sensitivity of the chosen soft X-ray techniques and combining them with electronic structure calculations. The results indicate that the molecule is strongly hybridized with the cobalt surface. Specifically, we find that the core level spectra reflect a reduction of the magnetic moments of the cobalt atoms, bonded to the molecules, which, in turn, lose their radical character.

Our work presents an original approach for investigating not just the radical/cobalt interface, but also many other interfacial systems. Additionally, the measurements give access to both the molecular and the metallic side at the same time, at room temperature, with the advantage of minimizing the risk of potential discrepancies in the results which can instead occur when different techniques, working under different conditions, are used for the two subsystems.

Results and Discussion

We evaporated Blatter-pyr on polycrystalline cobalt using organic molecular beam deposition (OMBD) which allows precise control of the evaporation parameters.[15] In this experiment, this approach also minimizes the possible contamination of the cobalt surface and avoids generating a non-defined interface.

The films were investigated by X-ray photoelectron spectroscopy (XPS) which is a powerful element-sensitive analytical method.[16] Its signal reflects the chemical state of the investigated systems and when coupled with calculations gives a clear insight into their electronic structure, including at the interface. Introducing this technique to the investigation of radical thin films has revealed its ability to identify whether the unpaired electron of the radical is involved in charge transfer, with or without chemisorption, losing its imparity and, consequently, with the molecule losing its radical character.[11,17]

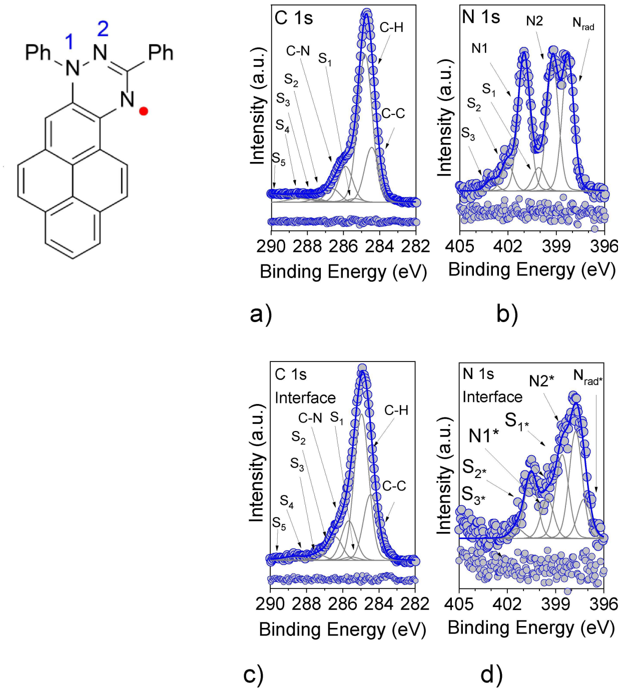

Figure 1. Blatter-pyr films deposited on polycrystalline cobalt. a) C 1s and b) N 1s core-level spectra of a thicker film (nominally 6.0 nm) compared to the interfacial layer (0.4 nm) spectra c) and d), together with their fit components, named as shown in the Blatter-pyr molecular structure (left panel, Ph stands for the phenyl ring). The residuals are also shown. For the fit details see the Supporting Information.

Looking in detail at the C 1s and N 1s core-level spectra, we found that the main lines have a complex shape that depends on the different chemical environments of each element in the radical (Figures 1a and 1b). XPS C 1s core level spectra of the thick films of Blatter-pyr deposited on polycrystalline cobalt (Figure 1a and Figure 2a) are characterized by a main line at around 284.6 eV which is attributed to photoelectrons emitted from the carbon atoms of the aromatic sites (C–C and C–H bound carbons), and by a second feature at higher binding energies (285.8 eV) due to contributions of photoelectrons from the carbon atoms bound to nitrogen atoms (C–N).[12c] Accordingly, the N 1s core level spectra (Figure 1b and Figure 2b) are characterized by three contributions (at around 398.3, 399.2, and 401.0 eV with $\Delta E_{\mathrm{N1-Nrad}} = 2.7$ eV, $\Delta E_{\mathrm{N1-N2}} = 1.8$ eV, and $\Delta E_{\mathrm{N2-Nrad}} = 0\ .9$ eV) that correspond to the three different nitrogen atom chemical environments, as expected for an intact Blatter-pyr.[12c] In addition to the effects due to the different chemical environments, we also observe the presence of several satellite features (in this work indicated with S_i, $i=1,2,3\ldots$), the so-called shake-up satellites, which are typical in photoemission and appear as an effect of the relaxation processes, caused by the core hole left behind by the photoemitted electron.[18] Their intensity has to be taken into account when calculating the stoichiometry of the investigated systems by using XPS (see the Supporting Information).[16,19]

The stoichiometry of the films is proved by using a well-established fit routine,[12c,20] systematically correlated with electron paramagnetic resonance (EPR) results on a variety of different radicals.[11–12,20a,21] The fits indicate that all components are stoichiometrically meaningful (Tables S1–S2 in the Supporting Information). Thus, we can conclude that the XPS spectra reflect the expectations for thin films with the EPR pattern corresponding to intact Blatter-pyr.[12c,20a,21c]

To understand in detail the interface we have performed a thickness-dependent investigation of the core levels spectra. Comparing the spectra of the thicker films with those of the interfacial layer (i.e., the first organic layer formed by the molecule directly in contact with the metallic ferromagnet) and looking at the thickness-dependent behavior of the spectroscopic lines, we observe pronounced changes (Figure 1 and Figure 2). In particular, the experimental spectroscopic lines of the interfacial radical layer are broadened and shifted towards lower binding energies

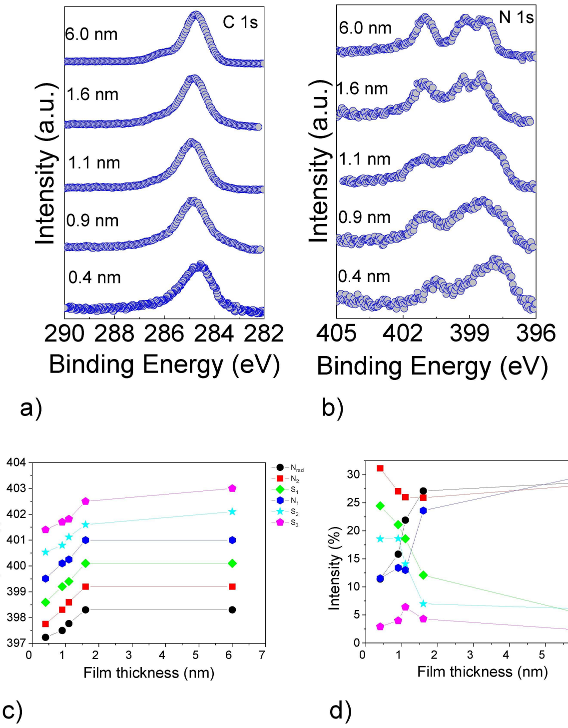

Figure 2. Thickness-dependent a) C 1s and b) N 1s core-level spectra of Blatter-pyr thin films on polycrystalline cobalt. Evolution of c) the energy position and d) the relative intensities of the single components in the N 1s core-level spectra with increasing the nominal film thickness, as obtained from the fit procedure applied to the N 1s core-level spectra in b) (details in the Supporting Information).

(~1 eV). The fit analysis applied to the thickness-dependent spectra shows how the intensity and the binding energy of the single contributions evolve versus thickness (Figures 2c and 2d). This behavior indicates a strong interaction, of a chemical nature, between the Blatter-pyr and cobalt.[1d,22] Also, the intensity of the satellite features is higher. This is another indication of the strong chemisorption of the Blatter-pyr on cobalt.[22b,23] The radical character in films of intact molecules is represented by the feature at lower binding energy (Nrad in Figure 1d) and correlates with its intensity.[12c,21c,24] This feature has a lower intensity in the interfacial film N 1s core level spectrum than in the thicker films (Figure 1d, compare with Figure 1b) revealing only a residual radical character. This is because the chemical environment of molecules in contact with the cobalt surface is significantly different than in the volume of the radical films owing to the bond with cobalt (Figures 1c and 1d, the interfacial features are indicated with an asterisk to underline their different chemical environment and Table S4 in the Supporting Information).

The finding that Blatter-pyr is chemisorbed on cobalt is further supported by the Near Edge X-ray Absorption Fine Structure (NEXAFS) spectra measured on the interfacial layers (Figure 3) at the C K edge. The signal arises from transitions from the C 1s core levels to the unoccupied states. The spectra are substantially different from the spectra of the thick films (Figure S1),[9c,24] lacking the pre-edge feature attributed to the transitions from the C 1s core levels to the singly unoccupied molecular orbital (SUMO), and the peaks in the 288–290 eV photon energy region (Figure S1).[9c,24] This result suggests that the SUMO becomes occupied due to the occurrence of charge transfer from the cobalt surface to the radical film. It corroborates the XPS results, evidencing the chemisorption of the radical on the cobalt. We also observe that the NEXAFS spectra for two different polarizations of the incident light with respect to the surface of the polycrystalline cobalt do not show any strong dichroism,[24] revealing a high degree of azimuthal disorder in the interfacial layer.

Combining XPS and NEXAFS has provided a detailed description of the phenomena at the interface influencing the radical character of the first molecular layer deposited on cobalt.

Therefore, we now address the cobalt side. We measured the NEXAFS Co $L_{2,3}$ edge spectra (corresponding to transitions from the Co 2p core level states to the 3d unoccupied states) before and after the deposition of the radical films (Figure 4).

In the literature, spectra are compared to understand the influence of the alloying, oxidation, or ligands on the cobalt bulk.[25] Conversely, here we use this approach to investigate a hybrid organic radical/inorganic interface.

Cobalt is a highly reactive material, which leads to the formation of various oxides and hydroxides if left exposed to ambient conditions or oxygen contaminants in high vacuum.[25g,26] Therefore, it is important to rule out oxidation as a cause for the potential changes. The cobalt L_3 absorption edge shows distinctive features, depending on the oxidation state and the ligand field splitting (if applicable), such as peak splitting and shoulders in the peaks.[25f,g,27] The line shape of the cobalt NEXAFS spectra after deposition does not deviate prominently from that of the clean cobalt surface (Figure 4). Neither splitting nor additional shoulders are present in the absorption spectra of the Blatter-pyr/cobalt interface after film deposition. This is a clear indication that no significant oxidation of the cobalt occurs upon radical deposition.

The signal difference evidences a slight increase in intensity after film deposition (red curve, Figure 4). The enhanced intensity indicates a lower electronic population in the final states after deposition,[3c,25f] concomitant with cobalt-to-radical charge transfer as evinced with XPS and NEXAFS at the molecular side.

Taking inspiration from the data analysis performed on electron energy loss spectroscopy (EELS),[25a–d] we have adapted it to the NEXAFS spectra to quantify the differences in the spectra before and after evaporation. We have calculated the $I(L_3)/I(L_2)$ ratio, the branching ratio $I(L_3)/I(L_2)+I(L_3)$, and the normalized white lines (i.e., $I(L_2)+I(L_3)$ normalized to the continuum),[25c,d] being $I(L_3)$ and $I(L_2)$ the peak areas of the Co L_2 and Co L_3 edges (see Table S5 and the Supporting Information for definitions and

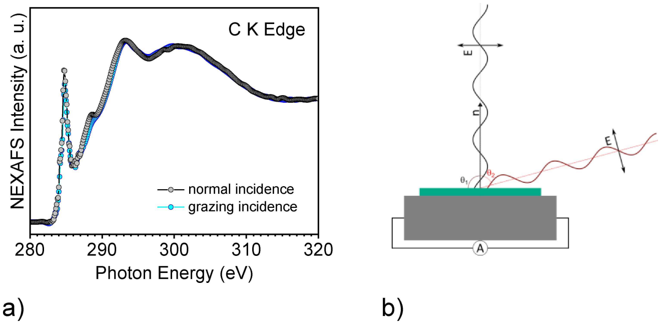

Figure 3. a) C K edge of an interfacial Blatter-pyr film deposited on polycrystalline cobalt. b) Geometry of the experiment, normal incidence ($\theta_1=90°$) and grazing incidence ($\theta_2=20°$).

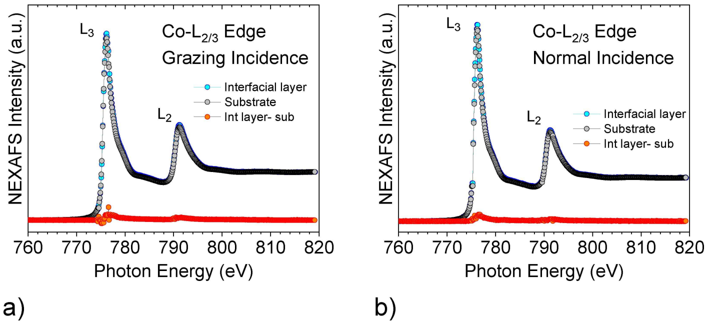

Figure 4. Co L2,3 NEXAFS spectra of the polycrystalline cobalt surface before and after deposition of an interfacial layer of Blatter-pyr, as indicated, for a) grazing incidence and b) normal incidence (see also Figure 3).

details). We find that the I(L_3)/I(L_2) ratio is lower after the layer deposition, indicating lower d orbital occupancy.[25a,c,d,f,g] Considering methods previously used for EELS spectra;[25c,d] it is also possible to obtain a numerical estimate of the d orbital occupancy that confirms that it is lower after chemisorption of the Blatter-pyr (see Table S5). The analysis of the spectra reveals a consistent pattern: the cobalt surface loses charge to the radical, as indicated by all the calculated values (Table S5).

At this point, the question is how the interaction with the radical monolayer and the consequent charge transfer influence the magnetic properties of the cobalt surface. We answer this question through a detailed examination of the electronic configuration of the unoccupied states in the polycrystalline cobalt, both pre- and post-evaporation of the interfacial film: we have calculated the difference in the magnetic moment before and after deposition by using the calculated I(L_3)/I(L_2) ratio, the branching ratio I(L_3)/I(L_2)+I(L_3), and the normalized white lines.[25a,b,28] We could determine a difference in magnetic moment of $-0.05\ \mu_B$ after evaporation (see the Section Methods in the Supporting Information). Although this value is a simple estimation what is important is the tendency identified by the calculation, i.e., the cobalt magnetic moment is lower after evaporation.

In pursuit of further exploring this aspect, we returned to XPS (because of its higher surface sensitivity in comparison with NEXAFS) and directed our focus towards analyzing the Co 3 s core level spectra, characterized by the multiplet splitting that may occur when unpaired electrons occupy valence states.[29] We fitted the Co 3 s core level spectra before and after the deposition of the interfacial film, by using a Doniach-Sunjic line shape (Figure 5).[29] We find that the doublet binding energy separation is around 3.5 eV, in agreement with the literature for polycrystalline cobalt and cobalt compounds.[30] The energy separation between the two peaks correlates with the 3s–3d exchange interaction energy, while the peak intensities of the doublet features correlate with the total spin and, thus, with the magnetic moment.[29,31]

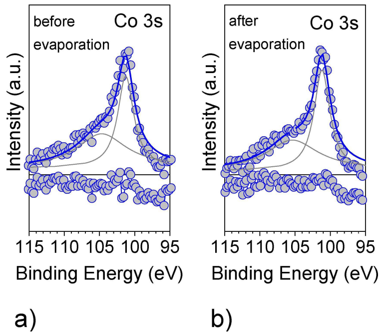

Figure 5. Co 3 s core-level spectra a) before and b) after evaporation of the interfacial radical layer, together with their fit. The residuals are also shown. For the fit details see the Supporting Information.

We calculated the magnetic moment, obtaining $1.79\ \mu_B$ and $1.50\ \mu_B$ before and after evaporation (see the Section Methods in the Supporting Information and Tables S6 and S7). Thus, by examining both the occupied and unoccupied states, we come to the result that the cobalt magnetic moment decreases due to the chemisorption of the Blatter-pyr. Here, we like to mention that this method gave good values of the magnetic moment in cobalt-based materials, chromium compounds, and iron alloys,[29–32] however some critical issues have been reported in other cases.[33] Differences in the fitting procedure might lead to different values of the magnetic moment. In our opinion, these values must be considered as tendencies, useful to make comparisons among different chemical conditions of the cobalt surface. We also note that the difference in the magnetic moment using this method is $-0.29\ \mu_B$ after evaporation, higher than for the NEXAFS analysis. This is because the X-ray penetration depth and the information depth are different in the two cases, being even more surface sensitivity in XPS (see the Supporting Information).

To support our method and further elucidate the experimental results we performed electronic structure calculations based on Density Functional Theory (DFT) following the same approach used in other studies about radical molecules and their adsorption on surfaces.[12b,21c,34] Blatter-pyr is a planar molecule, except for the phenyl ring bonded to N1, which forms a dihedral angle, $\vartheta = 44.3^{o}$, with the Blatter core because of the steric interaction with the pyrene unit. The electronic structure of Blatter-pyr is typical of a radical with spin $S = 1/2$.[9c,12b,21c,24,34a,35] It presents an unpaired electron and, therefore, a singly occupied (and a singly unoccupied) molecular orbital SOMO (and SUMO) (Figure S2 in the Supporting Information). These are mostly localized on the three nitrogen atoms (N1, N2, N3 = Nrad) of the Blatter core, with a small contribution from the fused pyrene unit, as seen in the spin density isosurface in Figure 6a. The results are overall consistent with previous DFT calculations for the same molecule.[9c,21c,24,35c] The simulated N 1s core level spectrum is displayed in Figure 6a. It resembles the experimental one for thick layers. We observe three main peaks that correspond to the three different N atoms. The peak at the lowest binding energy is associated with N3 (= Nrad), the one at the highest binding energy to N1, and the one at the intermediate binding energy to N2. All peak binding energies are underestimated by about 20 eV compared to the experimental values because of the employed approximations (see computational methods in the Supporting Information). Despite that, we observe that the energy splitting of the three peaks, $\Delta E_{N1-N3} = 2.9$ eV, $\Delta E_{N1-N2} = 1.9$ eV, and $\Delta E_{N2-N3} = 1$ .0 eV, agrees very well with the experimental results (see above). Thus, the calculations confirm the correct interpretation of the core spectra as previously discussed.

The cobalt/molecule interface is modeled by placing one molecule on a Co slab. We consider the Co (0001) surface, which is the prevalent surface in our polycrystalline samples.[36] Here we only consider one adsorption geometry, shown in Figure 6d. Different geometries are discussed in the Supporting Information. After the geometry optimiza-

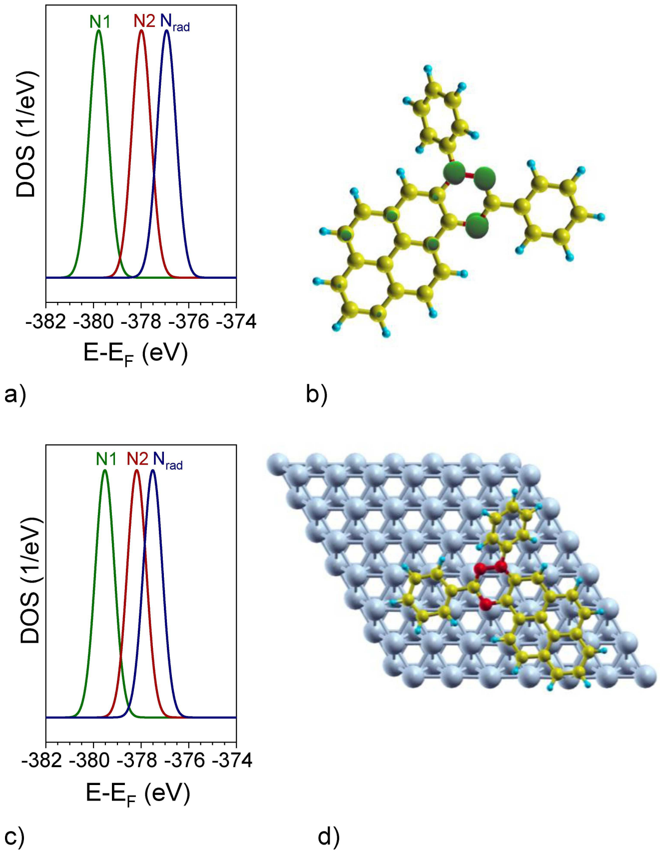

Figure 6. Simulated N 1s XPS spectrum (DOS) for the a) the isolated molecule and c) the molecule on the Co surface. The zero-energy reference is set to the Fermi level. b) Spin density isosurface for the isolated molecule. d) Top view of the slab used in the calculations.

tion, the calculated average adsorption distance is about 2.1 Å which is typical for organic molecules strongly chemisorbed on ferromagnetic transition metals.[4a,8c] The radical nature of the molecule is not preserved. The calculated magnetic moment of the Blatter core is only about 0.12 μ_B. The molecular features, such as the SOMO and the SUMO, in the electronic structure near the Fermi level, disappear as a result of the hybridization with Co, and they merge into very broad states (see Figure S3 in the Supporting Information), similar to those found for other organic molecules on ferromagnetic transition metals.[4a] In turn, the magnetic moments of Co atoms bonded to the molecule are reduced from about 1.7 μ_B, the value for the clean surface, to about 1.3 μ_B, reproducing the tendency of the experimental observation.

The simulated N 1s core level spectrum of the molecule on the Co slab is shown in Figure 6c. The energy splitting between the three characteristic peaks is strongly reduced compared to that seen for the isolated molecule. We obtain that $\Delta E_{\mathrm{N1-N3}} = 2.0$ eV, $\Delta E_{\mathrm{N1-N2}} = 1.4$ eV, and $\Delta E_{\mathrm{N2-N3}} = 0.6$ eV. This explains the broadened line shapes of the N 1s core level curve that we observed experimentally at the interface (Figure 1d). Overall, our DFT results fully support the arguments used to interpret the experiments. The molecule is strongly hybridized with the surface, and the change in the core level spectra reflects the modification of the molecule's and cobalt's electronic structure induced by the bonding across the interface.

Conclusions

We have investigated the effect of a Blatter-pyr layer deposited on polycrystalline cobalt. We find that Blatter-pyr loses its radical character. This is irrelevant in this study because our focus is on the interface as a system. Future work might envisage the necessity of an intact radical decorating the cobalt surface. This can be achieved by designing the radical molecule with functional groups that attach to the ferromagnetic surface, hindering the chemisorption of the radical moiety, as, for example, on gold surfaces.[20b,34a,37]

We show that it is possible to predict the impact of the organic interfacial layer on the magnetic properties of the polycrystalline cobalt, analyzing in extreme detail X-ray photoemission and absorption data at room temperature. Comparing this system to the prototypical C_{60}/cobalt interface, the effect of depositing a radical layer turns out to be promising. Depositing 20 nm of C_{60} on a 5 nm cobalt thin film decreases the magnetic moment of a cobalt atom on average of around 0.27 μ_B,[6] similar to the value that we found in this work for the Blatter-pyr/cobalt interface.

Despite their importance for spintronics, the number of investigated organic materials that are known to influence the cobalt properties remains quite limited because describing the electronic and magnetic properties of such an interface requires a large variety of different techniques, high surface sensitivity, and often high fields and low temperatures, too. In this respect the versatility of our approach plays an important role, allowing preselecting, beforehand, organic/ferromagnetic and radical/ferromagnetic interfaces, identifying the most promising for spintronic applications.

Supporting Information

The authors have cited additional references within the Supporting Information.[12a,c,20b,25a–d,28–29,32d,38]

Acknowledgements

The authors would like to thank Helmholtz-Zentrum Berlin (HZB) for providing beamtime at BESSY II, and Dr M. Pink for the X-ray structure of the radical. Financial support from HZB, the German Research Foundation (DFG, contract CA852/11-3, project number: 394233453), the Federal Ministry of Education and Research (BMBF) in the framework of the program "Erforschung von Universum und Materie—ErUM-Pro" (RadicalQuantum, Grant number 05K22VT1), Science Foundation Ireland, the Royal Society through the University Research Fellowships URF-R1-191769 and the Chemistry Division of National Science Foundation (grants CHE-1955349 and CHE-2247170) is gratefully acknowledged. This work was supported by the European Union's Horizon 2020 Research and Innovation program under grant agreement no. 965046, FET-Open project Interfast (Gated INTERfaces for FAST information processes). Open Access funding enabled and organized by Projekt DEAL.

Conflict of Interest

The authors declare no conflict of interest.

Data Availability Statement

The data that support the findings of this study are available from the corresponding author upon reasonable request.

Keywords: radical thin films · cobalt · interface · density functional theory · soft x-rays

---

[1] a) N. Koch, *ChemPhysChem* **2007**, *8*, 1438; b) G. Heimel, I. Salzmann, S. Duhm, N. Koch, *Chem. Mater.* **2011**, *23*, 359; c) N. Koch, *Phys. Status Solidi RRL* **2012**, *6*, 277; d) G. Heimel, S. Duhm, I. Salzmann, A. Gerlach, A. Strozecka, J. Niederhausen, C. Burker, T. Hosokai, I. Fernandez-Torrente, G. Schulze, S. Winkler, A. Wilke, R. Schlesinger, J. Frisch, B. Broker, A. Vollmer, B. Detlefs, J. Pflaum, S. Kera, K. J. Franke, N. Ueno, J. I. Pascual, F. Schreiber, N. Koch, *Nat. Chem.* **2013**, *5*, 187; e) N. Koch, N. Ueno, A. T. S. Wee, *The Molecule-Metal Interface*, Wiley **2013**; f) E. Umbach, *Prog. Surf. Sci.* **1990**, *35*, 113.

[2] a) S. Sanvito, *Nat. Phys.* **2010**, *6*, 562; b) V. Dediu, L. E. Hueso, I. Bergenti, A. Riminucci, F. Borgatti, P. Graziosi, C. Newby, F. Casoli, M. P. De Jong, C. Taliani, Y. Zhan, *Phys. Rev. B* **2008**, *78*, 115203; c) C. Barraud, P. Seneor, R. Mattana, S. Fusil, K. Bouzehouane, C. Deranlot, P. Graziosi, L. Hueso, I. Bergenti, V. Dediu, F. Petroff, A. Fert, *Nat. Phys.* **2010**, *6*, 615; d) M. Cinchetti, K. Heimer, J.-P. Wüstenberg, O. Andreyev, M. Bauer, S. Lach, C. Ziegler, Y. Gao, M. Aeschlimann, *Nat. Mater.* **2009**, *8*, 115; e) S. Lach, A. Altenhof, K. Tarafder, F. Schmitt, M. E. Ali, M. Vogel, J. Sauther, P. M. Oppeneer, C. Ziegler, *Adv. Funct. Mater.* **2012**, *22*, 989; f) S. Steil, N. Großmann, M. Laux, A. Ruffing, D. Steil, M. Wiesenmayer, S. Mathias, O. L. A. Monti, M. Cinchetti, M. Aeschlimann, *Nature Phys.* **2013**, *9*, 242; g) A. Droghetti, P. Thielen, I. Rungger, N. Haag, N. Großmann, J. Stöckl, B. Stadtmüller, M. Aeschlimann, S. Sanvito, M. Cinchetti, *Nat. Commun.* **2016**, *7*, 12668.

[3] a) M. Cinchetti, V. A. Dediu, L. E. Hueso, *Nat. Mater.* **2017**, *16*, 507; b) M. Galbiati, S. Tatay, C. Barraud, A. V. Dediu, F. Petroff, R. Mattana, P. Seneor, *MRS Bull.* **2014**, *39*, 602; c) S. Shi, Z. Sun, A. Bedoya-Pinto, P. Graziosi, X. Li, X. Liu, L. Hueso, V. A. Dediu, Y. Luo, M. Fahlman, *Adv. Funct. Mater.* **2014**, *24*, 4812.

[4] a) N. Atodiresei, J. Brede, P. Lazić, V. Caciuc, G. Hoffmann, R. Wiesendanger, S. Blügel, *Phys. Rev. Lett.* **2010**, *105*, 066601; b) J. Brede, N. Atodiresei, S. Kuck, P. Lazić, V. Caciuc, Y. Morikawa, G. Hoffmann, S. Blügel, R. Wiesendanger, *Phys. Rev. Lett.* **2010**, *105*, 047204.

[5] a) K. V. Raman, A. M. Kamerbeek, A. Mukherjee, N. Atodiresei, T. K. Sen, P. Lazic, V. Caciuc, R. Michel, D. Stalke, S. K. Mandal, S. Blugel, M. Munzenberg, J. S. Moodera, *Nature* **2013**, *493*, 509; b) M. Callsen, V. Caciuc, N. Kiselev, N. Atodiresei, S. Blügel, *Phys. Rev. Lett.* **2013**, *111*, 106805.

[6] T. Moorsom, M. Wheeler, T. Mohd Khan, F. Al Ma'Mari, C. Kinane, S. Langridge, D. Ciudad, A. Bedoya-Pinto, L. Hueso, G. Teobaldi, V. K. Lazarov, D. Gilks, G. Burnell, B. J. Hickey, O. Cespedes, *Phys. Rev. B* **2014**, *90*, 125311.

[7] K. Bairagi, A. Bellec, V. Repain, C. Chacon, Y. Girard, Y. Garreau, J. Lagoute, S. Rousset, R. Breitwieser, Y.-C. Hu, Y. C. Chao, W. W. Pai, D. Li, A. Smogunov, C. Barreteau, *Phys. Rev. Lett.* **2015**, *114*, 247203.

[8] a) K. Bairagi, A. Bellec, V. Repain, C. Fourmental, C. Chacon, Y. Girard, J. Lagoute, S. Rousset, L. Le Laurent, A. Smogunov, C. Barreteau, *Phys. Rev. B* **2018**, *98*, 085432; b) M. Benini, G. Allodi, A. Surpi, A. Riminucci, K.-W. Lin, S. Sanna, V. A. Dediu, I. Bergenti, *Adv. Mater. Interfaces* **2022**, *9*, 2201394; c) A. Halder, S. Bhandary, D. D. O'Regan, S. Sanvito, A. Droghetti, *Phys. Rev. Mater.* **2023**, *7*, 064409.

[9] a) D. Gatteschi, R. Sessoli, J. Villain, *Molecular Nanomagnets*, Oxford University Press Inc., New York **2006**; b) A. Rajca, *Chem. Rev.* **1994**, *94*, 871; c) T. Junghoefer, A. Calzolari, I. Baev, M. Glaser, F. Ciccullo, E. Giangrisostomi, R. Ovsyannikov, F. Kielgast, M. Nissen, J. Schwarz, N. M. Gallagher, A. Rajca, M. Martins, M. B. Casu, *Chem* **2022**, *8*, 801.

[10] a) S. Nakazawa, S. Nishida, T. Ise, T. Yoshino, N. Mori, R. D. Rahimi, K. Sato, Y. Morita, K. Toyota, D. Shiomi, M. Kitagawa, H. Hara, P. Carl, P. Höfer, T. Takui, *Angew. Chem. Int. Ed.* **2012**, *51*, 9860; b) S. Sproules, in *Electron Paramagnetic Resonance: Volume 25, Vol. 25*, The Royal Society of Chemistry **2017**, pp. 61; c) K. Oyaizu, H. Nishide, *Adv. Mater.* **2009**, *21*, 2339; d) T. Suga, H. Konishi, H. Nishide, *Chem. Commun.* **2007**, 1730; e) M. R. Wasielewski, M. D. E. Forbes, N. L. Frank, K. Kowalski, G. D. Scholes, J. Yuen-Zhou, M. A. Baldo, D. E. Freedman, R. H. Goldsmith, T. Goodson, M. L. Kirk, J. K. McCusker, J. P. Ogilvie, D. A. Shultz, S. Stoll, K. B. Whaley, *Nat. Chem. Rev.* **2020**, *4*, 490.

[11] M. B. Casu, *Acc. Chem. Res.* **2018**, *51*, 753.

[12] a) S.-A. Savu, I. Biswas, L. Sorace, M. Mannini, D. Rovai, A. Caneschi, T. Chassé, M. B. Casu, *Chem. Eur. J.* **2013**, *19*, 3445; b) R. Kakavandi, A. Calzolari, Y. B. Borozdina, P. Ravat, T. Chassé, M. Baumgarten, M. B. Casu, *Nano Res.* **2016**, *9*, 3515; c) F. Ciccullo, N. M. Gallagher, O. Geladari, T. Chasse, A. Rajca, M. B. Casu, *ACS Appl. Mater. Interfaces* **2016**, *8*, 1805.

[13] a) H. M. Blatter, H. Lukaszewski, *Tetrahedron Lett.* **1968**, *9*, 2701; b) C. P. Constantinides, P. A. Koutentis, H. Krassos, J. M. Rawson, A. J. Tasiopoulos, *J. Org. Chem.* **2011**, *76*, 2798.

[14] a) M. Liebs, K. Hummler, M. Fähnle, *Phys. Rev. B* **1995**, *51*, 8664; b) Y. Kakehashi, *Phys. Rev. B* **1991**, *43*, 10820; c) M. J. Besnus, A. J. P. Meyer, R. Berninger, *Phys. Lett. A* **1970**, *32*, 192.

[15] S. R. Forrest, *Chem. Rev.* **1997**, *97*, 1793.

[16] K. Siegbahn, C. Nordling, A. Fahlman, R. Nordberg, K. Hamrin, J. Hedman, G. Johansson, T. Bergmark, S.-E. Karlsson, I. Lindgren, B. Lindberg, *ESCA, Atomic, Molecular and Solid State Structure Studied by Means of Electron Spectroscopy*, Almqvist and Wiksells, Uppsala **1967**.

[17] a) J. Z. Low, G. Kladnik, L. L. Patera, S. Sokolov, G. Lovat, E. Kumarasamy, J. Repp, L. M. Campos, D. Cvetko, A. Morgante, L. Venkataraman, *Nano Lett.* **2019**, *19*, 2543; b) M. R. Ajayakumar, C. Moreno, I. Alcón, F. Illas, C. Rovira, J. Veciana, S. T. Bromley, A. Mugarza, M. Mas-Torrent, *J. Phys. Chem. Lett.* **2020**, *11*, 3897.

[18] S. Hüfner, *Photoelectron Spectroscopy*, 3 ed., Springer-Verlag Berlin Heidelberg **2003**.

[19] a) K. M. Siegbahn, *Vol. 2020*, Nobelprize.org. Nobel Media AB 2014. Web; b) O. Travnikova, K. J. Børve, M. Patanen, J. Söderström, C. Miron, L. J. Sæthre, N. Mårtensson, S. Svensson, *J. Electron Spectrosc. Relat. Phenom.* **2012**, *185*, 191.

[20] a) S. Zhang, M. Pink, T. Junghoefer, W. Zhao, S.-N. Hsu, S. Rajca, A. Calzolari, B. W. Boudouris, M. B. Casu, A. Rajca, *J. Am. Chem. Soc.* **2022**, *144*, 6059; b) T. Junghoefer, E. M. Nowik-Boltyk, J. A. de Sousa, E. Giangrisostomi, R. Ovsyannikov, T. Chassé, J. Veciana, M. Mas-Torrent, C. Rovira, N. Crivillers, M. B. Casu, *Chem. Sci.* **2020**, *11*, 9162.

[21] a) R. Kakavandi, P. Ravat, S. A. Savu, Y. B. Borozdina, M. Baumgarten, M. B. Casu, *ACS Appl. Mater. Interfaces* **2015**, *7*, 1685; b) R. Kakavandi, S.-A. Savu, L. Sorace, D. Rovai, M. Mannini, M. B. Casu, *J. Phys. Chem. C* **2014**, *118*, 8044; c) F. Ciccullo, A. Calzolari, K. Bader, P. Neugebauer, N. M. Gallagher, A. Rajca, J. van Slageren, M. B. Casu, *ACS Appl. Mater. Interfaces* **2019**, *11*, 1571.

[22] a) S. A. Savu, G. Biddau, L. Pardini, R. Bula, H. F. Bettinger, C. Draxl, T. Chasse, M. B. Casu, *J. Phys. Chem. C* **2015**, *119*, 12538; b) M. Häming, A. Schöll, E. Umbach, F. Reinert, *Phys. Rev. B* **2012**, *85*, 1; c) T.-C. Tseng, C. Urban, Y. Wang, R. Otero, S. L. Tait, M. Alcamí, D. Écija, M. Trelka, J. M. Gallego, N. Lin, M. Konuma, U. Starke, A. Nefedov, A. Langner, C. Wöll, M. Á. Herranz, F. Martín, N. Martín, K. Kern, R. Miranda, *Nat. Chem.* **2010**, *2*, 374; d) Y. Zou, L. Kilian, A. Schöll, T. Schmidt, R. Fink, E. Umbach, *Surf. Sci.* **2006**, *600*, 1240; e) A. Franco-Cañellas, Q. Wang, K. Broch, D. A. Duncan, P. K. Thakur, L. Liu, S. Kera, A. Gerlach, S. Duhm, F. Schreiber, *Phys. Rev. Mater.* **2017**, *1*, 013001.

[23] A. Schöll, Y. Zou, T. Schmidt, R. Fink, E. Umbach, *J. Phys. Chem. B* **2004**, *108*, 14741.

[24] E. M. Nowik-Boltyk, T. Junghoefer, M. Glaser, E. Giangrisostomi, R. Ovsyannikov, S. Zhang, C. Shu, A. Rajca, A. Calzolari, M. B. Casu, *ACS Appl. Mater. Interfaces* **2023**, *15*, 30935.

[25] a) S. Ii, K. Hirayama, K. Matsunaga, H. Fujii, S. Tsurekawa, *Scr. Mater.* **2013**, *68*, 253; b) D. M. Pease, A. Fasihuddin, M. Daniel, J. I. Budnick, *Ultramicroscopy* **2001**, *88*, 1; c) D. H. Pearson, C. C. Ahn, B. Fultz, *Phys. Rev. B* **1993**, *47*, 8471; d) D. H. Pearson, B. Fultz, C. C. Ahn, *Appl. Phys. Lett.* **1988**,

53, 1405; e) T. Mizokawa, L. H. Tjeng, P. G. Steeneken, N. B. Brookes, I. Tsukada, T. Yamamoto, K. Uchinokura, *Phys. Rev. B* **2001**, *64*, 115104; f) L. Chen, F. Hu, H. Duan, Q. Liu, H. Tan, W. Yan, T. Yao, Y. Jiang, Z. Sun, S. Wei, *Appl. Phys. Lett.* **2016**, *108*; g) D. K. Bora, X. Cheng, M. Kapilashrami, P. A. Glans, Y. Luo, J. H. Guo, *J. Synchrotron Radiat.* **2015**, *22*, 1450.

[26] a) C. R. Brundle, T. J. Chuang, D. W. Rice, *Surf. Sci.* **1976**, *60*, 286; b) K. P. Reddy, R. Jain, M. K. Ghosalya, C. S. Gopinath, *J. Phys. Chem. C* **2017**, *121*, 21472; c) H. G. Tompkins, J. A. Augis, *Oxid. Met.* **1981**, *16*, 355.

[27] a) M. C. Biesinger, B. P. Payne, A. P. Grosvenor, L. W. M. Lau, A. R. Gerson, R. S. C. Smart, *Appl. Surf. Sci.* **2011**, *257*, 2717; b) K. Rode, R. Mattana, A. Anane, V. Cros, E. Jacquet, J.-P. Contour, F. Petroff, A. Fert, M.-A. Arrio, P. Sainctavit, P. Bencok, F. Wilhelm, N. B. Brookes, A. Rogalev, *Appl. Phys. Lett.* **2008**, *92*.

[28] M. Stöger-Pollach, *Scr. Mater.* **2013**, *69*, 820.

[29] *Surface analysis by Auger and X-ray photoelectron spectroscopy*, IM Publications and SurfaceSpectra Limited, Cromwell Press, Trowbridge, UK **2003**.

[30] J. C. Carver, G. K. Schweitzer, T. A. Carlson, *J. Chem. Phys.* **2003**, *57*, 973.

[31] N. Sirica, F. Bondino, S. Nappini, I. Píš, L. Poudel, A. D. Christianson, D. Mandrus, D. J. Singh, N. Mannella, *Phys. Rev. B* **2015**, *91*, 121102.

[32] a) I. Pollini, *Philos. Mag.* **2005**, *85*, 2641; b) D. G. Van Campen, L. E. Klebanoff, *Phys. Rev. B* **1994**, *49*, 2040; c) A. T. Kozakov, A. G. Kochur, A. V. Nikolsky, K. A. Googlev, V. G. Smotrakov, V. V. Eremkin, *J. Electron Spectrosc. Relat. Phenom.* **2011**, *184*, 508; d) I. N. Shabanova, N. S. Terebova, *Surf. Interface Anal.* **2010**, *42*, 846.

[33] a) G. Garreau, V. Schorsch, E. Beaurepaire, J. Parlebas, C. O. Speder, P. Rennert, *J. Phys. IV* **1994**, *4*, C9; b) J. F. van Acker, Z. M. Stadnik, J. C. Fuggle, H. J. W. M. Hoekstra, K. H. J. Buschow, G. Stroink, *Phys. Rev. B* **1988**, *37*, 6827; c) F. U. Hillebrecht, R. Jungblut, E. Kisker, *Phys. Rev. Lett.* **1990**, *65*, 2450.

[34] a) V. Mugnaini, A. Calzolari, R. Ovsyannikov, A. Vollmer, M. Gonidec, I. Alcon, J. Veciana, M. Pedio, *J. Phys. Chem. Lett.* **2015**, *6*, 2101; b) G. Seber, A. V. Rudnev, A. Droghetti, I. Rungger, J. Veciana, M. Mas-Torrent, C. Rovira, N. Crivillers, *Chem. Eur. J.* **2017**, *23*, 1415.

[35] a) W. H. Appelt, A. Droghetti, L. Chioncel, M. M. Radonjić, E. Muñoz, S. Kirchner, D. Vollhardt, I. Rungger, *Nanoscale* **2018**, *10*, 17738; b) A. Droghetti, I. Rungger, *Phys. Rev. B* **2017**, *95*, 085131; c) A. Calzolari, A. Rajca, M. B. Casu, *J. Mater. Chem. C* **2021**, *9*, 10787; d) T. Junghoefer, N. M. Gallagher, K. Kolanji, E. Giangrisostomi, R. Ovsyannikov, T. Chassé, M. Baumgarten, A. Rajca, A. Calzolari, M. B. Casu, *Chem. Mater.* **2021**, *33*, 2019.

[36] a) R. A. Ciufo, S. Han, M. E. Floto, G. Henkelman, C. B. Mullins, *Chem. Commun.* **2020**, *56*, 2865; b) R. Tran, Z. Xu, B. Radhakrishnan, D. Winston, W. Sun, K. A. Persson, S. P. Ong, *Sci. Data* **2016**, *3*, 160080; c) M. E. Bridge, C. M. Comrie, R. M. Lambert, *Surf. Sci.* **1977**, *67*, 393.

[37] a) M. R. Ajayakumar, I. Alcón, S. T. Bromley, J. Veciana, C. Rovira, M. Mas-Torrent, *RSC Adv.* **2017**, *7*, 20076; b) J. A. de Sousa, F. Bejarano, D. Gutiérrez, Y. R. Leroux, E. M. Nowik-Boltyk, T. Junghoefer, E. Giangrisostomi, R. Ovsyannikov, M. B. Casu, J. Veciana, M. Mas-Torrent, B. Fabre, C. Rovira, N. Crivillers, *Chem. Sci.* **2020**, *11*, 516.

[38] a) B. V. Crist, *Commercially Pure Binary Oxides and a few Common Carbonates and Hydroxides, Vol. 2*, XPS International, LLC **2005**; b) R. Ovsyannikov, P. Karlsson, M. Lundqvist, C. Lupulescu, W. Eberhardt, A. Fohlisch, S. Svensson, N. Martensson, *J. Electron Spectrosc. Relat. Phenom.* **2013**, *191*, 92; c) E. Giangrisostomi, R. Ovsyannikov, F. Sorgenfrei, T. Zhang, A. Lindblad, Y. Sassa, U. B. Cappel, T. Leitner, R. Mitzner, S. Svensson, N. Mårtensson, A. Föhlisch, *J. Electron Spectrosc. Relat. Phenom.* **2018**, *224*, 68; d) V. Blum, R. Gehrke, F. Hanke, P. Havu, V. Havu, X. Ren, K. Reuter, M. Scheffler, *Comput. Phys. Commun.* **2009**, *180*, 2175; e) J. P. Perdew, K. Burke, M. Ernzerhof, *Phys. Rev. Lett.* **1996**, *77*, 3865; f) J. P. Perdew, K. Burke, M. Ernzerhof, *Phys. Rev. Lett.* **1997**, *78*, 1396; g) in *Biophysico-Chemical Processes Involving Natural Nonliving Organic Matter in Environmental Systems*; h) M. B. Casu, P. Cosseddu, D. Batchelor, A. Bonfiglio, E. Umbach, *J. Chem. Phys.* **2008**, *128*, 014705; i) M. B. Casu, A. Scholl, K. R. Bauchspiess, D. Hubner, T. Schmidt, C. Heske, E. Umbach, *J. Phys. Chem. C* **2009**, *113*, 10990; j) J. Stöhr, *NEXAFS Spectroscopy*, Springer **2003**; k) A. Schöll, Y. Zou, T. Schmidt, R. Fink, E. Umbach, *J. Electron Spectrosc. Relat. Phenom.* **2003**, *129*, 1; l) C. J. Powell, *J. Electron Spectrosc. Relat. Phenom.* **1988**, *47*, 197; m) B. L. Henke, E. M. Gullikson, J. C. Davis, *At. Data Nucl. Data Tables* **1993**, *54*, 181; n) M. P. Seah, W. A. Dench, *Surf. Interface Anal.* **1979**, *1*, 2; o) S.-A. Savu, M. B. Casu, S. Schundelmeier, S. Abb, C. Tonshoff, H. F. Bettinger, T. Chassé, *RSC Adv.* **2012**, *2*, 5112.

Manuscript received: February 19, 2024
Accepted manuscript online: June 6, 2024
Version of record online: July 22, 2024

Angewandte Chemie
Eine Zeitschrift der Gesellschaft Deutscher Chemiker

Supporting Information

Radical-Induced Changes in Transition Metal Interfacial Magnetic Properties: A Blatter Derivative on Polycrystalline Cobalt

*E. M. Nowik-Boltyk, T. Junghoefer, E. Giangrisostomi, R. Ovsyannikov, C. Shu, A. Rajca, A. Droghetti, M. B. Casu**

Radical-Induced Changes in Transition Metal Interfacial Magnetic Properties: A Blatter Derivative on Polycrystalline Cobalt

Ewa Malgorzata Nowik-Boltyk,[a] Tobias Junghoefer,[a] Erika Giangrisostomi,[b] Ruslan Ovsyannikov,[b] Chan Shu,[c] Andrzej Rajca,[c] Andrea Droghetti,[d] M. Benedetta Casu*[a]

---

[a] E. M. Nowik-Boltyk, Dr. T. Junghöfer, Prof. Dr. M. B. Casu
Institute of Physical and Theoretical Chemistry
University of Tübingen
72076 Tübingen, Germany
E-mail: benedetta.casu@uni-tebingen.de

[b] Dr. E. Giangrisostomi, Dr. R. Ovsyannikov
Institute Methods and Instrumentation for Synchrotron Radiation Research
Helmholtz-Zentrum Berlin,
12489 Berlin, Germany

[c] Dr. C. Shu, Prof. Dr. A Rajca
Department of Chemistry
University of Nebraska
Lincoln, NE 68588, United States

[d] Dr. A. Droghetti
School of Physics and CRANN,
Trinity College, the University of Dublin,
Dublin, Ireland

Table of contents

1) Methods.

2) Brief description of the fit procedure and parameters for the C 1s and N 1s core level spectra.

3) C Kedge NEXAFS spectra: thick versus interfacial layer.

4) Calculated I(L_3)/I(L_2) ratio, the I(L_3)/I(L_2)+I(L_3) branching ratio and normalized white lines.

5) Fit parameters for the XPS Co 3s core level spectra as in Figure 5.

6) Comparison of different adsorption geometries.

7) Density of states at the Fermi level.

8) References.

1) Methods

Experimental section

The in-situ sample preparation and XPS measurements were carried out in a multi-chamber UHV system that consisted of three chambers: an analysis chamber, a preparation chamber, and a chamber for organic material deposition. Polycrystalline cobalt foils (MaTeck, 99,9% purity) were cleaned by repeated cycles of argon sputtering (2 kV) and annealing at around 573 K. XPS was used to check the cleanliness of the surface. Blatter-pyr was synthesized as described in Ref [1]. The radical thin films were prepared by OMBD (evaporation rate: 0.1-0.6 nm/min). The evaporation rate was estimated with a quartz microbalance and the film thickness was calculated from the attenuation of the substrate Co 2p photoemission line upon radical deposition. The XPS measurements were performed in the measuring chamber equipped with a monochromatic Al Kα source (SPECS Focus 500) and a SPECS Phoibos 150 MCD hemispherical electron analyzer. The survey spectra were recorded at 50 eV pass energy and the high-resolution spectra at 20 eV pass energy. The XPS binding energies were calibrated by setting the Co 2p signal at 778.3 eV.[2] The energy resolution was 0.4 eV. All photoemission measurements were performed in normal emission.

NEXAFS measurements were conducted at the LowDosePES end-station at the PM4 beamline ($E/\Delta E$ = 6000 at 400 eV) of the BESSY II synchrotron facility in Berlin.[3] The end-station is a multi-chamber set-up with a separate preparation chamber, used for sputtering and annealing the cobalt surface and film deposition. Film evaporation was done using the same calibrated cells as in the above-described XPS experiments. The measuring chamber base pressure was 4×10^{-10} mbar. The spectra were recorded in total electron yield (TEY) at normal incidence (θ_1= 90°) and grazing incidence (θ_2= 20°).

They were normalized by the ring current and the signal of the clean substrate and scaled to an equal edge jump for comparison.[4]

The measurements were performed on freshly prepared films. All samples were carefully monitored to avoid radiation damage during beam exposure.

Data analysis: NEXAFS

By using methods previously developed for EELS spectra;[5] to calculate the absolute intensities, the L_3/L_2-ratio, and branching ratios, the step edge in the NEXAFS spectra was fitted using a sigmoidal curve with the inflection point positioned at the respective peak maximum. After subtracting the step edge, the absolute intensities were calculated from the spectra by integration over their full width (11 eV for the L_3-peak and 8 eV for the L_2-peak, in agreement with the published literature[5]). The calculation of $\mathscr{L}_{3,2}$ (defined as $(I(L_2)+I(L_3)$ normalized to the continuum) requires a normalization factor. The $I(L_2)+I(L_3)$ must be divided by the integrated intensity in the energy window in the continuum (normalization factor). In the literature,[5] the normalization factor, i.e., how to define the width of the energy window, is not discussed.

We define the normalization factor as the factor needed to normalize the 3d occupancy to 7 e/atom in the metallic cobalt surface.[5] We obtained 35 eV as the width of the energy window. The 3d occupancy was calculated according to the equation $n_{3d} = \frac{1-(\mathscr{L}_{3,2}/1.04)}{0.088}$. [5]

To determine the magnetic moment using the ratio $I(L_3)/I(L_2)$, and the linearization of the $I(L_3)/I(L_2)$ ratio,[6] we used the results obtained in the grazing incidence geometry of the NEXAFS experiment.

Note that the experimentally estimated magnetic moment for the molecule/Co interface represents an average value across all Co surface atoms, bonded or not with the molecules.

Data analysis: Cobalt XPS

We estimated the penetration depth of the incident X-ray beam in cobalt around the Co L-edge (defined as the depth in the material at which the intensity of the incident X-rays is $1/e$ of its initial value, and given by $1/\mu$ where μ is the X-ray absorption coefficient in cm^{-1}[4c]) by using the X-ray absorption cross section (in cm^2/g).[7] We obtain penetration depths of around 510 nm in the pre-edge region and 88 nm in the continuum of the L-edge in NEXAFS and 300 nm for the home lab Al K-α radiation.

The information depth in XPS is defined as 3λ, λ being the electron inelastic mean free path (IMFP).[8] To calculate λ corresponding to the electrons emitted from the cobalt 3s core-levels we used the equation[9] $\lambda_n = \frac{A_n}{E_{kin}^2} + B_n\sqrt{E_{kin}}$.

A_n and B_n are empirical, dimensionless factors given for the IMFP of electrons in inorganic (A_n = 641 and B_n = 0.096) and organic solids (A_n = 31 and B_n = 0.087), and E_{kin} being the kinetic energy of the emitted electrons. For the photon energy corresponding to the Al K-α radiation, we obtained 12.1 nm in the inorganic solid and 9.8 nm in the organic solid.

To calculate the magnetic moment from the XPS Co 3s spectra, we used the relationship: $I(S+1/2)/I(S-1/2)= (S+1)/S$ where I are the intensities of the doublets obtained from the fits and S is the total spins of the unpaired electrons.[10] The spectroscopic lines were fitted by using a Doniach-Sunjic line shape.[10] The magnetic moment was calculated using the equation $\mu = 2\mu_B\sqrt{(S+1)S}$.[10-11]

Also in this case the experimentally estimated magnetic moment for the molecule/Co interface represents an average value across all Co surface atoms.

Calculation details

DFT calculations were carried out with the all-electron code FHI-AIMS.[12] The Perdew–Burke–Ernzerhof (PBE)[13] generalized gradient approximation was assumed for the exchange-correlation density functional. The preconstructed “light” and “tight” default settings were employed for the numerical localized orbital basis sets of the molecule and of the Co atoms, respectively. The calculations of the molecule did not use periodic boundary conditions. The interface was instead simulated through a supercell containing the molecule on the top surface of a four-layer Co slab and including over 20 Å of vacuum. A 3x3x1 k-point grid was chosen. Co was considered in its most common hcp structure with the experimental lattice constant equal to 2.51 Å. The geometry optimizations were performed until the ionic forces were smaller than 0.01 eV. In the case of the slab, the two bottom layers were maintained fixed. XPS simulations were carried out within the initial state approximation and by looking at the density of states (DOS) projected on the basis functions of the individual atoms. A Gaussian broadening of 0.4 eV was applied to the DOS to obtain smooth peaks. The spin magnetic moment of the atoms was estimated through the Mulliken population analysis.

2) Brief description of the fit procedure and parameters for the C 1s and N 1s core level spectra.

A careful best-fit procedure with constraints based on stoichiometry and electronegativity is a powerful tool to gain a deeper insight into the XPS core level spectra. A detailed description of the fit procedure used for the radicals is given in Ref. [14], and a general approach for fitting XPS spectra of organic thin films is also described in Ref [15].

The fit procedure systematically holds for all samples of the film/interface of a specific molecule, prepared and measured under the same conditions. In this way, we can also identify the samples that do not correspond to the expected stoichiometry. We work on sets of measured samples that are large enough to be statistically significant.

The three nitrogen peaks in the Blatter-pyr N 1s spectra are assigned to photoelectrons emitted from the nitrogen bound also to the phenyl ring (N1) and the N2 atom (a carbon atom and a nitrogen atom as neighbors), see also the electronic structure calculations in the main text. Because of the delocalization of the unpaired electron, the peak at lower binding energy is assigned to photoelectrons emitted from the nitrogen radical (N3=Nrad).

Fit parameters for the C 1s and N 1s spectra of a thicker Blatter-pyr film as in Figure 1. R-squared (R^2) = 0.99961, and R^2= 0.98997 for the C 1s, and the N 1s fit, respectively. The expected stoichiometric values for the C 1s and N 1s elemental analyses are C-C = 24%, C-H = 62%, C-N = 14%, and Nrad = N1 = N2 = 33%.

Table S1

	Energy (eV)	**Lorentzian Width (eV)**	**Gaussian Width (eV)**	**Intensity (%)**
C-C	284.4	0.08	0.90	17.7
C-H	284.8	0.08	0.90	47.9
S_1	285.4	0.08	0.90	1.2
C-N	285.9	0.08	0.90	11.6
S_2	286.6	0.08	0.90	4.3
S_3	287.5	0.08	0.90	1.1
S_4	288.4	0.08	1.44	2.0
S_5	291.6	0.08	5.14	14.2

C-C + S_1+S_3+S_4=22.0%, C-H+ S_5=62.1%, C-N + S_2=15.9%

Table S2

	Energy (eV)	**Lorentzian Width (eV)**	**Gaussian Width (eV)**	**Intensity (%)**
Nrad	398.3	0.1	0.8	28.6
N2	399.2	0.1	0.8	28.1
S_1	400.1	0.1	0.8	5.2
N1	401.0	0.1	0.8	29.7
S_2	402.1	0.1	0.8	6.1
S_3	403.0	0.1	0.8	2.3

Nrad+S_1= 33.8%, N2+S_2= 34.2 %, N1+S_3=32.0%

Fit parameters for the C 1s and N 1s spectra of an interfacial Blatter-pyr layer as in Figure 1. R^2= 0.99884 and R^2= 0.92913 for the C 1s and the N 1s fit, respectively.

Table S3

	Energy (eV)	Lorentzian Width (eV)	Gaussian Width (eV)	Intensity (%)
C-C	284.5	0.08	0.90	22.5
C-H	285.0	0.08	0.90	49.8
S_1	285.5	0.08	0.90	1.2
C-N	285.7	0.08	0.90	13.5
S_2	286.4	0.08	0.90	8.0
S_3	287.3	0.08	0.90	1.9
S_4	288.6	0.08	1.44	1.8
S_5	290.5	0.08	5.14	1.3

Table S4

	Energy (eV)	Lorentzian Width (eV)	Gaussian Width (eV)	Intensity (%)
Nrad*	397.2	0.1	0.9	11.4
N2*	397.8	0.1	0.9	31.1
S_{1*}	398.6	0.1	0.9	24.5
N1*	399.5	0.1	0.9	11.5
S_{2*}	400.5	0.1	0.9	18.6
S_{3*}	401.4	0.1	0.9	2.9

3) C Kedge NEXAFS spectra: thick versus interfacial layer.

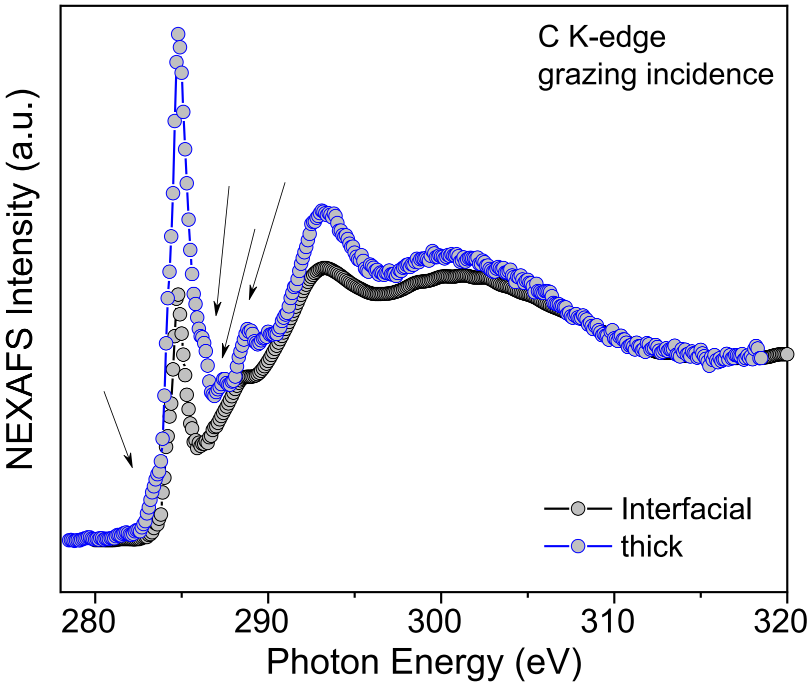

Figure S1. Comparison of the Blatter-pyr C K edge NEXAFS spectra of a thick and an interfacial film, as indicated. The arrows indicate the major differences in the intensity of the two signals as described in the main text.

4) Calculated I(L_3)/I(L_2) ratio, the branching ratio I(L_3)/I(L_2)+I(L_3), and normalized white lines at normal incidence (NI) and grazing incidence (GI).

Table S5.

		I(L_3)	**I(L_2)**	**I(L_3)/I(L_2)**	**I(L_3)/I(L_2)+I(L_3)**	$\mathscr{L}_{3,2}$	**n (e/atom)**
Substrate	NI	10.15	3.75	2.71	0.73	0.39	7.05
	GI	9.06	3.38	2.68	0.73	0.35	7.50
Films	NI	10.43	3.91	2.68	0.73	0.41	6.93
	GI	9.37	3.58	2.62	0.72	0.37	7.36

5) Fit parameters for the XPS Co 3s core level spectra as in Figure 5.

R^2= 0.93347 and R^2= 0.90616 for the fit before and after evaporation.

Table S6

Substrate	**Energy (eV)**	**Δ (eV)**	**Asymmetry parameter**	**Width (eV)**
Component 1	101.3	3.5	0.001	1.4
Component 2	104.8		0.03	4.2
Interfacial film				
Component 1	101.2	4.3	0.001	1.4
Component 2	105.5		0.03	4.4

Table S7

	Intensity I_2/I_1	**Calculated magnetic moment μ_s (μ_B)**
Substrate	0.34	1.78
Film	0.29	1.53

6) Comparison of different adsorption geometries

Since the experiments revealed a high degree of azimuthal disorder in the interfacial layer, DFT calculations were carried out for three different radical/Co geometries checking to what extent the XPS spectrum depends on the molecular adsorption details. All geometries were fully optimized as described in the Methods here in the Supplementary Information. The first geometry [Fig. S2 (b)] is the one presented in the paper; the pyrene unit is oriented along the Co[1010] direction. The phenyl ring attached to N1 remains tilted out of the surface forming a dihedral angle with the rest of the molecule, like in the isolated case. The second geometry [Fig. S2 (c)] presents the molecule rotated so that the pyrene unit is parallel to the Co [0110] direction. Finally, the third geometry [Fig. S2 (d)] is like the first one, but the phenyl ring attached to N1 is forced to be in plane with the rest of the molecule.

The simulated N 1s core level XPS spectra are quite similar for the three geometries, as shown in Fig. S2. The energy splitting between the three characteristic peaks is strongly reduced compared to that seen for the isolated molecule, and overall the spread of the result is within the broadening of the experimental data. The estimated energy splitting for the various geometries is summarized in table S8 (note that the absolute energy of the peaks is not accurately described in our calculations because of the employed approximations, and only the energy splitting is analyzed here).

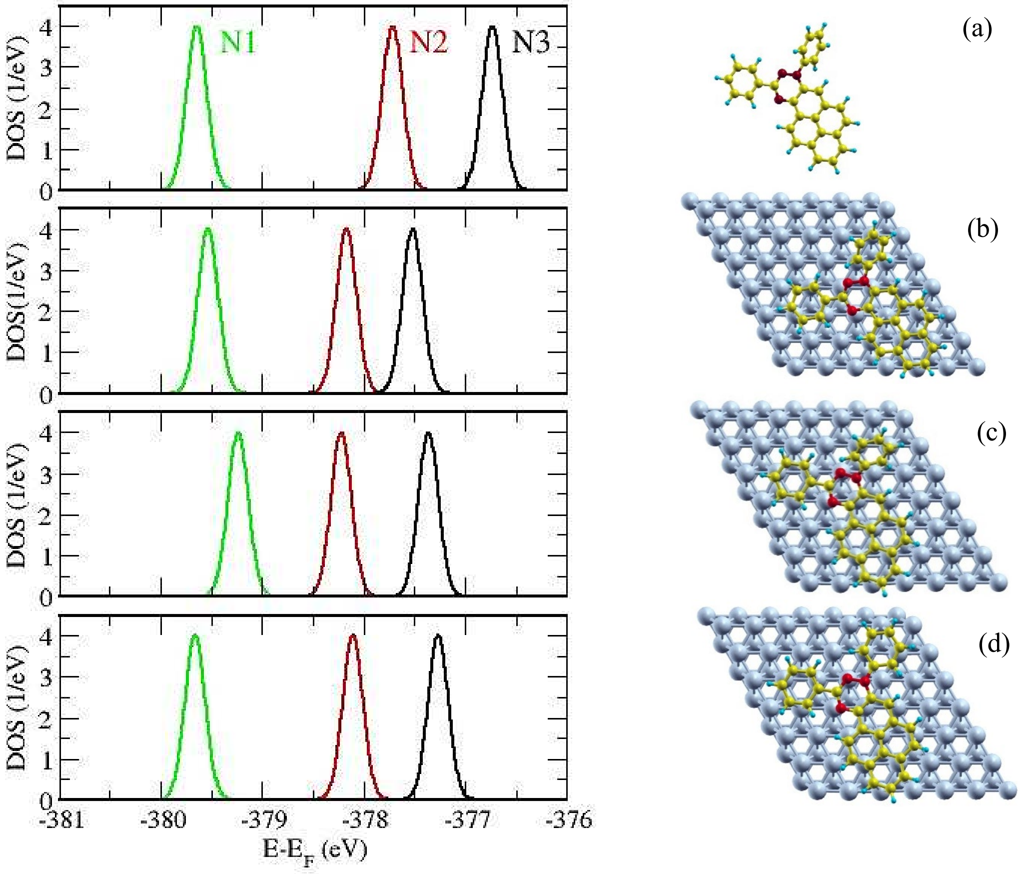

Figure S2. Simulated N 1s XPS spectrum (DOS) for the isolated molecule (a) and three different radical/Co geometries (b, c, d). Each spectrum on the left corresponds to geometry on the right.

Table S8

	ΔE_{N1-N2} (eV)	ΔE_{N1-N3} (eV)	ΔE_{N2-N3} (eV)
isolated (a)	1.92	2.88	0.96
radical/Co (b)	1.37	2.02	0.65
radical/Co (c)	1.02	1.86	0.84
radical/Co (d)	1.54	2.39	0.85

7) Density of states at the Fermi level

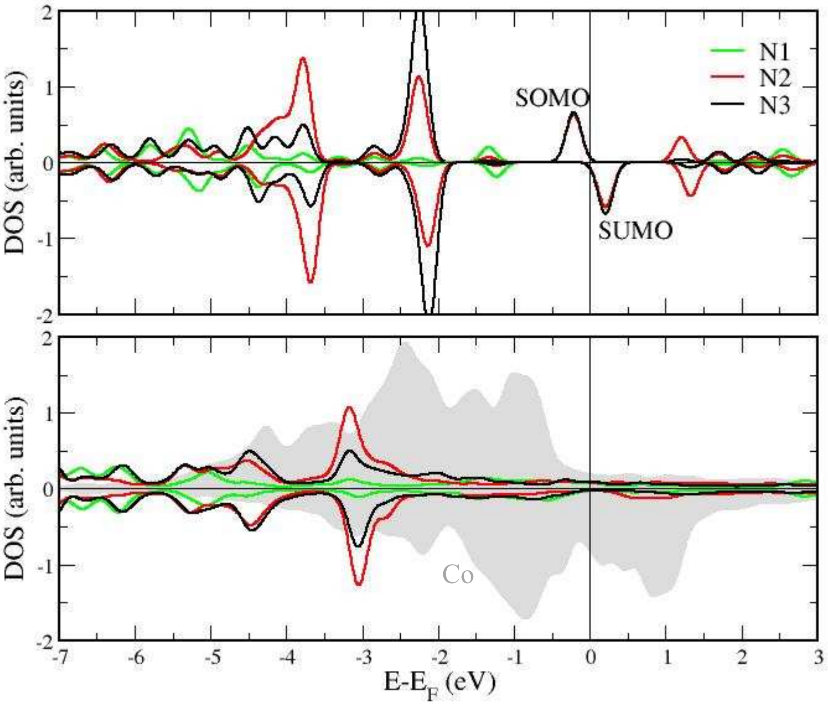

Figure S3. DOS projected over the three N atoms of Blatter-pyr (top panel) and of Blatter-pyr on Co (bottom panel). The single occupied and single unoccupied molecular orbitals, SOMO and SUMO, are indicated in the case of Blatter-pyr. The molecular features disappear when Blatter-pyr is adsorbed on Co. The DOS of the N atoms appears very broad around the Fermi level as results of the strong hybridization with the Co *3d* DOS (grey shadowed area).

8) References

[1] F. Ciccullo, N. M. Gallagher, O. Geladari, T. Chasse, A. Rajca, M. B. Casu, *ACS Appl. Mater. Interfaces* **2016**, *8*, 1805–1812.

[2] B. V. Crist, *Commercially Pure Binary Oxides and a few Common Carbonates and Hydroxides, Vol. 2*, XPS International, LLC, **2005**.

[3] a) R. Ovsyannikov, P. Karlsson, M. Lundqvist, C. Lupulescu, W. Eberhardt, A. Fohlisch, S. Svensson, N. Martensson, *Journal of Electron Spectroscopy and Related Phenomena* **2013**, *191*, 92-103; b) E. Giangrisostomi, R. Ovsyannikov, F. Sorgenfrei, T. Zhang, A. Lindblad, Y. Sassa, U. B. Cappel, T. Leitner, R. Mitzner, S. Svensson, N. Mårtensson, A. Föhlisch, *J. Electron. Spectros. Relat. Phenomena* **2018**, *224*, 68-78.

[4] a) M. B. Casu, P. Cosseddu, D. Batchelor, A. Bonfiglio, E. Umbach, *J. Chem. Phys.* **2008**, *128*, 014705; b) M. B. Casu, A. Scholl, K. R. Bauchspiess, D. Hubner, T. Schmidt, C. Heske, E. Umbach, *J. Phys. Chem. C* **2009**, *113*, 10990-10996; c) J. Stöhr, *NEXAFS Spectroscopy*, Springer, **2003**; d) A. Schöll, Y. Zou, T. Schmidt, R. Fink, E. Umbach, *J. Electron. Spectros. Relat. Phenomena* **2003**, *129*, 1-8.

[5] a)D. H. Pearson, B. Fultz, C. C. Ahn, *Appl. Phys. Lett.* **1988**, *53*, 1405-1407; b) D. H. Pearson, C. C. Ahn, B. Fultz, *Phys Rev. B* **1993**, *47*, 8471-8478.

[6] a) S. Ii, K. Hirayama, K. Matsunaga, H. Fujii, S. Tsurekawa, *Scr. Mater.* **2013**, *68*, 253-256; b) M. Stöger-Pollach, *Scr. Mater.* **2013**, *69*, 820-822; c) D. M. Pease, A. Fasihuddin, M. Daniel, J. I. Budnick, *Ultramicroscopy* **2001**, *88*, 1-16.

[7] B. L. Henke, E. M. Gullikson, J. C. Davis, *Atomic Data and Nuclear Data Tables* **1993**, *54*, 181-342.

[8] C. J. Powell, *Journal of Electron Spectroscopy and Related Phenomena* **1988**, *47*, 197-214.

[9] M. P. Seah, W. A. Dench, *Surface and Interface Analysis* **1979**, *1*, 2-11.

[10] *Surface analysis by Auger and X-ray photoelectron spectroscopy*, IM Publications and SurfaceSpectra Limited, , Cromwell Press, Trowbridge, UK, , **2003**.

[11] I. N. Shabanova, N. S. Terebova, *Surf. Interface Anal.* **2010**, *42*, 846-849.

[12] V. Blum, R. Gehrke, F. Hanke, P. Havu, V. Havu, X. Ren, K. Reuter, M. Scheffler, *Comput. Phys. Commun.* **2009**, *180*, 2175-2196.

[13] a)J. P. Perdew, K. Burke, M. Ernzerhof, *Phys. Rev. Lett.* **1996**, *77*, 3865-3868; b) J. P. Perdew, K. Burke, M. Ernzerhof, *Phys Rev Lett* **1997**, *78*, 1396-1396.

[14] T. Junghoefer, E. M. Nowik-Boltyk, J. A. de Sousa, E. Giangrisostomi, R. Ovsyannikov, T. Chassé, J. Veciana, M. Mas-Torrent, C. Rovira, N. Crivillers, M. B. Casu, *Chem. Sci.* **2020**, *11*, 9162-9172.

[15] a) S.-A. Savu, I. Biswas, L. Sorace, M. Mannini, D. Rovai, A. Caneschi, T. Chassé, M. B. Casu, *Chem.-Eur. J.* **2013**, *19*, 3445-3450; b) S.-A. Savu, M. B. Casu, S. Schundelmeier, S. Abb, C. Tonshoff, H. F. Bettinger, T. Chassé, *RSC Adv.* **2012**, *2*, 5112-5118.

Acknowledgements

First, I express my gratitude to my doctoral adviser, Prof. Dr. Benedetta Casu, a recognized female scientist, for the opportunity to join her research group, her guidance and support during my doctoral program, and her valuable life lessons. I sincerely thank you for your "gentle" push when I needed it, for refilling my passion and dedication to finishing this work.

A special thanks goes to Dr. Tobias Junghöfer for his technical support during my measurements and assistance with data analysis and software issues. He always found the time and patience to answer all my questions on various topics. Thank you for your delightful companionship on our journeys to other cities.

I am also grateful to Dr. Arkaprava Das for his help on the last experiments and our enriching conversations about science and life.

I also thank Prof. Dr. Heiko Peisert and his group members Maren Klein, Carolin Schüle and Eric Juriatti for their technical assistance during the repairs of the Mono machine and for the enjoyable time we spent together.

I am also grateful to Dr. Erika Giangrisostomi, Dr. Ruslan Ovsyannikov and Dr. Danilo for the technical support during the beamtimes at Bessy II facility.

I would like to thank Elke Nadler for SEM measurements.

My work was partly supported by the Federal Ministry of Education and Research (BMBF) through the project “RadicalQuantum” (contract number 05K22VT1).

I want to thank all members of the Casu group for a rewarding and joyful time together. It was a pleasure to participate in our culinary endeavours, filled with delicious food, cortados, and the best pizza in Italy.

I want to express my deepest gratitude to my parents, Zofia and Henryk Bochenek, for providing me with the access to early education, which set the first step on my journey to the PhD program.

I am grateful to my parents in low Bozena and Jerzy Nowik-Boltyk for taking care of Luke when I was not at home and for making the family and PhD work.

Finally, I want to thank my two men, my husband Patryk and my son Luke Nowik-Boltyk, with all my heart for their love, for always encouraging me, lifting me up, and waiting for me at home.